Title
Synthesis and Magnetic Properties of Two-Coordinate Transition Metal Complexes

Author
Bunting, Philip Colin

Publication Date
2019

Peer reviewed|Thesis/dissertation

Synthesis and Magnetic Properties of Two-Coordinate Transition Metal Complexes

by

Philip C. Bunting

A dissertation submitted in partial satisfaction of the

requirements for the degree of

Doctor of Philosophy

in

Chemistry

in the Graduate Division

of the

University of California, Berkeley

Committee in charge:

Professor Jeffrey R. Long, Chair
Professor Christopher J. Chang
Professor Michael F. Crommie

Spring 2019

Synthesis and Magnetic Properties of Two-Coordinate Transition Metal Complexes

Philip C. Bunting

Abstract

Synthesis and Magnetic Properties of Two-Coordinate Transition Metal Complexes

by

Philip C. Bunting

Doctor of Philosophy in Chemistry

University of California, Berkeley

Professor Jeffrey R. Long, Chair

Chapter 1 of this dissertation provides an introduction to the field of single-molecule magnetism through the lens of two-coordinate transition metal complexes. Single-molecule magnets are a class of materials which display magnetic properties, such as magnetic hysteresis, typically only observed for bulk materials. Given their small size, with many single-molecule magnets utilizing only one magnetic ion, these materials are also subject to quantum effects. The marriage of classical and quantum properties provides intriguing possibilities for the applications of these materials. From the perspective of basic research, they provide the challenge of controlling the electronic structure of these molecules down to the magnetic microstate level. Two-coordinate transition metal complexes provide excellent insight to the field as a whole, as it is possible to understand the relationships between molecular structure, electronic structure, and magnetic microstate structure and mixing. By understanding their electronic structure and magnetic anisotropy, it is also possible to gain insight into the mechanisms by which magnetic relaxation occurs.

Chapter 2 and *Chapter 3* are closely related. Calculations on a hypothetical complex which featured a linear C–Co–C moiety, $Co(C(SiMe_3)_3)_2$, predicted a magnetic anisotropy near the physical limit (determined by the Co(II) spin-orbit coupling constant) arising from a non-Aufbau electronic structure, $(d_{x^2-y^2}, d_{xy})^3(d_{xz}, d_{yz})^3(d_{z^2})^1$. These calculations ignited a synthetic endeavor to isolate the first dialkyl Co(II) complex. *Chapter 2* details the first success in this endeavor with the isolation of $Co(C(SiMe_2OPh)_3)_2$. However, long-range Co···O interactions led to a significantly bent C–Co–C axis, and thus $Co(C(SiMe_2OPh)_3)_2$ behaved as an unremarkable single-molecule magnet. Other complexes of the type $M(C(SiMe_2OPh)_3)_2$ (M = Cr, Mn, Fe, Zn) were synthesized in an effort to understand the deviation from linearity. Ultimately the bend in the in the C–Co–C axis arises from a compromise of several stabilizing forces. The ligand field stabilization energy is relatively weak and interligand non-covalent interactions are essential for the stability of the complexes; when those interligand interactions are not sufficiently strong, the metal moves closer to the nearby oxygen atom for additional stabilization. Though this metal-oxygen distance is longer than an actual metal-oxygen bond, the interaction is sufficient to both stabilize the molecule and destroy the magnetic anisotropy expected from the linear moiety.

Chapter 3 details the end result of a search for a ligand which would support a linear C–Co–C moiety. By moving from phenyl to naphthyl substituents, the interligand non-covalent interactions were greatly enhanced. The complex, $Co(C(SiMe_2ONaph)_3)_2$, exhibits a non-Aufbau ground

state—an unprecedented electronic structure for a transition metal molecule—which arises from an extremely weak and high symmetry ligand field. The electronic structure is confirmed by dc magnetic susceptibility, *ab initio* calculations, and experimental charge density maps. Additionally, the electronic structure has the maximal orbital angular momentum for a transition metal complex, a property that was only recently observed in cobalt adatoms and is novel for a molecule. Due to the unquenched orbital angular momentum this molecule displays magnetic anisotropy that is near a physical limit for transition metals. The spin-reversal barrier, determined by a combination of variable-field far-IR spectroscopy and ac magnetic susceptibility, is the largest spin-reversal barrier (450 cm^{-1}) for any transition metal containing molecule.

Chapter 4 provides the beginning of a new synthetic endeavor for linear transition metal complexes. Magnetic anisotropy is typically limited by the spin-orbit coupling constant of the constituent magnetic ions. For mononuclear transition metal complexes, metal-ligand covalency nearly always diminishes magnetic anisotropy compared to the free-ion values. One possible exception to this trend is through the use of heavy ligands (i.e. ligands of the 4p, 5p, etc. rows), which have been shown to enhance magnetic anisotropy. Thus, complexes of the type $[Fe(SiR_3)_2]^{0/-}$ were targeted. While no such complex was successfully synthesized, there are several promising leads in this direction. Specifically, the novel ligands $[Si(carbazole)_3]^-$ and $[Si(2,7\text{-dimethylcarbazole})_3]^-$ provide several interesting new structures, including a new two-coordinate zinc complex, $Zn(Si(carbazole)_3)_2$.

Table of Contents

Acknowledgements

These are perhaps the hardest few pages I'll have to write during my PhD. For one, they are the only pages that will be read by the majority of people who touch my dissertation.[1] Secondly, I am certain that there will be people who I leave out who helped me in some way or another in the past six and a half years. While I'm sure they know how much I appreciate them, it is unfortunate that my future biographer(s) will not have an exhaustive list of people who helped me on my path to saving the world with magnets.

Thanks first to my parents, the rest of my family, and my friends from home. My parents helped me start my academic career by helping me with homework and proofreading my papers at the kitchen table many years ago and have continued to off their assistance through grad school, with my dad offering to look at my Excel spreadsheets and my mom sending me roughly 500 boxes of brownies, cookies, donuts, and other treats. My friends from home—Adam, Bryan, Chris, Eugene, and Ken—have provided near daily distractions and entertainment over the last decade. Adam is perhaps my biggest fan in terms of my writing and my science. Eugene, despite being halfway across the country, has propped me up during the particularly difficult periods of grad school and helped turn challenging periods into opportunities for personal growth.

My scientific career in its current form began with my high school chemistry teacher, Tom Wisard, whose introduction to chemistry laid the foundation for much of what became my chemical intuition. At Ohio State I was incredibly fortunate to be taken under the mentorship of Chris Hadad, who helped me start my research career in a grand fashion by encouraging me to apply to the Beckman Scholars program and has continued to provide helpful advice at each stage of grad school (usually over a gyro at Buckeye Donuts). At the end of my freshman year I joined Malcolm Chisholm's lab. Despite having nearly 700 publications at the time, Malcolm ran his group by having personal relationships with each lab member. I distinctly remember him shaking my hand and congratulating me when he saw two well isolated reduction waves in a mixed valence complex, despite the fact that I had no idea what had just happened. When it came time to write the manuscript, he wrote the first draft by hand with my help. I worked with two postdocs in Malcolm's lab who were both excellent mentors and friends: Ben Lear and Vesal Naseri. Ben has continued to provide both excellent advice and an excuse to skip half a day of ACS conferences to get drinks.

I came to Berkeley in the summer before my first year of grad school and was quickly adopted by the older students in the group, particularly Eric Bloch and Joe Zadrozny. Joe immediately became my magnet mentor. Single-molecule magnetism is not very accessible for first year grad students; without Joe it would have taken me significantly longer to build the foundation necessary to ultimately do unique research in the field. In this respect thanks also to Katie Meihaus, who continues to give helpful feedback on both magnetism and writing.

I officially joined the lab in the fall of 2012. Jeff was immediately excited and supportive of my ideas on magnetic double exchange. This dissertation is not at all about double exchange. In fact, none of the things I did in my first two years are in this dissertation. I pitched a lot of project

[1] The obvious exception being future grad students trying to figure out what a completed dissertation looks like and/or what sort of formatting is acceptable. For those in the latter category, I highly recommend having figures and captions take the entire width of the page. While it doesn't look as nice as if you had in-line figures that fit snuggly into corners of pages, it is significantly easier, and the only people who will really notice will be future future grad students looking at your dissertation trying to figure out what a completed dissertation looks like and/or what sort of formatting is acceptable.

ideas in those two years and Jeff's reactions were always at least neutral, sometimes positive, and he never discouraged me from trying new things. I mostly appreciate his patience. When I got more invested in the projects involving two-coordinate transition metal complexes, he was significantly less worried about how long the project was taking than I was. The project that ultimately became the *Science* paper would not have happened in another lab, partially because it took so long, and also because Jeff was able to help me assemble an excellent team of collaborators.

On the subject of collaborators, I was able to work with many excellent scientists over the past few years on projects, some of which have work which significantly contributed to the work in this dissertation. I wish I could print my emails with Mihail Atanasov and publish them as their own chapter, the title of which would be "Questions you've always wanted to ask a theorist but were too embarrassed to ask."

As for my peers at Berkeley, I could not have asked for a better group of coworkers and friends. My friends outside of grad school helped me maintain a healthy, balanced life. I especially appreciate all of my friends at BCF for providing an atmosphere in which I could work on long term fitness goals under the guise of hanging out with friends. It was also great to spend time with so many fellow grad students who weren't necessarily in the Long lab or even chemistry: my lunch crews of Nick Settineri, Parker Deal, Tyler Hurlburt, and Rodi Torres-Gavosto as well as all of my teammates on Soctopus, Strawspeedies, and the CoC Fighters.

Finally, I can't understate how much I appreciated my coworkers in the Long lab. I'm looking forward to the work coming out of the current magnetism subgroup with Alex Vincent, Dan Lussier, Colin Gould, and Job Chakarawet. Special thanks to Colin and Job—Colin for letting me ask him very simple organic chemistry questions and Job for his crystallography help. My cohort was fantastic. Doug Reed was the first person I knew in Berkeley; we became visit weekend friends and then lived together for two(ish) years. Matt Kapelewski kickstarted my social life in my first year by saying "we should hang out more." This level of directness is something that I appreciate in Matt and is part of the reason we remain good friends. Lucy Darago ran the magnetism subgroup during most of my time here and for that I am extremely grateful. She also was a sounding board for many of my ideas and it was nice that her desk was within chair-rolling distance of mine (with an aggressive roll). And a final thanks to Mercedes Taylor, with whom I shared *a lot* of frozen yogurt with and talked about anything that happened to be going on in our lives (chemistry and otherwise).

As previously stated, it is impossible to properly thank everyone who helped me get to this point, so I'll have to end here. As the saying goes, "it takes a village to isolate a transition metal complex with a non-Aufbau ground state and maximal orbital angular momentum and then write that (and other things) into a few papers to get some sort of advanced degree out of it."

Chapter 1: Single-Molecule Magnetism Through the Lens of Linearly Coordinated Transition Metal Ions

1.1 Introduction

Nearly three decades after their initial discovery,[1] several single-molecule magnets have now displayed slow magnetic relaxation near or above 77 K. In this recent family of dysprocenium complexes,[2] the highest temperature 100 second relaxation time is 65 K[2d]—compared to the previous record of 20 K[3]—which, given sufficiently fast field-sweep rates, gives rise to magnetic hysteresis at 80 K. This Beamonesque jump in blocking temperatures has reignited a discussion about what exactly the physical limits are for magnetic anisotropy and relaxation times in single-molecule magnets.

Single-molecule magnets are a class of materials which display bulk-like magnetic properties arising from individual molecules.[4] Since their discovery, researchers have been intrigued by their ability to show properties of both bulk systems, such as magnetic hysteresis, and quantum systems, such as tunneling of magnetization. The coexistence of classical and quantum properties allows for possible applications in, for example, information storage,[5] spintronics,[6] and dark matter detection.[7] As a pursuit in fundamental science, they offer the challenge of ultimate fine control of electronic structure—chemists must concern themselves not only with the relationship between molecular structure and orbital structure, but also must consider how, using the tools available to a synthetic chemist, to affect magnetic microstate structure as well as the mixing of these microstates.

Early work in the field focused on the use of ferro- or ferrimagnetically coupled clusters of transition metal ions to obtain large spin states with modest magnetic anisotropy. A paradigm shift in the field occurred in 2003 when a complex featuring a single Dy(III) ion showed single-molecule magnetic properties.[8] Since then the more common approach to single-molecule magnet design is to use relatively few magnetic centers (often just one) in carefully designed coordination environments to maximize the effect of magnetic anisotropy. It took slightly longer to observe single-molecule magnetic properties in a complex featuring a single transition metal,[9] but the field of transition metal mononuclear single-molecule magnetism has arguably progressed more quickly than the lanthanide counterpart, as several of such complexes have been shown to have magnetic anisotropy at or near the physical limits defined by the metal ion.[10-12]

Mononuclear transition metal single-molecule magnets will never have the magnetic anisotropies or relaxation times of mononuclear lanthanide complexes, as the lanthanides possess significantly larger spin-orbit coupling constants. However, transition metal complexes provide valuable insight into all aspects of single-molecule magnetism as their electronic structure is comparatively simple. Herein, we use mononuclear transition metal complexes to discuss the way in which molecular geometry affects magnetic anisotropy, the nature of the magnetic microstates, and magnetic relaxation. We also conceptually link concepts between transition metal and lanthanide electronic structure to provide general guidance on the future of single-molecule magnetism.

1.2 A Note on Terminology

In single-molecule magnetism literature, there is some ambiguity in terminology regarding "spin-reversal barriers" and "effective spin-reversal barriers." Here we use the term "spin-reversal barrier" to mean the magnetic excited state through which thermally activated relaxation occurs, as determined by fitting variable temperature relaxation data from ac magnetic susceptibility

experiments, ideally in combination with spectroscopy or calculations. For many complexes this excited state is the first in the microstate (M_J or M_S) manifold, though for high-performing single-molecule magnets it may be a higher energy microstate. Relaxation processes occurring at energies below this microstate are through-barrier relaxation processes. We suggest adopting the term "magnetic anisotropy energy" to describe the total splitting of the ground S or J states, which closely resembles the definition used in bulk magnetism to describe the energy required to rotate the magnetic moment from parallel to perpendicular to the magnetic axis. The blocking temperature is temperature at which the dc magnetic relaxation time is 100 s; the choice of 100 s is arbitrary and if an application arises which depends on millisecond relaxation time, it would make sense to change this reporting standard. The temperatures at which magnetic hysteresis loops close or susceptibility splits in the field-cooled and zero-field cooled susceptibility measurements are dependent on field and temperature sweep rates, respectively, and make for difficult comparisons across many studies.

1.3 Magnetic Anisotropy

The models for understanding and quantifying magnetic anisotropy differ slightly based on the system under investigation. The systems can be placed into four categories: transition metal complexes with quenched orbital angular momentum, transition metal complexes with unquenched orbital angular momentum, lanthanide complexes, and actinide complexes. We will focus our discussion on transition metal magnetism but will conceptually connect the models used for transition metals to the magnetism of the f-elements.

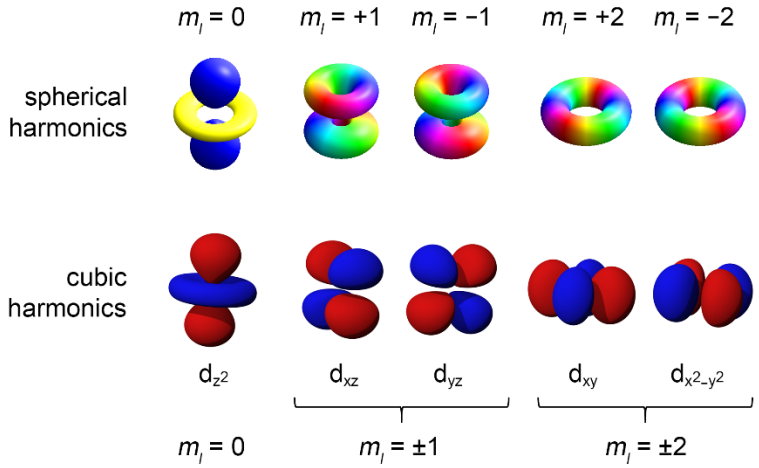

Figure 1.1.[14] Spherical and cubic harmonics for the d-orbitals ($l = 2$). The colors depict the phase of the eigenfunction. Note that orbital angular momentum (m_l) is present in individual spherical harmonics, while for the cubic harmonics it is necessary for conjugate orbital pairs to be degenerate to display non-zero orbital angular momentum.

Magnetic anisotropy arises from orbital angular momentum through spin-orbit coupling. In a classical picture,[13] from an electron's perspective, a charged nucleus orbits an electron with angular momentum l which, through Ampere's law, gives rise to a magnetic moment. The one-electron spin-orbit coupling constant, $\zeta = \hbar^2 ZA\langle r^{-3}\rangle$, where Z is atomic number, r is the orbital radius, and A is a constant, can be intuitively understood from this simple explanation using Ampere's law: spin-orbit coupling increases with more highly charged nuclei with more contracted orbitals. The key component for an orbital magnetic moment (and in turn, magnetic anisotropy) is

orbital angular momentum. Orbital angular momentum is present in the orbitals which are spherical harmonics, which are themselves linear combinations of the orbitals more familiar to chemists—the cubic harmonics, e.g. p_x, d_{z2}, etc. For example, a linear combination of the d_{x2-y2} and d_{xy} orbitals yields the spherical harmonic with $m_l = \pm 2$. When considering the magnetic properties of molecules, the key point to remember is that an electron sitting in a non-degenerate orbital does not have orbital angular momentum; cubic harmonics are like standing waves (Figure 1.1[14]). Orbital angular momentum arises when an electron can circulate between multiple orbitals, either through an orbital degeneracy or excited state interactions.

When considering a single electron sitting in a degenerate pair of d-orbitals, there are eight combinations of d-orbitals which have non-zero orbital angular momentum.[15] Orbitals with $|m_{l,1}|-|m_{l,2}| = \pm 2$ have $L_i = 0$, orbitals with $|m_{l,1}|-|m_{l,2}| = \pm 1$ have $L_i \neq 0$ (i = x or y), and orbitals with $|m_{l,1}|-|m_{l,2}| = 0$ have $L_z = |m_l|$ (recall that d_{z2} has $m_l = 0$, d_{xz} and d_{yz} have $m_l = \pm 1$, and d_{x2-y2} and d_{xy} have $m_l = \pm 2$). An electron in a pair of degenerate orbitals which are rotationally symmetric will have orbital angular momentum along the rotation axis.

When applying this knowledge of orbital angular momentum to single-molecule magnetism there are two points of note. First, magnetic anisotropy of molecules is usually described in terms of a single magnetic axis, and second, the overwhelming majority of transition metal complexes do not have the requisite orbital degeneracy. Regarding the first point, when the magnetic moment prefers to align along a specific axis (the z-axis by convention) defined with respect to the molecular geometry (or crystal lattice) the system has axial magnetic anisotropy, and when the magnetic moment prefers to lie in a plane the system has planar magnetic anisotropy. In systems with axial anisotropy (the majority of single-molecule magnets), when an electron contributes orbital angular momentum (and magnetic anisotropy) in the x or y directions, these contributions are collectively termed transverse anisotropy.

Transition metal complexes typically have orbitally non-degenerate ground states and quenched orbital angular momentum, i.e. $L = 0$. Even in complexes with symmetries that would allow for degenerate orbitals and unquenched orbital angular momentum, Jahn-Teller distortions typically remove any potential orbital degeneracies. For example $Co(Tp)_2$ (Tp = tris(pyrazolyl)borate) features a Co(II) ion in a trigonal prismatic coordination environment, yielding a d-orbital filling of $(d_{z2})^2(d_{x2-y2},d_{xy})^3(d_{xz},d_{yz})^2$. However, Jahn-Teller distortions remove the degeneracy of the d_{x2-y2} and d_{xy} orbitals[16] and this[17] and similar[18] complexes are typically treated as having $L = 0$.

The model for understanding magnetic anisotropy in systems with $L = 0$ employs the phenomenological zero-field splitting (ZFS) Hamiltonian ($\mathbf{H}_{zfs}$) given in Equation 1,[4]

$$\mathbf{H}_{ZFS} = \mathbf{S} \cdot \mathbf{D} \cdot \mathbf{S} \qquad (1)$$

where $\mathbf{D}$ is a symmetric and traceless tensor and has a physical origin in the creation of magnetic anisotropy via excited state interactions as described by Equation 2,[4]

$$\mathbf{D} = -\lambda^2 \sum_n \frac{\langle g|\mathbf{L}|n\rangle\langle n|\mathbf{L}|g\rangle}{E_n - E_g} \qquad (2)$$

where $|g\rangle$ is the ground state function, $|n\rangle$ are functions of excited states, and E_g and E_n are ground and excited state(s) energies; $\mathbf{L}$ is the orbital angular momentum operator, and λ is the spin-orbit coupling parameter which is related to the one electron spin-orbit coupling constant by $\lambda = \pm \zeta/_{2S}$, where the sign is positive (negative) for orbital subshell less (more) than half full. The ZFS Hamiltonian is usually written in terms of axial and transverse anisotropy parameters, D and E respectively, and combined with terms describing the Zeeman interaction, as show in Equations 3-5:[4]

$$H = DS_z^2 + E\left(S_x^2 - S_y^2\right) + g_{\parallel}\mu_B S_z H_z + g_{\perp}\mu_B S_{\perp} H_{\perp} \qquad (3)$$

$$D = 3D_{zz}/2 \qquad (4)$$

$$E = \left|D_{xx} - D_{yy}\right|/2 \qquad (5)$$

where D_{uu} (u = x, y, z) are the principle values of the **D** tensor, and H_u is the applied field. Because $L = 0$ the electronic state of interest is the ground S state, which splits into $2S + 1$ microstates, M_S, where M_S describes the projection of S along the magnetic axis. When D is negative, the system has axial anisotropy and the $M_S = \pm S$ are stabilized; when D is positive, the system has planar anisotropy and the $M_S = 0$ or $\pm 1/2$ states are stabilized.

In some cases, it is trivial to predict the sign of D based on a d-orbital splitting diagram. Excited states which arise from the movement of an electron between two orbitals of the same m_l value will contribute only to axial anisotropy (negative contributions to D) while excited states arising from the movement of an electron between two orbitals of differing m_l values will contribute to planar (positive contributions to D) and transverse anisotropy (positive or negative contributions to E).[19] Per Equation 2, the magnitude of the contribution of a specific excited state is inversely proportional to the ground to excited state energy difference. Referring again to $Co(Tp)_2$, the origin of the large axial anisotropy is clear: to a first approximation the d-orbital occupation is $(d_{z2})^2(d_{x2-y2},d_{xy})^3(d_{xz},d_{yz})^2$ and although a Jahn-Teller distortion removes the degeneracy of the d_{x2-y2} and d_{xy} orbitals, the excited state which contributes the most to magnetic anisotropy arises from an electron moving between d_{x2-y2} and d_{xy} orbitals ($m_l = \pm 2$).

With this predictive power, synthetic chemists can be deliberate in their ligand and molecule design in an effort to synthesize molecules with large magnetic anisotropy. For example, in homoleptic $[Co(SR)_4]^{2-}$ complexes, computational studies show that the axial anisotropy parameter D can vary from −80 to 20 cm^{-1} by changing the S–Co–S angle in a tetragonally distorted CoS_4 moiety,[20] and that for a fixed geometry of the central CoS_4 moiety D can vary from −250 to 50 cm^{-1} depending on the R–S–Co–S torsion angle.[21] Indeed, some of the largest anisotropies observed in systems with a single transition metal ion with $L = 0$ are tetragonally elongated pseudotetrahedral Co(II) complexes with acute L_1–Co–L_2 angles (with L_1 and L_2 being related by a C_2 rotation around the z-axis).[22,23] In both cases, the acute bond angles are enforced by having L_1 and L_2 be part of a bidentate ligand, and the anisotropy arises from having the lowest energy excited state be from an electron moving between the $m_l = \pm 2$ orbitals.

While the magnetic properties of the vast majority of transition metal complexes are best explained assuming $L = 0$, a handful of complexes possess unquenched orbital angular momentum and must be treated in a different manner. The only way to achieve $L \neq 0$ is with linear coordination environments, which are not susceptible to Jahn-Teller distortions.[24] In systems with $L \neq 0$, the explanation of magnetic properties begins with the spin-orbit coupling Hamiltonian shown in Equation 6,

$$\mathbf{H}_{SOC} = \lambda \mathbf{LS} = \pm\left(\zeta/_{2S}\right)\sum_i \mathbf{l}_i \mathbf{s}_i \qquad (6)$$

where λ is the effective spin-orbit coupling constant, ζ is the atomic spin-orbit coupling constant, and $\mathbf{L} = \sum_i \mathbf{l}_i$ and $\mathbf{S} = \sum_i \mathbf{s}_i$ are the operators for the orbital and spin-angular momenta, respectively; the index i sums over individual electrons and the sign is positive (negative) when the orbital shell is less (more) than half full. In systems with doubly degenerate ground states $\mathbf{H}_{SOC}$ can be simplified to[25]

$$\mathbf{H}_{SOC} \approx \pm\left(\zeta/_{2S}\right)\sum_i \mathbf{l}_{z,i} \mathbf{s}_i \qquad (7)$$

where only the z-component of the orbital angular momentum operator is used. This simplification ignores electron excitations between orbitals of differing m_l values. It is important to remember

that in this treatment, L_z is a good quantum number, but L is not. Similarly, the total angular momentum of these systems is described by $J_z = S + L_z$. In this approximation, it is straightforward to predict the splitting of the microstates of J_z by spin-orbit coupling, as shown in Equation 8,

$$E(M_J) = \left(\zeta/_{2S}\right) M_L M_S \qquad (8)$$

where M_J, M_L, and M_S are the projections of total angular momentum, orbital angular momentum, and spin angular momentum along the z axis. Several energy diagrams are shown for key known and hypothetical linearly coordinated transition metal ions in Figure 1.2. Note that when Equation 8 is applicable, the magnetic anisotropy energy is ζM_L and the ground to first excited M_J state energy separation is equal to $\zeta M_L/2S$. A closer look at several of these diagrams will illuminate the inner workings of Equation 7. Consider the complex $Fe(C(SiMe_3)_3)_2$.[10,25-27] It has a d-orbital filling of $(d_{x2-y2},d_{xy})^3(d_{xz},d_{yz})^2(d_{z2})^1$, where d_{x2-y2} and d_{xy} as well as d_{xz} and d_{yz} are degenerate due to the C_3 symmetry, and that degeneracy is unaffected by Jahn-Teller distortions. Orbital angular momentum arises from the three electrons in the degenerate $m_l = \pm 2$ orbitals; thus the ground state has $S = 2$, $L_z = 2$, $J_z = 2$. The J_z state is split by spin-orbit coupling ($\zeta(Fe^{2+}) = 410$ cm^{-1})[28] to give a magnetic anisotropy energy of 820 cm^{-1} and a ground to first excited M_J energy difference equal to 205 cm^{-1}. In reality, *ab initio* calculations suggest a magnetic anisotropy energy of 800 cm^{-1} (ref. 25) and a ground to first excited state energy difference of 180 cm^{-1} (which in this case is also the spin-reversal barrier, as determined by variable temperature relaxation data).[27]

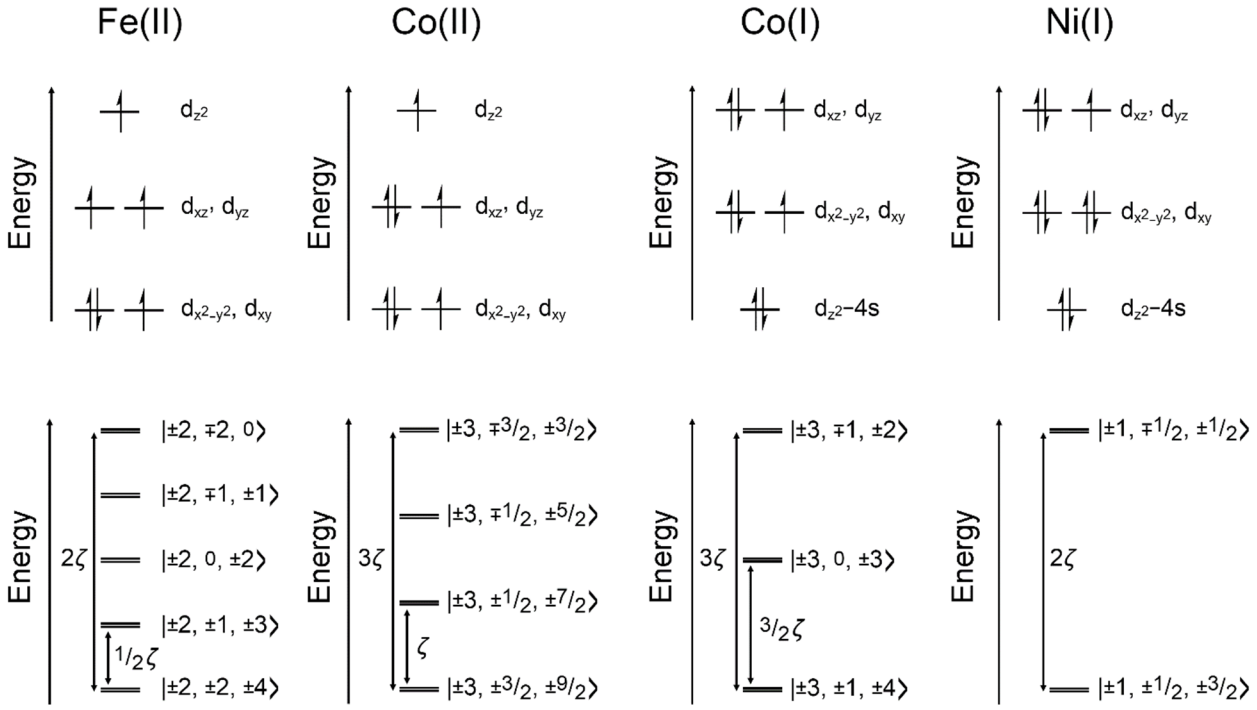

Figure 1.2. Orbital energy diagrams (top) and their corresponding microstate energy diagrams (bottom) for several ML_2 complexes where M is a 3d metal ion and ML_2 has cylindrical symmetry along the z-axis. The eigenfunctions of the microstate doublets are described by $|M_L, M_S, M_J\rangle$, where the three terms describe the projection of orbital angular momentum L, spin S, and total angular momentum J, along the z-axis. The energy splitting of the microstates is determined by H_{SOC}.

In comparing the back-of-the-napkin picture of linear Co(II) versus $Co(C(SiMe_2ONaph)_3)_2$ we can begin to see breakdown of Equations 7 and 8. The predicted ground to first excited M_J state energy difference is 533 cm^{-1} (ref. 28) while the experimentally determined value is 450 cm^{-1}.[12]

In general, real systems will have smaller magnetic anisotropy energies than predicted because Equations 7 and 8 use free ion values of ζ, and any metal-ligand covalency will decrease the actual spin-orbit coupling value. One possible exception to this trend would be through the use of heavy ligands, which have been shown to slightly increase magnetic anisotropy.[29] Deviations from high symmetry will also decrease magnetic anisotropy, as illustrated by a series of linear or near-linear Fe(II) complexes.[25,30]

Systems with slight deviations from axial symmetry illustrate the connection between H_{SOC} and H_{ZFS}. Consider again a linear L–Fe(II)–L system with a ^{5}E ground state with a d-orbital filling $(d_{x2-y2},d_{xy})^3(d_{xz},d_{yz})^2(d_{z2})^1$. As the L–Fe–L bond angle moves away from 180°, the degeneracy of the two sets of *e* orbitals will lift, and microstates with $\Delta M_S = 0$ will begin to mix. This mixing is partially suppressed by spin-orbit coupling, with mixing increasing with decreasing M_S values. At some bond angle it will no longer be a useful approximation to call the ground state degenerate with unquenched orbital angular momentum; instead, the ^{5}E system will split into two non-degenerate quintet states, with d-orbital fillings of $(d_{x2-y2})^2(d_{xy})^1(d_{xz})1(d_{yz})^1(d_{z2})^1$ and $(d_{x2-y2})^1(d_{xy})^2(d_{xz})1(d_{yz})^1(d_{z2})^1$, respectively. As these two states are still relatively close in energy, excited state contributions will still yield large magnetic anisotropy according to H_{ZFS}, as depicted in Figure 1.3.

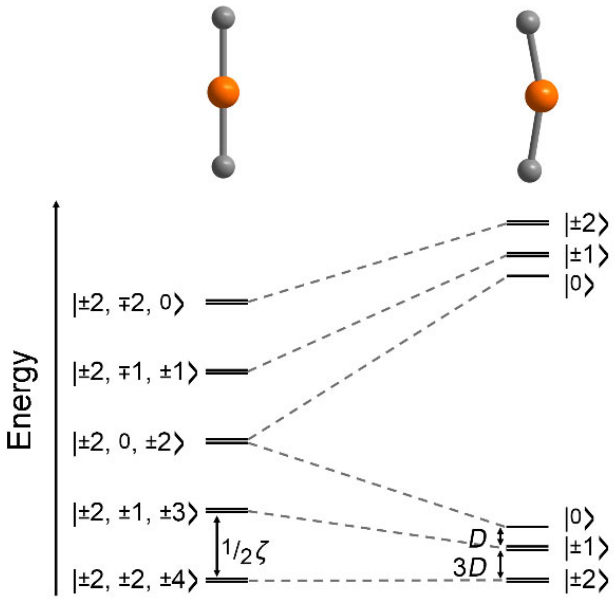

Figure 1.3. Microstate splittings of a two-coordinate system that is either linear or bent. When linear, the microstates are split according to H_{SOC} and are described by $|M_L, M_S, M_J\rangle$. When the molecule bends sufficiently to remove orbital degeneracies, the microstates are described by $|M_S\rangle$ and their splitting is determined by H_{ZFS}. The energy of the excited quintet in the bent orientation is primarily determined by the energy of the lowest energy d-d transition, and the splitting of both the ground and excited quintets arises from microstate mixing between the two sets.

Two structure types are proposed in Figure 1.2 which have not yet been observed, but would have potentially interesting magnetic properties. Linear Co(I) and Ni(I) complexes could provide exceptionally large magnetic anisotropy, provided they are in the right coordination environment. The d-orbital fillings proposed for these systems account for the mixing of $3d_{z2}$ and 4s orbitals which is known for M(I) complexes and lowers the energy of the resulting molecular orbital below the d_{x2-y2} and d_{xy} orbitals. Both complexes would have ground to first excited M_J energies larger

than what was observed for $Co(C(SiMe_2ONaph)_3)_2$, and the linear Ni(I) complex would have a significantly larger magnetic anisotropy energy. While a number of two-coordinate Co(I)[31-35] and Ni(I)[35-41] complexes are known, none have the requisite threefold symmetry for unquenched orbital angular momentum.[42]

Complexes with a linearly coordinated transition metal ion are sometimes described as "free ion like,"[26] but in some ways they are also similar to lanthanide complexes, which always display unquenched orbital angular momentum. The case of Co(II) is an excellent example of how complexes with linearly coordinated transition metal ions are similar to lanthanide complexes, while ultimately still being in their own category. The d-orbital filling observed for $Co(C(SiMe_2ONaph)_3)_2$ is $(d_{x2-y2},d_{xy})^3(d_{xz},d_{yz})^3(d_{z2})^1$, instead of the expected $(d_{x2-y2},d_{xy})^4(d_{xz},d_{yz})^2(d_{z2})^1$.[12] The deviation from the expected Aufbau filling of electrons arises because the ligand field is so weak that both interelectron repulsion and spin-orbit coupling have significant affects on the electronic ground state, as is always the case for lanthanide complexes. However, a major difference arises in the microstate structure of $Co(C(SiMe_2ONaph)_3)_2$. The ground state has $S = {}^3/_2$, $L_z = 3$, $J_z = {}^9/_2$, with spin-orbit coupling splitting the ground J_z state into M_J states $\pm{}^9/_2$, $\pm{}^7/_2$, $\pm{}^5/_2$, and $\pm{}^3/_2$, with a notable absence of $M_J = \pm{}^1/_2$. This is in stark contrast to, for example, a Dy(III) complex with $S = {}^5/_2$, $L = 5$, and $J = {}^{15}/_2$. Because L is a good quantum number, the microstates of the ground $J = {}^{15}/_2$ state split into eight doublets with $M_J = \pm{}^{15}/_2$, $\pm{}^{13}/_2 \ldots \pm{}^1/_2$. While it is typically not wise to assign f-orbital fillings for lanthanide complexes, it can provide a useful comparison in this case. For $Co(C(SiMe_2ONaph)_3)_2$, the ground state L_z value arises because there are two sets of three electrons in the $m_l = \pm 2$ and $m_l = \pm 1$ orbitals. When constructing microstate diagrams as in Figure 1.2, an L_z value other than 3 requires the promotion of an electron to a relatively high energy excited state (an $L_z = 0$ state lies at 1500 cm^{-1}).[12] In contrast, the theoretical complex $[DyO]^+$ has an f-orbital filling of $(f_{y(3x2-y2)},f_{x(x2-3y2)})^3(f_{z(x2-y2)},f_{xyz})^3(f_{yz2},f_{xz2})^2(f_{z3})^1$ (ref. 43) which, in the strong field regime[44] would have $S = {}^5/_2$, $L_z = 5$, and $J_z = {}^{15}/_2$; because the movement of electrons between f-orbitals is relatively uninhibited in lanthanide complexes, $L = 5$ and $J = {}^{15}/_2$ remain good quantum numbers.

It is possible, at least *in silico*, to make the microstate structure of a transition metal ion look like that of a lanthanide—all that matters is the ratio of ligand field strength to spin-orbit coupling strength. Here we will use the splitting of d- and f-orbitals as a proxy for ligand field strength. Calculations on $Co(C(SiMe_2ONaph)_3)_2$ determine that the d-orbitals span 5500 cm^{-1};[12] the spin-orbit coupling constant ζ for Co(II) is 513 cm^{-1}.[28] Modeling of spectroscopic data of $Dy(N(SiMe_3)_2)_3$ determine that the f-orbitals span 1300 cm^{-1} and calculate a spin-orbit coupling term of 1914 cm^{-1}.[45] If the C–Co–C moiety were stretched such that the d-orbitals spanned only 250 cm^{-1}, a microstate structure would emerge that would be similar to that of, for example, $[DyO]^+$ (Figure 1.4).[43] In cylindrical symmetry, the ground ^4F Co(II) free ion term splits into $^4\Phi$, $^4\Sigma^-$, $^4\Pi$, and $^4\Delta$ states.[12] It was previously mentioned that the ground $^4\Phi$ state of $Co(C(SiMe_2ONaph)_3)_2$ lacks a $M_J = \pm{}^1/_2$ microstate; this missing microstate is in the excited $^4\Sigma^-$, $^4\Pi$, and $^4\Delta$ states. As the C–Co–C moiety stretches the ligand field states collapse and the $M_J = \pm{}^1/_2$ microstate reemerges. Simultaneously, because the movement of electrons between d-orbitals is now relatively uninhibited, L becomes a good quantum number. The presence of L_x and L_y in determining magnetic anisotropy yields a microstate picture in which the lowest energy M_J states have relatively large splitting compared to the splitting of higher energy microstates.

It is also possible, at least *in papyro*, to make the microstate structure of a lanthanide ion look like that of a linearly coordinated transition metal ion. As mentioned above, a linearly coordinated lanthanide has an f-orbital filling of $(f_{y(3x2-y2)},f_{x(x2-3y2)})^3(f_{z(x2-y2)},f_{xyz})^3(f_{yz2},f_{xz2})^2(f_{z3})^1$. In the strong

field regime this yields a ground state with $S = {}^5/_2$, $L_z = 5$, and $J_z = {}^{15}/_2$, and microstates that span from $M_J = \pm{}^{15}/_2$ to $M_J = \pm{}^5/_2$. Given $\zeta_{Gd(III)} = 1600$ cm^{-1},[46] the magnetic anisotropy energy in this case is 8000 cm^{-1} and the splitting between each microstate is 1600 cm^{-1}. This is the upper limit of anisotropy for a Dy(III) system. However, considering that calculations of $[DyO]^+$ on an MgO surface suggest a magnetic anisotropy energy of 4100 cm^{-1},[43] it is unlikely that this limit will be reached, at least under ambient conditions.

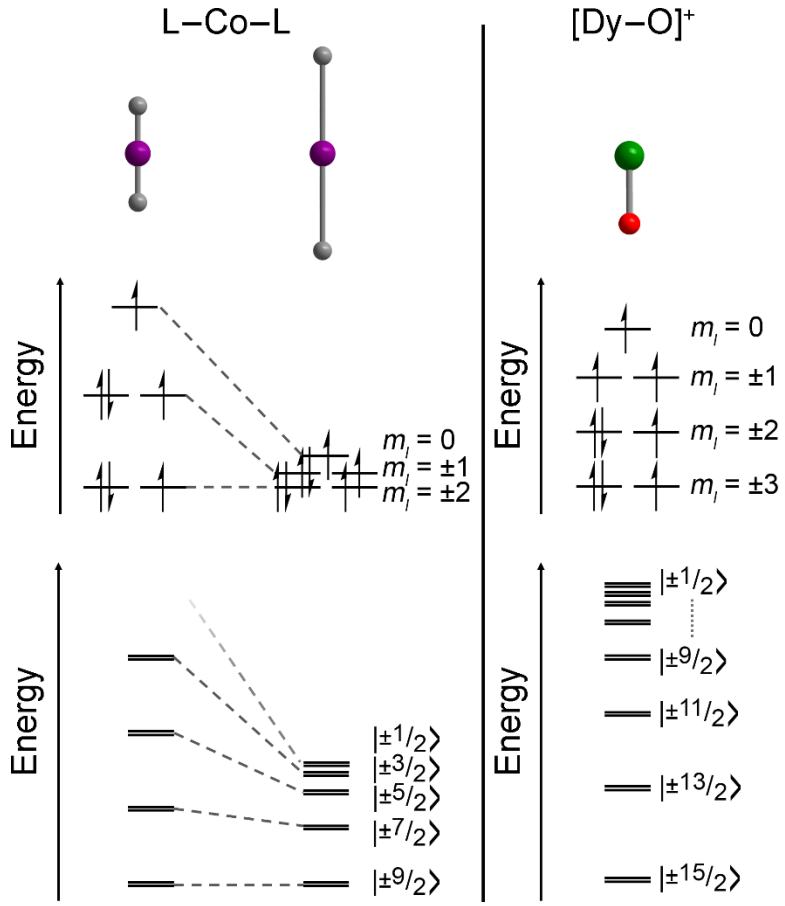

Figure 1.4. Orbital energy diagrams (top) and corresponding microstate energy diagrams (bottom) for CoL_2 in the strong (left) and weak (field) field limits, and $[DyO]^+$ as calculated.[43] Note that the energy scales for CoL_2 and $[DyO]^+$ are not the same.

1.4 Magnetic Relaxation

Early work in the field of single-molecule magnetism focused on clusters of transition metal ions that were ferro- or ferrimagnetically coupled to form high spin ground states, which then split into $2S + 1$ M_S states according to H_{ZFS}. Relaxation in these systems was relatively simple: the process of moving from the $M_S = +S$ to $M_S = -S$ state either excitations from $M_S = +S$ to $M_S = +(S - 1)$, with successive excitations until reaching $M_S = 0$ or $+{}^1/_2$ at the top of the microstate manifold then relaxation down to the $M_S = -S$ state in a similar fashion, or a tunneling transition between $M_S = +S$ and $M_S = -S$ states. A good introduction to both processes can be found in ref. [47] The former process is referred to as an Orbach process, and is a two-phonon process in which the system moves through a real excited state.[48]

In the development of mononuclear single-molecule magnets it quickly became apparent that other relaxation processes were at play, as the spin-reversal barriers measured by fitting variable temperature relaxation data were frequently much smaller than the spin-reversal barriers expected from the microstate structures, which could be determined by static magnetic measurements or spectroscopy. The first attempt at accounting for this discrepancy came by applying other relaxation processes described by Orbach, specifically Raman and direct relaxation processes.[49] Raman relaxation is also a two-phonon process which it proceeds through a virtual excited state. Direct relaxation is only applicable in applied fields and is a one-phonon process in which a molecule transitions directly between the ground microstates of opposite sign. The four processes contribute to relaxation according to Equation 9,

$$\tau^{-1} = \tau_{tunnel}^{-1} + BH^{m}T + CT^{n} + \tau_{0}^{-1}\exp\left(\frac{U}{k_{B}T}\right) \qquad (9)$$

where the four terms represent contributions from tunneling, direct, Raman, and Orbach relaxation processes, respectively. The terms B, C, and τ_0 contain physical constants as well as spin-phonon coupling terms; U is the spin-reversal barrier and correspond to excited microstates within the ground S or J manifold. A generic Arrhenius plot shows the effect of these relaxation processes in Figure 1.5.

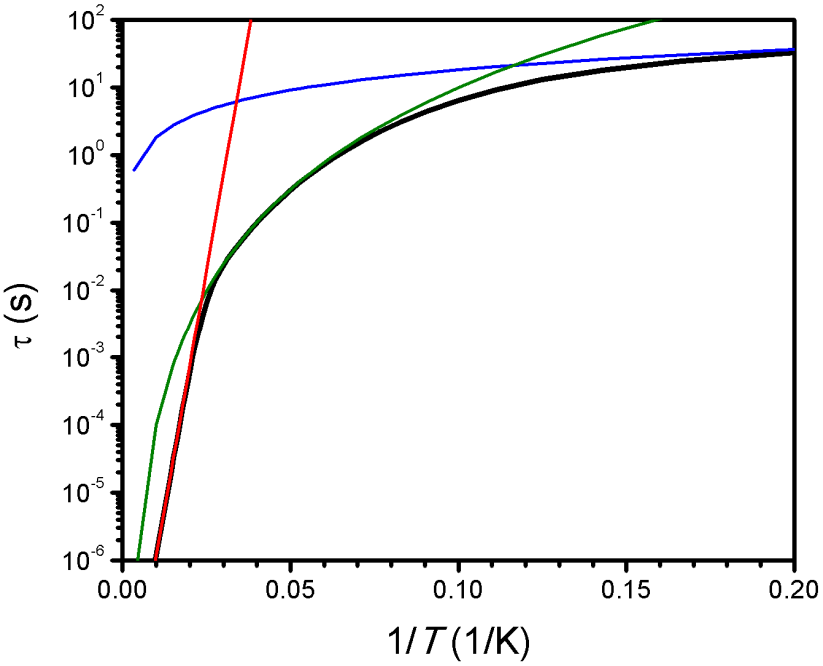

Figure 1.5. A general picture of magnetic relaxation as depicted by Orbach.[48] The blue, green, and red lines correspond to direct, Raman, and Orbach relaxation processes as described in Equation 9. The black line is the sum of these components. Direct relaxation is only applicable under applied fields, if relaxation times were collected under zero applied field the direct process would be replaced by a tunneling relaxation process.

More recently it has become clear that the underlying assumptions of Orbach's model are problematic in many single-molecule magnets. This has been discussed in detail elsewhere,[50] but in short—Orbach's model assumes that the system can be described as a Debye solid, where there is a predictable phonon density of states. It has been suggested that the Debye solid approximation is only valid, at best, up to 30 K for molecular solids.[51] Additionally, the model assumes that spin-phonon coupling is constant for a given system.

The Orbach relaxation process is still valid for single-molecule magnets; however, the spin-reversal barrier that determines the Orbach relaxation times is only indirectly related to properties such as blocking temperature, remanence and coercivity, and in general, low temperature relaxation behavior. Especially for mononuclear single-molecule magnets, at low temperatures relaxation is dominated by through-barrier relaxation processes. These through-barrier relaxations processes can be conceptually understood by further developing the microstate pictures like the ones in Figure 1.2.

The relative likelihood of a transition between two microstates, m_1 and m_2, is determined by their transition magnetic moment matrix element.[43] This value is minimized when the projection of the total angular momentum of microstates m_1 and m_2 along the z axis is large. For example, in an L–Co–L system with axial symmetry, the transition matrix elements will be smallest for transitions between $M_J = +^9/_2$ and $M_J = -^9/_2$, slightly larger for $M_J = +^7/_2$ and $M_J = -^7/_2$, etc. and will be comparatively large for transitions between $M_J = +^9/_2$ and $M_J = +^7/_2$. In general terms, transition matrix elements are minimized when the microstates under consideration are pure M_J states. Conversely, any perturbation which mixes microstates will facilitate faster relaxation.

There are a number of ways in which microstates can mix, and it is best to start by considering the mixing in a static picture. Conceptually it is easier to understand microstate mixing in the phenomenological crystal field approximation, which neglects metal-ligand covalency. Though the model is only quantitatively useful for lanthanides, we will apply it to transition metal systems for illustrative purposes. The crystal field Hamiltonian is given by Equation 10,

$$H_{CF} = \sum \sum_{k=-q}^{q} B_k^q \, O_k^q \qquad (10)$$

where B_k^q is a fit parameter describing the crystal field, O_k^q is an operator equivalent, both of rank k and order q. The necessary B_k^q and O_k^q terms are determined by the symmetry of the crystal field surrounding the metal ion. A full explanation of the crystal field Hamiltonian is beyond the scope of this work, and B_k^q and O_k^q terms for specific molecular symmetries have been given elsewhere.[52] The necessary information in this discussion is that operators with $q = 0$ only affect the separation of microstate doublets, while operators with $q = n$ will cause mixing of states with $\Delta M_J = n$; the magnitude of the B_k^q parameter determines the magnitude of mixing.

In an L–Co–L system with cylindrical symmetry, the eight microstates split into four doublets whose eigenfunctions have pure M_J values; these eigenfunctions, $|M_J\rangle$, are $|\pm 9/2\rangle$, $|\pm 7/2\rangle$, $|\pm 5/2\rangle$, and $|\pm 3/2\rangle$. The strength of the cylindrical crystal field is described by B_2^0 and B_4^0 crystal field terms, the effect of which determines the splitting of the microstates. Adding an element of symmetry by, for example, adding atoms to the ligands, changes the necessary terms to describe the crystal field. In the hypothetical complex $Co(CH_3)_2$ in S_6 symmetry, the crystal field is described by B_2^0, B_4^0, and B_4^3 terms. The first two terms serve the same purpose as before, but the B_4^3 determines the mixing of microstates with $\Delta M_J = 3$. Thus, the ground doublet previously described by $M_J = |\pm 9/2\rangle$ now has some component of $M_J = |\pm 3/2\rangle$. Simply by adding a symmetry component, transitions between the ground doublet are now more facile (Figure 1.6). As the B_k^q and O_k^q terms in use are determined by the symmetry of the complex, one strategy to minimize microstate mixing is to use special symmetries which only have axial crystal field terms (i.e. B_2^0, B_4^0, and B_6^0), such as D_{5d}.[53-56] Molecules investigated under this approach did have large spin-reversal barriers but ultimately still had fast through-barrier relaxation, possibly as a result of weakly bound axial ligands that gave access to low energy vibrations which facilitate microstate mixing (*vide infra*).

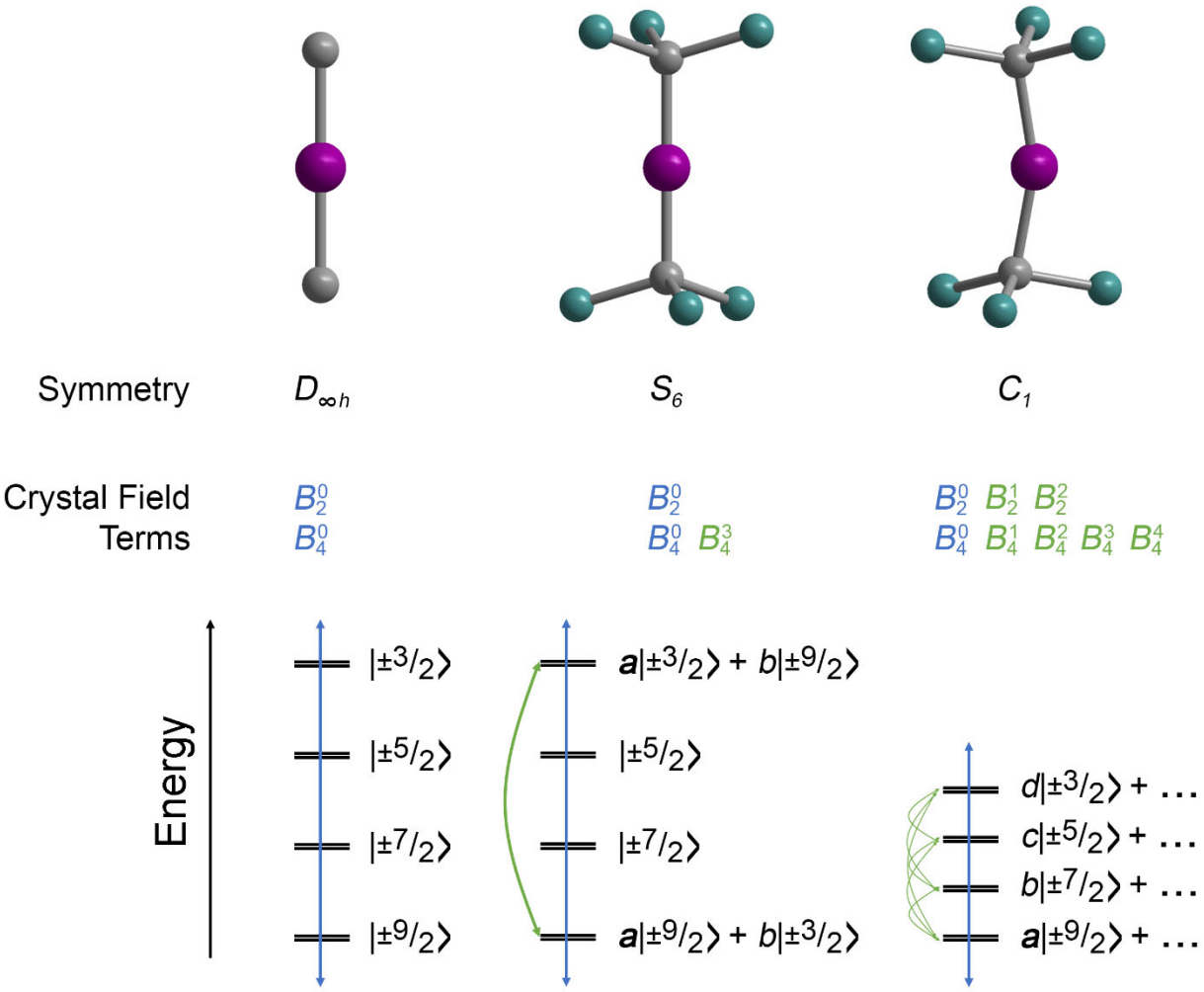

Figure 1.6. The mixing of microstates in a two-coordinate Co(II) complex in various symmetries according to the crystal field approximation. The symmetry of the complex determines which crystal field terms B_k^q are applicable; microstates with $\Delta M_J = q$ are allowed to mix.

The secondary coordination sphere of a metal ion is not frequently considered when discussing magnetic anisotropy and relaxation, however it may have large effects on low temperature relaxation. For example, $[Fe(C(SiMe_3)_3)_2]^-$ has longer low temperature relaxation times[11] than $Co(C(SiMe_2ONaph)_3)_2$,[12] despite the fact that the latter has larger orbital angular momentum and a spin-reversal barrier nearly twice as large as the former. One possible explanation is that microstate mixing is greater in $Co(C(SiMe_2ONaph)_3)_2$. The crystal field of both systems are described by B_2^0, B_4^0, and B_4^3. In $[Fe(C(SiMe_3)_3)_2]^-$ the threefold symmetry (and thus the B_4^3term) is imposed on the Fe(I) ion by the electrons in the C–Si bond. This relatively weak effect makes the mixing of the ground $M_J = |\pm 7/2\rangle$ state with $M_J = |\pm 1/2\rangle$ relatively small. In contrast, the lone pairs of the oxygen atoms in $Co(C(SiMe_2ONaph)_3)_2$ directly interact with the Co 4s orbital, which is weakly mixed into the $3d_{z2}$ orbital. Although this interaction is still very weak (compared to a bonding interaction), the Co(II) ion may "feel" the threefold symmetry more than the Fe(I) ion, possibly resulting in a larger B_4^3term. Thus, the ground $M_J = |\pm 9/2\rangle$ state of $Co(C(SiMe_2ONaph)_3)_2$

may have a comparatively large component of $M_J = |\pm 3/2\rangle$, yielding comparatively fast transitions between the ground doublet microstates.

The static crystal field picture merely marks the beginning of the microstate mixing process, as molecules are not static. Lattice vibrations and molecular vibrations and rotations can affect the geometry around the metal ion, which in turn affects the microstate picture and relaxation dynamics. Consider again the hypothetical $Co(CH_3)_2$ complex. If a vibrational mode that bends the C–Co–C axis is activated, during the course of the vibration the molecule no longer has threefold symmetry. If we were to take a snapshot of the molecule during the vibration and consider the effects of the bent C–Co–C on the microstate picture, we would see that magnetic anisotropy decreases as the bend removes orbital degeneracy and that the microstates become heavily mixed, as the C_1 symmetry will include many B_k^q terms which ultimately allow mixing of each microstate (Figure 1.6). The effect of vibrations on anisotropy[25] and relaxation[43] has been discussed by others. Recently the discussion has shifted to assigning spin-phonon coupling strengths for individual vibrations.[50,57,58] In the context of the above discussion, the qualitative description of what affects spin-phonon coupling is simple: vibrations which most effect anisotropy and the mixing of microstates will have large spin-phonon coupling strengths and thus have the greatest effect on facilitating through-barrier relaxation. Metal-centered vibrations will have the largest spin-phonon coupling terms.

The discussion of spin-phonon coupling in the previous paragraph focuses on phonon modes and molecular vibrations that are below the spin-reversal barrier. It is also important to understand the spin-vibronic coupling of vibrations near the spin-reversal barrier, as the energy required for relaxation through an excited magnetic microstate must somehow come from the lattice. Spectroscopic and computational analysis of $[Co(L^{2-})_2]^{2-}$ (L^{2-} = 1,2-bis(methanesulfonomido benzoate) show that there are two absorptions near the spin-reversal barrier which are field dependent and split into four transitions under applied fields.[59] One of the most interesting insights from this investigation is that microstate mixing in these vibrations is field dependent; thus, the relaxation times from these through-barrier processes are field dependent. This is in contrast to Orbach's description of Raman relaxation, which has no field dependence.[48]

Finally, microstate mixing is also facilitated by transverse magnetic fields, which is of particular importance in half-integer spin systems (Kramers complexes). In this case, the mixing is between microstates of the same doublet and is quantified by the tunneling gap, Δ_{tun}. In integer-spin systems (non-Kramers complexes) the mixing occurs directly through the crystal field and is referred to as an intrinsic tunneling gap, $\Delta_{int} = \langle -n|H_{CF}|n\rangle$, and can yield very fast relaxation via tunneling. Thus, the best single-molecule magnets are typically Kramers complexes, as Kramers theorem states that the ground microstates of a half-integer spin system must remain degenerate.[60] However, Kramers theorem breaks down in the presence of transverse magnetic fields and a tunneling gap arises according to $\Delta_{tun} = {}^{\mu_B}/_2 \left(g_x^2 H_x^2 + g_y^2 H_y^2\right)^{1/2}$, where g_x and g_y are the transverse components of the g factors of the microstates, and H_x and H_y are the x and y components of the magnetic field. In cylindrically symmetric systems which have microstates described by pure M_J values, g_x and g_y will be zero for the ground doublet. Any mixing between ground and excited microstates—either through the crystal field or through vibrations—will increase g_x and g_y and facilitate the mixing between the microstates of the ground doublet should the system be exposed the transverse magnetic fields, the presence of which seems to be unavoidable. Aside from applied magnetic fields, the two main sources of transverse magnetic fields are nuclear magnetic moments and dipolar interactions. The former can be mitigated by only using nuclei with no nuclear spins (e.g. ^{56}Fe, ^{164}Dy). The latter is mitigated in magnetically dilute

samples, implemented by co-crystallizing isostructural paramagnetic and diamagnetic complexes (e.g. Co(II) and Zn(II)) with low concentrations of the paramagnetic complexes. Several experiments have been done on isotopically pure ^{164}Dy complexes[56,61] and magnetic dilutions are fairly standard experiments in single-molecule magnetism studies; both methods decrease tunneling relaxation times. A particularly rigorous experiment utilizing both methods on a series of Dy complexes show that the tunneling relaxation mechanism slows but is not eliminated when both nuclear and dipolar magnetic fields are removed from the sample.[62]

Developing a full understanding of relaxation dynamics in fine detail in just one single-molecule magnet is a monumental task. Using microstate mixing as a proxy for understanding relaxation pathways, we can see the various ways in which through-barrier relaxation occurs. In the static picture, microstates are mixed by the ligand field and transverse magnetic fields. Considering dynamic effects, each vibration uniquely affects microstate mixing, and the mixing of microstates for a specific vibration is field dependent.

A practical understanding of relaxation is perhaps more attainable. A combination of efforts[12,57,58] to understand spin-phonon coupling has led to a new proposed equation to model variable temperature relaxation dynamics,

$$\tau^{-1} = \tau_{tunnel}^{-1} + \sum_{\alpha}\left(\frac{V_{\alpha}^{2}}{\hbar}\frac{\Delta_{\alpha}(2n_{\alpha}+1)}{[\Delta_{\alpha}^{2}+(\hbar\omega_{\alpha})^{2}]}\right) + \tau_{0}^{-1}\exp(-U/k_{B}T), \qquad (11)$$

where the first term represents quantum tunneling and the last term represents Orbach relaxation. A term for direct relaxation could be added if the experiment were carried out in an applied field. The second term represents relaxation through the α-th phonon mode, V represents spin-phonon coupling, Δ is the phonon linewidth, n is the phonon occupation number, and ω is the phonon frequency. Both Δ and n are dependent on both temperature and ω,

$$\Delta_{\alpha}^{2} = \frac{(\hbar\omega_{\alpha})^{2}\exp(ß\hbar\omega_{\alpha})}{(\exp(ß\hbar\omega_{\alpha})-1)^{2}} \qquad (12)$$

$$n_{\alpha} = \frac{1}{\exp(ß\hbar\omega_{\alpha})-1} \qquad (13)$$

where n_{α} is the phonon occupation number and $\beta = 1/k_{B}T$. Equation 12 defines the phonon line-shape. The energy Δ_{α} describes the amplitude of the Gaussian probability distribution of the phonon α mode's energy fluctuations. A general depiction of relaxation described by Equation 11 is shown in Figure 1.7.

Though undoubtedly more accurate for single-molecule magnets than the depiction of through-barrier relaxation as described by Orbach, Equation 11 is significantly harder to use. At minimum it requires knowledge of the low energy phonon spectrum, which can be obtained through spectroscopy.[12] However, as there will be many absorptions in this region and it is not clear which contribute the most to relaxation. An entirely computational approach has been taken for one system, in which both the low-energy phonon spectrum and individual spin-phonon coupling terms are calculated for each phonon.[57,58] It is possible that a hybrid approach may suffice, where calculations determine which absorptions in the experimentally determined spectra are metal-centered (or have the highest spin-phonon coupling strengths). Both these additional experiments and expensive calculations require significant effort, and this effort may not be warranted in all cases. This deeper investigation of relaxation should perhaps be reserved for high-performing single molecule magnets, possibly as a separate endeavor from their original syntheses. In this respect, it is good practice to make the relaxation data readily available in supporting information tables. In instances where a study does not warrant a full investigation of relaxation dynamics, we should adopt a "first do no harm" approach and not use a relaxation model simply because it makes a fit line that goes through all data points if the model itself is not physically meaningful for that

system. Thus, in some cases it is best to consider high temperature relaxation data and give upper and lower limits for U and τ_0, respectively.

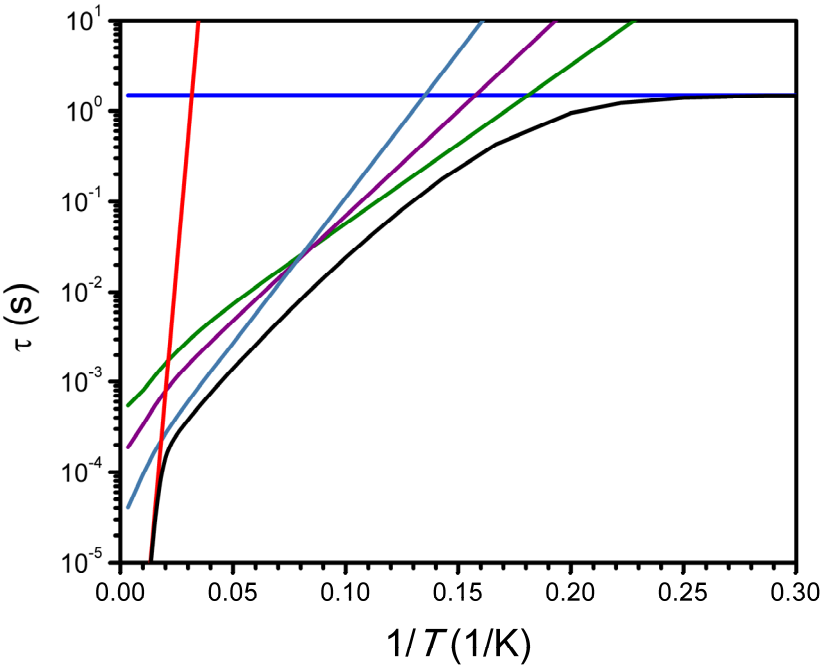

Figure 1.7. A general picture of magnetic relaxation as described by Equation 11. Blue and red lines represent contributions from tunneling and Orbach relaxation, respectively. The green, purple, and turquoise lines represent contributions from vibration-mediated coupling of ground microstates. Note that these processes are slightly temperature dependent at high temperatures. Their slopes are determined by the phonon energies and the y-intercepts are determined by the spin-phonon coupling strengths. The black line a is a sum of these relaxation processes.

1.5 Outlook

There are physical limits for magnetic anisotropy. For transition metals, these limits are approached by using linear coordination environments, and small improvements on current systems may be made by manipulating the nature of the M–L bond to make the effective spin-orbit coupling constant approach that of the free-ion value, or through the use of the heavy ligand effect.[29] Linear 4d or 5d complexes, where the weak ligand field imposed by the low coordination number may allow for high-spin ground states, would take advantage of spin-orbit coupling constants that are over twice as large as the 3d metals. For the lanthanides, it is unlikely that a molecule will move to the strong-field regime which would have an anisotropy limit of 8000 cm^{-1}. However, $[(Cp^{iPr5})Dy(Cp^*)]^+$ has the largest spin-reversal barrier of 1541 cm^{-1} and a calculated magnetic anisotropy energy of 2104 cm^{-1},[2d] which is still far from the calculated magnetic anisotropy energy of ~4100 cm^{-1} for $[DyO]^+$ on an MgO surface.[43] A two-coordinate Dy(III) complex with the strongest possible crystal field remains the obvious target for maximizing magnetic anisotropy energy in a mononuclear single-molecule magnet.

There are also physical limits on relaxation times. In any vibration-mediated relaxation pathway, relaxation time is dependent on spin-phonon coupling strength and the energy of that phonon. In this sense it has been suggested to use light, rigid frameworks to move the phonons responsible for relaxation to higher energies.[50,57,58] Spin-phonon coupling strength, however, is determined by the metal-ligand interaction strength. Optimization of this parameter may be at odds

with optimization of magnetic anisotropy energy; the former benefits from a weak metal-ligand interaction and the latter benefits from strong, axial ligand fields.

We have largely neglected discussing actinide single-molecule magnets and will only briefly do so here. All mononuclear actinide single-molecule magnets have reported effective spin reversal barriers below 100 cm^{-1},[63] despite the fact that the actinides have significantly larger spin-orbit coupling constants than the lanthanides. One possible explanation for this trend is that the strong metal-ligand covalency of the actinides gives them spin-phonon coupling constants similar to transition metal complexes, however because the actinide ions themselves are heavier than transition metals, the phonons responsible for magnetic relaxation are at comparatively low energies. A recent publication on $[UCp^{iPr4}_2]^+$ provides some unique insight—relaxation times under an applied dc field of a polycrystalline sample and frozen solution were nearly identical in the 2.2 to 8 K range.[64] It is frequently suggested that Orbach's description of relaxation is valid under 30 K as that is the roughly the maximum temperature in which the Debye approximation is valid for molecular solids.[51] However, the phonon spectrum should change significantly between the two samples and yet relaxation times do not, suggesting that the relaxation process is of molecular origin. Thus, for the actinides, it is perhaps best to move forward with multinuclear species which will benefit from the metal-ligand covalency in the form of relatively strong magnetic coupling.

For synthetic chemists the future of single-molecule magnetism lies either in pursuit of either mononuclear complexes with fine-tuned axial ligand fields or in the development of new multinuclear complexes. The shift from multinuclear to mononuclear complexes originally occurred because it was shown that the spin-reversal barrier is inversely related to magnetic anisotropy.[65] Additionally, there are challenges relating to the ratio of magnetic coupling to magnetic anisotropy where, for transition metals the microstates of neighboring states within the spin ladder begin to overlap and shortcut the barrier of the ground spin state,[66] and for lanthanides having strong coupling with weak anisotropy yields a mixing of microstates that facilitates fast relaxation. In an effort to not rehash the early work in the field we suggest two pathways forward: the use of magnetic double exchange to facilitate magnetic coupling up to high temperatures[67] or the use of directly coupled magnetic centers in which high-spin states arise from a molecular orbital picture.[68] It is unlikely that these complexes will have anisotropy energies similar to mononuclear species, however the hope is that a sufficiently high spin state will mitigate the effects of through-barrier relaxation. While some progress has been made in these directions, the coordination environments of the metal centers in these complexes has not been optimized in the same way that they have for mononuclear complexes.

1.6 References

(1) (a) Lis, T. *Acta Crystallogr.*, **1980**, *B36*, 2042. (b) Caneschi, A.; Gatteschi, D.; Sessoli, R.; Barra, A. L.; Brunel, L. C.; Guillot, M. *J. Am. Chem. Soc.*, **1991**, *113*, 5873. (c) Sessoli, R.; Tsai, H.-L.; Schake, A. R.; Wang, J. B.; Folting, K.; Gatteschi, D.; Christou, G.; Hendrickson, D. N. *J. Am. Chem. Soc.*, **1993**, *115*, 1804. (d) Sessoli, R.; Gatteschi, D.; Caneschi, A.; Novak, M. A. *Nature*, **1993**, *365*, 141.

(2) (a) Goodwin, C. A. P.; Ortu, F.; Reta, D.; Chilton, D. R.; Mills, D. P. *Nature*, **2017**, *548*, 439. (b) Guo, F.-S.; Day, B. M.; Chen, Y.-C.; Tong, M.-L.; Mansikkamäki, A.; Layfield, R. A. *Angew. Chem. Int. Ed.*, **2017**, *56*, 11445. (c) McClain, K. R.; Gould, C. A.; Chakarawet, K.; Teat, S. J.; Groshens, T. J.; Long, J. R.; Harvey, B. G. *Chem. Sci.*, **2018**, *9*, 8492. (d)

Guo, F.-S.; Day, B. M.; Chen, Y.-C.; Tong, M.-L.; Mansikkamäki, A.; Layfield, R. A. *Science*, **2018**, *362*, 1400.
(3) Demir, S.; Gonzalez, M. I.; Darago, L. E.; Evans, W. J.; Long, J. R. *Nature Commun.*, **2017**, *8*, 2144.
(4) Gatteschi, D.; Villain, J.; Sessoli, R. *Molecular Nanomagnets*, Oxford University Press, Inc., New York, **2006**, Ch. 2.
(5) Mannini, M.; Pineider, F.; Sainctavit, P.; Danieli, C.; Otero, E.; Sciancalepore, C.; Talarico, A. M.; Arrio, M.-A.; Cornia, A.; Gatteschi, D.; Sessoli. R. *Nat. Mater.* **2009**, *8*, 194.
(6) Bogani, L.; Wernsdorfer. W. *Nat. Mater.*, **2008**, *7*, 179.
(7) Bunting, P. C.; Gratta, G.; Melia, T.; Rajendran, S. *Phys. Rev. D*, **2017**, *95*, 095001.
(8) Ishikawa, N.; Sugita, M.; Ishikawa, T.; Koshihara, S.; Kaizu, Y. *J. Am. Chem. Soc.*, **2003**, *125*, 8694.
(9) Freedman, D. E.; Harman, W. H.; Harris, T. D.; Long, G. J.; Chang, C. J.; Long, J. R. *J. Am. Chem. Soc.*, **2010**, *132*, 1224.
(10) Zadrozny, J. M.; Atanasov, M.; Bryan, A. M.; Lin, C.-Y.; Rekken, B. D.; Power, P. P.; Neese, F.; Long, J. R. *Chem. Sci.*, **2013**, *4*, 125.
(11) Zadrozny, J. M.; Xiao, D. J.; Atanasov, M.; Long, G. J.; Grandjean, F.; Neese, F.; Long, J. R. *Nature Chem.*, **2013**, *5*, 577.
(12) Bunting, P. C.; Atanasov, M.; Damgaard-Møller, E.; Perfetti, M.; Crassee, I.; Orlita, M.; Overgaard, J.; van Slageren, J.; Neese, F.; Long, J. R. *Science*, **2018**, *362*, eaat7319
(13) Orchard, A. F. *Magnetochemistry*, Oxford University Press, Inc., New York, **2003**, Ch. 2.
(14) Figures adapted from the following websites under the Creative Commons license: https://en.wikipedia.org/wiki/File:Atomic_orbitals_n1234_m-eigenstates.png; https://en.wikipedia.org/wiki/File:D3M0.png; https://en.wikipedia.org/wiki/File:Dxz_orbital.png; https://en.wikipedia.org/wiki/File:Dyz_orbital.png; https://en.wikipedia.org/wiki/File:Dxy_orbital.png; https://en.wikipedia.org/wiki/File:Dx2-y2_orbital.png
(15) Kahn, O. *Molecular Magnetism*, Wiley-VCH, Germany, **1993**, p. 359.
(16) Gruden-Pavlović, M.; Stepanović, S.; Perić,, M.; Güellc, M.; Swart, M. *Phys. Chem. Chem. Phys.*, **2014**, 16, *14514*.
(17) Jesson, J. P. *J. Chem. Phys.*, **1966**, *45*, 1049.
(18) Zhang, Y.-Z.; Gómez-Coca, S.; Brown, A. J.; Saber, M. R.; Zhang, X.; Dunbar, K. R. *Chem. Sci.*, **2016**, *7*, 6519.
(19) Ruamps, R.; Batchelor, L. J.; Maurice, R.; Gogoi, N.; Jiménez-Lozano, P.; Guihéry, N.; de Graaf, C.; Barra, A.-L.; Sutter, J.-P.; Mallah, T. *Chem. Eur. J.* **2013**, *19*, 950.
(20) Suturina, E. A.; Nehrkorn, J.; Zadrozny, J. M.; Liu, J.; Atanasov, M.; Weyhermüller, T.; Maganas, D.; Hill, S.; Schnegg, A.; Bill, E.; Long, R. J.; Neese, F. *Inorg. Chem.*, **2017**, *56*, 3102.
(21) Maganas, D.; Sottini, S.; Kyritsis, P.; Groenen, E. J. J.; Neese, F. *Inorg. Chem.*, **2011**, *50*, 8741.
(22) Rechkemmer, Y.; Breitgoff, F. D.; van der Meer, M.; Atanasov, M.; Hakl, M.; Orlita, M.; Neugebauer, P.; Neese, F.; Sarkar, B.; van Slageren, J. *Nature Commun.*, **2016**, *7*, 10467.
(23) Fataftah, M. S.; Zadrozny, J. M.; Rogers, D. M.; Freedman, D. E. *Inorg. Chem.*, **2014**, *53*, 10716.

(24) Jahn, H. A.; Teller, E.; Donnan, F. G. *Proc. Royal Soc. Lond. A*, **1937**, *161*, 905.
(25) Atanasov, M.; Zadrozny, J. M.; Long, J. R.; Neese, F. *Chem. Sci.* **2013**, *4*, 139.
(26) Reiff, W. M.; LaPointe, A. M.; Witten, E. H. *J. Am. Chem. Soc.*, **2004**, *126*, 10206.
(27) Zadrozny, J. M.; Xiao, D. J.; Long, J. R.; Atanasov, M.; Neese, F.; Grandjean, F.; Long, G. J. *Inorg. Chem.*, **2013**, *52*, 13123.
(28) Griffith, J. S. *The Theory of Transition-Metal Ions*, Cambridge University Press, New York, **1961**, Appendix 6.
(29) Karunadasa, H. I.; Arquero, K. D.; Berben, L. A.; Long, J. R. *Inorg. Chem.* **2010**, *49*, 4738. (b) Ye, S.; Neese, F. *J. Chem. Theory Comput*. **2012**, *8*, 2344. (c) Zadrozny, J. M.; Telser, J.; Long, J. R. *Polyhedron* **2013**, *64*, 209. (d) Pearson, T. J.; Fataftah, M. S.; Freedman, D. E. *Chem. Commun.* **2016**, *52*, 11394. (e) Yao, X.-N.; Yang, M.-W.; Xiong, J.; Liu, J.-J.; Gao, C.; Meng, Y.-S.; Jiang, S.-D.; Wang, B.-W.; Gao, S. *Inorg. Chem. Front.* **2017**, *4*, 701. (f) Pearson, T. J.; Fataftah, M. S.; Freedman, D. E. *Chem. Commun.* **2016**, *52*, 11394.
(30) Atanasov, M.; Aravena, D.; Suturina, E.; Bill, E.; Maganas, D.; Neese, F. *Coord. Chem. Rev.*, **2015**, *289*, 177.
(31) Meng, Y.-S.; Mo, Z.; Wang, B.-W.; Zhang, Y.-Q.; Deng, L.; Gao, S. *Chem. Sci.*, **2015**, *6*, 7156.
(32) Hicks, J.; Jones, C. *Organometallics*, **2015**, *34*, 2118.
(33) Ni, C.; Stich, T. A.; Long, G. J.; Power, P. P. *Chem. Commun.*, **2010**, *46*, 4466.
(34) Mo, Z.; Chen, D.; Leng, X.; Deng, L. *Organometallics*, **2012**, *31*, 7040.
(35) Lin, C.-Y.; Fettinger, J. C.; Grandjean, F.; Long, G. J.; Power, P. P. *Inorg. Chem.*, **2014**, *53*, 9400.
(36) Lipshutz, M. I.; Yang, X.; Chatterjee, R.; Tilley, T. D. *J. Am. Chem. Soc.*, **2013**, *135*, 15298.
(37) Laskowski, C. A.; Morello, G. R.; Saouma, C. T.; Cundari, T. R.; Hillhouse, G. L. *Chem. Sci.*, **2013**, *4*, 170.
(38) Dong, Q.; Yang, X.-J.; Gong, S.; Luo, Q.; Li, Q.-S.; Su, J.-H.; Zhao, Y.; Wu, B. *Chem. Eur. J.*, **2013**, *19*, 15240.
(39) Laskowski, C. A.; Bungum, D. J.; Baldwin, S. M.; Del Ciello, S. A.; Iluc, V. M.; Hillhouse, G. L. *J. Am. Chem. Soc.*, **2013**, *135*, 18272.
(40) Laskowski, C. A.; Hillhouse, G. L. *J. Am. Chem. Soc.*, **2008**, *130*, 13846.
(41) Lipschutz, M. I.; Tilley, T. D. *Organometallics*, **2014**, *33*, 5566.
(42) As a minor point of pedantry, in the pursuit of systems with record spin-reversal barriers and/or magnetic anisotropy energies, linear d^9 systems may simultaneously be the best and worst single-molecule magnets, depending on the analysis. A d^9 system as shown in Figure 1.2 in which the d_{xz} and d_{yz} orbitals are strictly degenerate will likely have the largest magnetic anisotropy energy for a transition metal. A d^9 system with an orbitally non-degenerate ground state is relatively uninteresting for single-molecule magnetism, as the $M_S = \pm 1/2$ states are not capable of zero field splitting. It is possible near-linear d^9 system could be interpreted in both ways—it will either have $M_J = \pm 3/2$ and $M_J = \pm 1/2$ states which arise from H_{SOC} and are increasingly mixed with increasing deviation from linearity, or the same states could be interpreted as arising from two nearby non-degenerate states which then mix through H_{ZFS}.
(43) Ungur, L.; Chibotaru, L. F. *Inorg. Chem.*, **2016**, *55*, 10043.
(44) In this context, the "strong field regime" is the point at which the ligand field becomes sufficiently strong such that L is no longer a good quantum number, but L_z is. Linear

transition metal complexes are all in the strong field regime while lanthanides are in the weak field regime.
(45) Jank, S.; Reddmann, H.; Amberger, H.-D. *Inorg. Chim. Acta.*, **2008**, *631*, 2154.
(46) Kurzen, H.; Bovigny, L; Bulloni, C.; Daul, C. *Chem. Phys. Lett.*, **2013**, *574*, 129.
(47) Gatteschi, D.; Sessoli, R. *Angew. Chem. Int. Ed.*, **2003**, *42*, 268.
(48) Orbach, R.; Bleaney, B. *Proc. Royal Soc. Lond. A*, **1961**, *264*, 1319.
(49) Harman, W. H.; Harris, T. D.; Freedman, D. E.; Fong, H.; Chang, A.; Rinehart, J. D.; Ozarowski, A.; Sougrati, M. T.; Grandjean, F.; Long, G. J.; Long, J. R.; Chang, C. J. *J. Am. Chem. Soc.*, **2010**, *132*, 18115.
(50) Escalera, L.; Baldovi, J. J.; Gaita-Ariño, A.; Coronado, E. *Chem. Sci.*, **2018**, *9*, 3265.
(51) Eaton, S. S.; Eaton, G. R. *Biol. Magn. Reson.*, **2000**, *19*, 29.
(52) Benelli, C.; Gatteschi, D. *Introduction to Molecular Magnetism: From Transition Metals to Lanthanides*, Wiley-VCH, Germany, **2016**, Ch. 3.
(53) Chen, Y.-C.; Liu, J-L.; Ungur, L.; Liu, J; Li, Q.-W.; Wang, L.-F.; Ni, Z.-P.; Chibotaru, L. F.; Chen, X.-M.; Tong, M.-L. *J. Am. Chem. Soc.*, **2016**, *138*, 2829.
(54) Ding, Y.-S.; Chilton, N. F.; Winpenny, R. E. P.; Zheng, Y.-Z. *Angew. Chem. Int. Ed.*, **2016**, *55*, 16071.
(55) Gupta, S. K.; Rajeshkumar, T.; Rajaraman, G.; Murugavel, R. *Chem. Sci.*, **2016**, *7*, 5181.
(56) Ding, Y.-S.; Yu, K.-X.; Reta, D.; Ortu, F.; Winpenny, R. E. P.; Zheng, Y.-Z.; Chilton, N. F. *Nature Commun.*, **2018**, *9*, 3134.
(57) Lunghi, A.; Totti, F.; Sessoli, R.; Sanvito, S. *Nature Commun.*, **2017**, *8*, 14620.
(58) Lunghi, A.; Totti, F.; Sanvito, S.; Sessoli, R. *Chem. Sci.*, **2017**, *8*, 6051.
(59) Atanasov, A.; Neese, F. *manuscript in preparation*
(60) Kramers, H. A. *Proc. Amsterdam Acad.*, **1930**, *33*, 959.
(61) Kishi, Y.; Pointillart, F.; Lefeuvre, B.; Riobé, F.; Le Guennic, B.; Golhen, S.; Cador, O.; Maury, O.; Fujiwara, H.; Ouahab, L. *Chem. Commun.*, **2017**, *53*, 3575.
(62) Ortu, F.; Reta, D.; Ding, Y.-S.; Goodwin, C. A. P.; Gregson, M. P.; McInnes, E. J. L.; Winpenny, R. E. P.; Zheng, Y.-Z.; Liddle, S. T.; Mills, D. P.; Chilton, N. F. *ChemRxiv*, **2018**, doi: 10.26434/chemrxiv.6790568.v1
(63) Meihaus, K. R.; Long, J. R. *Dalton Trans.*, **2015**, *44*, 2517.
(64) Boreen, M. A.; Lussier, D. J.; Hohloch, S. A.; Shuh, D. K.; Long, J. R.; Arnold, J. *manuscript in preparation*
(65) Neese, F.; Pantazis, D. A. *Faraday Disc.*, **2011**, *229*, 229.
(66) Milios, C. J.; Vinslava, A.; Wernsdorfer, W.; Moggach, S.; Parsons, S.; Perlepes, S. P.; Christou, G.; Brechin, E. K. *J. Am. Chem. Soc.*, **2007**, *129*, 2754.
(67) (a) Beissel, T.; Birkelbach, F.; Bill, E.; Glaser, T.; Kesting, F.; Krebs, C.; Weyhermüller, T.; Wieghardt, K.; Butzlaff, C.; Trautwein, A. X. *J. Am. Chem. Soc.*, **1996**, *118*, 12376 (b) Saal, C.; Mohanta, S.; Nag, K.; Dutta, S. K.; Werner, R.; Haase, W.; Duin, E.; Johnson, M. K. *Ber. Bunsenges. Phys. Chem.*m **1996**, *100*, 2086 (c) Shores, M. P.; Long, J. R. *J. Am. Chem. Soc.*, **2002**, *124*, 3512 (d) Drüeke, S.; Chaudhuri, P.; Pohl, K.; Wieghardt, K.; Ding, X.-Q.; Bill, E.; Sawaryn, A.; Trautwein, A. X.; Winkler, H.; Gurman, S. J. *Chem. Commun.*, **1989**, *1*, 59 (e) Ding, X.-Q.; Bominaar, E. L.; Bill, E.; Winkler, H.; Trautwein, A. X.; Drüeke, S.; Chaudhuri, P.; Wieghardt, K. *J. Chem. Phys.*, **1990**, *92*, 178 (f) Gamelin, D. R.; Bominaar, E. L.; Kirk, M. L.; Wieghardt, K.; Solomon, E. I. *J. Am. Chem. Soc.*, **1996**, *118*, 8085 (g) Barone, V.; Bencini, A.; Ciofini, I.; Daul, C. A.; Totti, F. *J. Am. Chem. Soc.*, **1998**, *120*,

8357 (h) Bechlars, B.; D'Alessandro, D. M.; Jenkins, D. M.; Iavarone, A. T.; Glover, S. D.; Kubiak, C. P.; Long, J. R. *Nature Chem.*, **2010**, *2*, 362 (i) Gaudette, *A. I.*; Jeon, I.-R.; Anderson, J. S.; Grandjean, F.; Long, G. J.; Harris, T. D. *J. Am. Chem. Soc.*, **2015**, *137*, 12617.

(68) (a) Sánchez, R. H.; Betley, T. A. *J. Am. Chem. Soc.*, **2015**, *137*, 13949. (b) Chakarawet, K.; Bunting, P. C.; Long, J. R. *J. Am. Chem. Soc.*, **2018**, *140*, 2058.

Chapter 2: Synthesis and Single-Molecule Magnetism of Transition Metal Dialkyl Complexes

2.1 Introduction

Single-molecule magnets are a class of materials which possess magnetically bistable ground states separated by an energy barrier, U.[1] Molecules in either of these ground states have magnetic moments in an "up" or "down" orientation on an axis defined by the molecular geometry, and when thermal energy is small relative to U, molecules will retain their magnetization even in the absence of an applied field. A primary focus in molecular magnetism research is developing molecules with long relaxation times at high temperatures. The relaxation times of single-molecule magnets depends on a number of factors, such as barrier height (magnetic anisotropy) and symmetry. A sufficiently large barrier is required to slow over-barrier relaxation pathways, while symmetry affects through-barrier relaxation pathways by affecting the mixing of and transitions between magnetic sublevels.[2] Highly axial coordination environments can yield both large magnetic anisotropy and can mitigate through-barrier relaxation pathways.

We recently reported on the synthesis, electronic structure, and magnetic properties of $Co(C(SiMe_2ONaph)_3)_2$ (where Naph is a naphthyl group).[3] The molecule has a d-orbital filling of $(d_{x^2-y^2}, d_{xy})^3(d_{xz}, d_{yz})^3(d_{z^2})^1$, a non-Aufbau ground state that arises from an exceptionally weak ligand field. This electronic structure possesses maximal orbital angular momentum for a transition metal (L = 3) and, as a result, very large magnetic anisotropy. The spin-reversal barrier of 450 cm^{-1} is the largest for any transition metal containing complex.

Our pursuit of a linear cobalt(II) dialkyl complex began after calculations on the hypothetical complex $Co(C(SiMe_3)_3)_2$ predicted the unusual electronic structure and large magnetic anisotropy.[4] We were unable to isolate the complex, and others later showed that the $[C(SiMe_3)_3]^-$ ligand was too reducing for cobalt(II).[5] The complex $Co(C(SiMe_2ONaph)_3)_2$ was able to support the C–Co–C moiety due to the fact that the electron withdrawing naphthyl groups reduced the basicity of the carbanion[6] and that the naphthyl rings aligned in such a way to provide significant stabilization via interligand sp^3-CH···π and sp^2-CH···π interactions. Unsurprisingly, the ligand bearing the naphthyl substituent was not the first ligand we tried. Assuming that any electron withdrawing group would have the desired effect at the central carbon, we made a variety of ligands of the type $HC(SiMe_2OR)_3$, where –OR groups were a variety of aryloxides and alkoxides.

Herein we describe the synthesis and characterization of a series of two-coordinate transition metal complexes $M(C(SiMe_2OPh)_3)_2$ (M = Cr (**1**), Mn (**2**), Fe (**3**), Co (**4**), Zn (**5**)). While this ligand did allow for the isolation of a cobalt(II) dialkyl species, long range Co···O interactions led to a bent C–Co–C axis. The magnetic properties of this species, in comparison to those of $Co(C(SiMe_2ONaph)_3)_2$, provide a dramatic illustration of the effects of symmetry on magnetic anisotropy. Structural characterization of other divalent 3d metal complexes show that the bend is due to long range M···O interactions and not crystal packing or ligand bulkiness. Further, we reduced the iron congener (**3**) and compare the magnetic properties of the reduced species $[Fe(C(SiMe_2OPh)_3)_2]^-$ (**6**) to $[Fe(C(SiMe_3)_3)_2]^-$ and observe that the secondary coordination sphere has a small effect on anisotropy but a large effect on low-temperature relaxation times.

2.2 Experimental Information

General considerations

All synthesis and characterization were done under N_2 or Ar using standard Schlenk and glove box techniques. Solvent was dried by a commercial solvent purification system made by JC Meyer

Solvent Systems and either used immediately or stored over 4 Å sieves for later use. Unless otherwise stated, all materials are available from commercial sources and were used as received. $(DME)_2KC(SiMe_2OPh)_3$ and **4a** were prepared by known methods.[3] NMR spectra were obtained with a Bruker AVQ-400. Elemental analyses were performed by the Microanalytical Facility at the University of California, Berkeley.

Synthesis of $M(C(SiMe_2OPh)_3)_2$, M = Cr (1), Mn (2), Fe (3), Co (4a, 4b), Zn (5)

Solid MCl_2 (0.14 mmol) was added at room temperature to a stirring THF solution (15 mL) of $(DME)_2KC(SiMe_2OPh)_3$ (0.200 g, 0.290 mmol). After stirring for 2 hours at 60 °C, solvent was removed *in vacuo*. The residue was extracted with hot hexanes (15 mL) and filtered through diatomaceous earth. Solvent was reduced *in vacuo* and allowed to sit at −30 °C for 12 hours to form large crystals suitable for x-ray diffraction. **1·THF**, blue crystals, 0.078 g, 51%. Anal. Calcd. for $CrC_{50}H_{66}Si_6O_6$: C, 61.44; H, 7.07. Found: C, 61.36; H, 6.96. **2**, colorless crystals, 0.0880 g, 60%. Anal. Calcd. for $MnC_{50}H_{66}Si_6O_6$: C, 60.88; H, 6.74. Found: C, 60.94; H, 6.60. **3**, pale yellow crystals, 0.0964 g, 67%. Anal. Calcd. for $FeC_{50}H_{66}Si_6O_6$: C, 60.82; H, 6.74. Found: C, 61.15, H, 6.96. **4b·C_6H_{14}**, brown crystals, 0.073 g, 65%. Anal. Calcd. for $CoC_{56}H_{80}Si_6O_6$: C, 62.47; H, 7.49. Found: C, 62.34; H, 7.44. **5·C_6H_{14}**, colorless crystals, 0.051 g, 32%. Anal. Calcd. for $ZnC_{56}H_{80}Si_6O_6$: C, 62.10; H, 7.45. Found: C, 61.69; H, 6.84.

Two structures of **4** were isolated. Crystals grown from saturated solutions crystallized in *C*2/c with no solvent in the unit cell (**4a**),[3] while crystals grown from unsaturated solutions crystallized in *R*-3 with a disordered hexane molecule in the lattice (**4b**). For the scale of reactions shown here, crystals of **4a** grew from 5 mL of hexanes and crystals of **4b** grew from 15 mL of hexanes. Crystals of **4b** were dried by passing argon over them.

Synthesis of [K(2.2.2-Cryptand)][$Fe(C(SiMe_2OPh)_3)_2$] (6)

To a stirring Et_2O solution (10 mL) of **3** (0.182 g, 0.184 mmol) and 2.2.2-Cryptand (0.069 g, 0.184 mmol) was added solid KC_8 (0.025 g, 0.184 mmol). The reaction was stirred for 2 hours until a dark green solid precipitated from solution. The yellow solution was filtered through diatomaceous earth to remove the graphite and a dark green solid. The dark green solid was redissolved in difluorobenzene and added to the yellow Et_2O solution to form a cloudy yellow mixture. Yellow crystals suitable for x-ray diffraction grew from this mixture in hours. Anal. Calcd. for $FeKC_{66}H_{102}N_2Si_6O_{12}$: C, 58.12; H, 7.33; N, 2.00. Found: C, 58.05; H, 7.19; N, 2.01.

Single-Crystal X-ray diffraction

X-ray diffraction experiments were performed at 100 K on crystals coated with Paratone-N oil and mounted on Kapton loops. X-ray data were collected at the Small Molecule X-ray Crystallography Facility at the University of California, Berkeley using a Bruker QUAZAR diffractometer equipped with a microfocus sealed X-ray source (Mo Kα radiation; λ = 0.71073 Å) and a Bruker APEX-II detector. Raw data were integrated and corrected for Lorentz and polarization effects using Bruker AXS SAINT[7] software and corrected for absorption using SADABS.[8] Space group assignments were determined by examination of systematic absences, E-statistics, and successive refinement of the structures. All structures were solved by intrinsic phasing using SHELXT.[9] Additional refinement was performed with SHELXL[10] operated within

the OLEX2[11] interface. Thermal parameters were refined anisotropically for all non-hydrogen atoms. Hydrogen atoms were placed in ideal positions and refined using a riding model. Disorder in the structures of $Cr(C(SiMe_2OPh)_3)_2 \cdot C_4H_8O$ and $Fe(C(SiMe_2OPh)_3)_2$ required the use of displacement parameter (SIMU and RIGU) and distance (SADI and DFIX) restraints in the refinement. The structures of $Co(C(SiMe_2OPh)_3)_2 \cdot C_6H_{14}$ and $Zn(C(SiMe_2OPh)_3)_2 \cdot C_6H_{14}$ contained residual electron density due to highly disordered hexane molecules (determined by elemental analysis) that could not be modelled. Consequently, these hexane molecules were omitted from the refinement but not the formula and, the unassigned electron density in these structures was accounted for using SQUEEZE[12] as implemented in the PLATON[13] interface.

Magnetic Measurements

Magnetic susceptibility data were collected on a Quantum Design MPMS-XL SQUID magnetometer. Microcrystalline powders of **3** (65.4 mg), **4a** (34.6 mg), **4b** (42.1 mg), and **6** (17.9 mg) were ground into microcrystalline powders and embedded in eicosane (70.3, 70.9, 55.6, and 44.8 mg for **3**, **4a**, **4b**, and **6**, respectively) in a vacuum-sealed quartz tube (5 mm i.d., 7 mm o.d.) with a raised quartz platform. Dc susceptibility measurements were taken over a range of 2-300 K under 0.1, 1, and 7 T dc fields. Dc magnetization measurements were taken from 2-15 K under 1, 2, 3, 4, 5, 6, and 7 T dc fields. Ac susceptibility measurements were taken under zero applied dc fields with ac frequencies in the 1-1488 Hz range and a probe field amplitude of 4 Oe. Diamagnetic corrections for the eicosane and the sample's core diamagnetism were accounted for using Pascal's constants.[14] Fits of the dc magnetic data were performed using the freely available program PHI.[15]

Ac susceptibility data was fit to a generalized Debye model which accounts for relaxation time (τ), isothermal susceptibility (χ_T), adiabatic susceptibility (χ_S), and the presence of a distribution of relaxation times (α).[16] Some of the ac data (notably for **4a** and **6**) have broad features in the low χ', high χ'' region (noticeable mostly in the Cole-Cole plots in the Supporting Information). We fit the data to both a single relaxation process as well as a two-relaxation process equation. While the two-process equation gave better fits, τ, changed by <3% and we could no longer fit the second process in the high temperature data, as the affected data had moved well beyond the frequency limit of the instrument. As such, all ac data was fit using the single-process equation. Fits of the variable temperature relaxation data were obtained by minimizing the sum of squared errors in the plot of $\ln(\tau)$ vs. $1/T$, so as to not give extra weight to the low-temperature data. Thus, the standard errors of the estimate (σ_{EST}) are directly applicable to the plot of $\ln(\tau)$ vs. $1/T$ and not τ vs. T.

Mössbauer Spectroscopy

The iron-57 Mössbauer spectra of **6** were obtained between 5 and 290 K with a constant acceleration spectrometer and a cobalt-57 rhodium source. Prior to measurements the spectrometer was calibrated at 295 K with α-iron foil and the isomer shifts reported herein are relative to 295 K α-iron. A powder absorber with a thickness of 100 mg/cm^2, or 6.0 mg/cm^2 of iron, was prepared and transferred to the cold finger of a closed-cycle refrigerator under an inert atmosphere in order to avoid oxidation of this highly air-sensitive compound.

2.3 Results and discussion

Synthesis and structures

Our initial attempts at synthesizing a dialkyl cobalt(II) complex used the tris(trimethylsilyl)methyl ligand used to isolate $Mn(C(SiMe_3)_3)_2$ and $Fe(C(SiMe_3)_3)_2$, the only other reported paramagnetic dialkyl M(II) complexes at the time.[17] Our reactions of $CoCl_2$ and $[Li(THF)_4][Li(C(SiMe_3)_3)_2]$ yielded intractable mixtures of solids. The isolation of $[Co\{C(SiMe_2Ph)_3\}]_2$ from an *in situ* reduction of Co(II)[5] confirmed our suspicion that the tris(trimethylsilyl)methyl ligand was too reducing to isolate Co(II) products. Thus, we turned our attention to derivatives of this ligand with electron withdrawing groups.

Replacing a methyl group in $[C(SiMe_3)_3]^-$ with an alkoxide significantly reduced the electronic density at the anionic carbon. The zwitterionic compound $Na[C(SiMe_2OCH_2CH_2OMe)_3]$ has a $pK_{(DMSO)}$ of 22.5 compared to the much more basic $Li[C(SiMe_3)_3]$ with a $pK_{(THF)}$ of 36.6.[6] With the assumption that many alkyl or aryloxides would have a similar effect, we chose to use the simpler $HC(SiMe_2OPh)_3$ ligand. Reaction of $HC(SiMe_2OPh)_3$ with MeK at room temperature in a Et_2O/DME mixture quickly gave the desired metalated product, $(DME)_2K(C(SiMe_2OPh)_3$.[3]

Salt metathesis reactions between $(DME)_2K(C(SiMe_2OPh)_3$ and MCl_2 yielded $M(C(SiMe_2OPh)_3)_2$ in moderate yield (M = Cr (**1**), Mn (**2**), Fe (**3**), Co (**4**), Zn (**5**)). Two structures of **4** were obtained depending on crystallization conditions; **4a** crystallizes in C2/c with no solvent in the crystal lattice and is isostructural to **2** and **3**, while **4b** crystallizes in R-3 with a disordered hexane in the crystal lattice. These compounds decompose in days at room temperature and in months when stored at −30 °C. Our initial focus was on likely candidates for single-molecule magnets (Fe, Co), however the bend in the C–M–C axis (*vide infra*) prompted us to make the rest of the series to glean information on the extent of the metal oxygen interaction. We also attempted to make the nickel congener. The standard reduction potentials for Fe^{2+}/Fe, Co^{2+}/Co, and Ni^{2+}/Ni are -0.447, -0.280, and -0.257 V, respectively, so it seemed plausible that a ligand suitable for Co would behave similarly with Ni. However, reactions with $NiBr_2$ yielded intractable dark amorphous solids.

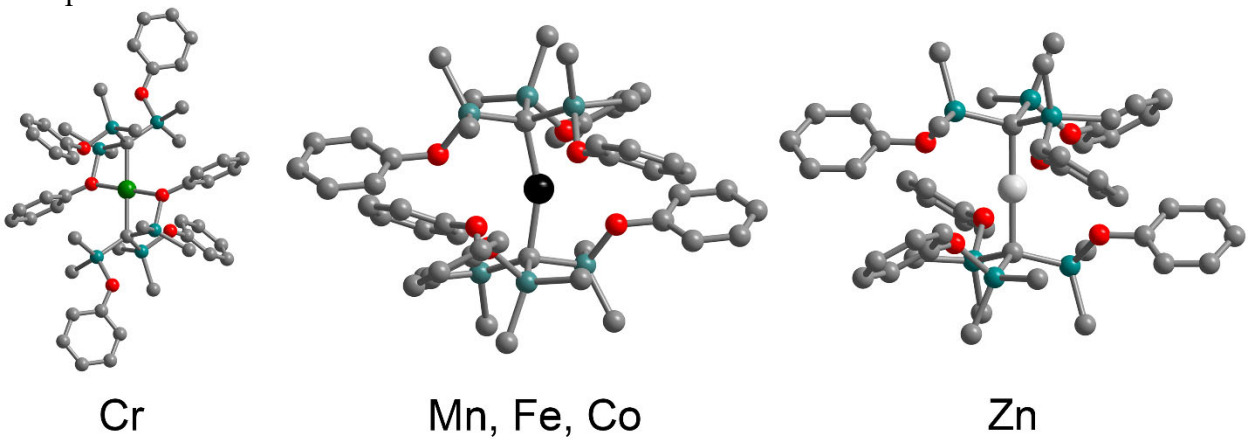

Figure 2.1. Molecular structures of $M(C(SiMe_2OPh)_3)_2$ (M = Cr (**1**), Mn (**2**), Fe (**3**), Co (**4a**), Zn (**5**)). Grey, red, turquoise, green, and white spheres represent C, O, Si, Cr, and Zn atoms, respectively. The black sphere represents either Mn, Fe, or Co. Hydrogen atoms have been omitted for clarity.

Compounds **2**, **3**, and **4a** crystallize in C2/c, are isostructural, and feature a two-coordinate metal center with a bend in the C–M–C axis (Figure 2.1). The metal atom is disordered over two positions related by a crystallographic inversion center. Metal-carbon distances of 2.110(2) and 2.208(2) Å for **2**, 2.079(3) and 2.115(3) Å for **3**, and 2.038(2) and 2.068(2) Å for **4a** are slightly longer than 2.102(4) and 2.0505(14) Å seen for $Mn(C(SiMe_3)_3)_2$ and $Fe(C(SiMe_3)_3)_2$,[17] respectively, and are similar to $Co(C(SiMe_2ONaph)_3)_2$ (2.066(2) Å).[3] The C–M–C bond angle

deviates significantly from 180° bond angles of 160.91(4)°, 157.99(5)°, and 160.59(4)°, for **2**, **3**, and **4a**.

The metal-oxygen interaction is strongest for **1**, in which there is an actual Cr–O bond (2.0685(16) Å) that is shorter than the Cr–C bond (2.226(2) Å). The Cr ion occupies an inversion center and has approximately square planar geometry.

Compound **5** crystallizes in *R*-3 and the Zn ion occupies a crystallographic inversion center to yield a linear C–Zn–C axis. The Zn–C distance 1.967(5) Å is the shortest in the series of compounds, and is shorter than the Zn–C distances in $Zn(C(SiMe_3)_3)_2$ (1.982(2) Å)[18] and $Zn(C(SiMe_2ONaph)_3)_2$ (1.995(3) Å).[3] At first glance **4b** appears to be isostructural to **6**, however in **4b** the Co ion is again disordered, this time over six positions. The C–Co–C angle (163.16°) is slightly larger than in **4a** (160.59(4)°).

The bend in the C–M–C axis is the result of a delicate balance of long-range M···O interactions and interligand π-interactions. Indeed, these interactions are likely primarily responsible for the stability of the molecules; calculations on $Co(C(SiMe_2ONaph)_3)_2$ show that metal-ligand bond formation only provides a minor stabilizing effect (4.7 kcal/mol).[3] We are pursuing an in-depth computational analysis of these interactions, but for now a comparison of interaction distances in several molecules is useful. Table 2.1 gives comparisons for **4a**, **4b**, **5**, and $Co(SiMe_2ONaph)_3)_2$ in four categories: M–C, sp^3-CH···π, sp^2-CH···π, and M···O distances (for the π interactions only those of a single aryl ring are listed; distances are given between H atoms and C atoms of the rings). Within the $M(C(SiMe_2OPh)_3)_2$ series, the M···O distances follow expected trends with oxophilicity—the most oxophilic metal, Cr, forms a Cr–O bond (2.0685(16) Å), while the least oxophilic metal, Zn, has a very long M···O distance (2.9368(10) Å). Compounds **2**, **3**, **4a**, and **4b** have M···O distances of 2.5449(17), 2.463(5), 2.5207(15), and 2.662(15) Å, respectively, which are all longer than the sum of M^{2+} and O^{2-} ionic radii (~2.2 Å) but significantly shorter than the Zn···O distance in **5**. Notably, the disordered metal ion for **2**, **3**, **4a**, and **4b** is always in the direction of an O atom.

Table 2.1. Distances of key structural parameters for compounds **1**-**5** and $Co(C(SiMe_2ONaph)_3)_2$. Non-covalent interligand π-interactions are important for the stability of the dialkyl complexes.

	M–C (Å)	sp^3-CH···π (Å)[a]	sp^2-CH···π (Å)[a]	shortest M···O (Å)
1	2.226	-	-	2.0685
2	2.110, 2.208	2.917, 2.988	2.749, 3.052	2.5449
3	2.077, 2.105	2.808, 2.869	2.807, 3.065	2.4749
4a	2.038, 2.068	2.861, 2.804	2.799, 3.064	2.5207
4b	2.12	2.750, 2.942	3.047	2.662
5	1.967	2.760, 2.948	3.170	3.015
$Co(C(SiMe_2ONaph)_3)_2$ (ref. 3)	2.066	2.692, 3.004	2.918, 2.914, 2.953, 2.822, 3.056	3.1051

[a] The H···C(ring) distances for a single phenyl ring. For **1**, **2**, **3**, and **4a** there are three unique phenyl rings; distances are given for the phenyl ring with the shortest distances.

There are two types of interligand π interactions: the sp^3-CH···π interaction between a methyl proton and phenyl ring, and the sp^2-CH···π edge-to-face interaction between phenyl groups. A review of these interactions states that sp^3-CH···π interactions occur at 2.75 ± 0.10 Å and sp^2-CH···π occur at 2.73 ± 0.13 Å, where the distance is between the proton and the plane of the ring.[19] In the following we give distances between protons and nearby carbon atoms in the phenyl ring.

Compounds **2**, **3**, **4a**, **4b**, and **5** all have two sp^3-CH···π interactions per phenyl ring. Compounds **4b** and **5** have both the shortest and longest sp^3-CH···π distances, while **4a** has two intermediate sp^3-CH···π distances. Compared to the *R*-3 structures, the C2/c structures appear to

provide greater stability via the sp^2-CH···π. Structure **4a** has two relatively short sp^2-CH···π interactions (2.799 Å, 3.064 Å) per ring, while **4b** has only one (3.047 Å). Thus, as an isolated molecule **4a** (and the rest of the C2/c structures) is likely more stable than **4b** considering both the shorter M···O distance and the additional interligand π-interactions. Obviously we have not yet considered intermolecular packing in this analysis. While the orientation of methyl groups and phenyl rings between molecules is set up for these same types of interactions, there are no H···π distances shorter than 3 Å between molecules for any of the compounds discussed here.

When considering the same interactions in $Co(C(SiMe_2ONaph)_3)_2$, it is clear why that molecule contains a linear C–Co–C axis while **4a** and **4b** have bent axes. In addition to having similar sp^3-CH···π interactions, each naphthyl ring in $Co(C(SiMe_2ONaph)_3)_2$ has two protons which can interact with an adjacent naphthyl ring, resulting in five sp^2-CH···π distances between 2.822 and 3.056 Å.[3] Thus, any distortion to obtain stabilization from a M···O interaction would lose many of these contacts, destabilizing the molecule as a whole.

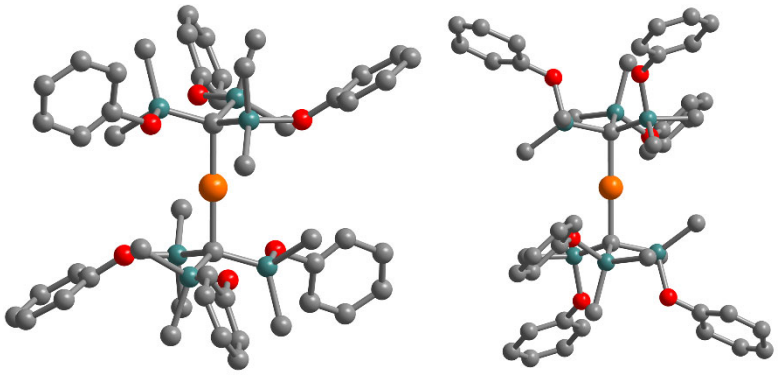

Figure 2.2. Molecular structures of the two $[Fe(C(SiMe_2OPh)_3)_2]^-$ ions in the crystal structure of **6**. Grey, red, turquoise, and orange spheres represent C, O, Si, and Fe atoms, respectively. Hydrogen atoms have been omitted for clarity.

The reduction of **5** with KC_8 in the presence of 2.2.2-Cryptand gave [K(2.2.2-Cryptand)][$Fe(C(SiMe_2OPh)_3)_2$] (**6**). Moving to a less oxophilic iron center upon reduction, **6** has a strictly linear coordination environment with no Fe–O interactions (shortest Fe–O distance is 3.2633(16) Å). The complete removal of the O atom from the coordination sphere of Fe is not entirely surprising; $[Fe(N(SiMe_3)_2]_2$ is a dinuclear complex with three coordinate Fe(II) centers,[20] but reduction yields a two coordinate $[Fe(N(SiMe_3)_2]^-$ ion.[21] There are two unique $[Fe(C(SiMe_2OPh)_3)_2]^-$ ions in the unit cell; both have iron atoms on crystallographic inversion centers (Figure 2.2). Despite being a larger ligand, the Fe–C bond lengths in the two ions in **6** (2.041(2) and 2.033(4) Å) are slightly shorter than the Fe–C bond lengths in [K(2.2.2-Cryptand)][$Fe(C(SiMe_3)_3)_2$] (2.058(4) and 2.062(4) Å).[22]

Static magnetic properties

Variable temperature dc magnetic susceptibilities for **3**, **4a**, and **4b** show non-Curie behavior indicated by the temperature dependence of $\chi_M T$ (Figure 2.3). Compounds **3**, **4a**, and **4b** have room temperature $\chi_M T$ values of 4.64, 4.72, and 4.78 $cm^3\ K\ mol^{-1}$, respectively. The gradual decrease below 150 K is indicative of significant zero field splitting.

The room temperature $\chi_M T$ values are significantly larger than the expected spin-only values of 3.00 ($S = 2$) and 1.87 ($S = {}^3/_2$) $cm^3\ K^{-1}\ mol^{-1}$, indicating a significant orbital contribution to the magnetic moment. The isotropic Landé *g*-values from the room temperature $\chi_M T$ values are 2.48

(**3**), 3.17 (**4a**), and 3.19 (**4b**). The *g* value for **5** is comparable to that of $Fe(C(SiMe_3)_3)_2$ (2.53).[23] Both values are on the high side of the range of reported values for two-coordinate Fe^{II} and Co^{II} complexes. The only similar compounds with significantly larger *g* values are $Fe\{N(H)Ar^{Pri6}\}_2$ (3.06),[24] $Co\{N(H)Ar^{Pri6}\}_2$ (3.25),[25] and $Co(C(SiMe_2ONaph)_3)_2$ (3.23).[3]

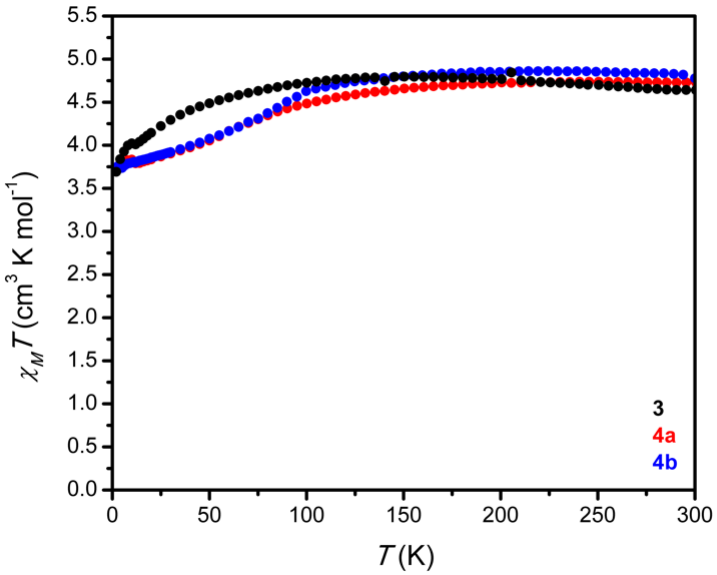

Figure 2.3. Variable-temperature magnetic susceptibility times temperature ($\chi_M T$) for **3** (black), **4a** (red), and **4b** (blue) collected under a dc field of 1000 Oe.

Low temperature magnetization data shows non-superimposable isofield lines when plotted against *H*/*T*—another indication of magnetic anisotropy (Figure S2.1-S2.3). Using the program PHI[15] we fit these data with the zero-field splitting Hamiltonian

$$H = DS_z^2 + E\left(S_x^2 - S_y^2\right) + g_{\parallel}\mu_B S_z H_z + g_{\perp}\mu_B S_{\perp} H_{\perp} \quad (1)$$

to quantify the axial (*D*) and transverse (*E*) anisotropy as well as the corresponding components of *g*. The results are summarized in Table 2.2. In all three cases modest axial anisotropy is observed along with significant contributions from transverse anisotropy. Surveys of the surrounding parameter space are given in Figures S2.10-S2.12. Rationalizing the presence of axial anisotropy for both compounds is not trivial. In high symmetry structures where there is, to a first approximation, unquenched orbital angular momentum or an obvious low-lying excited state it is relatively straightforward to predict the sign of *D*.[26] In these complexes, however, the long-range M···O interactions destroy the high symmetry required for unquenched orbital angular momentum. Given the exceptionally weak ligand field observed for $Co(C(SiMe_2ONaph)_3)_2$,[3] the magnetic anisotropies in compounds **3**, **4a**, and **4b** are likely the result of several excited contributions to an orbitally non-degenerate ground state.

Table 2.2. Parameters used for the fits of magnetization data for **3**, **4a**, and **4b** using Equation 1.

	D (cm^{-1})	$\lvert E/D \rvert$	$g_{\parallel}$	$g_{\perp}$
3	-14.2	0.15	2.79	1.4
4a	-17.1	0.12	3.69	1.07
4b	-16.5	0.21	3.77	0.83

The dc susceptibility of **6** showed significant field dependence of the $\chi_M T$ product (Figure S2.7), similar to what was observed for $[Fe(N(SiMe_3)_2)_2]^-$.[21] As before, we attribute this field dependence to the presence of a paramagnetic impurity, the presence of which seems unavoidable given the fast decomposition of this compound in solution.[27] Qualitatively, at high fields we see the temperature dependent $\chi_M T$ product expected for a system with significant magnetic anisotropy. Similar to what was observed for $[Fe(C(SiMe_3)_3)_2]^-$ (ref. 22) and $[Fe(N(SiMe_3)_2)_2]^-$ (ref. 21), this likely arises from the three electrons in the degenerate $m_l = 2$ orbitals; the expected *d*-orbital splitting for **6** is $(d_{z2})^2(d_{x2-y2},d_{xy})^3(d_{xz},d_{yz})^2$.

Temperature Dependence of the Mössbauer Spectra

The iron-57 Mössbauer spectra of **6** obtained at selected temperatures between 5 and 290 K are shown in Figure 2.4. A complete set of the observed Mössbauer spectra is shown in Figure S2.7. Between 5 and 30 K, the spectra are very similar and exhibit two sharp sextets of equal area, shown in blue and red in Figure 2.4, sextets that can be assigned to the two inequivalent crystallographic iron(I) sites in **6**. A tentative assignment of each of these sextets to either Fe1 or Fe2 site is discussed in the supplementary information. Between 40 and 70 K, the two sextets broaden considerably but can still be clearly identified. Above 100 K, the sextets are no longer resolved and the spectra appear as highly asymmetric doublets. This temperature dependence of the Mössbauer line shape profile is characteristic of the relaxation[28] of the hyperfine field on a timescale that is comparable with the Larmor precession time of the iron-57 nuclear moment about the hyperfine field; the precession corresponds to 10^{-8} to 10^{-9} s depending upon the magnitude of the hyperfine field.

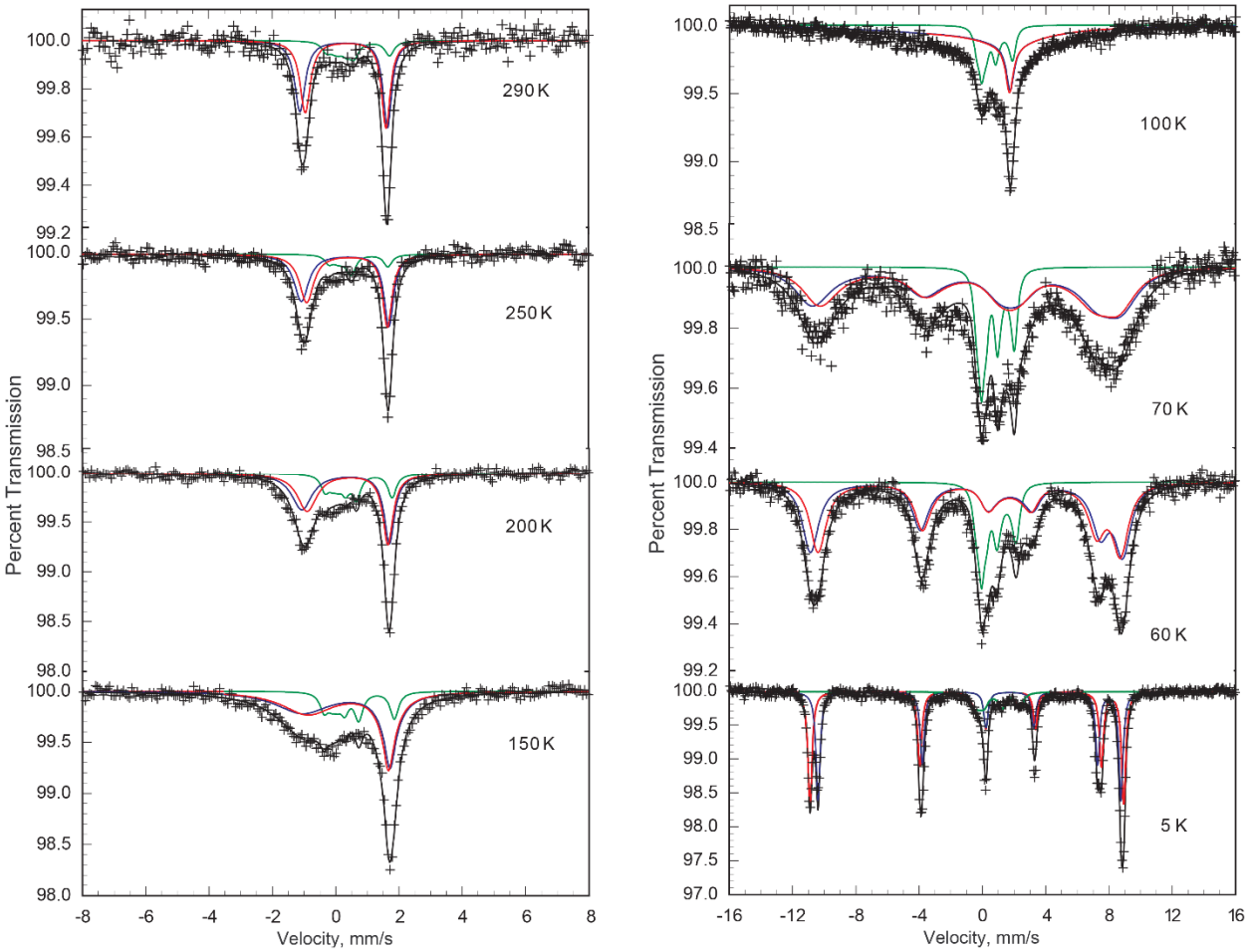

Figure 2.4. The iron-57 Mössbauer spectra of **6** obtained at the indicated higher, left, and lower, right, temperatures. The solid lines are the results of the fits described in the text; the reader should note the difference in the velocity scale in the two plots.

The iron-57 nucleus in **6** at 5 K experiences an effectively static hyperfine field and the 0.310(5) mm/s line width observed at 5 K agrees well with that observed for α-iron at 5 K and ±16 mm/s under the same experimental conditions. Note that this observation of static relaxation is in accord with the ac susceptibility results obtained in a zero dc applied magnetic field, an observation that revealed a relaxation time of ca. 9 x10^{-3} s at 5 K, a timescale that is much longer than the Larmor precession time of the iron-57 nuclear moment about the hyperfine field.

The magnetic impurity observed in the dc susceptibility data is equally apparent in the Mössbauer spectra. Unfortunately, the presence of an iron(II) impurity with a relative area of 11 and 15 percent at 5 and 290 K, respectively, complicates the analysis of the spectra. This component, shown in green in Figures 2.4 and S2.14 has been analyzed as a slightly broadened sextet with hyperfine parameters characteristic of iron(II), see Table S2.3; no further discussion of this component will be given herein.

The determination of the effective internal hyperfine field, H_{int}, isomer shift, δ, and quadrupole interaction, $e^2Qq/2$, in the presence of the strong influence of slow paramagnetic relaxation requires modeling the relaxation profile. Thus, the spectra of **6** have been fitted with a relaxation model of the hyperfine field by using the Dattagupta and Blume formalism.[29] In this fitting model, for both iron(I) sites in **6**, the hyperfine field was assumed to be oriented parallel to the principal

axis of the electric field gradient tensor, which was taken to be the C–Fe–C linear axis with the asymmetry parameter, η, of the electric field gradient tensor, fixed at zero in agreement with the approximate C_3 symmetry axis found at both iron(I) sites.

Table 2.3. Mössbauer Spectral Parameters Obtained for **6**[a]

T, K	Area, (%e)(mm/s)	δ_1,[b] mm/s	H_1,[c] T	$\Delta E_{Q,1}$,[d] mm/s	A_1, %	δ_2,[b] mm/s	H_2,[c] T	$\Delta E_{Q,2}$,[d] mm/s	A_2, %	ν, MHz
290	0.89(3)	0.265(10)	61.41	–2.766	42.0[d]	0.325(10)	59.49	–2.553	42.0[d]	23700(7300)
275	1.07(3)	0.28(1)	61.41	–2.766	43.5(9)	0.33(1)	59.49	–2.553	43.5(9)	14400(2300)
250	1.43(3)	0.29(1)	61.41	–2.766	42.5(6)	0.35(1)	59.49	–2.553	42.5(6)	9940(1000)
225	1.85(3)	0.30(1)	61.41	–2.766	42.0(6)	0.36(1)	59.49	–2.553	42.0(6)	6110(420)
200	2.27(3)	0.315(10)	61.41	–2.766	39.4(5)	0.375(10)	59.49	–2.553	39.4(5)	4780(250)
150	3.27(4)	0.34(1)	61.41	–2.766	41.9(4)	0.40(1)	59.49	–2.553	41.9(4)	1300(50)
100	4.52(6)	0.365(10)	61.41	–2.766	41.5(3)	0.425(10)	59.49	–2.553	41.5(3)	199(8)
80	4.90(9)	0.37(1)	61.41	–2.766	41.7(3)	0.43(1)	59.49	–2.553	41.7(3)	64(1)
70	5.24(9)	0.375(10)	61.41	–2.766	42.2(3)	0.435(10)	59.49	–2.553	42.2(3)	28.6(8)
60	5.54(6)	0.383(10)	61.41	–2.766	42.1(2)	0.443(10)	59.49	–2.553	42.1(2)	10.9(2)
50	5.93(6)	0.388(10)	61.41	–2.766	42.2(2)	0.448(10)	59.49	–2.553	42.2(2)	3.3(1)
40	6.32(5)	0.392(10)	61.41	–2.766	45.0(1.0)	0.449(10)	59.49	–2.549	39.0(6)	0.70(6)
30	6.53(7)	0.397(10)	61.45	–2.763	46.0(1.0)	0.453(10)	59.47	–2.556	39.5(7)	0.10(5)
25	6.82(5)	0.397(10)	61.51	–2.770	44.0(8)	0.454(10)	59.5	–2.556	42.3(4)	0.09(5)
20	7.05(6)	0.40(1)	61.53	–2.768	44.0(1.0)	0.454(10)	59.45	–2.553	42.3(6)	0.08(5)
15	7.09(6)	0.402(10)	61.48	–2.763	46.2(9)	0.456(10)	59.39	–2.553	42.2(5)	0.05(3)
5	7.20(5)	0.398(10)	61.51	–2.771	45.1[c]	0.459(10)	59.43	–2.553	43.9[c]	0.05(7)

[a]The statistical fit uncertainties for the varied parameters are given in parentheses; the actual uncertainties may be two to three times larger. The line width of components 1 and 2 have been constrained equal to 0.31 mm/s. The parameters of the impurity component are given in Table S2.3. [b]Relative to *a*-iron at 295 K. [c]Parameter constrained to the value given. [d]$\Delta E_Q = e^2Qq/2$. The asymmetry parameter, η, and the polar angle of the hyperfine field, θ, are fixed to zero because of the C_3 symmetry axis along the C–Fe–C direction.

All the above assumptions are identical to those used[15b] earlier for the fits of the Mössbauer spectra of $[Fe(C(SiMe_3)_3)_2]^-$. The hyperfine field reverses along the C–Fe–C linear axis with a relaxation frequency, ν, or with a relaxation period, $\tau = 1/\nu$. Because the relaxation of the hyperfine field leads to a broadening of the spectral lines, as is observed in the spectra of **6** above 30 K, a minimum experimental line width, as well as a constant hyperfine field, were determined as discussed below and used to fit the spectra to obtain a reliable temperature dependence of the relaxation period for **6**.

The fits obtained below 40 K indicate no broadening of the lines through relaxation. Further, the two hyperfine fields of 61.4(1) and 59.5(1) T remain constant within their corresponding accuracies between 5 and 30 K. Hence, in the relaxation fits obtained above 30 K, the value of H_{int} for the two spectral components were constrained to 61.41 and 59.49 T, shown in blue and red respectively, values that were obtained from fitting the 40 K spectrum in the absence of relaxation. These hyperfine fields are only slightly smaller than the hyperfine field of 63.55 T obtained from the fits[22b] of the Mössbauer spectra of the single iron(I) site found in $[Fe(C(SiMe_3)_3)_2]^-$.

The higher-temperature spectra were also fitted with the relaxation model described above for a fixed line width of 0.31 mm/s; the resulting spectral parameters are given in Tables 2.3 and S2.7, and the two components and the fitted profiles are shown as the blue, red, and black solid lines in

Figures 2.4 and S2.14. The quadrupole interactions have been fitted between 5 and 30 K and constrained to their average value of –2.766(5) and –2.553(5) mm/s above 40 K for the blue and red sextets, respectively. These values are similar to the value of –2.555(2) mm/s reported[22b] for $[Fe(C(SiMe_3)_3)_2]^-$. Between 5 and 40 K the fitted ratio of the relative areas of the blue and red sextets is between 1.00(4) and 1.15(5), in good agreement with the equal population of the two crystallographically inequivalent iron(I) sites present in **6**; essentially identical fits are obtained if the relative areas are constrained to one to one.

The temperature dependences of the isomer shifts and logarithm of the spectral absorption areas of **6** are shown in Figure S2.15, where the solid lines are the result of fits[30] with the Debye model for a solid. The Mössbauer temperature, Θ_M, and the Debye temperature, Θ_D, for **6**, obtained from a fit of the temperature dependence of the isomer shift and spectral absorption area between 5 and 250 K are 338(25) and 137(1) K, respectively; values that compare well with the temperatures of 313(16) and 141(2) K obtained[22b] previously for $[Fe(C(SiMe_3)_3)_2]^-$. Furthermore, the Debye temperatures of ca. 150 K are characteristic[31] of organometallic compounds and, as is well known, Θ_M is typically observed to be two to three times larger than Θ_D, because the temperature dependence of the isomer shift is more sensitive to the higher energy phonons than the temperature dependence of the spectral absorption area.

The analysis of the H_{int} values of 61.41 and 59.49 T used for the calculation of the relaxation profiles for **6**, in terms of three contributions, the Fermi contact field, H_{Fermi}, the dipolar field, H_{dip}, and the orbital field, H_{orb}, as previously reported[22b] for $[Fe(C(SiMe_3)_3)_2]^-$ leads to large positive orbital contributions of ca. +76 and +74 T, respectively, contributions that are however smaller by ca. 2 and 4 T than those obtained for $[Fe(C(SiMe_3)_3)_2]^-$.

The 5 K isomer shifts of 0.398 (10) and 0.459(10) mm/s in **6**, for the blue and red sextets, are equal and significantly more positive on average, than the isomer shift of 0.402(1) mm/s reported[22b] for $[Fe(C(SiMe_3)_3)_2]^-$; the same comparison is also valid at 295 K. The relatively low iron(I) isomer shifts have been explained earlier[22b] in terms of the large calculated 4*s* electron density at the iron-57 nucleus and the strong $4s–3d_{z^2}$ orbital mixing; the same explanation seems to be valid for **6**. The more positive average iron(I) isomer shift in $[Fe(C(SiMe_2OPh)_3)_2]^-$, **6**, as compared with that of $[Fe(C(SiMe_3)_3)_2]^-$, corresponds to a lower s-electron density at the iron(I) nucleus of **6** as compared with the iron(I) in the latter anion. This difference is an indication of the better electron withdrawing properties of the OPh moiety in the ligands of **6** as compared with the methyl moiety in the ligands of the latter compound.

Dynamic magnetic properties

With the knowledge that compounds **3**, **4a**, **4b**, and **6** were indeed magnetically anisotropic, we performed ac magnetic susceptibility experiments to check for the presence of slow magnetic relaxation. Despite being magnetically anisotropic, compound **3** did not show a signal in out-of-phase susceptibility (χ''). This is likely due to the presence of fast relaxation via a quantum tunneling mechanism, a frequently seen process for mononuclear systems that are non-Kramers ions, as the ground states in non-Kramers systems are allowed to directly mix.[32] Tunneling can be effectively shut down in an applied field, so we measured ac susceptibility under applied dc fields of 500 to 3000 Oe yet still did not see a signal in χ''. The complete absence of slow-magnetic relaxation even in applied fields is somewhat surprising but can perhaps be attributed to the large transverse anisotropy component, which is known to facilitate fast relaxation.[33]

Compounds **4a**, **4b**, and **6** showed a χ'' signal in the absence of an applied field. For **4a** and **4b** we collected data under both zero and 1500 Oe applied dc fields over temperature ranges of 2-9 K. For **6** we collected data under zero applied field over the temperature range of 2-24 K. The data was then fit to a generalized Debye model[16] (Figure S2.6-S2.19) to extract relaxation times, which are shown in Figures 2.5 and 2.6, and Tables S2.10-2.14. It was clear based on the ac data that relaxation in **6** would be sufficiently slow to observe hysteresis in a variable-field magnetization scan. As shown in Figure 2.6, a waist restricted hysteresis occurs below 4.4 K (compared to 6.5 K for $[Fe(C(SiMe_3)_3)_2]^-$)[22] with a field sweep rate of 40 Oe/s.

Relaxation times extracted from the ac susceptibility for **4a** and **4b** and a combination of ac susceptibility and Mössbauer spectroscopy for **6** are shown in the Arrhenius plots in Figures 2.5 and 6, respectively. Note that the relaxation times for **6** below 40 K could not be obtained from the Mössbauer spectra because the timescale of the relaxation at these temperatures is much longer than the Larmor precession time. The non-linearity in the Arrhenius plots indicate the presence of multiple relaxation processes. A temperature independent low temperature regime is indicative of a tunneling relaxation pathway[33] while a linear high temperature region is ascribed to Orbach relaxation (a two-phonon process through a real excited state).[34] The intermediate temperature range can be modeled using either Raman relaxation, as described in detail by Orbach[34] and Shrivastava,[35] or the coupling of states through specific phonon modes.[36] Historically, Raman relaxation has been used to model relaxation in magnetically dilute extended solids with only modest anisotropy[34,35] and was first applied to single-molecule magnets relatively recently.[37] Others have discussed in detail the problems with applying Orbach and Shrivastava's models to single-molecule magnets, specifically that the model assumes that the system can be described as a Debye solid and that each phonon has the same spin-phonon coupling strength.[36] For **4a** and **4b**, however, because our relaxation data are below 9 K,[38] it is possible that the relevant phonon spectrum is Debye-like and that Orbach and Shrivastava's models are acceptable. We use the same model for **6** primarily to make comparisons to $[Fe(C(SiMe_3)_3)_2]^-$ (ref. 22), which used the same model. A more accurate description of relaxation in **6** will require at least experimental knowledge of the low energy phonon spectrum, and ideally calculations of individual spin-phonon coupling strengths as well. For this reason, we have included all relaxation data in Tables S2.10-S2.14 should a more thorough investigation of relaxation in these systems be pursued in the future.

We fit the relaxation data of **4a**, **4b**, and **6** to Equation 2,

$$\tau^{-1} = \tau_{tunnel}^{-1} + BH^4T + CT^n + \tau_{0,1}^{-1}\exp\left(\frac{U_1}{k_BT}\right) + \tau_{0,2}^{-1}\exp\left(\frac{U_2}{k_BT}\right) \qquad (2)$$

where the five terms represent contributions from tunneling, direct, Raman, and two Orbach relaxation processes, respectively. The terms B, C, and τ_0 contain physical constants as well as spin-phonon coupling terms.[34,35] U_1 and U_2 are the thermal barriers to spin-reversal and correspond to excited microstates within the ground S or J manifold.

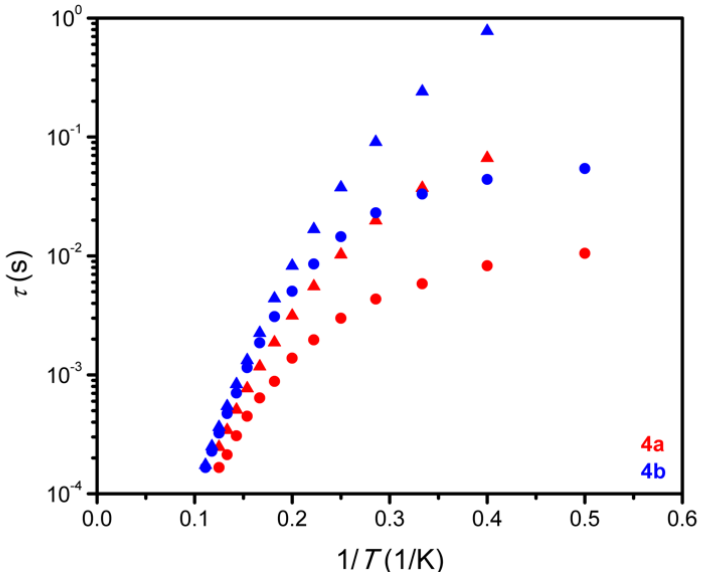

Figure 2.5. Arrhenius plot showing the log of relaxation time, τ, versus inverse temperature for **4a** (red) and **4b** (blue) under either zero (circles) or 1500 Oe (triangles) applied dc fields. Plots of the individual data sets with fits are given in the supporting information.

The relaxation data collected under 0 and 1500 Oe dc fields for **4**a and **4b** were fit simultaneously (Table 4 and Figures S2.26-2.27). The tunneling time for **4b** is about five times longer than that for **4a**, which is perhaps related to **4b** being closer to the ideal linear structure than **4a**. Neither fit used a term for Orbach relaxation; however, looking solely at the highest temperature data points of the 1500 Oe data can yield lower and upper limits for U and τ_0 which are 27 cm^{-1} and 1.8×10^{-6} s for **4a** and 35 cm^{-1} and 6.0×10^{-7} s for **4b**. The calculated barrier heights ($U = 2(D^2 + 3E^2)^{1/2}$) from the magnetization data are 34.9 and 35.1 cm^{-1} for **4a** and **4b**, respectively.

The relaxation data for **6** was fit with all terms of Equation 2. Based on the analysis of $[Fe(C(SiMe_3)_3)_2]^-$ (ref. 22) and $[Fe(N(SiMe_3)_2)_2]^-$ (ref. 21,39), the two spin-reversal barriers U_1 and U_2 correspond to excitations from the ground $M_J = {}^7/_2$ state to the excited $M_J = {}^5/_2$ and $M_J = {}^3/_2$, respectively. The stark difference in low temperature relaxation behavior between $[Fe(C(SiMe_3)_3)_2]^-$ and **6** suggests that through-barrier relaxation is significantly more sensitive to deviations from high symmetry than is anisotropy. The U_1 value for **6** (199.1 cm^{-1}) is only 20% smaller than that of $[Fe(C(SiMe_3)_3)_2]^-$ (246 cm^{-1}), yet the relaxation times at 9 K (the lowest data point collected for $[Fe(C(SiMe_3)_3)_2]^-$) is over two orders of magnitude faster for **6** than for $[Fe(C(SiMe_3)_3)_2]^-$.[22] Indeed, the lowest temperature relaxation data for both **6** and $[Fe(N(SiMe_3)_2)_2]^-$ are both clearly dominated by a relatively fast tunneling mechanism, while at the same temperatures relaxation in $[Fe(C(SiMe_3)_3)_2]^-$ is due to slower Raman relaxation.

Table 2.4. Parameters used for the fits of relaxation data for **4a**, **4b**, and **6** using Equation 2.

	τ_{tunnel} (s)[a]	B (s^{-1} K^{-1} T^{-4})[b]	C (s^{-1} T^{-n})	n	$\tau_{0,1}$ (s)	U_1 (cm^{-1})	$\tau_{0,2}$ (s)	U_2 (cm^{-1})	σ_{est}
4a	1.05×10^{-2}	3.35×10^{3}	5.49×10^{-2}	5.50					0.341,[a] 0.195[b]
4b	5.42×10^{-2}		2.67×10^{-3}	6.66					0.248,[a] 0.0450[b]
6	1.31×10^{-2}		2.13×10^{-1}	2.83	1.07×10^{-9}	199.1	6.96×10^{-12}	468.0	0.151

[a] Applicable for data collected under 0 Oe dc field. [b] Applicable for data collected under 1500 Oe dc field.

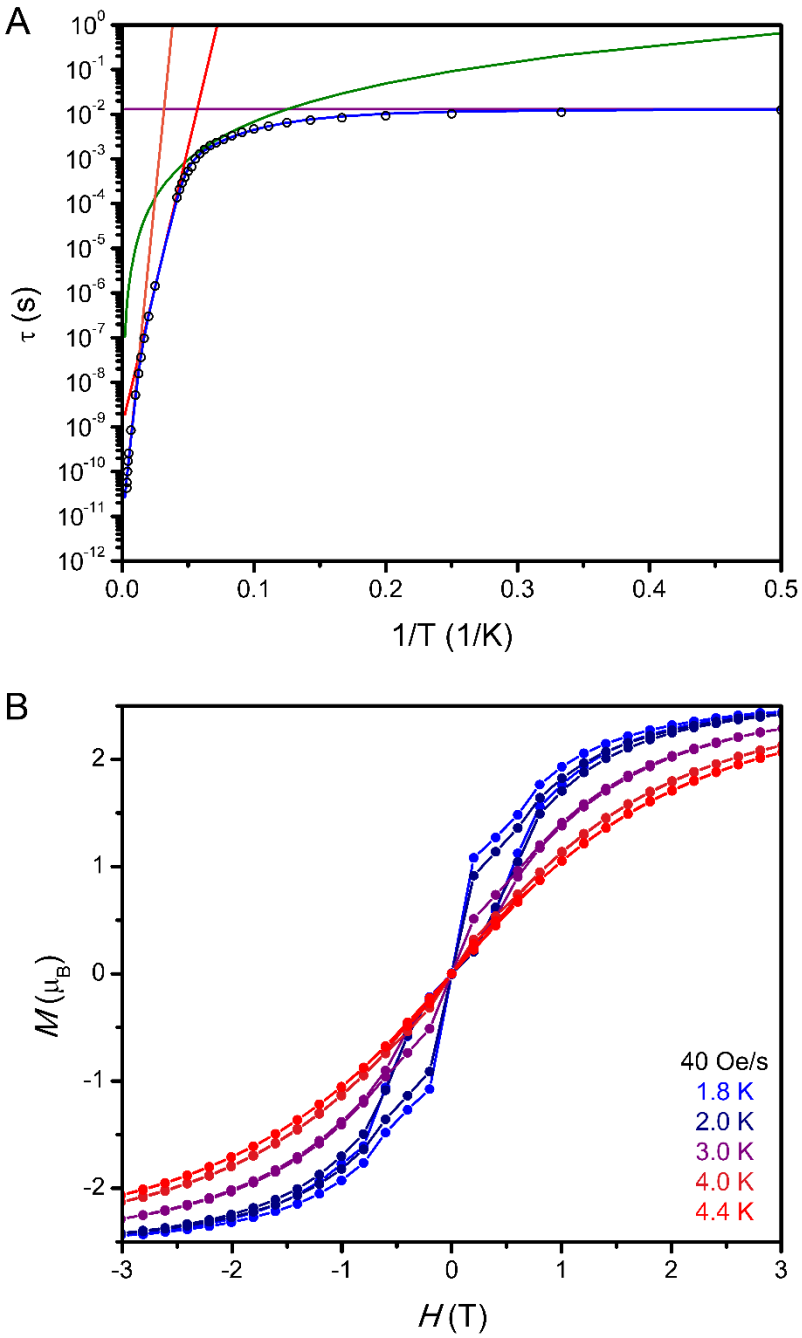

Figure 2.6. (A) Arrhenius plot showing the log of relaxation time, τ, versus inverse temperature for **6** under zero applied dc field. The blue line is a fit from Equation 2, with purple and green lines representing contributions from quantum tunneling and Raman relaxation processes, and red and orange lines representing Orbach relaxation processes through the first and second magnetic excited state, respectively. (B) Variable-field magnetization data for **6** collected at temperatures between 1.8 and 4.4 K at a sweep rate of 40 Oe/s.

2.3 Conclusions

Compounds **2**, **3**, **4a**, **4b**, and **6** are among only a handful of paramagnetic dialkyl complexes, with the preceding complexes being either $[M(C(SiMe_3)_3)_2]^{0/-}$ (ref. 22, 40) or $Co(C(SiMe_2ONaph)_3)_2$.[3] The use of electron withdrawing phenoxides was essential for the isolation of the dialkyl Co(II) complex, however the weakness of the metal-ligand bond led to a

situation where compounds **2**, **3**, **4a**, and **4b** utilized additional stabilization via long range M···O interactions.

Linearly-coordinated magnetic ions provide a number of synthetic targets in single-molecule magnetism. A 3d complex with heavy ligands (e.g. $M(SiR_3)_2$) may show enhanced anisotropy through a heavy ligand effect,[41] while two-coordinate complexes of heavy transition metals (4d, 5d) or the f-elements will have greatly increased anisotropy due to their significantly larger spin-orbit coupling constants. The stability of these target molecules will likely depend on the interligand non-covalent interactions seen herein as well as for $Co(C(SiMe_2ONaph)_3)_2$ and other two-coordinate complexes. We are particularly interested in the use of large aryl groups in the ligands of such complexes, as they allow for interdigitation of opposing arms and strong sp^3-CH···π and sp^2-CH···π interactions.

The deviation from linearity in **4a** and **4b** has a dramatic effect on magnetic properties. A 180° C–Co–C bond angle in $Co(C(SiMe_2ONaph)_3)_2$ yielded maximal orbital angular momentum and anisotropy, with a spin-reversal barrier height of 450 cm^{-1}.[3] The ~20° bend in **4a** and **4b** yielded quenched orbital angular momentum and a 90% decrease in spin-reversal barrier height. This is particularly interesting in comparison to the family of $[DyCp_2]^+$ molecules that have recently set new records in single-molecule magnetism.[42] Within this architecture, presumably the best magnetic properties would arise from a molecule with a 180° Cp–Dy–Cp angle and short Cp–Dy distances. The largest reported barrier reported thus far is 1541 cm^{-1} for $[(Cp^{iPr5})(Cp^*)Dy]^+$, which has a Cp–Dy–Cp bond angle of 162.5°,[43] while $[Dy(Cp^{iPr4})_2]^+$ has a Cp–Dy–Cp bond angle of 147.2° and a barrier height of 1285 cm^{-1}.[44] The decreased sensitivity of $[DyCp_2]^+$ to deviations from linearity compared to $Co(CR_3)_2$ is perhaps an illustration of the difference in the nature of metal-ligand bonding for transition metals versus lanthanides.

Given the recent emphasis on through-barrier relaxation processes,[36] it is tempting to suggest that barrier heights should no longer be prioritized in the design of new single-molecule magnets. In reality, minimizing the effects of through-barrier relaxation can be both directly and indirectly related to barrier heights. Through-barrier relaxation pathways are enhanced with increased mixing of low-lying microstates; or, systems with highly axial microstates are less prone to through-barrier relaxation.[45] Compound **6** has a barrier height of 199.1 cm^{-1} versus 246 cm^{-1} for $[Fe(C(SiMe_3)_3)_2]^-$, but has low-temperature relaxation times nearly two orders of magnitude faster than those for $[Fe(C(SiMe_3)_3)_2]^-$. The deviations from high symmetry in the secondary coordination sphere for **6** may introduce transverse anisotropy which decreases axiality of the ground microstates. Thus, the strategies currently being developed to minimize the effect of vibration-mediated relaxation pathways should be applied on top of the strategies already developed to maximize barrier height.

2.4 References

(1) D. Gatteschi, R. Sessoli and J. Villain. Molecular Nanomagnets (Oxford Univ. Press, 2006)
(2) L. Ungur and L. F. Chibotaru, *Inorg. Chem.*, 2016, **55**, 10043.
(3) P. C. Bunting, M. Atanasov, E. Damgaard-Møller, M. Perfetti, I. Crassee, M. Orlita, J. Overgaard, J. van Slageren, F. Neese and J. R. Long, *Science*, 10.1126/science.aat7319.
(4) M. Atanasov, D. Aravena, E. Suturina, E. Bill, D. Maganas and F. Neese, *Coord. Chem. Rev.*, 2015, **289**, 177.
(5) P. Zhao, Z. Brown, J. C. Fettinger, F. Grandjean, G. J. Long and P. P. Power, *Organometallics*, 2014, **33**, 1917.

(6) a) H. Li, A. J. A. Aquino, D. B. Cordes, F. Hung-Low, W. L. Hase and C. Krempner, *J. Am. Chem. Soc.*, 2013, **135**, 16066; b) H. Li, A. J. A. Aquino, D. B. Cordes, W. L. Hase, C. Krempner. *Chem. Sci.* 2017**, 34**, 1164.
(7) Bruker Analytical X-ray Systems, Inc. *SAINT and APEX 2 Software for CCD Diffractometers*; Bruker Analytical X-ray Systems, Inc.: Madison, WI, USA, 2000.
(8) Sheldrick, G. M. *SADABS*; Bruker Analytical X-ray Systems, Inc.: Madison, WI, USA, 2014.
(9) Sheldrick, G. M. *Acta Crystallogr A Found Adv* **2015**, *71* (Pt 1), 3–8.
(10) Sheldrick, G. M. *SHELXL*; University of Göttingen, Germany: University of Göttingen, Germany, 2014.
(11) Dolomanov, O. V.; Bourhis, L. J.; Gildea, R. J.; Howard, J. A. K.; Puschmann, H. *Journal of Applied Crystallography* **2009**, *42* (2), 339–341.
(12) Spek, A. L. *Acta Crystallogr C Struct Chem* **2015**, *71* (Pt 1), 9–18.
(13) Spek, A. L. *Journal of Applied Crystallography* **2003**, *36* (1), 7–13.
(14) G. A. Bain and J. F. Berry, *J. Chem. Educ.* 2008, **85**, 532.
(15) N. F. Chilton, R. P. Anderson, L. D. Turner, A. Soncini and K. S. Murray, *J. Comput. Chem.*, 2013, **34**, 1164.
(16) K. S. Cole and R. H. Cole, *J. Chem. Phy.* 1941, **9**, 341.
(17) a) N. H. Buttrus, C. Eaborn, P. B. Hitchcock, J. D. Smith and A. C. Sullivan, *J. Chem. Soc., Chem. Commun.*, 1985, **20**, 1380; b) T, Viefhaus, W, Schwarz, K, Hubler, K, Locke and J. Weidlein, *Z. Anorg. Allg. Chem.*, 2001, **627**, 715.
(18) M. Westerhausen and B. Rademacher. *J. Organomet. Chem.*, 1991, **421**, 175.
(19) M. Nishio, *Phys. Chem. Chem. Phys.*, 2011, **13**, 13873.
(20) M. M. Olmstead, P. P. Power and S. C. Shoner, *Inorg. Chem.* 1991, **30**, 2547.
(21) C. G. Werncke, P. C. Bunting, C. Duhayon, J. R. Long, S. Bontemps, S. Sabo-Etienne, *Angew. Chem. Int. Ed.* 2015, **54**, 245.
(22) (a) J. M. Zadrozny, D. J. Xiao, M. Atanasov, G. J. Long, F. Grandjean, F. Neese, J. R. Long, *Nature Chem.*, 2013, **5**, 577. (b) J. M. Zadrozny, D. J. Xiao, J. R. Long, M. Atanasov, F. Neese, F. Grandjean, and G. J. Long, *Inorg. Chem.*, 2013, **52**, 13123.
(23) J. M. Zadrozny, M. Atanasov, A. M. Bryan, C.-Y. Lin, B. D. Rekken, P. P. Power, F. Neese and J. R. Long, *Chem. Sci.*, 2013, **4**, 125.
(24) W. A. Merill, T. A. Stich, M. Brynda, G. J. Yeagle, J. C. Fettinger, R. D. Hont, W. M. Reiff, C. E. Shulz, R. D. Britt and P. P. Power, *J. Am. Chem. Soc.* 2009, **131**, 12693.
(25) A. M. Bryan, W. A. Merrill, W. M. Reiff, J. C. Fettinger and P. P. Power, *Inorg. Chem.* 2012, **51**, 3366.
(26) R. Ruamps, L. J. Batchelor, R. Maurice, N. Gogoi, P. Jiménez-Lozano, N. Guihéry, C. de Graaf, A.-L. Barra, J.-P. Sutter and T. Mallah, *Chem. Eur. J.* 2013, **19**, 950.
(27) This impurity is present even in pristine crystalline samples that pass elemental analysis. It is also evident in the Mössbauer data. The impurity precludes quantitative analysis of dc magnetic susceptibility or magnetization measurements as the absolute values of the magnetic moment are heavily influenced by the impurity. Importantly, however, the dynamic magnetic properties are invariant across multiple samples with different amounts of the impurity.
(28) a) M, Blume and J. A. Tjon, *Phys. Rev.*, 1968, **165**, 446; b) J. A. Tjon and M. Blume, *Phys. Rev.*, 1968, **165**, 456; c) S. Mørup in *The Time Domain in Surface and Structural Dynamics*

NATO-ASI Series C Vol. 228, Eds G.J. Long and F. Grandjean, (Publ. Kluwer, 1988); d) H. H. Wickman in *Mössbauer Effect Methodology*, edited by I. J. Gruvermann, (New York, Plenum Press, 1966).
(29) S. Dattagupta and M. Blume, *Phys. Rev. B.*, 1974, **10**, 4540.
(30) G. K. Shenoy, F. E. Wagner, G. M. Kalvius in *Mössbauer Isomer Shifts*, edited by G. K. Shenoy and F. E. Wagner (North-Holland, Amsterdam, 1978), p. 49.
(31) a) T. Owen, F. Grandjean, G. J. Long, K. V. Domasevitch, and N. N. Gerasimchuk, *Inorg. Chem.*, 2008, **47**, 8704; b) S. Hazra, S. Sasmal, F. Fleck, F. Grandjean, M. T. Sougrati, M. Ghosh, T. D. Harris, P. Bonville, G. J. Long, S. Mohanta, *J. Chem. Phys.*, 2011, **134**, 174507.
(32) H. A. Kramers, *Proc. R. Acad. Sci. Amsterdam*, 1930, **33**, 959
(33) D. Gatteschi and R. Sessoli, *Angew. Chem., Int. Ed.* 42, **2003**, 268.
(34) R. Orbach, *Proc. R. Soc. London Ser. A.* 1961, **264**, 458.
(35) a) K. N. Shrivastava, *Phys. Status Solidi B*, 1972, **51**, 377; b) K. N. Shrivastava, *Phys. Status Solidi B*, 1983, **117**, 437
(36) a) A. Lunghi, F. Totti, R. Sessoli and S. Sanvito. Nat. Commun. 2017, **8**, 14620; b) A. Lunghi, F. Totti, S. Sanvito and R. Sessoli. Chem. Sci. 2017, **8**, 6051; c) L. Escalera-Moreno, J. J. Baldoví, A. Gaita-Ariño and E. Coronado. Chem. Sci. 2018, **9**, 3265
(37) W. H. Harmon, T. D. Harris, D. E. Freedman, H. Fong, A. Chang, J. D. Rinehart, A. Ozarowski, T. Sougrati, F. Grandjean, G. J. Long, J. R. Long, and C. J. Chang, *J. Am. Chem. Soc.* 2010, **132**, 18115.
(38) S. S. Eaton and G. R. Eaton, *Biol. Magn. Reson.*, 2000, **19**, 29.
(39) G. C. Werncke, E. Suturina, P. C. Bunting, L. Vendier, J. R. Long, M. Atanasov, F. Neese, S. Sabo-Etienne, and S. Bontemps, *Chem. Eur. J.* 2016, **22**, 1668
(40) a) T. Viefhaus, W. Schwarz, K. Hübler, K. Locke, and J. Weidlein, *Z. Anorg. Allg. Chem.*, 2001, **627**, 715; b) N. H. Bruttrus, C. Eaborn, P. B. Hitchcock, J. D. Smith, and A. C. Sullivan, *J. Chem. Soc., Chem. Commun.*, 1985, **0**, 1380; c) C.-Y. Lin, J. C. Fettinger, N. F. Chilton, A. Formanuik, F. Grandjean, G. J. Long, and P. P. Power, *Chem. Commun.*, 2015, **51**, 13275.
(41) a) H. I. Karunadasa, K. D. Arquero, L. A. Berben, and J. R. Long, *Inorg. Chem.* 2010, **49**, 4738; b) S. Ye and F. Neese, *J. Chem. Theory Comput*. 2012, **8**, 2344; c) J. M. Zadrozny, J. Telser, and J. R. Long, *Polyhedron* 2013, **64**, 209; d) T. J. Pearson, M. S. Fataftah, and D. E. Freedman, *Chem. Commun.* 2016, **52**, 11394; e) X.-N. Yao, M.-W. Yang, J. Xiong, J.-J. Liu, C. Gao, Y.-S. Meng, S.-D. Jiang, B.-W. Wang, and S. Gao, *Inorg. Chem. Front.* 2017, **4**, 701.
(42) a) C. A. P. Goodwin, F. Ortu, D. Reta, N. F. Chilton, and D. P. Mills, *Nature*, 2017, **548**, 439; b) F.-S. Guo, B. M. Day, Y.-C. Chen, M.-L. Tong, A. Mansikkamäki, and R. A. Layfield, *Angew. Chem. Int. Ed.* 2017, **56**, 11445.
(43) F.-S. Guo, B. M. Day, Y.-C. Chen, M.-L. Tong, A. Mansikkamäki, and R. A. Layfield, *Science*, 2018, 10.1126/science.aav0652
(44) K. R. McClain, C. A. Gould, K. Chakarawet, S. J. Teat, T. J. Groshens, J. R. Long, and B. G. Harvey, *Chem. Sci.*, 2018, **9**, 8492.
(45) L. Ungur and L. F. Chibotaru, *Inorg. Chem.*, 2016, **55**, 10043.

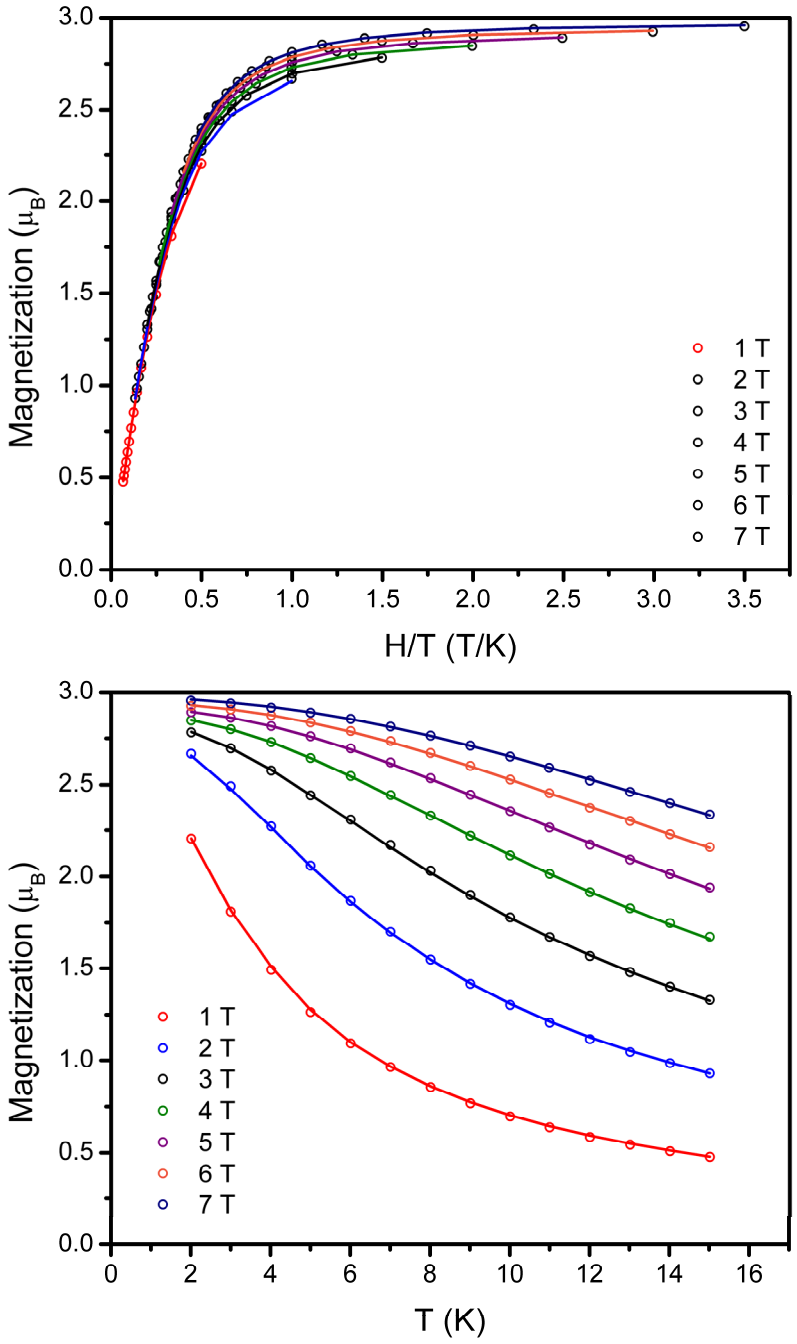

Figure S2.1. (top) Reduced magnetization data for **3** collected at temperatures from 2 to 15 K under dc fields of 1 to 7 T. (bottom) Variable-temperature magnetization data for **3** collected at temperatures from 2 to 15 K under dc fields of 1 to 7 T. Solid lines are from fits of the data using the zero-field splitting Hamiltonian in Equation 1.

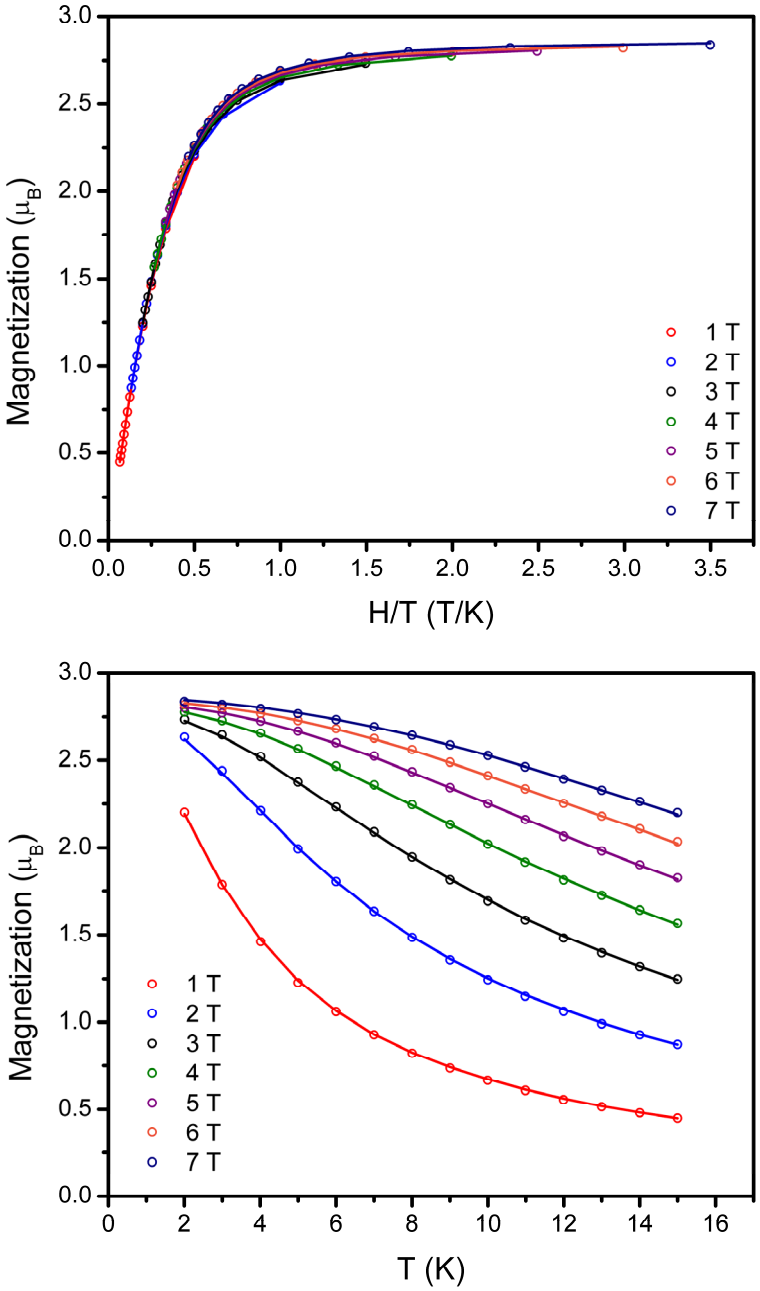

Figure S2.2. (top) Reduced magnetization data for **4a** collected at temperatures from 2 to 15 K under dc fields of 1 to 7 T. (bottom) Variable-temperature magnetization data for **4a** collected at temperatures from 2 to 15 K under dc fields of 1 to 7 T. Solid lines are from fits of the data using the zero-field splitting Hamiltonian.

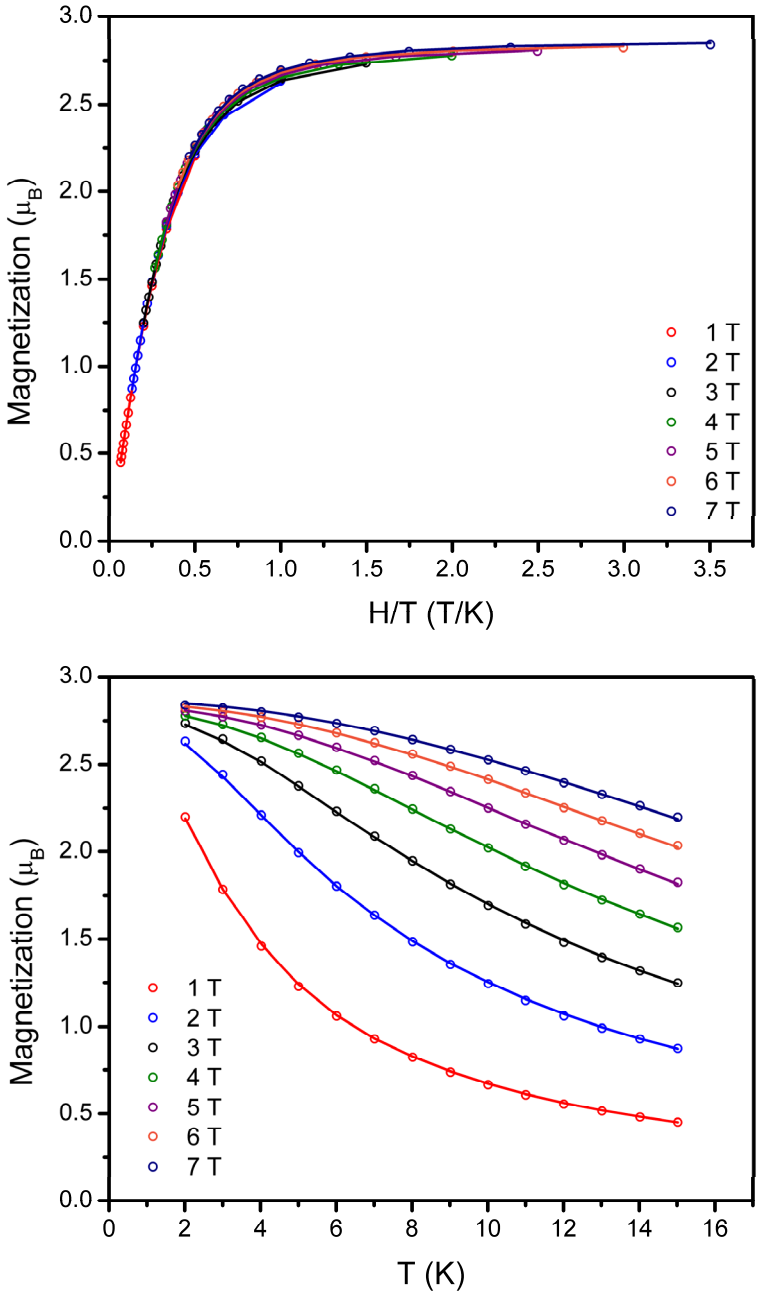

Figure S2.3. (top) Reduced magnetization data for **4b** collected at temperatures from 2 to 15 K under dc fields of 1 to 7 T. (bottom) Variable-temperature magnetization data for **4b** collected at temperatures from 2 to 15 K under dc fields of 1 to 7 T. Solid lines are from fits of the data using the zero-field splitting Hamiltonian.

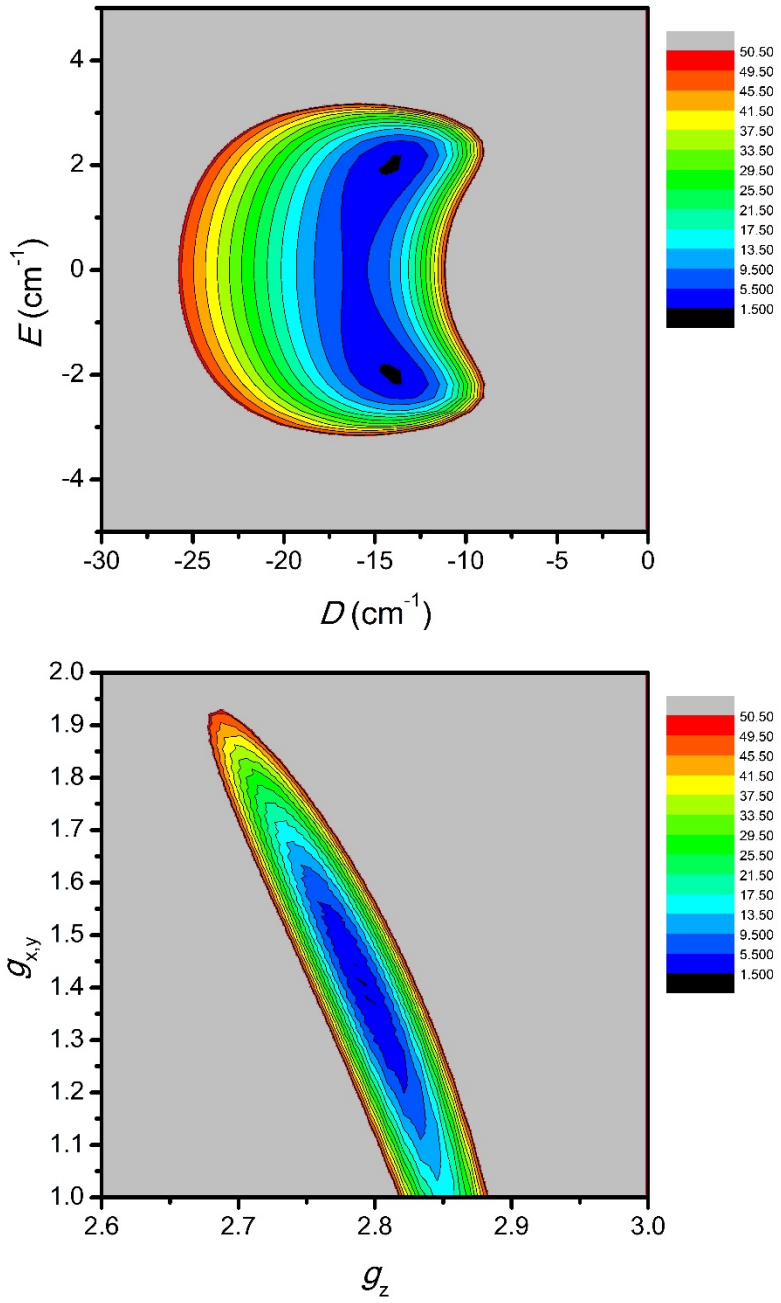

Figure S2.4. (top) Survey of the parameter space for D and E for **3**, where $g_{\parallel} = 2.79$ and $g_{\perp} = 1.40$. (bottom) Survey of the parameter space for $g_{\parallel}$ and $g_{\perp}$ for **3**, where $D = -14.2$ cm^{-1} and $E = 2.1$ cm^{-1}. The values on the legend are multiples of the minimum residual, 2.89×10^{-3}, obtained for $D = -14.2$ cm^{-1}, $E = 2.1$ cm^{-1}, $g_{\parallel} = 2.79$, and $g_{\perp} = 1.40$.

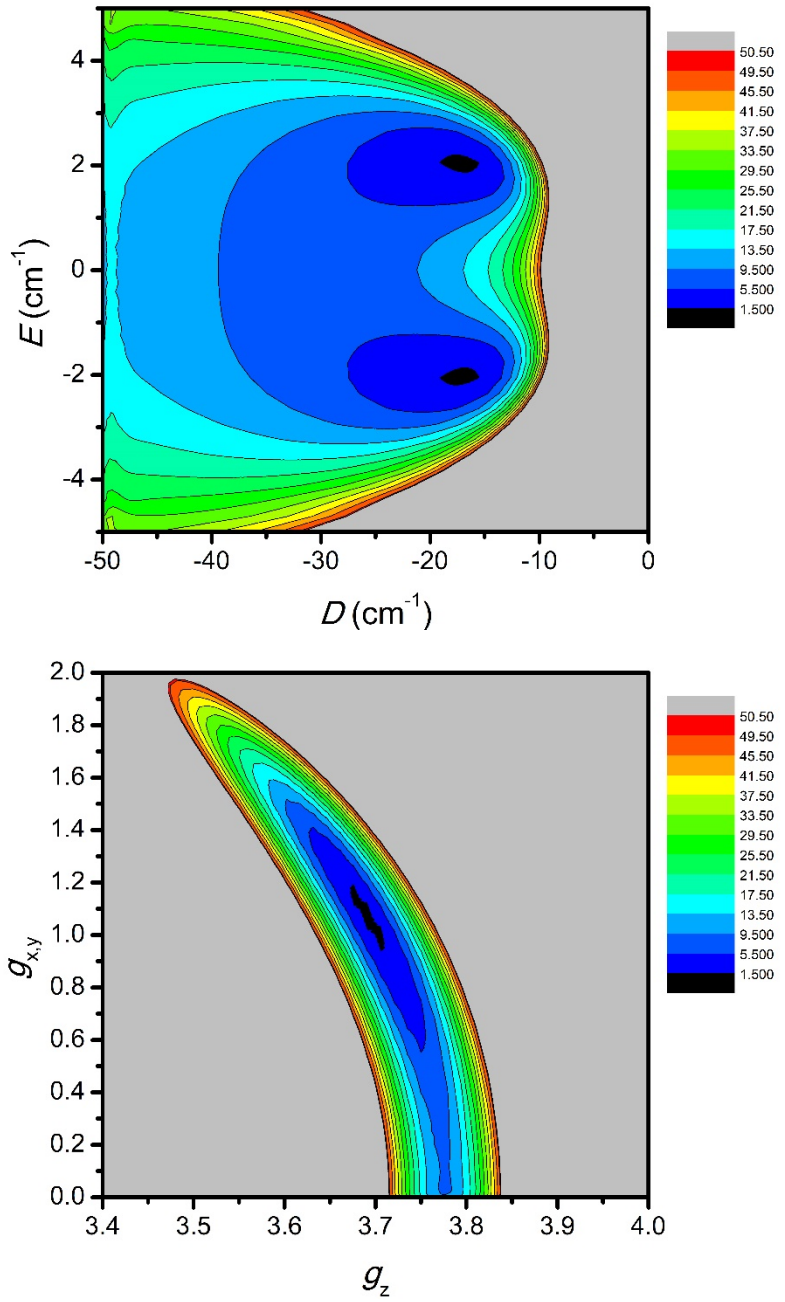

Figure S2.5. (top) Survey of the parameter space for D and E for **4a**, where $g_{\parallel} = 3.69$ and $g_{\perp} = 1.07$. (bottom) Survey of the parameter space for $g_{\parallel}$ and $g_{\perp}$ for **4a**, where $D = -17.1$ cm^{-1} and $E = 2.1$ cm^{-1}. The values on the legend are multiples of the minimum residual, 3.24×10^{-3}, obtained for $D = -17.1$ cm^{-1}, $E = 2.1$ cm^{-1}, $g_{\parallel} = 3.69$, and $g_{\perp} = 1.07$.

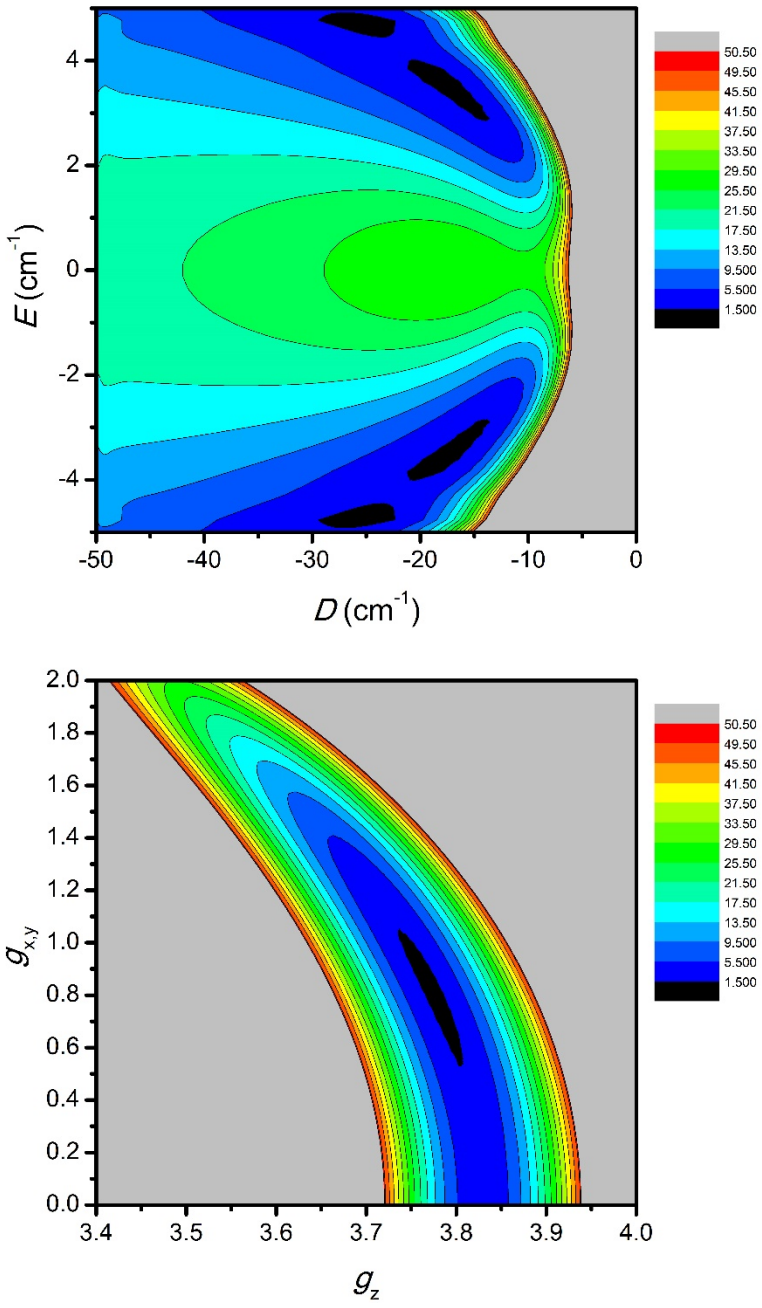

Figure S2.6. (top) Survey of the parameter space for D and E for **4b**, where $g_{\parallel} = 3.77$ and $g_{\perp} = 0.83$. (bottom) Survey of the parameter space for $g_{\parallel}$ and $g_{\perp}$ for **4b**, where $D = -16.5$ cm^{-1} and $E = 3.4$ cm^{-1}. The values on the legend are multiples of the minimum residual, 1.30×10^{-2}, obtained for $D = -16.5$ cm^{-1}, $E = 3.40$ cm^{-1}, $g_{\parallel} = 3.77$, and $g_{\perp} = 0.83$.

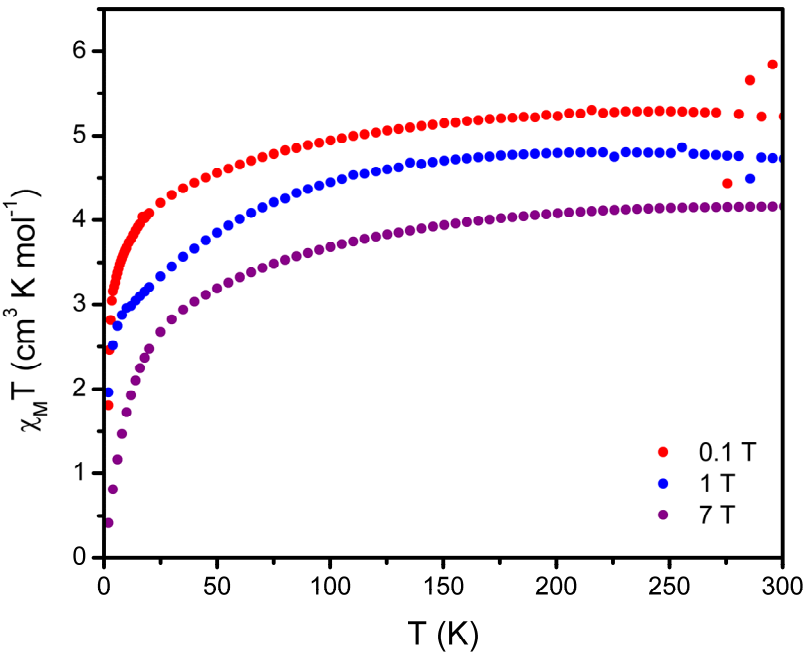

Figure S2.7. Variable-temperature molar magnetic susceptibility times temperature ($\chi_M T$) under applied fields of 0.1, 1, and 7 T for [K(2.2.2-cryptand)][Fe(C(SiMe$_2$OPh)$_3$)$_2$].

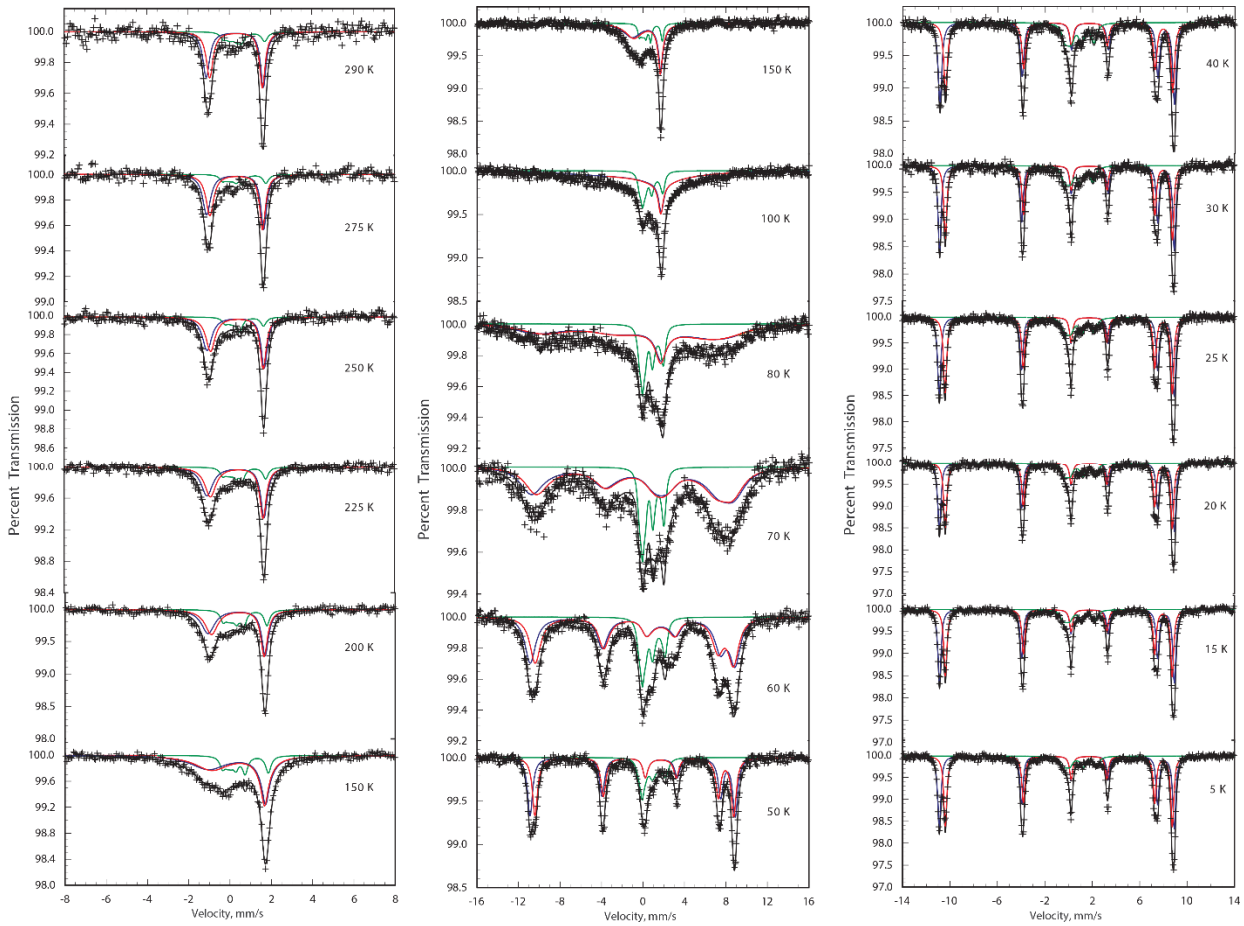

Figure S2.8. The iron-57 Mössbauer spectra of **6** obtained at the higher, left, intermediate, center, and lower, right, temperatures. The solid lines are the results of the fits discussed in the text.

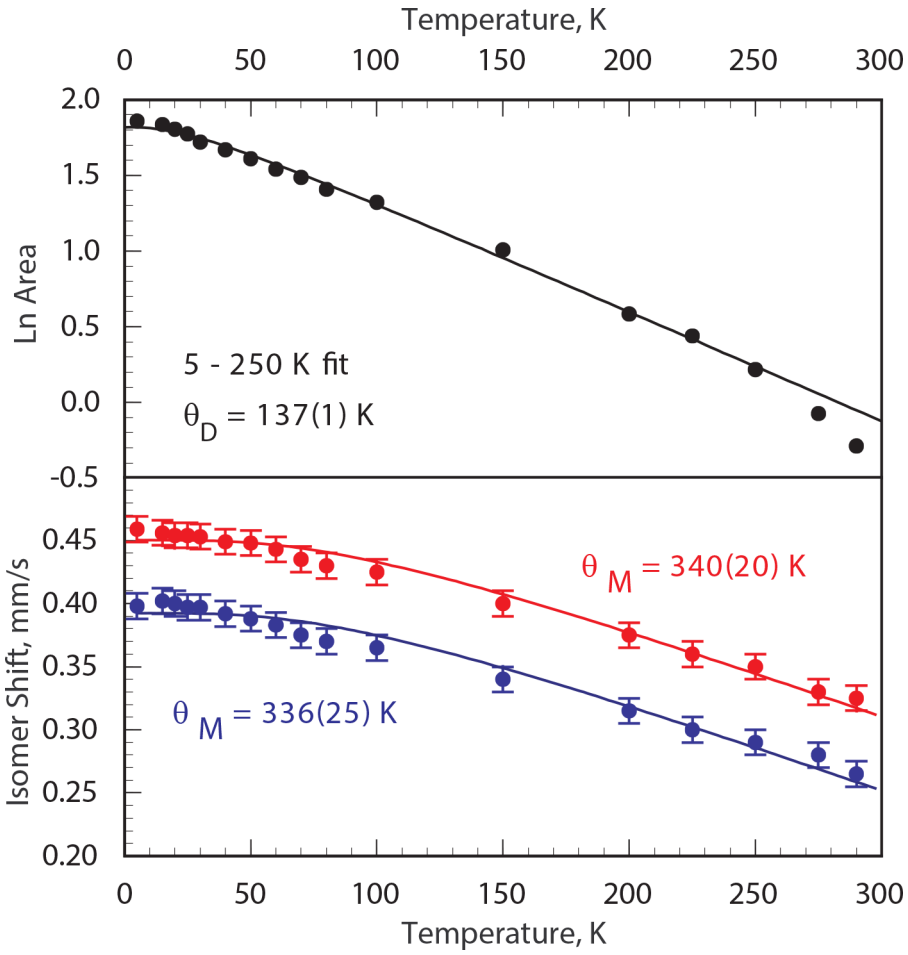

Figure S2.9. The temperature dependence of the isomer shifts and Mössbauer spectral absorption area of **6**. The solid lines are the result of fits with the Debye model for a solid.

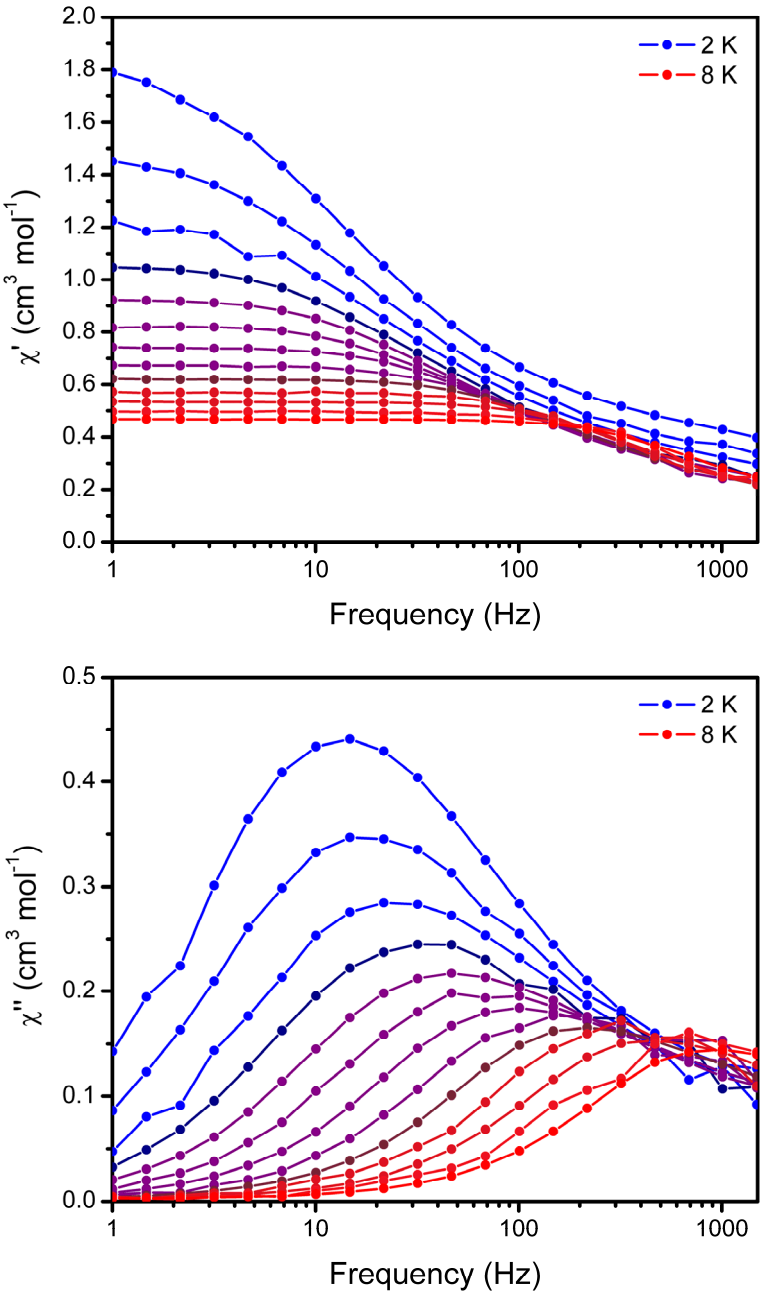

Figure S2.10. In-phase (χ') and out-of-phase (χ'') magnetic susceptibility for **4a** (in C2/c) collected under zero applied dc field from 2 to 8 K. The lines are a guide for the eye.

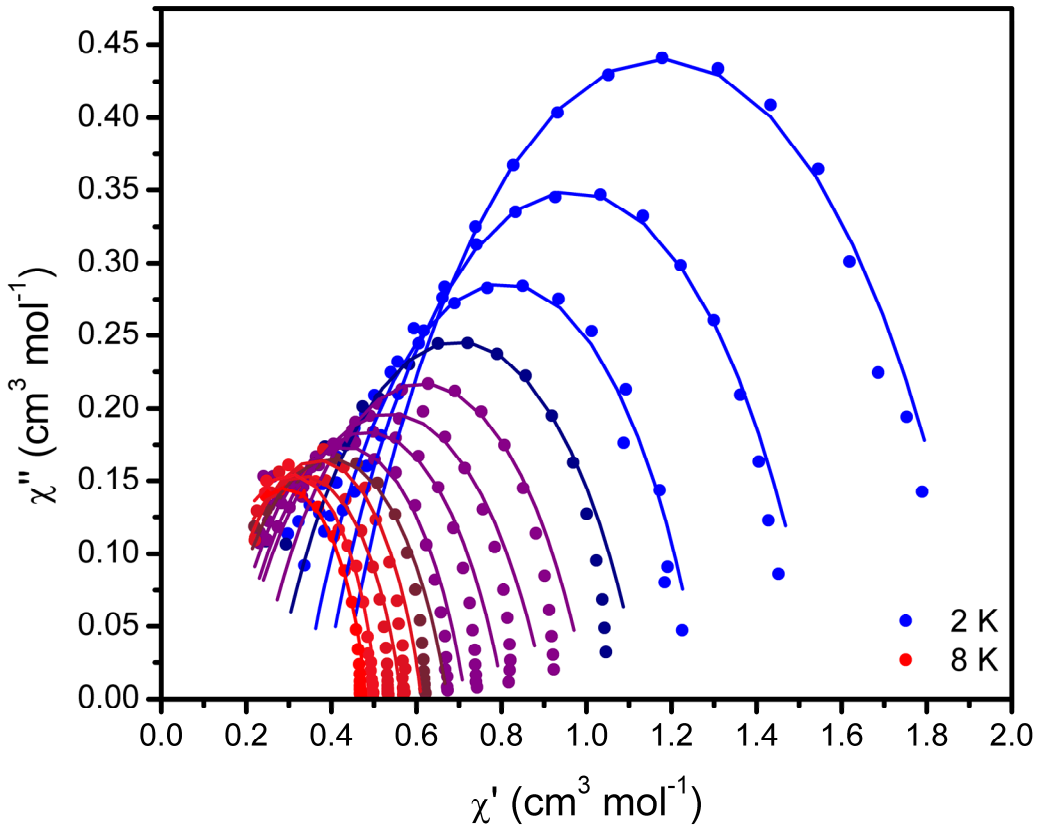

Figure S2.11. Cole-Cole plot for **4a** collected under zero applied dc field from 2 to 8 K. The lines are from fits of the data to a generalized Debye model.

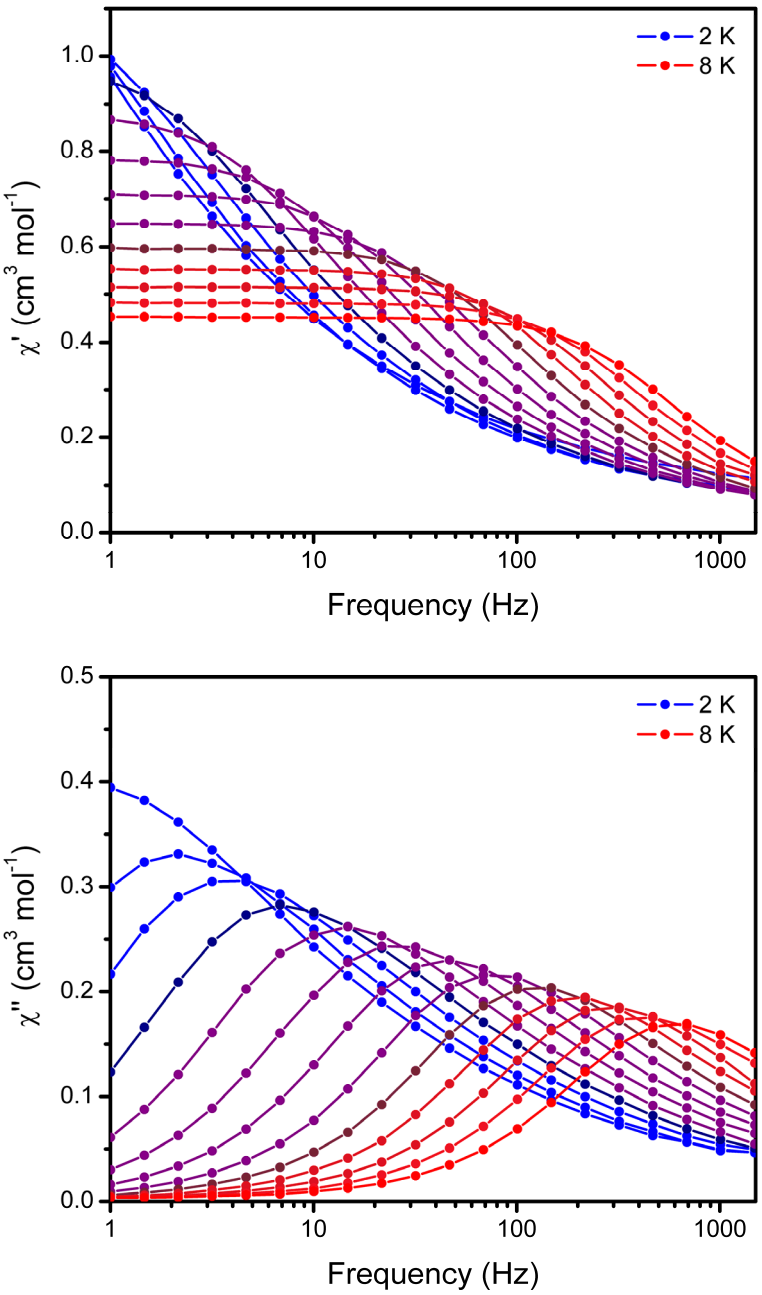

Figure S2.12. In-phase (χ') and out-of-phase (χ'') magnetic susceptibility for **4a** collected under an applied dc field of 1500 Oe from 2 to 8 K. The lines are a guide for the eye.

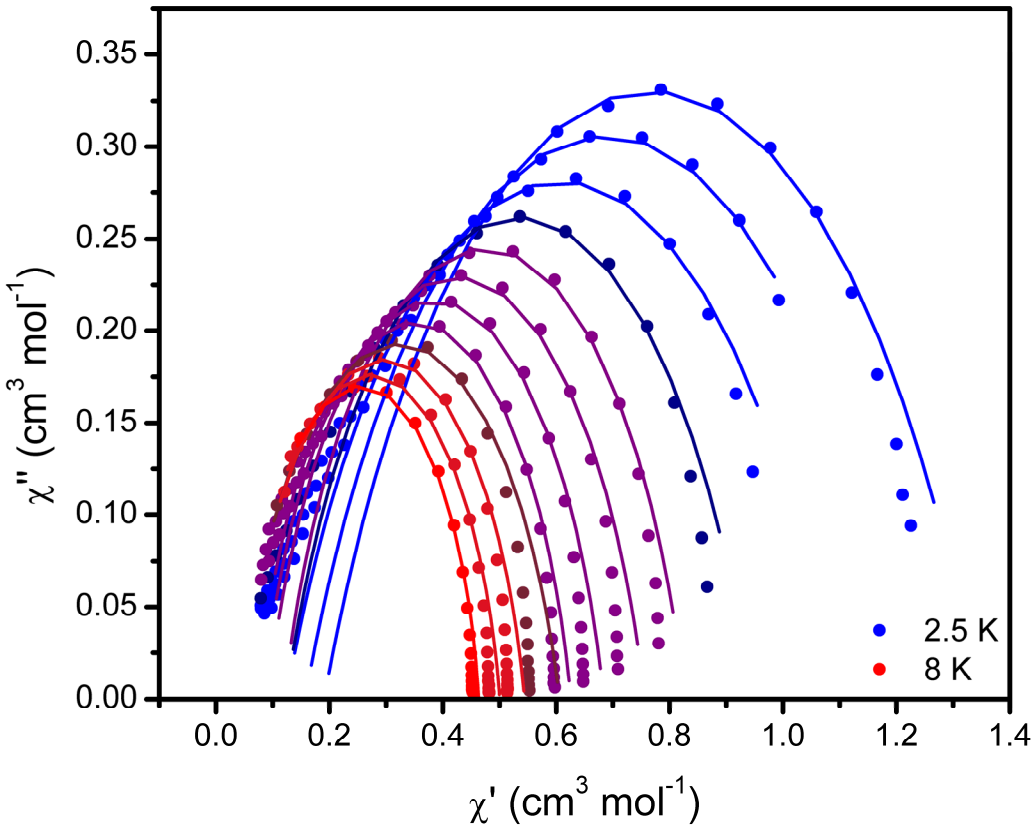

Figure S2.13. Cole-Cole plot for **4a** collected under an applied dc field of 1500 Oe from 2 to 8 K. The lines are from fits of the data to a generalized Debye model.

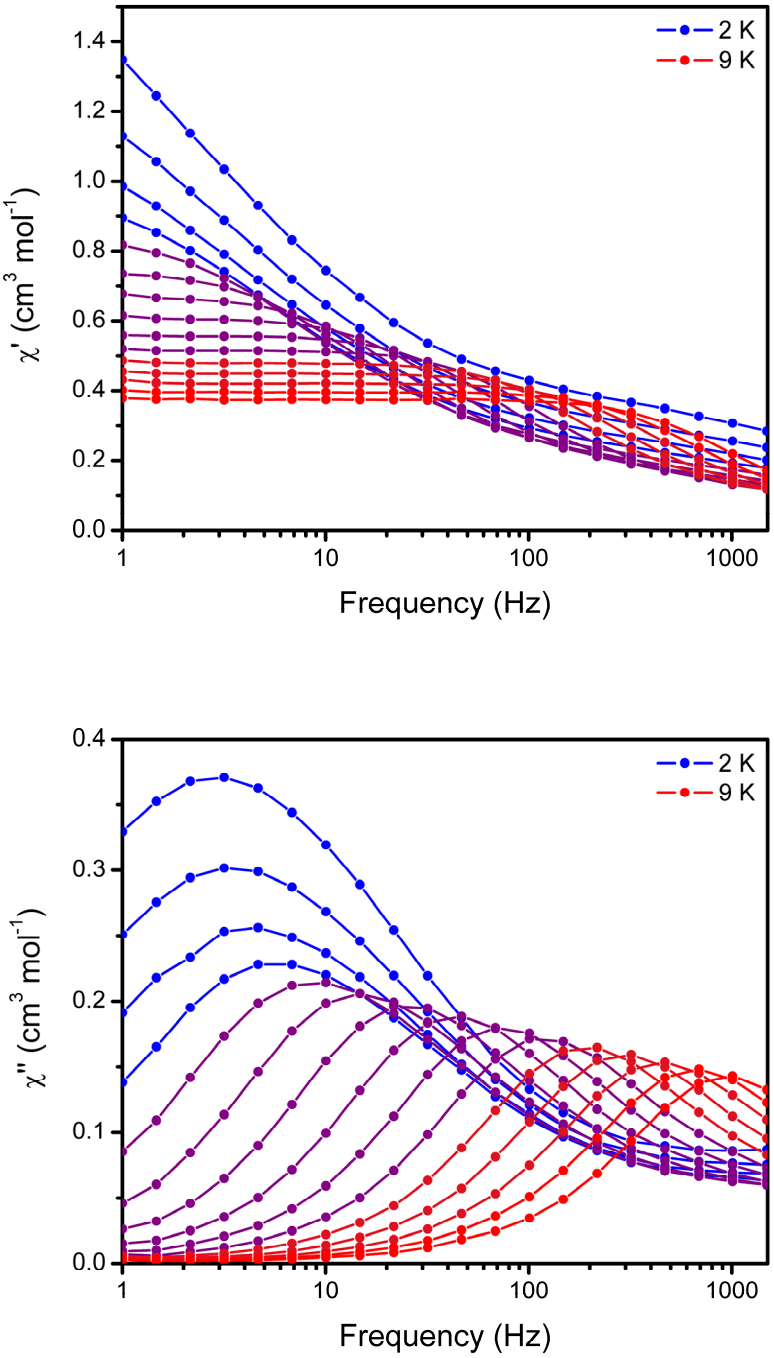

Figure S2.14. In-phase (χ') and out-of-phase (χ'') magnetic susceptibility for **4b** collected under zero applied dc field from 2 to 9 K. The lines are a guide for the eye.

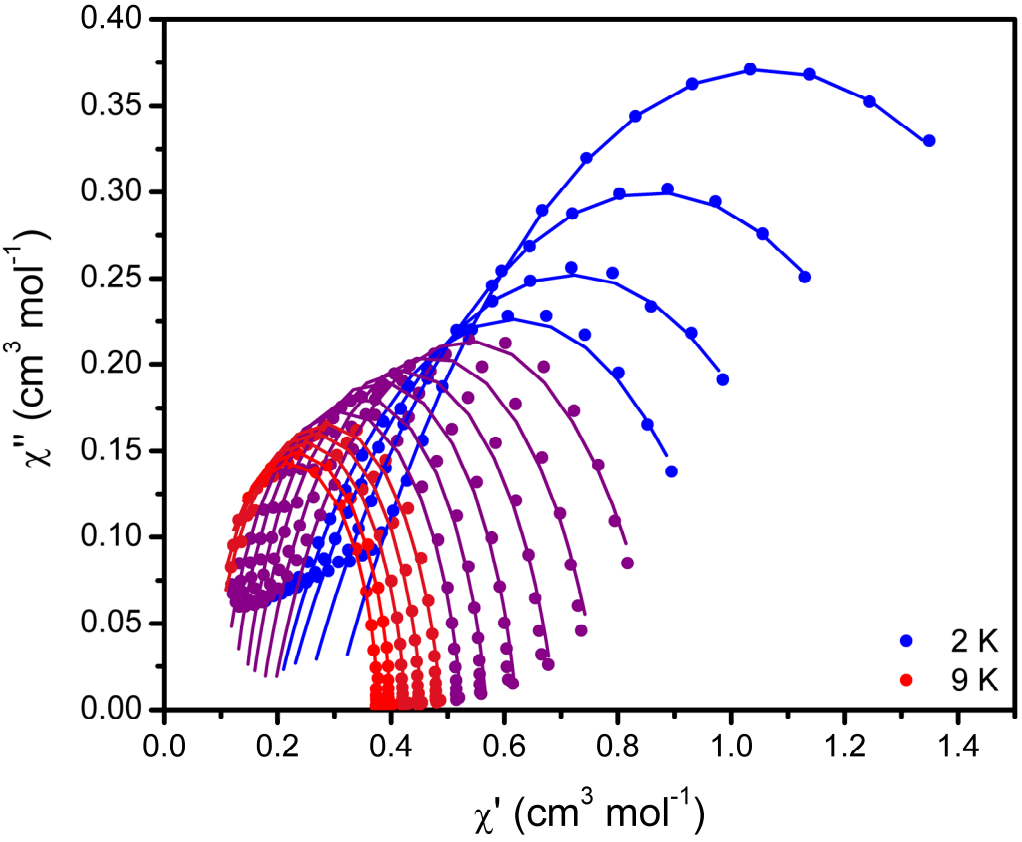

Figure S2.15. Cole-Cole plot for **4b** collected under zero applied dc field from 2 to 9 K. The lines are from fits of the data to a generalized Debye model.

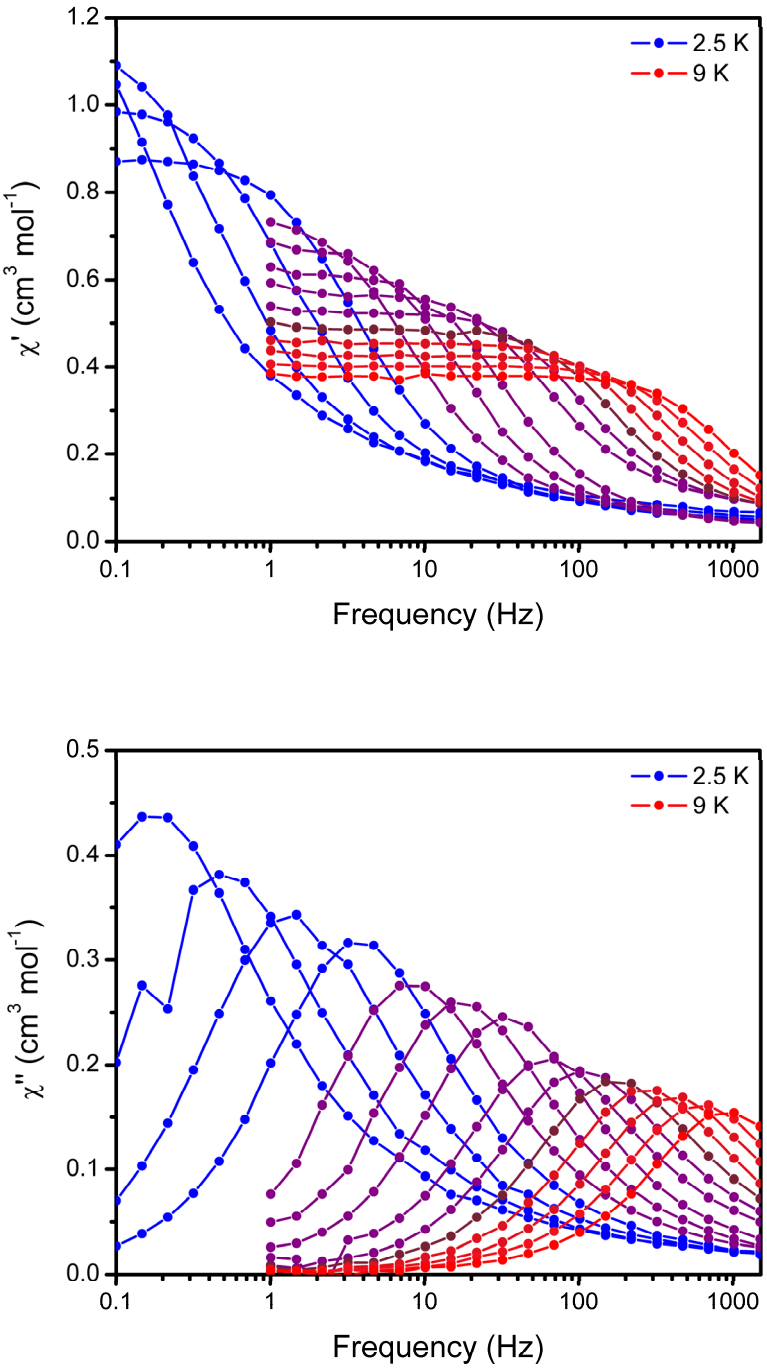

Figure S2.16. In-phase (χ') and out-of-phase (χ'') magnetic susceptibility for **4b** collected under an applied dc field of 1500 Oe from 2.5 to 9 K. The lines are a guide for the eye.

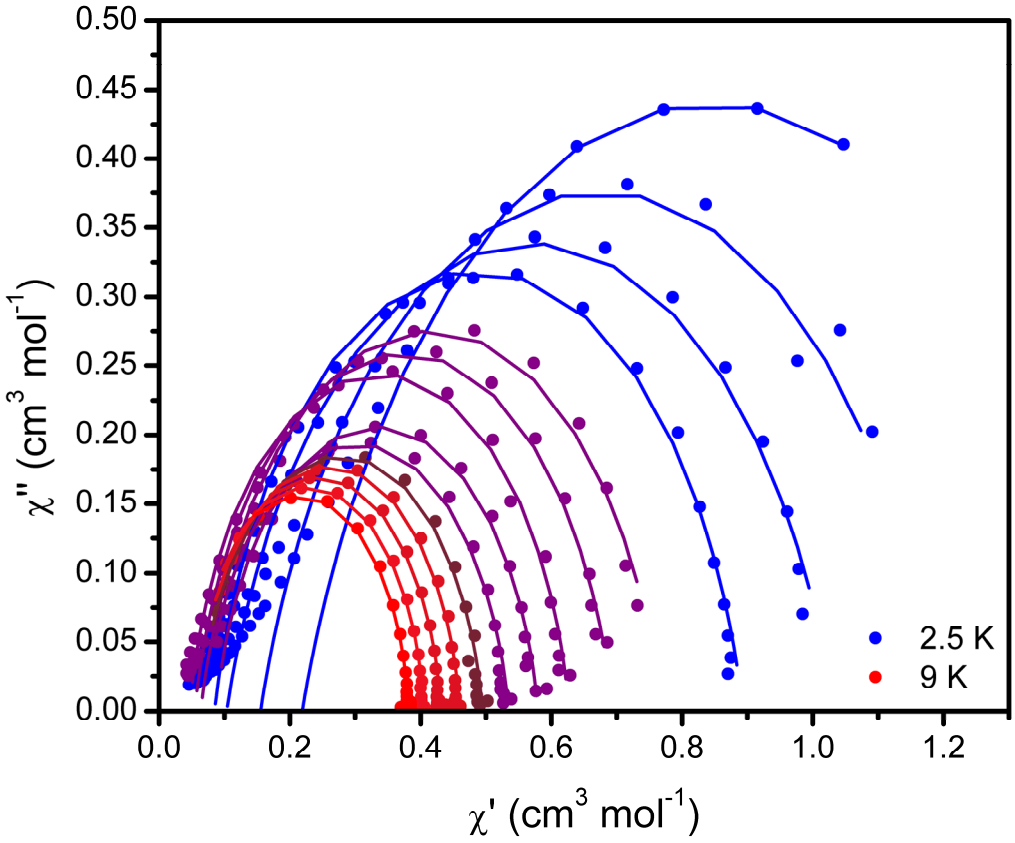

Figure S2.17. Cole-Cole plot for **4b** collected under an applied dc field of 1500 Oe from 2.5 to 9 K. The lines are from fits of the data to a generalized Debye model.

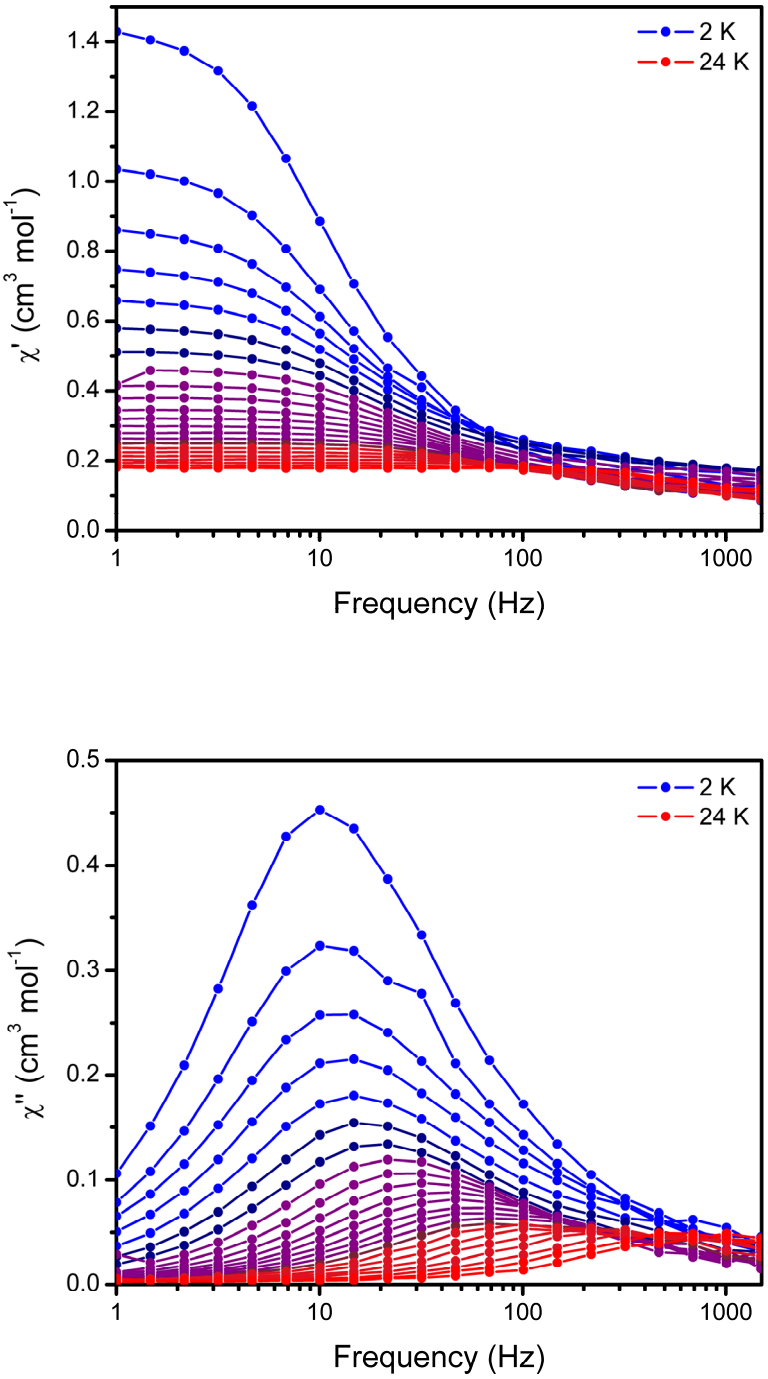

Figure S2.18. In-phase (χ') and out-of-phase (χ'') magnetic susceptibility for **6** collected under zero applied field from 2 to 24 K. The lines are a guide for the eye.

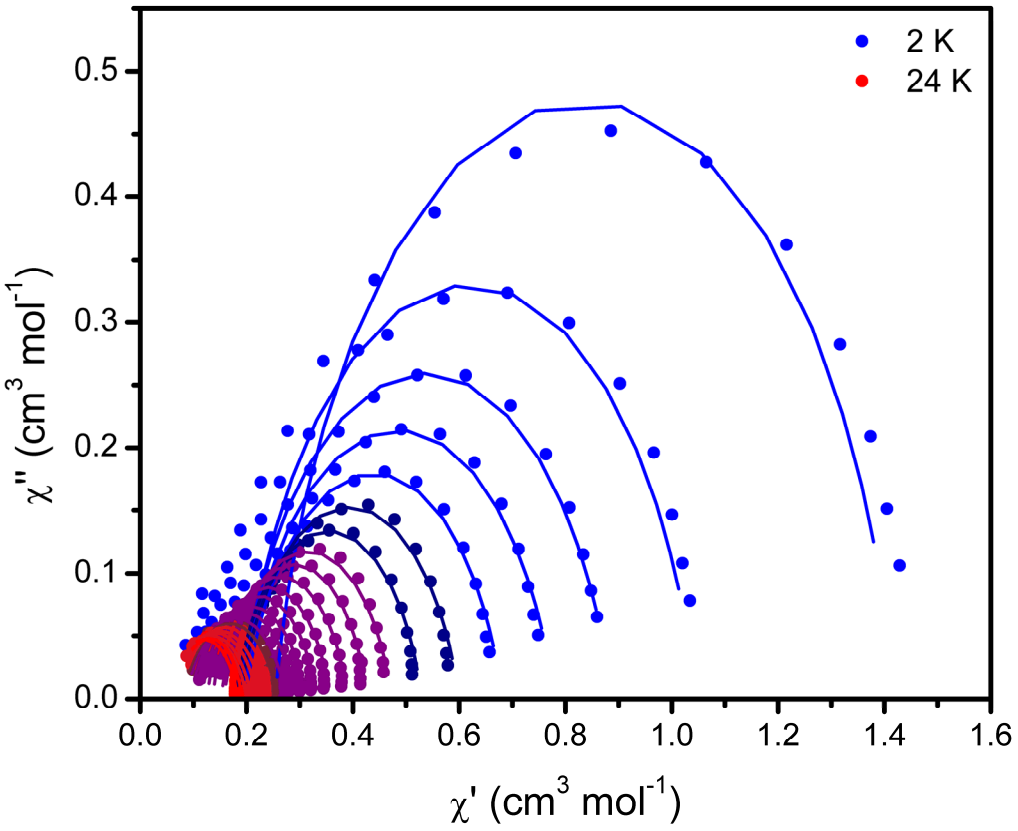

Figure S2.19. Cole-Cole plot for **6** collected under zero applied field from 2 to 24 K. The lines are from fits of the data to a generalized Debye model.

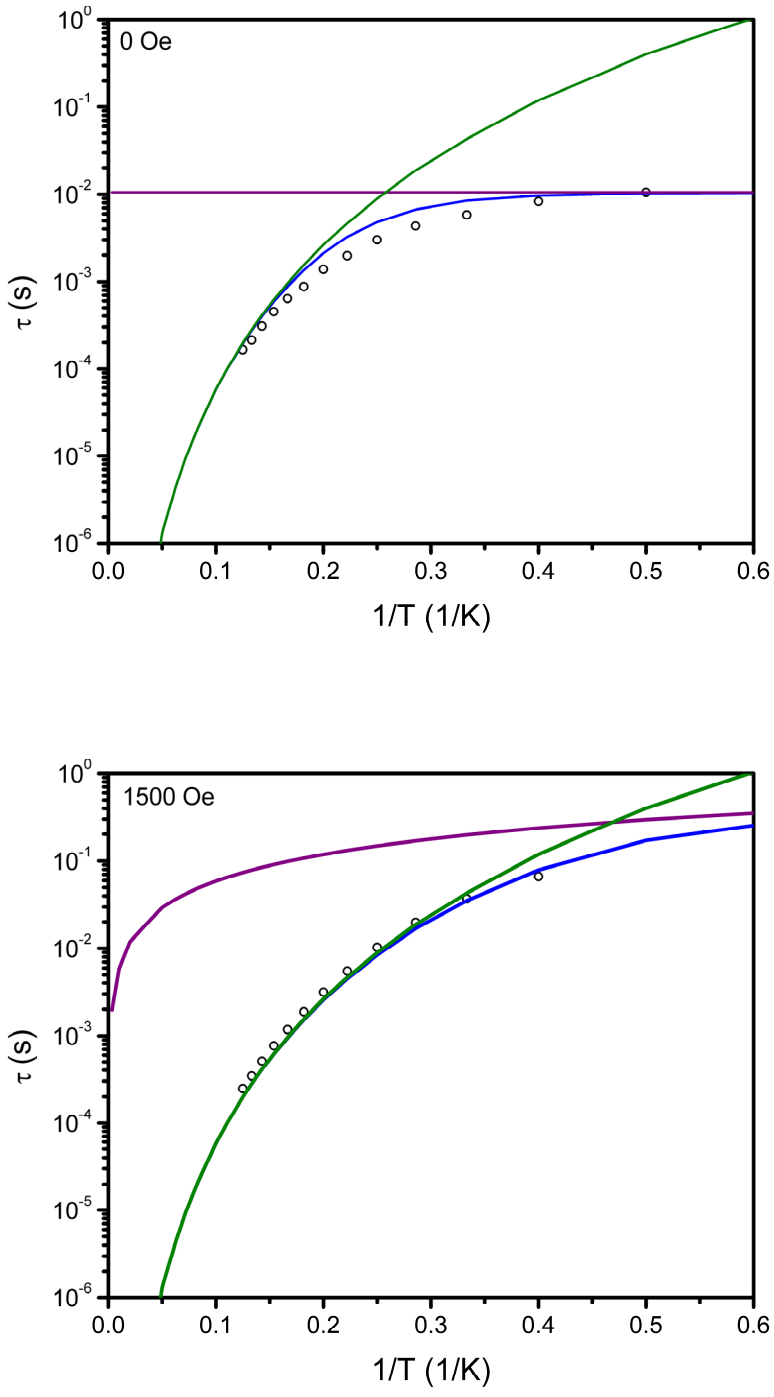

Figure S2.20. Relaxation data (black) for **4a** under 0 Oe dc field (top) and 1500 Oe (bottom). The blue line is a fit of the relaxation process as described by Eq. S2. The purple lines represents relaxation from tunneling (top) or direct (bottom) relaxation processes, while the green line represents relaxation from the Raman process.

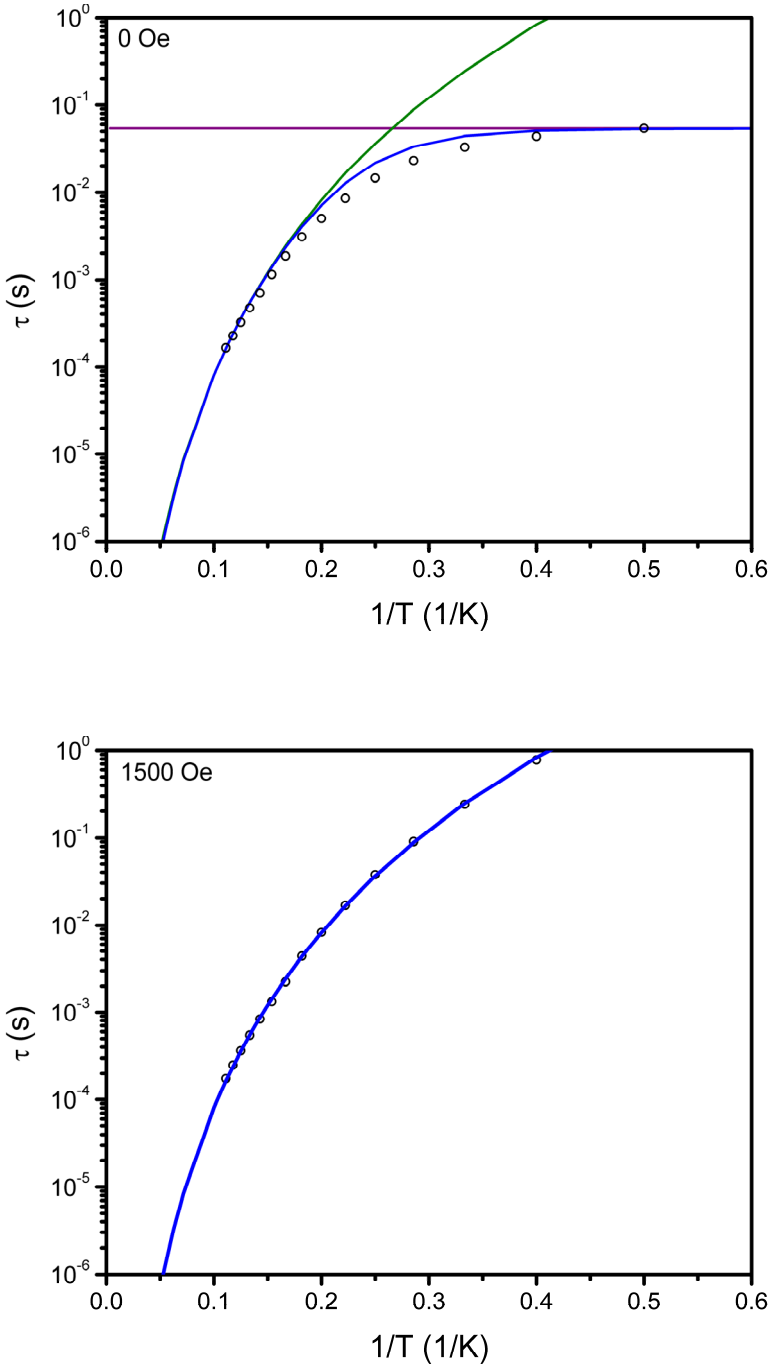

Figure S2.21. Relaxation data (black) for **4b** under 0 Oe dc field (top) and 1500 Oe (bottom). The blue line is a fit of the relaxation process as described by Eq. S2. The purple line represents relaxation from tunneling relaxation processes, while the green line represents relaxation from the Raman process. The 1500 Oe data is fit entirely with Raman relaxation and the green and blue lines are coincident.

Table S2.1. Crystallographic Data

	$Cr(C(SiMe_2OPh)_3)_2 \cdot C_4H_8O$	$Mn(C(SiMe_2OPh)_3)_2$	$Fe(C(SiMe_2OPh)_3)_2$
Formula	$C_{54}H_{74}CrO_7Si_6$	$C_{50}H_{66}MnO_6Si_6$	$C_{50}H_{66}FeO_6Si_6$
Temp. (K)	100(2)	100(2)	100(2)
Crystal System	Monoclinic	Monoclinic	Monoclinic
Space Group	$C2/c$	$C2/c$	$C2/c$
a, b, c (Å)	21.719(2), 11.2008(11), 22.411(3)	21.9375(11), 11.7458(7), 20.8246(11)	21.9897(7), 11.7188(3), 20.8759(6)
α, β, γ (°)	90, 91.160(7), 90	90, 95.484(2), 90	90, 95.121(2), 90
V, (Å^3)	5450.7(10)	5341.4(5)	5358.1(3)
Z	4	4	4
Radiation, λ (Å)	Mo K_α, 0.71073	Mo K_α, 0.71073	Mo K_α, 0.71073
2Θ Range for Data Collection (°)	3.636 to 50.694	3.730 to 50.794	3.720 to 50.786
Completeness to 2Θ	100.0% (2Θ = 50.694°)	99.8% (2Θ = 50.794°)	100.0% (2Θ = 50.786°)
Data / Restraints / Parameters	4993 / 35 / 337	4902 / 0 / 305	4922 / 196 / 397
Goodness of Fit on F^2	1.057	1.057	1.052
$R_1{}^a$, $wR_2{}^b$ (I>2σ(I))	0.0600, 0.1568	0.0385, 0.0990	0.0366, 0.0916
$R_1{}^a$, $wR_2{}^b$ (all data)	0.0692, 0.1713	0.0422, 0.1034	0.0441, 0.0987
Largest Diff. Peak and Hole (e Å^{-3})	0.969 and –1.096	0.381 and –0.260	0.262 and –0.259

$^a\boldsymbol{R_1} = \sum||\boldsymbol{F_o}| - |\boldsymbol{F_c}||/\sum|\boldsymbol{F_o}|$. $^b\boldsymbol{wR_2} = \{\sum[\boldsymbol{w}(\boldsymbol{F_o}^2 - \boldsymbol{F_c}^2)^2]/\sum[\boldsymbol{w}(\boldsymbol{F_o}^2)^2]\}^{1/2}$.

Table S2.2. Crystallographic Data

	[K(2.2.2-cryptand)] [Fe(C(SiMe$_2$OPh)$_3$)$_2$]	Co(C(SiMe$_2$OPh)$_3$)$_2$·C$_6$H$_{14}$	Zn(C(SiMe$_2$OPh)$_3$)$_2$·C$_6$H$_{14}$
Formula	$C_{68}H_{102}FeKN_2O_{12}Si_6$	$C_{56}H_{80}CoO_6Si_6$	$C_{56}H_{80}ZnO_6Si_6$
Temp. (K)	100(2)	100(2)	100(2)
Crystal System	Triclinic	Trigonal	Trigonal
Space Group	$P\bar{1}$	$R\bar{3}$	$R\bar{3}$
a, b, c (Å)	13.2159(5), 13.4488(5), 23.1448(8)	14.0809(4), 14.0809(4), 25.2359(8)	13.9178(7), 13.9178(7), 25.5208(14)
α, β, γ (°)	101.7409(18), 97.8732(19), 108.2139(17)	90, 90, 120	90, 90, 120
V, (Å^3)	3735.8(2)	4333.2(3)	4281.2(5)
Z	2	3	3
Radiation, λ (Å)	Mo K$_\alpha$, 0.71073	Mo K$_\alpha$, 0.71073	Mo K$_\alpha$, 0.71073
2Θ Range for Data Collection (°)	3.304 to 51.510	3.710 to 56.62	3.736 to 50.710
Completeness to 2Θ	99.2% (2Θ = 51.510°)	100.0% (2Θ = 50.484°)	100.0% (2Θ = 54.904°)
Data / Restraints / Parameters	14203 / 0 / 826	2413 / 0 / 98	1748 / 0 / 98
Goodness of Fit on F^2	1.032	1.023	1.114
R_1[a], wR_2[b] (I>2σ(I))	0.0415, 0.0905	0.0336, 0.0858	0.0305, 0.0858
R_1[a], wR_2[b] (all data)	0.0626, 0.1017	0.0381, 0.0889	0.0324, 0.0876
Largest Diff. Peak and Hole (e Å^{-3})	0.398 and –0.459	0.492 and –0.531	0.583 and –0.236

[a] $R_1 = \sum||F_o| - |F_c||/\sum|F_o|$. [b] $wR_2 = \{\sum[w(F_o^2 - F_c^2)^2]/\sum[w(F_o^2)^2]\}^{1/2}$.

Table S2.3. Mössbauer Spectral Parameters for the Fits Shown in Figure 4. The linewidth of components 1 and 2 have been Constrained Equal to 0.31 mm/s

T, K	Area, (%e) (mm/s)	δ_1,[a] mm/s	H_1,[b] T	$DE_{Q,1}$,[c] mm/s	A_1, %	δ_2,[a] mm/s	H_2,[b] T	$DE_{Q,2}$,[c] mm/s	A_2, %	δ_3,[a] mm/s	H_3, T	$DE_{Q,3}$,[c] mm/s	G_3,[b] mm/s	A_3, %	n, MHz
290	0.89(3)	0.265(10)	61.41	-2.766	42.0[c]	0.325(10)	59.49	-2.553	42.0[c]	0.595[c]	3.5[b]	1.12(8)	0.31	15[b]	23700(7300)
275	1.07(3)	0.28(1)	61.41	-2.766	43.5(9)	0.33(1)	59.49	-2.553	43.5(9)	0.595[c]	3.5[b]	1.22(7)	0.31	13(2)	14400(2300)
250	1.43(3)	0.29(1)	61.41	-2.766	42.5(6)	0.35(1)	59.49	-2.553	42.5(6)	0.610[c]	3.5[b]	0.97(7)	0.31	15(1)	9940(1000)
225	1.85(3)	0.30(1)	61.41	-2.766	42.0(6)	0.36(1)	59.49	-2.553	42.0(6)	0.600[c]	3.5[b]	1.19(3)	0.31	16(1)	6110(420)
200	2.27(3)	0.315(10)	61.41	-2.766	39.4(5)	0.375(10)	59.49	-2.553	39.4(5)	0.605[c]	3.5[b]	1.23(2)	0.31	21(1)	4780(250)
150	3.27(4)	0.34(1)	61.41	-2.766	41.9(4)	0.40(1)	59.49	-2.553	41.9(4)	0.625[c]	3.5[b]	1.33(2)	0.31	16.3(8)	1300(50)
100	4.52(6)	0.365(10)	61.41	-2.766	41.5(3)	0.425(10)	59.49	-2.553	41.5(3)	0.65(1)	3.5[b]	1.41(2)	0.31	17.0(5)	199(8)
80	4.90(9)	0.37(1)	61.41	-2.766	41.7(3)	0.43(1)	59.49	-2.553	41.7(3)	0.69(1)	3.5[b]	1.49(2)	0.31	16.6(6)	64(1)
70	5.24(9)	0.375(10)	61.41	-2.766	42.2(3)	0.435(10)	59.49	-2.553	42.2(3)	0.71(1)	3.5[b]	1.54(2)	0.31	15.6(5)	28.6(8)
60	5.54(6)	0.383(10)	61.41	-2.766	42.1(2)	0.443(10)	59.49	-2.553	42.1(2)	0.73(1)	4.0[b]	1.57(2)	0.34	15.8(3)	10.9(2)
50	5.93(6)	0.388(10)	61.41	-2.766	42.2(2)	0.448(10)	59.49	-2.553	42.2(2)	0.73(2)	4.4[b]	1.62(3)	0.34	15.5(3)	3.3(1)
40	6.32(5)	0.392(10)	61.41	-2.766	45.0(1.0)	0.449(10)	59.49	-2.549	39.0(6)	0.75(2)	3.3(1)	1.64(3)	0.55	15.5(4)	0.70(6)
30	6.53(7)	0.397(10)	61.45	-2.763	46.0(1.0)	0.453(10)	59.47	-2.556	39.5(7)	0.72(2)	3.3(1)	1.60(4)	0.55	14.8(5)	0.10(5)
25	6.82(5)	0.397(10)	61.51	-2.770	44.0(8)	0.454(10)	59.5	-2.556	42.3(4)	0.79(1)	3.2(1)	1.71(3)	0.55	13.6(3)	0.09(5)
20	7.05(6)	0.40(1)	61.53	-2.768	44.0(1.0)	0.454(10)	59.45	-2.553	42.3(6)	0.80(2)	3.3(1)	1.86(3)	0.55	13.6(4)	0.08(5)
15	7.09(6)	0.402(10)	61.48	-2.763	46.2(9)	0.456(10)	59.39	-2.553	42.2(5)	0.75(2)	3.30(4)	1.8(1)	0.55	11.6(4)	0.05(3)
5	7.20(5)	0.398(10)	61.51	-2.771	45.1[b]	0.459(10)	59.43	-2.553	43.9[b]	0.802[c]	3.512[b]	1.964[b]	0.55	11.0[b]	0.05(7)

[a]Relative to *a*-iron at 295 K. [b]Parameter constrained to the value given. [c]$DE_Q = e^2Qq/2$, The asymmetry parameter, η, and the polar angle of the hyperfine field, Θ, are assumed equal to zero because of the C_3 symmetry axis along the C–Fe–C direction.

Table S2.4. Assignment of the Two Iron(I) Sites in $[Fe(C(SiMe_2OPh)_3)_2]^-$, **1**, and a Comparison with $[Fe(C(SiMe_3)_3)_2]^-$

	$[Fe(C(SiMe_3)_3)_2]^-$	Fe1 in $[Fe(C(SiMe_2OPh)_3)_2]^-$	Fe2 in $[Fe(C(SiMe_2OPh)_3)_2]^-$
Fe – C, Å	2.060(4)	2.034(2)	2.055(2)
Fe – Si,^{ave} Å	3.135	3.07	3.11
δ,^{a} mm/s	0.402(1)[15b]	0.400(5)	0.459(5)
H,^{b} T	63.68(2)[15b]	61.51(2)	59.43(2)
ΔE_Q,^{c} mm/s	–2.555(2)[15b]	–2.771(5)	–2.553(5)
H_{orb},^{d} T	+78[15b]	+75.51	+73.43

^{a}The 5 K isomer shift relative to *a*-iron at 295 K. ^{b}The 5 K hyperfine field used at all temperatures. ^{c}The quadrupole splitting, $e^2Qq/2$, at all temperatures. ^{d}The orbital contribution to the hyperfine field, $H_{orb} = H - H_{Fermi} - H_{dip} = H + 38 - 24$.

The above assignment is based on the relationship between the short distances for Fe1 and the smaller isomer shift. The expectation is that the smaller the volume around the iron(I) nucleus, the higher is the *s*-electron density at the nucleus and the smaller is the isomer shift. Because this rule is very general, this assignment is preferred. With this assignment the isomer shift and hyperfine field for Fe1 are more similar to those[15b] in $[Fe(C(SiMe_3)_3)_2]^-$ but the quadrupole splitting is quite different. The distances for Fe1 are also rather different from those[15b] in $[Fe(C(SiMe_3)_3)_2]^-$.

Table S2.5. Reverse Assignment from that Given in Table S8.

	$[Fe(C(SiMe_3)_3)_2]^-$	Fe1 in $[Fe(C(SiMe_2OPh)_3)_2]^-$	Fe2 in $[Fe(C(SiMe_2OPh)_3)_2]^-$
Fe – C, Å	2.060(4)	2.034(2)	2.055(2)
Fe – Si,^{ave} Å	3.135	3.07	3.11
δ,^{a} mm/s	0.402(1)[15b]	0.459(5)	0.400(5)
H,^{b} T	63.68(2)[15b]	59.43(2)	61.51(2)
ΔE_Q,^{c} mm/s	–2.555(2)[15b]	–2.553(5)	–2.771(5)
H_{orb},^{d} T	+78[15b]	+73.43	+75.51

^{a}The 5 K isomer shift relative to *a*-iron at 295 K. ^{b}The 5 K hyperfine field used at all temperatures. ^{c}The quadrupole splitting, $e^2Qq/2$, at all temperatures. ^{d}The orbital contribution to the hyperfine field, $H_{orb} = H - H_{Fermi} - H_{dip} = H + 38 - 24$.

This assignment is based on the similarities between the distances and isomer shift and hyperfine field for $[Fe(C(SiMe_3)_3)_2]^-$ and for Fe2 in $[Fe(C(SiMe_2OPh)_3)_2]^-$. The quadrupole splittings are significantly different.

With both assignments, the orbital contributions to the hyperfine field are smaller than in $[Fe(C(SiMe_3)_3)_2]^-$. They also are significantly different for Fe1 and Fe2. One can only suggest that the splitting between the d_{x2-y2} and d_{xy} orbitals is somewhat different in all three cases and is the smallest in $[Fe(C(SiMe_3)_3)_2]^-$.

Table S2.6. Parameters of the fits of magnetic relaxation data for **4a** under 0 Oe dc field.

T (K)	χ_T (cm^3 mol^{-1})	χ_S (cm^3 mol^{-1})	α	τ (s)
2.0	1.93	0.422	0.327	1.05×10^{-2}
2.5	1.55	0.380	0.315	8.28×10^{-3}
3.0	1.27	0.335	0.303	5.84×10^{-3}
3.5	1.13	0.263	0.345	4.34×10^{-3}
4.0	1.00	0.220	0.355	2.99×10^{-3}
4.5	0.905	0.169	0.375	1.97×10^{-3}
5.0	0.806	0.164	0.337	1.38×10^{-3}
5.5	0.715	0.150	0.298	8.81×10^{-4}
6.0	0.673	0.126	0.308	6.40×10^{-4}
6.5	0.611	0.124	0.244	4.49×10^{-4}
7.0	0.564	0.105	0.251	3.07×10^{-4}
7.5	0.506	0.103	0.168	2.13×10^{-4}
8.0	0.481	0.100	0.172	1.66×10^{-4}

Table S2.7. Parameters of the fits of magnetic relaxation data for **4a** under 1500 Oe dc field.

T (K)	χ_T (cm^3 mol^{-1})	χ_S (cm^3 mol^{-1})	α	τ (s)
2.5	1.34	0.191	0.338	6.65×10^{-2}
3.0	1.22	0.157	0.335	3.73×10^{-2}
3.5	1.09	0.124	0.331	1.98×10^{-2}
4.0	0.944	0.123	0.278	1.03×10^{-2}
4.5	0.828	0.119	0.230	5.54×10^{-3}
5.0	0.757	0.0905	0.232	3.14×10^{-3}
5.5	0.684	0.0825	0.205	1.87×10^{-3}
6.0	0.626	0.0735	0.188	1.18×10^{-3}
6.5	0.606	0.0410	0.238	7.70×10^{-4}
7.0	0.544	0.0499	0.185	5.09×10^{-4}
7.5	0.501	0.0462	0.160	3.43×10^{-4}
8.0	0.463	0.0496	0.123	2.47×10^{-4}

Table S2.8. Parameters of the fits of magnetic relaxation data for **4b** under 0 Oe dc field.

T (K)	χ_T (cm^3 mol^{-1})	χ_S (cm^3 mol^{-1})	α	τ (s)
2.0	1.82	0.297	0.423	5.42×10^{-2}
2.5	1.48	0.244	0.425	4.40×10^{-2}
3.0	1.23	0.210	0.414	3.31×10^{-2}
3.5	1.04	0.194	0.373	2.30×10^{-2}
4.0	0.883	0.188	0.299	1.45×10^{-2}
4.5	0.770	0.170	0.239	8.55×10^{-3}
5.0	0.690	0.151	0.198	5.05×10^{-3}
5.5	0.621	0.140	0.150	3.08×10^{-3}
6.0	0.568	0.121	0.132	1.86×10^{-3}
6.5	0.524	0.103	0.122	1.15×10^{-3}
7.0	0.488	0.0804	0.131	7.03×10^{-4}
7.5	0.454	0.0744	0.107	4.73×10^{-4}
8.0	0.425	0.0701	0.0860	3.24×10^{-4}
8.5	0.399	0.0678	0.0653	2.28×10^{-4}
9.0	0.377	0.0689	0.0454	1.66×10^{-4}

Table S2.9. Parameters of the fits of magnetic relaxation data for **4b** under 1500 Oe dc field.

T (K)	χ_T (cm^3 mol^{-1})	χ_S (cm^3 mol^{-1})	α	τ (s)
2.5	1.47	0.219	0.220	9.01×10^{-1}
3.0	1.19	0.155	0.203	2.82×10^{-1}
3.5	1.03	0.103	0.198	1.00×10^{-1}
4.0	0.893	0.0849	0.150	3.92×10^{-2}
4.5	0.769	0.0634	0.157	1.68×10^{-2}
5.0	0.694	0.0545	0.134	8.27×10^{-3}
5.5	0.627	0.0468	0.110	4.39×10^{-3}
6.0	0.580	0.0878	0.112	2.25×10^{-3}
6.5	0.535	0.0700	0.116	1.33×10^{-3}
7.0	0.494	0.0622	0.100	8.33×10^{-4}
7.5	0.460	0.0582	0.0787	5.45×10^{-4}
8.0	0.431	0.0536	0.0668	3.63×10^{-4}
8.5	0.405	0.0508	0.0536	2.51×10^{-4}
9.0	0.381	0.0472	0.0428	1.74×10^{-4}

Table S2.10. Parameters of the fits of magnetic relaxation data for **6** under 0 Oe dc field. Low temperature data (2-24 K) is taken from fits of ac magnetic susceptibility and high temperature data (40-290 K) is taken from fits of Mössbauer spectra.

T (K)	χ_T (cm^3 mol^{-1})	χ_S (cm^3 mol^{-1})	α	τ (s)
2.0	1.03	0.0911	0.177	1.25E-02
3.0	0.762	0.0878	0.214	1.12E-02
4.0	0.643	0.0981	0.249	1.03E-02
5.0	0.562	0.112	0.266	9.26E-03
6.0	0.490	0.121	0.261	8.32E-03
7.0	0.429	0.123	0.247	7.39E-03
8.0	0.377	0.120	0.219	6.52E-03
9.0	0.329	0.115	0.180	5.46E-03
10.0	0.302	0.105	0.190	4.70E-03
11.0	0.275	0.0955	0.188	3.94E-03
12.0	0.251	0.0896	0.184	3.30E-03
13.0	0.234	0.0808	0.203	2.75E-03
14.0	0.217	0.0766	0.202	2.33E-03
15.0	0.203	0.0712	0.197	1.98E-03
16.0	0.191	0.0666	0.219	1.63E-03
17.0	0.181	0.0602	0.232	1.30E-03
18.0	0.171	0.0565	0.250	1.01E-03
19.0	0.163	0.0461	0.279	6.66E-04
20.0	0.154	0.0486	0.236	5.31E-04
21.0	0.147	0.0465	0.228	3.90E-04
22.0	0.140	0.0496	0.205	2.89E-04
23.0	0.133	0.0488	0.154	2.07E-04
24.0	0.128	0.0429	0.153	1.37E-04
40				1.44E-06
50				2.98E-07
60				9.68E-08
70				3.63E-08
80				1.57E-08
100				5.16E-09
150				8.44E-10
200				2.58E-10
225				1.72E-10
250				1.01E-10
275				5.74E-11
290				4.31E-11

Chapter 3: A Linear Cobalt(II) Complex with Maximal Orbital Angular Momentum from a Non-Aufbau Ground State

3.1 Introduction

All materials exhibiting a large magnetic anisotropy possess non-zero orbital angular momentum L arising from an electronic structure of partially-filled (but not half-filled) energetically degenerate orbitals. In trivalent lanthanide ions, the valence 4f orbitals are well-shielded and interact little with their coordination environment, allowing for a non-zero L that couples with the total spin S to give rise to a total angular momentum of $|L - S| \leq J \leq |L + S|$ and potentially a large magnetic anisotropy. In the case of transition metals, however, the ligand field typically removes any orbital degeneracy, leading to quenching of the orbital angular momentum ($L = 0$) and an appropriate description of the ground state in terms of S only. When magnetic anisotropy is present in such complexes, it is generally a weak effect that arises from mixing of electronic ground and excited states induced by spin-orbit coupling. Creating unquenched orbital angular momentum in molecular transition metal-based systems requires an exceptionally weak ligand field and/or two or more orbitals that are nearly degenerate. In this context, perhaps the simplest experimental system is a one-coordinate cobalt atom: individual cobalt atoms on a MgO surface (referred to as adatoms) were recently shown using scanning probe microscopy to possess a $J = {}^9/_2$ ($L = 3$, $S = {}^3/_2$) ground state and exhibit near maximal magnetic anisotropy in a half-integer spin 3*d* system (*1*).

In the regime of molecules, linearly coordinated transition metal complexes have garnered interest of late because they are energetically unaffected by Jahn-Teller distortions, allowing for the possibility of virtually unquenched orbital angular momentum (*2*). Analogously to lanthanide complexes, such transition metal systems with non-zero L are best described by a total angular momentum J, which is split by spin-orbit coupling and the ligand field into $2J + 1$ M_J states. Two transition metal complexes that have been described using this formalism are the iron(II) complex $Fe(C(SiMe_3)_3)_2$ and the iron(I) complex $[Fe(C(SiMe_3)_3)_2]^-$ (*3,4*). Both complexes have ground states with $L = 2$ due to electronic configurations which place three electrons in the degenerate orbital pair $d_{x^2-y^2}$ and d_{xy}, which arise from linear combinations of the hydrogen-like d-orbitals with $m_l = \pm 2$. A notable consequence of these electronic structures is that both complexes exhibit relatively large energy separations between their ground and first excited M_J states, making them prone to single-molecule magnet behavior (*5*). Indeed, ac magnetic susceptibility data revealed that both molecules exhibit slow magnetic relaxation (the former complex under an applied dc field and the latter in zero applied field) with effective spin-reversal barriers (U_{eff}) of 178 and 246 cm^{-1}, respectively (*6*)—values close to the calculated energy separations between their ground and first excited M_J states (*7*,*8*).

At first glance it may seem impossible to increase orbital angular momentum for a transition metal complex beyond $L = 2$. An $L = 3$ ground state requires two sets of degenerate orbitals, $d_{x^2-y^2}$, d_{xy} ($m_l = \pm 2$) and d_{xz}, d_{yz} ($m_l = \pm 1$), with an odd number of electrons in each. The Aufbau principle describes the manner in which electrons fill orbitals, typically from lowest to highest energy. A more rigorous consideration of electronic structure accounts for three main effects: ligand field stabilization, interelectron repulsion, and spin-orbit coupling. Ligand field effects typically dominate when considering transition metal complexes. When the ligand field stabilization and interelectron repulsion energies are similar in transition metal complexes, high spin electronic configurations arise. For example, placing three electrons in the orbitals ($d_{x^2-y^2}$, d_{xy})(d_{xz}, d_{yz}) could give the low-spin configuration ($d_{x^2-y^2}$, d_{xy})^3(d_{xz}, d_{yz})^0 if the energy separation between orbital pairs is larger than the electron pairing energy, or the high-spin configuration ($d_{x^2-y^2}$, d_{xy})^2(d_{xz}, d_{yz})^1 if the

orbital pairs are relatively close in energy. For six electrons, the expected Aufbau filling of these orbitals is $(d_{x^2-y^2}, d_{xy})^4(d_{xz}, d_{yz})^2$, and as the sixth electron must be paired in either orbital pair, there is no reason to assume there would be any stabilization from the non-Aufbau configuration, $(d_{x^2-y^2}, d_{xy})^3(d_{xz}, d_{yz})^3$.

Intriguingly, calculations on the hypothetical complex $Co(C(SiMe_3)_3)_2$ show a ground state with $L = 3$, which arises from a non-Aufbau 3d-orbital filling of $(d_{x^2-y^2}, d_{xy})^3(d_{xz}, d_{yz})^3(d_{z^2})^1$, and further predict a splitting between ground and first excited M_J states of 454 cm^{-1} (*9*). Efforts to synthesize this molecule both by our laboratory and others (*10*) were unsuccessful. Moreover, although nearly 70 two-coordinate, paramagnetic transition metal complexes have been synthesized (*11*), the only such compounds with alkyl ligands are of the type $[M(C(SiMe_3)_3)_2]^{0/1-}$, where M is Fe(II) (*12*), Fe(I) (4), Mn(II) (*13*) and Mn(I) (*14*). Several approximately linear cobalt(II) complexes have been studied, however, and one such molecule (sIPr)CoNDmp (where sIPr is an N-heterocyclic carbene and NDmp is an arylimido ligand) has a spin-reversal barrier of 413 cm^{-1}, more than 1.5 times that measured for $[Fe^{I}(C(SiMe_3)_3)_2]^-$, despite both molecules possessing the same total angular momentum of $J = {}^7/_2$ (*15*). Correspondingly, the increase in magnetic anisotropy for the Co(II) complex must arise from an increase in the spin-orbit coupling constant, a value which trends with effective nuclear charge. In another example, bent $[OCoO]^-$ anions inserted into the channels of an apatite-type structure were shown to have a spin-reversal barrier of 387 cm^{-1} (*16*). A semi-empirical method based on ligand field parameterization predicted that such a barrier could arise from a $J = {}^9/_2$ ground state, with increasing mixing of M_J states (and a concomitant diminishing of the barrier height) arising as the $[OCoO]^-$ anion becomes increasingly bent. In the extreme case of the cobalt adatoms mentioned above, a separation of 468 cm^{-1} was determined for the separation between $M_J = {}^9/_2$ and ${}^7/_2$ states (*1*).

Our motivations to isolate a dialkyl cobalt(II) complex were thus twofold: first, the proposed electronic structure violates the Aufbau principle and is analogous to what is commonly seen for lanthanides; second, realizing maximal orbital angular momentum should afford a very large magnetic anisotropy, a property that has important applications in the study of magnetism. Here, we present the synthesis and characterization of such a dialkyl cobalt(II) complex and confirm the proposed $J = {}^9/_2$ ground state through direct electronic and spectroscopic measurements, *ab initio* modeling, and magnetic susceptibility measurements. The energy separation between the $M_J = \pm{}^9/_2$ and $\pm{}^7/_2$ states leads to slow magnetic relaxation at temperatures as high as 70 K and low-temperature magnetic hysteresis.

3.2 Results and Discussion

Synthesis and structure of a linear cobalt dialkyl complex

Our attempts to synthesize $Co(C(SiMe_3)_3)_2$ from metathesis reactions of $[C(SiMe_3)_3]^-$ salts and CoX_2 (X = Cl, Br, I) gave only intractable amorphous black solids. Similar reactivity with $[C(SiMe_3)_3]^-$ was reported previously, but by switching to $[C(SiMe_2Ph)_3]^-$ it proved possible to isolate the dimer $[Co(C(SiMe_2Ph)_3)]_2$, a product formed by the *in situ* reduction of cobalt(II) (*10*). Thus, at least one challenge in isolating a dialkyl cobalt(II) complex is the strongly reducing nature of the carbanion. Others have shown that substituting electron-withdrawing alkoxides onto each silyl group significantly reduces the basicity and electron density of the carbanion (*17*). In an initial pursuit of this approach, we found that $[C(SiMe_2OPh)_3]^-$ did support a dialkyl cobalt(II) complex, $Co(C(SiMe_2OPh)_3)_2$, but long-range Co···O interactions led to a significantly bent C–Co–C axis

(Fig. S3.1). We next synthesized a number of $[C(SiMe_2OR)_3]^-$ derivatives (R = various alkyl or substituted phenyl groups) following the general reaction scheme outlined in Fig. 3.1A. Smaller substituents did not readily yield isolable products, and larger substituents supported only dinuclear complexes of the type $(R_3CCo)_2(\mu\text{-}X)_2$ (where X is a halide), similar to the structure of $((PhMe_2Si)_3CZn)_2(\mu\text{-}Cl)_2$ (*18*). In an effort to reduce the nucleophilicity of the oxygen atom, we also tried using electron withdrawing substituents such as perfluorophenyl, but found these ligands to be susceptible to Si–O cleavage, a challenge also encountered when trying to metallate other $HC(SiMe_2OR)_3$ complexes with MeLi (*19*). Ultimately, we determined that only the naphthol (R = Naph = $C_{10}H_7$) derivative yielded the requisite linear geometry.

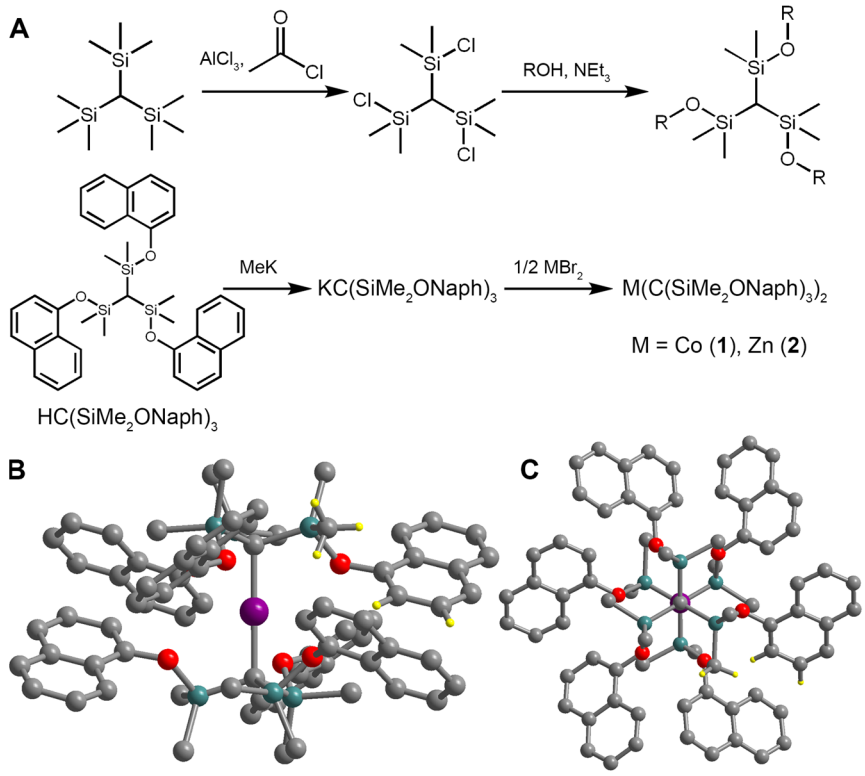

Fig. 3.1. Synthesis and structure of linear Co and Zn dialkyl complexes. (A) General synthetic scheme for ligands of the type $HC(SiMe_2OR)_3$ and synthesis of compounds **1** and **2**. **(B)** Molecular structure of $Co(C(SiMe_2ONaph)_3)_2$ (**1**). Purple, gray, turquoise, red, and yellow spheres represent Co, C, Si, O, and H atoms, respectively. Most hydrogen atoms have been omitted for clarity. Hydrogen atoms are shown on three carbons to illustrate the location of the CH-π interactions. **(C)** Molecular structure of $Co(C(SiMe_2ONaph)_3)_2$ viewed along the molecular *z*-axis.

The reaction of two equivalents of $KC(SiMe_2ONaph)$ with $CoBr_2$ in THF at 60 °C affords a green solution. After removal of the solvent *in vacuo* and redissolution into hexanes, dark red crystals of $Co(C(SiMe_2ONaph)_3)_2$ (**1**) emerged from the green solution over the course of several days at room temperature. Crystallization at −30 °C formed green crystals that were not suitable for X-ray diffraction, but elemental analysis of the thoroughly dried crystals suggested the isolation of the solvated complex, $Co(C(SiMe_2ONaph)_3)_2(THF)$. Compound **1** is insoluble in common organic solvents, and exposure to THF led to formation of a green solution which is likely the aforementioned solvated complex. The zinc congener, $Zn(C(SiMe_2ONaph)_3)_2$ (**2**), was obtained from the reaction of $KC(SiMe_2ONaph)$ and $ZnBr_2$ in Et_2O. After removal of KBr by filtration, colorless crystals of **2** grew from the Et_2O solution over the course of several days. Using the same

reaction conditions with a mixture of $ZnBr_2$ and $CoBr_2(THF)$ further enabled preparation of a magnetically dilute sample, $Co_{0.02}Zn_{0.98}(C(SiMe_2ONaph_7)_3)_2$ (**3**).

Single crystal x-ray diffraction analysis revealed compounds **1** and **2** to be isostructural, crystallizing in space group *R*–3 (no. 148) and featuring a linear C–M–C axis imposed by the S_6 site symmetry (Fig. 3.1B, 3.1C). The Co–C and Zn–C interatomic distances of 2.066(2) and 1.995(3) Å, respectively, are similar to the Fe–C separation of 2.0505(14) Å in $Fe(C(SiMe_3)_3)_2$ (*20*) and the and Zn–C separation of 1.982(2) Å in $Zn(C(SiMe_3)_3)_2$ (*21*). In addition, the Co···O distance of 3.1051(11) Å and Zn···O distance of 3.1240(16) Å are significantly longer than the sum of cobalt or zinc and oxygen ionic radii (~2.2 Å), suggesting minimal interactions. Instead, the staggered orientation of the ligands facilitates close sp^3-CH···π and sp^2-CH···π contacts of 2.692 and 2.822 Å, respectively (Fig. S3.3), which are in the range of weak CH-π interactions (*22*). This suggests that inter-ligand interactions may help stabilize **1**, consistent with reports of dispersion forces stabilizing other two-coordinate complexes (*23*).

Electronic structure calculations

Ab initio calculations performed on **1** using the crystal structure geometry reveal that the ^4F free ion state is split by the linear ligand field into three doubly-degenerate states $^4\Phi$, $^4\Pi$, and $^4\Delta$, and one non-degenerate state $^4\Sigma^-$ (here we employ $C_{\infty v}$ point group notation). Due to the exceptionally weak ligand field, the seven states of ^4F parentage are split by less than 3000 cm^{-1} (accounting also for interelectron repulsion energy). This splitting is small even relative to that of other two-coordinate complexes; for example, the ^5D and ^4F free ion states of $Fe(C(SiMe_3)_3)_2$ and $[Fe(C(SiMe_3)_3)_2]^-$ are split by 5000 and 6000 cm^{-1}, respectively (*3,4,7*). Excitations from the $^4\Phi$ ground state of **1** to the $^4\Sigma^-(^4P)$ and $^4\Pi(^4P)$ states were calculated to be spectroscopically accessible at 13,537 and 18,864 cm^{-1}, and indeed are observed in the ultraviolet-visible (UV-vis) diffuse reflectance spectrum at 12,000 and 15,000 cm^{-1} (Fig. S3.4). The splitting of the $^4\Phi$ ground state due to spin-orbit coupling results in four sets of Kramers doublets, best described by $M_J = \pm^9/_2$, $\pm^7/_2$, $\pm^5/_2$, and $\pm^3/_2$, in order of increasing energy. The total splitting of $^4\Phi$ is 1469 cm^{-1}, while the calculated separation between just $M_J = \pm^9/_2$ and $M_J = \pm^7/_2$ is 476 cm^{-1}. Additional calculations performed on a truncated model molecule show that inclusion of the carbon σ-bonding electrons in the complete active space have only a very minor effect (less than 3%) on the energies of both the non-relativistic and relativistic states (Tables S10-11).

Ligand-field analysis of the calculations revealed the $^4\Phi$ ground state to have the 3d-orbital filling $(d_{x^2-y^2}, d_{xy})^3(d_{xz}, d_{yz})^3(d_{z^2})^1$ (Fig. 3.2A), which deviates from the expected Aufbau orbital filling of $(d_{x^2-y^2}, d_{xy})^4(d_{xz}, d_{yz})^2(d_{z^2})^1$ ($^4\Sigma^-$) and can be explained by considering the competing effects of ligand field stabilization and interelectron repulsion. In general, inter-electronic repulsion is strongest for two electrons occupying the same orbital (necessarily with opposite spin). Two electrons with opposite spin in different orbitals alternatively experience medium-strong electron-electron repulsion, while two electrons with parallel spin (necessarily in different orbitals) repel each other least strongly owing to the presence of the Fermi-hole. Typically, only the electron pairing energy component of interelectron repulsion is important for transition metal complexes, and whether a complex is high- or low-spin is determined by considering whether the ligand field strength is small or large compared to the pairing energy. In the case of **1**, the ligand field strength is so small that not only does the molecule display a high-spin state, but it also maximizes its orbital angular momentum in keeping with the Hund rule for free atoms and ions, thus leading to a non-Aufbau ground state configuration. Clearly, the $(d_{x^2-y^2}, d_{xy})^3(d_{xz}, d_{yz})^3(d_{z^2})^1$ configuration

minimizes electron-electron repulsion relative to the alternative $(d_{x^2-y^2}, d_{xy})^4(d_{xz}, d_{yz})^2(d_{z^2})^1$ configuration that features an electronically crowded $(d_{x^2-y^2}, d_{xy})^4$ subshell. This stabilization is also reflected in the total orbital angular momentum of the ground state that is an approximately good quantum number in this system. Non-relativistic ligand field calculations without interelectron repulsion show the expected ground state of $^4\Sigma^-$ (with $L = 0$). Using ligand field parameters from *ab initio* NEVPT2 calculations and ligand field expressions for the $S = {}^3/_2$ states under linear symmetry with interelectron repulsion, the high orbital angular momentum $^4\Phi$ state (with $L = 3$) is stabilized by 1300 cm^{-1} relative to the $^4\Sigma^-$ state (Fig. 3.2B, Table S3.9). Spin-orbit coupling further stabilizes the $M_J = {}^9/_2$ component of the $^4\Phi$ ground state by 788 cm^{-1}.

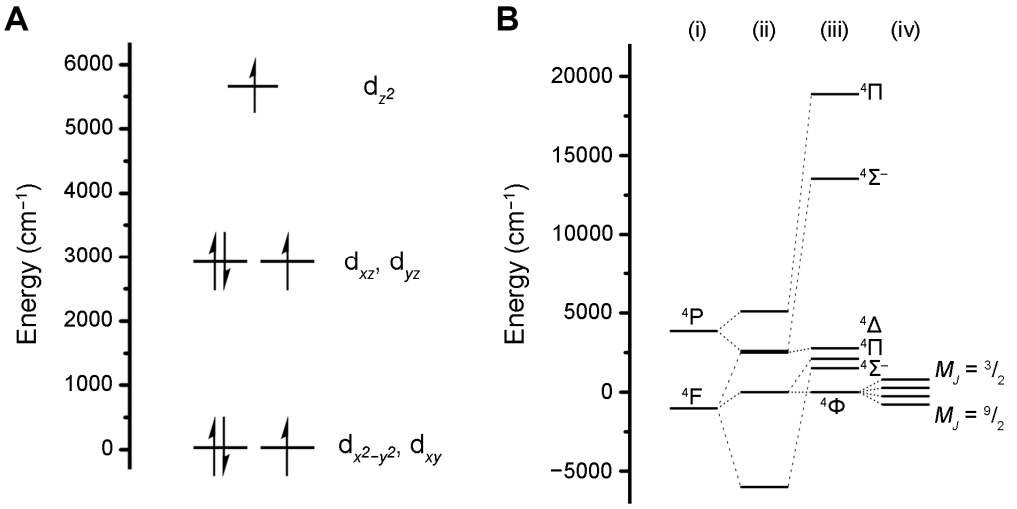

Fig. 3.2. Electronic structure analysis. (A) Energy diagram depicting the energy and electron occupations of the 3d-orbitals based on ligand field analysis of *ab initio* calculations. **(B)** Electronic structure of (i) a free Co(II) ion, (ii) $Co(C(SiMe_2ONaph)_3)_2$ (**1**) considering only ligand field interactions, (iii) $Co(C(SiMe_2ONaph)_3)_2$ considering both ligand field interactions and interelectron repulsion, and (iv) the splitting of the ground $^4\Phi$ state of $Co(C(SiMe_2ONaph)_3)_2$ due to spin orbit coupling according to *ab initio* calculations. Term symbols are for $C_{\infty v}$ symmetry. The splitting between the ground $M_J = {}^9/_2$ and maximal excited $M_J = {}^3/_2$ states is 1469 cm^{-1}.

This situation is completely distinct from that of established complexes with stronger ligand fields that can sometimes have electronic ground states with significant contributions from non-Aufbau configurations. For example, the iron(II) metallophthalocyanine complex (FePc) has a ground state with nearly equal contributions from Aufbau and non-Aufbau configurations, wherein the non-Aufbau component arises from an accidental orbital near-degeneracy (*24*). The essential difference between complex **1** and FePc, however, is in ligand field strength, with the two molecules calculated to exhibit total d-orbital splittings of 6000 and 165,000 cm^{-1},(*24*) respectively. Focusing on the orbitals that give rise to the non-Aufbau states, the $d_{x^2-y^2}$,d_{xy} and d_{xz},d_{yz} orbital pairs are separated by 2900 cm^{-1} in **1**, whereas for FePc the d_{xz},d_{yz} orbital pair and d_{z^2} orbital are separated by 19,000 cm^{-1} (*24*). Our calculations show that interelectron repulsion in **1** easily overwhelms the ligand field stabilization energy associated with the Aufbau configuration, destabilizing the $^4\Sigma^-(^4P)$ state by 12,000 cm^{-1} relative to the $^4\Phi$ state. No similar calculations appear to have been reported for FePc, but it is clear that it would be impossible to observe a pure non-Aufbau ground state as long as the ligand field stabilization energy is of the same magnitude as interelectron repulsion. Once the ligand field requirement for a non-Aufbau ground state is met, it is also possible to observe maximal orbital angular momentum. The maximal orbital angular

momentum of $L = 3$ for transition metals requires degenerate $d_{x^2-y^2}$, d_{xy} and d_{xz}, d_{yz} orbital pairs, and thus the molecule should also be linear to avoid Jahn-Teller distortions.

The ligand-field analysis elucidates another challenge in isolating a dialkyl cobalt complex, namely the ligand field stabilization energy suggests that metal-ligand bond formation provides only a minor stabilizing effect of 4.8 kcal/mol (1700 cm^{-1}). This result is perhaps intuitively understood by considering that the formal Co–C bond order is approximately one half, because the d_{xz}, d_{yz} orbitals have slight π-antibonding character and are destabilized primarily by electrostatic interactions. It is not until we consider transmetallic dispersion and electrostatic (CH···π) forces that **1** appears to be stable.

Charge density determination

The molecular charge density (CD) of **1** was obtained from multipolar refinement of single crystal x-ray diffraction data measured at 20 K using synchrotron radiation. A small amount of disorder (~6%) is present in the structure due to flipping of the naphthalene groups (also involving the O and Si atoms); however, a detailed description of this disorder was possible and allowed us to extract quantitative information pertinent to the magnetic properties (see Methods for a detailed description of the experimental procedure).

The experimental temperature of 20 K is low enough that the CD primarily represents the electronic properties of the relativistic ground state. We used an atom-centered multipole formalism to describe the CD, and thus a complete set of spherical harmonic functions for each atom was used to quantify the deviations from a spherical density distribution. The use of this formalism enables estimation of 3d-orbital populations on the central cobalt atom, under the assumption that the density around the metal originates solely from the atom itself (i.e., that no significant covalent bonding occurs). The parameterized CD also enables an analysis in the framework of quantum theory of atoms in molecules (QTAIM) (*25*) and estimates of atomic charges and the strength of chemical bonding. Defining the local coordination axes such that the Co–C direction is along the *z*-axis, the electron density of the cobalt valence shell is distributed in the following manner: 42.8% is in the $d_{x^2-y^2}$, d_{xy} orbitals, 41.2% is in the d_{xz}, d_{yz} orbitals, and 16.0% is in the d_{z^2} orbital. Furthermore, the same distributions of electrons in the cobalt 3d-orbitals was obtained regardless of the manner in which the naphthalene disorder was treated.

Variable-field far-infrared spectroscopy

We sought to confirm experimentally the magnitude of the separation between the ground and first excited magnetic states in **1** using variable-field far-IR spectroscopy (*26*, *27*). Although such energy separations are more commonly determined by fitting low-temperature magnetization data or high-temperature magnetic relaxation data, these approaches give values that are sensitive to fitting procedures and provide only an indirect measure of the representative ground to excited state energy separation. Additionally, given the calculated energy splitting of 476 cm^{-1} for the lowest M_J states, dc susceptibility measurements would provide limited information on the position of excited states, as the Boltzmann population of the ground state doublet is still 90% at 300 K. Thus, not only is spectroscopy a more direct measurement, but in this case, it is also necessary to gain information on the excited states. Transmission spectra in the 30 to 600 cm^{-1} energy range were collected at a temperature of 4.2 K under applied fields ranging from 0 to 11 T (Fig. 3.3A). Although absorption bands associated with magnetic dipole transitions are usually

significantly weaker than those of electronic dipole transitions, a pronounced field dependence is immediately evident in the data upon dividing the applied field spectra by the zero-field spectrum (Fig. 3.3B). The only peak visible in this energy range is at 450 cm^{-1} and is attributable to the transition from $M_J = \pm^9/_2$ to $\pm^7/_2$ in good agreement with the calculated separation of 476 cm^{-1}. A steadily increasing blueshift of the IR absorption maximum is observed with increasing applied fields (Fig. S3.5) and is in good agreement with a simulation of the spectral envelope magnetic dipole $M_J = \pm^9/_2$ to $\pm^7/_2$ transitions (Fig. S3.6). In addition to the blueshift there is a concomitant decrease in absorption intensity and peak broadening with increasing field, giving rise to the derivative shape observed in Fig 3B.

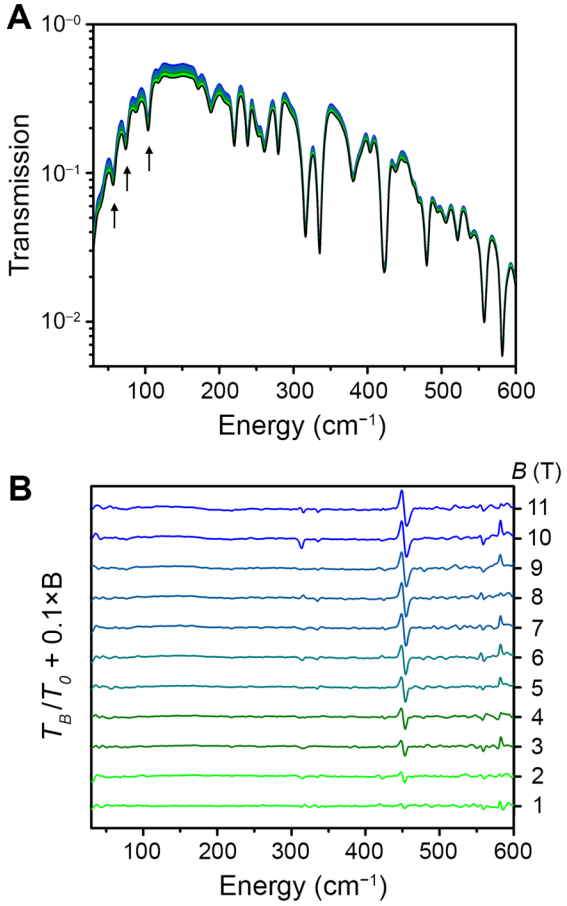

Fig. 3.3. Variable-field, far-IR spectroscopy. (A) Absolute transmission spectra for **1** collected at 4.2 K under applied fields ranging from 0 to 11 T. Phonon energies used in Eq. 2 to describe magnetic relaxation are marked with arrows. **(B)** Plots of applied field spectra divided by the zero-field spectrum. The peak at 450 cm^{-1} corresponds to the transition from $M_J = ^9/_2$ to $M_J = ^7/_2$.

Magnetic properties

Variable-temperature dc magnetic susceptibility data for **1** are shown in Fig. 3.4A. The gradual decrease in the product of the molar magnetic susceptibility and temperature ($\chi_M T$) with decreasing temperature is indicative of magnetic anisotropy, while the strong field dependence at low temperature arises from an increased Zeeman splitting at higher fields. The room temperature $\chi_M T$ value of 4.89 cm^3 K mol^{-1} is consistent with a well-isolated $M_J = ^9/_2$ ground state (the theoretical $\chi_M T$ value for an isotropic $J = ^9/_2$ ion is 5.47 cm^3 K mol^{-1}), and reduced magnetization plots (Fig.

3.4B) show a saturation magnetization of 3.00 μ_B. The simulated $\chi_M T$ and reduced magnetization data from *ab initio* calculations (solid lines, Fig. 3.4) are in close agreement with the experimental data, further corroborating the well-isolated $M_J = {}^9/_2$ ground state.

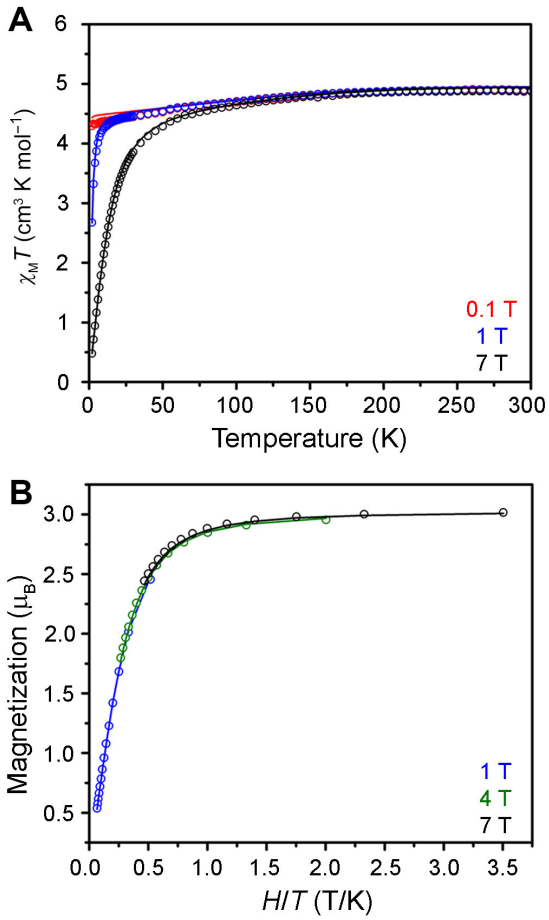

Fig. 3.4. Magnetic susceptibility and reduced magnetization analysis. (A) Variable-temperature molar magnetic susceptibility times temperature ($\chi_M T$) for **1** collected under dc fields of 0.1, 1, and 7 T; solid lines are simulated data from *ab initio* calculations. **(B)** Reduced magnetization data for **1** collected at temperatures from 2 to 15 K under dc fields of 1, 4, and 7 T; solid lines are simulated data from *ab initio* calculations.

Ac susceptometry was employed to probe magnetic relaxation in the 10^{-4} to 10^{1} s (10^{4} to 10^{-1} Hz) range. By fitting the in-phase (χ') and out-of-phase (χ'') susceptibility (Fig. S3.8-S3.11) to a generalized Debye model, we obtained relaxation times for **1**, as shown in the Arrhenius plot in Fig. 3.5A. The temperature dependence of magnetic relaxation time (τ) in molecules exhibiting slow magnetic relaxation is typically described by the expression

$$\tau^{-1} = \frac{A_1}{1+A_2H^2} + BH^4T + CT^n + \tau_0^{-1}\exp(-U/k_BT), \qquad (1)$$

where the four terms represent quantum tunneling, direct, Raman, and Orbach relaxation processes, respectively (*28*,*29*,*30*). However, we were unable to fit the relaxation data for **1** to the total sum of these processes. An alternative model for through-barrier relaxation has recently been proposed, wherein specific phonon modes may facilitate relaxation through direct doublet transitions (*31*,*32*). Building on the results of Lunghi and coworkers, we derived the expression

$$\tau^{-1} = \tau_{tunnel}^{-1} + \sum_{\alpha}\left(\frac{V_{\alpha}^{2}}{\hbar}\frac{\Delta_{\alpha}(2n_{\alpha}+1)}{[\Delta_{\alpha}^{2}+(\hbar\omega_{\alpha})^{2}]}\right) + \tau_{0}^{-1}\exp(-U/k_{B}T), \qquad (2)$$

where the first term represents quantum tunneling and the last term represents Orbach relaxation. The second term represents relaxation through the α-th phonon mode, V represents spin-phonon coupling, Δ is the phonon linewidth, n is the phonon occupation number, and ω is the phonon frequency. Both Δ and n are dependent on both temperature and ω. Values for U and ω are taken from the variable-field, far-IR data, while τ_{tunnel}, V, and τ_0 are fit parameters (see equations S1-S4 for details). From this equation we were able to obtain reasonable fits (σ_{EST} = 0.17 and 0.21 for **1**, and **3**, respectively) to the relaxation data in Fig. 3.5A.

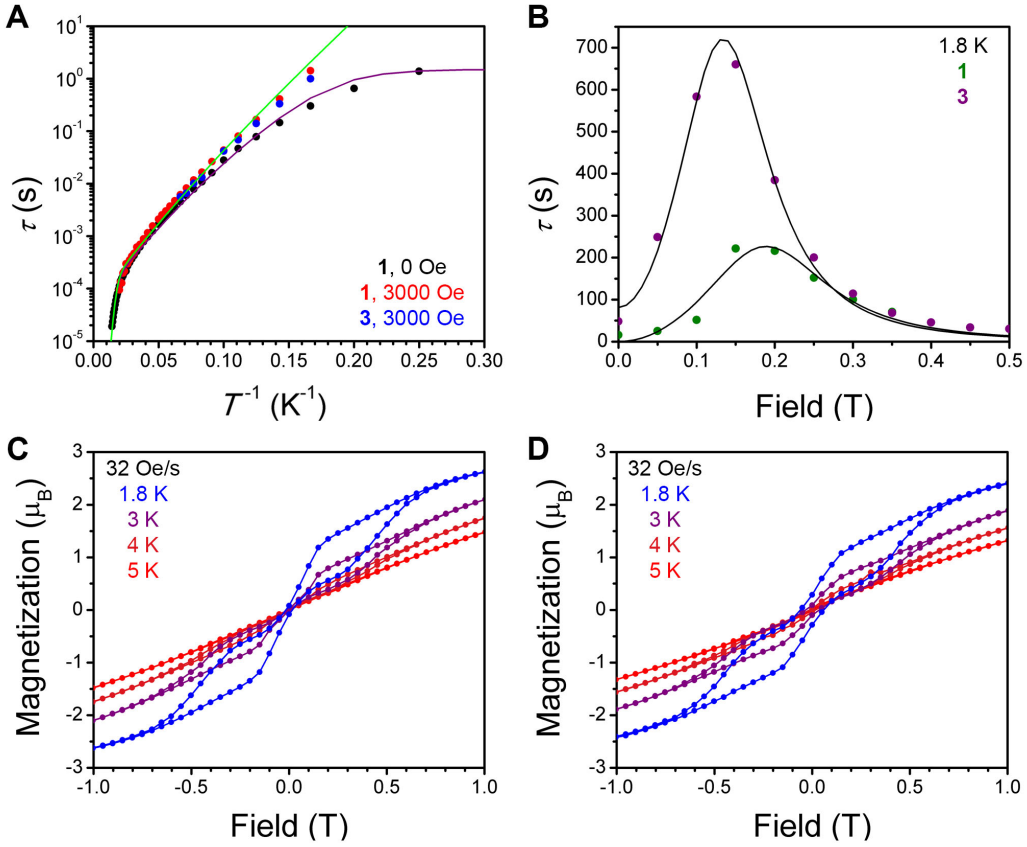

Fig. 3.5. Magnetic relaxation dynamics. (A) Arrhenius plot showing the natural log of relaxation time, □, versus inverse temperature for **1** in the absence of an applied dc field (black circles), **1** under a 3000 Oe dc field (red circles), and **3** in the absence of an applied dc field (blue circles). Relaxation times are determined from fits of ac susceptibility measurements over the temperature range of 4 to 70 K. The purple and green lines represent fits of the relaxation data for **1** under 0 and 3000 Oe, respectively. **(B)** Dc relaxation and magnetization times for **1** (green circles) and **3** (purple circles). The solid lines are from fits describing relaxation via tunneling and direct relaxation processes as described in the text and Methods. **(C)** Variable-field magnetization data for **1** collected at temperatures ranging from 1.8 to 5 K at a field sweep rate of 32 Oe/s. **(D)** Variable-field magnetization data for **3** collected at temperatures ranging from 1.8 to 5 K at a field sweep rate of 32 Oe/s.

To further examine the effect of any tunneling relaxation process, we collected data under a 3000 Oe field. The lack of a temperature-independent region at low temperature under zero and applied field indicates that molecular quantum tunneling is not a dominant relaxation pathway above 4 K; however, the observed increase in relaxation times upon application of a dc field (Fig. 3.5A) demonstrates that it is a contributing factor. To some extent, the tunneling relaxation rate can be slowed through magnetic dilution (*33*), and indeed measurements of a magnetically dilute

sample prepared with a 1:49 ratio of cobalt to zinc (**3**) exhibits lower relaxation rates than **1** under zero field. The lack of a linear temperature dependence at the highest temperatures indicates that two-phonon Orbach relaxation (involving excitation to and relaxation from a real excited state) is not yet dominant at 70 K. Using the value of $U = 450$ cm^{-1} obtained from far-IR spectroscopy, however, we determined an upper bound for τ_0 of 1.79×10^{-9} s, which is a reasonable value for a single-molecule magnet (*5*).

The low temperature relaxation dynamics of **1** and **3** were also probed using dc relaxation and magnetization experiments (Fig. 3.5B). The tunneling and direct relaxation terms introduced above were used in fits of the variable-field relaxation data and are discussed in detail in the Methods section. The relaxation times extracted at 1.8 K and zero applied field are 16.4 ± 0.7 and 48.2 ± 4.7 s for **1** and **3**, respectively, and these values slow to 221 and 660 s at 1.8 K under a 1500 Oe applied field. These relaxation times suggest that magnetic hysteresis should be apparent in variable-field magnetization data, and indeed **1** and **3** show waist-restricted hysteresis loops between ±0.7 T up to 5 K. A sudden decline in the magnetization as the field approaches zero can be ascribed to rapid relaxation induced by tunneling of the magnetization (Fig. 3.5C, 3.5D), and this decline results in small values of the remnant magnetization for **1** (0.08 μ_B) and **3** (0.28 μ_B) at 1.8 K that diminish to near zero at higher temperatures. Despite the relatively fast relaxation at zero field, **1** has a coercive field, H_c, of 180 Oe at 1.8 K, as measured with a field sweep rate of 32 Oe/s. Under the same conditions, the magnetically dilute sample, **3**, exhibits $H_c = 600$ Oe.

3.3 Outlook

These results have clear implications toward technologies that require a large magnetic anisotropy. For a magnetic bit to retain its magnetization for information storage, the magnetic anisotropy energy must be significantly greater than the thermal energy. For the cobalt adatom on MgO, the separation between the ground ($M_J = \pm 9/2$) and first excited ($M_J = \pm 7/2$) states was determined to be 468 cm^{-1}, and it was suggested that this value was near a physical limit for magnetic anisotropy for 3d transition metals. This limit can be quantified using the phenomenological spin-orbit coupling Hamiltonian, $H_{SOC} = \lambda \mathbf{L}\cdot\mathbf{S} = (\zeta/2S)\sum_i \mathbf{l}_i\mathbf{s}_i$, where λ is the effective spin-orbit coupling constant, ζ is the atomic spin-orbit coupling constant, and $\mathbf{L} = \sum_i \mathbf{l}_i$ and $\mathbf{S} = \sum_i \mathbf{s}_i$ are the operators for the orbital and spin-angular momenta, respectively (the index i sums over individual electrons). In systems with a doubly degenerate ground state, the energies of the M_J states (where $M_J = M_S + M_L$) are given by $E(M_J) = (\zeta/2S)M_L \cdot M_S$; the separation between lowest and highest M_J states is equal to $L\zeta$, and the separation between adjacent states is $(L/2S)\zeta$. Thus, the actual limit for the energy separation between ground and first excited state would be found in a system with $L = 3$ and $S = 1$. However, in order to maximize relaxation times, it is advantageous to employ half-integer spin systems, as the crystal field cannot couple the two components of the lowest doublet and the tunneling relaxation pathway is therefore suppressed (*34*). The maximal total angular momentum for a transition metal with half-integer spin is $J = 9/2$, exhibited by both the cobalt adatom and compound **1**. The magnetic M_J states of **1** span a substantial calculated energy range of 1469 cm^{-1}, and the separation between the ground ($M_J = \pm 9/2$) and first excited ($M_J = \pm 7/2$) states alone is 450 cm^{-1}. Within a rigorously linear manifold, it may be possible to further increase the magnetic anisotropy by changing the nature of the Co–L bond and by increasing the spin-orbit coupling constant. However, at present the barrier of $U_{eff} = 450$ cm^{-1} determined here for **1** is the largest measured to date for any transition metal single-molecule magnet, with the second largest being $U_{eff} = 413$ cm^{-1} from the aforementioned

(sIPr)CoNDmp complex (*15*). Given the similarity between the cobalt adatom and **1**, it is indeed possible that this value is near the physical limit. Our calculations for the Co adatom on MgO indicate that the $^4\Phi(^4F)$ ground state is also well isolated in this system, suggesting that spin-orbit coupling is also the dominant factor determining the energies of the M_J states here (Table S3.13). Although information storage will certainly require longer zero-field relaxation times than observed here, we note that magnetic relaxation times can be significantly affected by the molecular environment, as has been observed for $Tb(Pc)_2$ molecules in bulk solids (*35*) and on a variety of surfaces (*36-41*). A comparison of the relaxation times of the cobalt adatom on MgO and those of compound **1** indicates such an environmental effect is indeed at play. Both cobalt centers have similar electronic structures, yet the relaxation time for the adatom at 0.6 K is on the order of 10^{-4} s, whereas a much longer relaxation time on the order of 10^1 s is observed for **1** at 1.8 K.

Beyond the implications for molecular magnetism, an intriguing potential use of the linear L–Co^{II}–L moiety is in the pursuit of lanthanide-free bulk magnets. Generally speaking, orbital angular momentum and spin-orbit coupling tie the magnetic moment to lattice (*42*). In bulk magnetism, orbital angular momentum is responsible for magnetocrystalline anisotropy, the main determinant of magnetic coercivity, which is why the strongest magnets, such as $Nd_2Fe_{14}B$ and $SmCo_5$, feature lanthanide ions with unquenched orbital angular momentum.Our results show how linearly coordinated transition metal ions could provide a similar effect. For example, the extended solid $Li_2(Li_{1-x}Fe_x)N$ features linear iron(I) centers similar to those in $[Fe(C(SiMe_3)_3)_2]^-$, and in high concentration (x = 0.28) this material displays an extremely large coercivity (H_c = 11.6 T at 2 K) (*43*). The magnetic anisotropy of compound **1** is nearly twice as large as in $[Fe(C(SiMe_3)_3)_2]^-$, and incorporation of the L–Co^{II}–L moiety in an extended solid could therefore in principle lead to permanent magnets with an even greater coercivity.

3.4 Methods

General considerations

Unless otherwise noted, all manipulations were carried out using standard air-free Schlenk line and glove box techniques under an argon atmosphere. Reagents were purchased from commercial vendors. Anhydrous $CoBr_2$ and $ZnBr_2$ were used as received, while 1-naphthol was sublimed and triethylamine (NEt_3) was dried over KOH and distilled prior to use. $HC(SiMe_2Cl)_3$ (*17*), MeK (*44*) were prepared according to literature procedures. Solvents were dried using a commercial solvent purification system designed by JC Meyer Solvent Systems. Elemental analysis was performed at the Microanalytical Laboratory of the University of California, Berkeley. NMR spectra were collected on a 500 MHz Bruker spectrometer; chemical shifts are reported in ppm referenced to residual protiated solvent.

Synthesis of $HC(SiMe_2OPh)_3$ and $HC(SiMe_2OC_{10}H_7)_3$

A 100 mL Schlenk flask containing a stir bar was charged with a THF solution (50 mL) of $HC(SiMe_2Cl)_3$ (3.73 g, 12.7 mmol) and NEt_3 (1.80 mL, 38.1 mmol). A separate 50 mL Schlenk flask was charged with a THF solution (25 mL) of 1-naphthol (5.58 g, 38.7 mmol). The 1-naphthol solution was added to the reaction flask over the course of several minutes with stirring, and a white precipitate immediately formed upon addition. The reaction was stirred at room temperature for 3 hours, after which air-free techniques were no longer required. Water (20 mL) was added to

the reaction flask and the organic layer was collected. The water was extracted with 3×20 mL Et_2O, and the combined organic layers were dried with $MgSO_4$. The ether solvent was removed under reduced pressure, leaving a colorless residue. The residue was washed with MeOH (50 mL) and the resulting white solid, $HC(SiMe_2OC_{10}H_7)_3$ (5.15 g, 66%), was collected by filtration. Anal. calcd for $C_{37}H_{40}O_3Si_3$: C, 72.03; H, 6.54. Found: C, 72.04; H, 6.75. ^{1}H NMR (500 MHz, THF-d8): δ 8.33 (3 H, d), 7.83 (3 H, d), 7.47 (3 H, d), 7.40 (6 H, m), 7.32 (3 H, t), 7.03 (3 H, d), 1.39 (1 H, s), 0.63 (18 H, s) ppm. ^{13}C NMR (500 MHz, THF-d8): δ 151.8, 136.0, 128.9, 128.3, 126.7, 126.4, 125.7, 123.4, 122.0, 114.4, 13.1, 2.9, 2.8 ppm.

The same method was used to synthesize $HC(SiMe_2OPh)_3$, which has been reported previously using a different synthetic method (*45*). The identity of $HC(SiMe_2OPh)_3$ was confirmed by ^{1}H NMR spectroscopy.

Synthesis of $(CH_3OCH_2CH_2OCH_3)_2KC(SiMe_2OPh)_3$

Solid MeK (0.11 g, 1.9 mmol) was slowly added to a stirring solution of **1** (0.91 g, 1.9 mmol) dissolved in Et_2O (10 mL) and dimethoxyethane (3 mL); bubbles evolved during the course of addition. The reaction was then allowed to stir for 3 hours, during which time a white microcrystalline solid precipitated from solution. The solid was collected by filtration and dried under vacuum (0.65 g, 0.95 mmol, 49%). Anal. Calcd for $KC_{33}H_{53}O_7Si_3$: C, 57.85; H, 7.80. Found: C, 57.83; H, 7.60. ^{1}H NMR (500 MHz, THF-d8): δ 7.15 (6 H, t), 6.91 (6 H, d), 6.83 (3 H, t), 3.42 (8 H, s), 3.26 (12 H, s), 0.24 (18 H, s) ppm. ^{13}C NMR (500 MHz, THF-d8): δ 158.3, 129.7, 122.2, 121.0, 72.7, 58.9, 16.8, 15.7, 5.2 ppm.

Synthesis of $KC(SiMe_2OC_{10}H_7)_3$

$HC(SiMe_2OC_{10}H_7)_3$ (0.967 g, 1.57 mmol) was dissolved in THF (15 mL). Freshly prepared MeK (0.0850 g, 1.57 mmol) was added as a solid to the stirring reaction mixture; bubbles evolved from the mixture over the course of an hour. After 3 hours, the reaction mixture was filtered through diatomaceous earth and solvent was removed under reduced pressure, leaving a sticky colorless residue. Hexane was added to precipitate a white solid, $KC(SiMe_2OC_{10}H_7)_3$ (1.20 g, 76%), which was collected by filtration. Anal. calcd for $KC_{37}H_{39}O_3Si_3$: C, 67.84; H, 6.00. Found: C, 67.59; H, 6.31. ^{1}H NMR (500 MHz, THF-d8): δ 8.42 (3 H, d), 7.71 (3 H, d), 7.49 (3 H, d), 7.28 (12 H, m), 0.38 (18 H, s) ppm. ^{13}C NMR (500 MHz, THF-d8): δ 154.8, 135.9, 129.7, 127.7, 126.9, 125.6, 124.4, 124.2, 118.7, 114.5, 16.2, 5.9, 5.8 ppm.

Synthesis of $Co(C(SiMe_2OPh)_3)_2$

Solid $CoCl_2$ (18.2 mg, 0.140 mmol) was added to a stirring THF solution (10 mL) of $(CH_3OCH_2CH_2OCH_3)_2KC(SiMe_2OPh)_3$ (200. mg, 0.290 mmol) at room temperature and then the mixture was stirred for 2 hours at 60 °C. The solvent was removed *in vacuo* and the resulting blue-green solid was dissolved in hexanes. The hexanes solution was stirred at 60 °C for 1 hour to form a yellow-green solution. The hexanes solution was filtered through diatomaceous earth and was concentrated *in vacuo*. Red-brown crystals of $Co(C(SiMe_2OPh)_3)_2$ (0.044g, 39%) suitable for x-ray diffraction grew in 2 hours at −30 °C. Anal. Calcd. for $CoC_{50}H_{66}Si_6O_6$: C, 60.63; H, 6.72. Found: C, 60.98; H, 6.84.

Synthesis of $Co(C(SiMe_2OC_{10}H_7)_3)_2$ (1)

Solid $CoBr_2$ (41.6 mg, 0.190 mmol) was added to a stirring THF (8 mL) solution of $KC(SiMe_2OC_{10}H_7)_3$ (249 mg, 0.380 mmol) at room temperature. The reaction mixture was stirred for 4 hours at 60 °C, after which time the solution had turned green. The reaction mixture was filtered through diatomaceous earth and solvent was removed under reduced pressure, leaving a green solid. The green solid was dissolved in hexanes (20 mL) and filtered to give an emerald green solution, from which brown-red crystals of **1** (17.8 mg, 7%) suitable for x-ray diffraction grew over the course of 3 days. Compound **1** is insoluble in all common organic solvents except THF, in which it forms a green solution. Anal. calcd for $CoC_{74}H_{78}O_6Si_6$: C, 68.85; H, 6.09. Found: C, 68.36; H, 6.03.

Cooling the green hexanes solution appears to favor precipitation of the THF solvate, $Co(C(SiMe_2OC_{10}H_7)_3)_2(THF)$. Green crystals not suitable for single crystal x-ray diffraction were grown from the green hexanes solution over 1 day at −30 °C, collected by filtration and thoroughly dried *in vacuo*. Anal calcd for $CoC_{78}H_{86}O_7Si_6$: C, 68.74; H, 6.36. Found: C, 68.66; H, 6.52.

Synthesis of $Zn(C(SiMe_2OC_{10}H_7)_3)_2$ (2)

At room temperature, a solution of $ZnBr_2$ (35.1 mg, 0.155 mmol) dissolved in THF (2 mL) was added to a solution of $KC(SiMe_2OC_{10}H_7)_3$ (206 mg, 0.314 mmol) dissolved in THF (8 mL), and the mixture was stirred at room temperature for 12 hours. The reaction mixture was subsequently filtered through diatomaceous earth and the THF solvent was removed under reduced pressure, leaving a white solid. The colorless solid was stirred in hexanes (20 mL) and filtered to give a pale-yellow solution, from which colorless crystals of **1** (36.7 mg, 9%) suitable for x-ray diffraction grew over the course of 1 day. Anal. calcd for $ZnC_{74}H_{78}O_6Si_6$: C, 68.51; H, 6.06. Found: C, 68.14; H, 5.92.

Synthesis of $Co_{0.02}Zn_{0.98}(C(SiMe_2OC_{10}H_7)_3)_2$ (3)

Initially, $CoBr_2(THF)$ was prepared by dissolving $CoBr_2$ (6.2 mg, 0.028 mmol) in THF (5 mL) and then removing the solvent under reduced pressure. A suspension of $CoBr_2(THF)$ (0.028 mmol) and $ZnBr_2$ (57.4 mg, 25.5 mmol) was prepared in Et_2O (4 mL), and this suspension was added to a stirring solution of $KC(SiMe_2OC_{10}H_7)_3$ (371 mg, 0.567 mmol) dissolved in Et_2O (6 mL). The mixture was stirred for 1 hour at room temperature and then filtered through diatomaceous earth. A light pink powder was collected from the reaction mixture and the resulting light green Et_2O filtrate was put in a 20 mL vial. Crystallization tubes were added to the vial to increase the amount of crystallization surfaces and Et_2O was added to fill the vial. Light pink crystals of of **3** (63.9 mg, 9%) suitable for x-ray diffraction grew over the course of 4 days. Successful dilution was confirmed by determination of a unit cell consistent with pure **1** and **2**, and the metal composition was determined from comparison of molar magnetization data for the pure and diluted samples.

Single Crystal X-Ray Diffraction

In an argon filled glovebox, crystals of $Co(C(SiMe_2OPh)_3$, **1**, **2**, and **3** were coated in Paratone-N oil in individual vials, which were then sealed and remained sealed until immediately prior to mounting. Crystals were mounted on Kaptan loops and cooled under a stream of N_2. Data were

collected using a Bruker QUAZAR diffractometer equipped with a Bruker MICROSTAR X-Ray source of Mo Kα radiation (λ = 0.71073 Å), and an APEX-II detector. Raw data were integrated and corrected for Lorentz and polarization effects using Bruker Apex3 v. 2016.5. Absorption corrections were applied using SADABS (*46*). The space group was determined by examination of systematic absences, E-statistics, and successive refinement of the structure. The crystal structure was solved with ShelXT (*47*) and further refined with ShelXL (*48*) operated in the Olex2 software (*49*). The crystal did not show any significant decay during data collection. Thermal parameters were refined anisotropically for all non-hydrogen atoms. Hydrogen atoms were placed in ideal positions and refined using a riding model for all structures. A checkcif report for **1** gave rise to a B level alert regarding the ratio of maximum/minimum residual density. The maximum residual density for **1** lies in the napthyl ring. In the case of the low temperature synchrotron data used for charge density modeling, disorder in the naphthyl ring was successfully modeled. For the data collected at 100 K used for the generation of the cifs for **1** and **2**, we were unable to fully model this disorder, however it is likely that the same disorder is responsible for the relatively large residual density.

UV-Visible-NIR Diffuse Reflectance

UV-visible-NIR diffuse reflectance spectra were collected using a CARY 5000 spectrophotometer interfaced with Varian Win UV software. The samples were prepared in a glovebox and held in a Praying Mantis air-free diffuse reflectance cell. Powdered $BaCO_3$ was used as a non-absorbing matrix. The spectra were collected in $F(R)$ vs wavenumber, where $F(R)$ is the Kubelka-Munk conversion $F(R) = (1 - R)^2/2R$ and R is reflectance.

Magnetometry

All magnetic measurements were carried out using a Quantum Design MPMS-XL SQUID Magnetometer, with the exception of the high frequency ac magnetic susceptibility data. High frequency data (up to 10,000 Hz) was collected at the Quantum Design facility in San Diego, CA, using a 9T PPMS instrument equipped with the ACMSII measurement option to probe the ac moment at frequencies above 1000 Hz. For the measurements using the MPMS instrument, polycrystalline samples of **1** (32.1 mg) and **3** (49.7 mg) were loaded into quartz tubes (5 mm i.d., 7 mm o.d.) with a raised quartz platform. Solid eicosane was then added on top of the samples (32.0 and y 61.2, respectively) to prevent crystallite torqueing and provide good thermal contact between the sample and the cryogenic bath. The tubes were fitted with Teflon sealable adapters, evacuated using a glovebox vacuum pump, and sealed under static vacuum using an H_2/O_2 flame. Following flame sealing, the solid eicosane was melted in a water bath held at 40 °C. When not in the magnetometer, the sealed samples were stored at −30 °C. Dc magnetic susceptibility data was collected for each sample from 2 to 300 K under dc fields ranging from 0 to 7 T. Ac magnetic susceptibility data collected using the MPMS instrument was obtained using a 6 Oe switching field; data from the PPMS instrument was collected using a 10 Oe switching field. All data were corrected for diamagnetic contributions of the eicosane and the individual samples using Pascal's constants (*50*).

The ac susceptibility data was fit using a generalized Debye model, which accounts for relaxation time (τ), attempt time (τ_0), isothermal susceptibility (χ_T), adiabatic susceptibility (χ_S), and the presence of a distribution of relaxation times (α) (*51*). Data for **1** collected under zero

applied field and below 7 K exhibited high frequency shoulders in χ'', and fits to the data yielded very large α values, suggesting a second, faster relaxation process might be operating at low temperatures. This second process may be related to the disordered molecules in the crystal. Data from 4 to 10 K were fit with two relaxation processes. Once the minor relaxation process moved out of frequency range of the magnetometer (0.1-1488 Hz), a one process fit was sufficient. The two fitting procedures gave only modestly different τ values for the 4 and 5 K data. The data for **3** and the applied field data for **1** were fit sufficiently well with one process. Data collected using the PPMS instrument (50-70 K, 100-10,000 Hz) gave some negative values for χ' at high frequency. Presumably this result is due to the fact that the PPMS sample consisted of less material (6.9 mg **1**, 29.0 mg eicosane) and, especially at high temperatures, exhibited a smaller paramagnetic response relative to the diamagnetic response. The negative values did not affect extraction of relaxation times, however. The method for fitting the relaxation data from 4 to 70 K is given in detail in the ESI.

Dc relaxation measurements were implemented using the hysteresis mode of the MPMS magnetometer, using small magnetizing fields such that the time to set the field was in the 10-30 second range; measurements were made every ~4 seconds. We found that the relaxation times had a small dependence on the magnetizing field for **1** and a larger dependence for **3** (Table S3.19-3.20); the times reported in the main text are averages of those times. The relaxation times were determined using a stretched exponential of the form $M_t = M_0 \exp[-(t/\tau)^n]$, where M_0 is the magnetization of the first data point measured, once the field was set, and n is a free variable (*52*).

Dc magnetization experiments were implemented by applying a field to a sample at zero magnetization and measuring the magnetization until it became constant. Relaxation times were determined using the equation $M_t = M_{sat} - (M_{sat} - M_0)\exp[-(t/\tau)^n]$, where M_{sat} is the saturation magnetization, M_0 is the magnetization of the first data point measured once the field was set, and n is a free variable. Magnetization times for **1** and **3** for each field are given in Tables S20-21; the main text reports the average of these values (16.4 and 48.2 s, respectively) and their standard deviations (0.7 and 4.7, respectively).

Variable field, FIR spectroscopy

Far-infrared spectra were recorded on a Bruker IFS 66v/s FTIR spectrometer with a globar source and a composite bolometer detector element located inside an 11 T magnet directly below the sample. Approximately 5 mg of **1** was diluted in eicosane (1:10 ratio) and pressed in the shape of a 5 mm pellet. The sample was prepared and measured under inert atmosphere. The sample was cooled to 4.2 K and irradiated with FIR light. Transmission spectra were recorded both in absence and in the presence of a magnetic field (0-11 T).

Charge density modeling

Crystals of **1** are rather air-sensitive, and thus all crystal manipulation was carried out inside of a glove box under an Ar atmosphere. A triangularly-shaped single crystal with a maximum dimension of 0.10 mm was selected, and it was mounted using cryo-protecting oil on a pre-centered glass fiber and then rapidly inserted into a cold He stream with a temperature of 20 K, to minimize any risk of air exposure and subsequent crystal decay.

The crystal was mounted on the goniometer of beamline BL02B1 at the SPring8 synchrotron in Japan. The X-ray energy was fixed to 40 keV, corresponding to a wavelength of 0.30988 Å. We

have previously experienced significant crystal decay due to radiation damage, and this high energy was chosen in an attempt to avoid this detrimental effect. As shown in Fig. S3.17, the frame scale factor, which accurately captures any crystal decay (as well as other systematic effects, such as beam intensity fluctuations), is scattered relatively close to 1.0, and importantly does not drop off systematically, indicating that there is no significant crystal decay.

The data was collected on a Fuji IP system using 36 ω-scans with a width of 5°, and an overlap of 0.5°, for a total of 180° with a scan speed of 1 min/degree. Given the high symmetry of the compound, this protocol provided a complete data set with sufficient redundancy. The diffraction data ceased to be significant already at $\sin(\theta)/\lambda = 0.9$ Å^{-1}. As we explain below, there is significant dynamic disorder in the crystal structure, which likely results in the lack of high angle data.

The diffraction data were integrated using dedicated Rigaku software RAPID AUTO v2.41, which only integrates the intensity of reflections estimated to be fully present on one frame, i.e., having been rotated fully through the Ewald sphere during one of the 5° rotations. This estimation obviously depends on the mosaicity of the crystal and the desired box size for integration. We experimented with these values in order to optimize the integration results, and those presented herein used mosaicity of 0.7° and a box size of 13×13 pixels. The raw images were scaled to accommodate the different sensitivities of the photomultiplier tubes, an effect which was uncovered in the summer of 2018.

The integration and subsequent scaling in RAPID AUTO provided a total of 43260 reflections, which were then averaged using the point group symmetry –3. This averaged data was reduced to 9008 unique reflections with an average redundancy of 4.8 and a completeness of 99.5%, using the program SORTAV. During refinement, it was noticed that ratio of F(obs) to F(calc) varied systematically, and thus we decided to include ten resolution-dependent scale factors that helped to alleviate this problem, as shown in Fig. S3.19.

These data were used to solve the crystal structure using SHELXT within the Olex2 interface. The structure solution was found to contain a minor, but clearly visible, disordered component, and the disorder is solely in the naphthalene moiety (see Fig. S3.18). The disorder is perhaps best explained as resulting from a mirror symmetry in the plane defined by C(1) (bonded to Co) and partially by Si(1) and O(1). This plane also very nearly includes C(2) (carbon bonded to O(1)). The occupation of the disordered parts is 4.8%, and including this disorder in the model leads to a significant improvement of the refinement.

Despite the significant disorder (one of the consequences of which is that some atoms in the structure are nearly overlapping, we decided to attempt multipole-based charge density modeling. The independent-atom model (IAM) structure from ShelX was exported to the program XD, which is based on the Hansen-Coppens multipole formalism. Herein, we kept the extent of disorder fixed on the values obtained from ShelX, and furthermore used isotropic thermal parameters for the disordered atoms. We did not apply multipole parameters to the disordered atoms, which were kept spherical. Given the nearly whole-molecule disorder, it is imperative to be extremely careful during the refinement procedure. Thus, we used constraints to avoid overfitting, which otherwise is a possibility in such a disordered system. The use of isotropic and spherical disordered atoms helps with this as well.

The final multipole model consists of hexadecapoles on Co and octopoles on all other non-H atoms (except the disordered atoms), while H-atoms were refined using one common monopole and bond-directed dipole. The model was reached after several refinements, in which the level of multipoles was increased by one for each step. Both neutral and ionic scattering factors were tested for Co. In the final model, a neutral scattering factor was used.

In the final refinement, the largest residuals were, as expected, near the Si and the Co atoms. The largest residuals were positive (the largest is around 1.2 $eÅ^{-3}$ and is close to the Co), and significantly larger than the most negative residual density peaks, which were around −0.55 $eÅ^{-3}$. Such large discrepancy between the positive and negative residuals may indicate that the disorder was not fully accounted for. The Co atom sits on a special position in the space group with a multiplicity of 6, and it is possible that the high residual density at this position is also a result of this high symmetry. The residual near Co does not indicate that the atom sits off-centered. However, it may be related to the disorder and perhaps it does not sit in a harmonic potential. We tried to refine anharmonic thermal parameters, but this refinement had no effect on the residual density.

The residual density distribution, interpreted using the fractal dimensionality plots as first presented by Henn and Meindl (Fig. S3.19), shows a somewhat distorted parabola, with a slight tendency to increase more toward the positive residuals. However, this increase is much smaller than expected from the significant residuals near Co and Si, and suggests that despite the disorder, the multipole model may be quantitatively useful.

It is important to note that Co sits on a −3 crystallographic position and therefore only four multipole parameters are symmetry-allowed. The most important parameter in this respect is the quadrupole along the z-axis. However, in the least squares refinement, this parameter correlates strongly with the thermal parameters, including U33, which represents the atomic vibration along the same z-direction. To avoid this correlation, we separated the refinement of multipole parameters from the refinement of atomic positions and vibrations. We first attempted a high angle refinement of the atomic vibrations and positions, but the resulting refinement of multipole parameters led to unphysical values, for instance atomic charges derived from monopole values of more than +2, and κ-parameters deviating by more than 20% from unity. Instead, we chose to use the full data set to independently refine the atomic positions and vibrations of all atoms, subsequently fixing these values and refining the multipole parameters until convergence. This approach represented the final model, from which we extracted the d-orbital population ratios. In the final model, the charge on Co was determined to be +1.3.

3.5 Acknowledgements

We thank Dr. Katie R. Meihaus for editorial assistance. **Funding:** This work was funded by NSF Grant CHE-1464841 (P.C.B., J.R.L.), Max-Planck Gesellschaft (M.A., F.N.), DNRF93 and Danscatt (E.D.-M., J.O.), and DFG SL104/5-1 (M.P., J.v.S.). **Author contributions:** Synthesis, magnetic characterization and analysis were performed by P.C.B. and J.R.L. *Ab initio* calculations and analysis were performed by M.A. and F.N. Applied-field, FIR spectra were collected and analyzed by M.P., I.C., M.O., and J.v.S. Charge density data collection and modeling were performed by E.D.-M. and J.O. **Competing interests:** The authors have no competing interests to claim. **Data and materials availability**: Crystallographic data for **1**, **2**, and $Co(C(SiMe_2OPh)_3)_2$ are freely available from the Cambridge Crystallographic Data Centre under CCDC numbers 1872361, 1872361, and 1872363, respectively. The supplementary materials include details on the fitting of magnetic relaxation data as well as computational methods.

3.6 References

(1) I. G. Rau, S. Baumann, S. Rusponi, F. Donati, S. Stepanow, L. Gragnaniello, J. Dreiser, C. Piamonteze, F. Nolting, S. Gangopadhyay, O. R. Albertini, R. M. Macfarlane, C. P. Lutz, B. A. Jones, P. Gambardella, A. J. Heinrich, H. Brune. Reaching the magnetic anisotropy limit of a 3*d* metal atom. *Science* **344**, 988 (2014).

(2) W. M. Reiff, A. M. LaPointe, E. H. Witten. Virtual Free Ion Magnetism and the Absence of Jahn-Teller Distortion in a Linear Two-Coordinate Complex of High-Spin Iron(II). *J. Am. Chem. Soc.* **126**, 10206 (2004).

(3) J. M. Zadrozny, M. Atanasov, A. M. Bryan, C.-Y. Lin, B. D. Rekken, P. P. Power, F. Neese, J. R. Long. Slow Magnetization Dynamics in a Series of Two-Coordinate Iron(II) Complexes. *Chem. Sci.* **4**, 125 (2013).

(4) J. M. Zadrozny, D. J. Xiao, M. Atanasov, G. J. Long, F. Grandjean, F. Neese, J. R. Long. Magnetic Blocking in a Linear Iron(I) Complex. *Nature Chem.* **5**, *577* (2013).

(5) D. Gatteschi, R. Sessoli, J. Villain. *Molecular Nanomagnets* (Oxford Univ. Press, 2006)

(6) J. M. Zadrozny, D. J. Xiao, M. Atanasov, G. J. Long, F. Grandjean, F. Neese, J. R. Long. Mössbauer Spectroscopy as Probe of Magnetization Dynamics in the Linear Iron(I) and Iron(II) Complexes $[Fe(C(SiMe_3)_3)_2]^{1-/0}$. *Inorg. Chem.* **52**, 13123 (2013).

(7) M. Atanasov, J. M. Zadrozny, J. R. Long, F. Neese. A Theoretical Analysis of Chemical Bonding, Vibronic Coupling, and Magnetic Anisotropy in Linear Iron(II) Complexes with Single-Molecule Magnet Behavior. *Chem. Sci.* **4**, 139 (2013).

(8) The term "spin-reversal barrier" is somewhat ambiguous in the single-molecule magnet literature. In the systems described here we define it as the separation between ground and first excited M_J (or M_S) states. Thus, "over-barrier" relaxation refers to excitation from $M_J = +J$ to $M_J = +(J - 1)$ states followed by relaxation to the $M_J = -J$ state (an Orbach mechanism). "Through-barrier" relaxation mechanisms are any that allow the system to go from $M_J = +J$ to $M_J = -J$ without excitation to the $M_J = +(J - 1)$ state.

(9) M. Atanasov, D. Aravena, E. Suturina, E. Bill, D. Maganas, F. Neese. First principles approach to the electronic structure, magnetic anisotropy and spin relaxation in mononuclear 3d-transition metal single molecule magnets. *Coord. Chem. Rev.* **289**, 177 (2015).

(10) P. Zhao, Z. Brown, J. C. Fettinger, F. Grandjean, G. J. Long, P. P. Power. Synthesis and Structural Characterization of a Dimeric Cobalt(I) Homoleptic Alkyl and an Iron(II) Alkyl Halide Complex. *Organometallics.* **33**, 1917 (2014).

(11) P. P. Power. Stable Two-Coordinate, Open-Shell (d^1-d^9) Transition Metal Complexes. *Chem. Rev.* **112**, 3482 (2012).

(12) T. Viefhaus, W. Schwarz, K. Hübler, K. Locke, J. Weidlein. The Variable Reaction Behavior of Base-Free Tris(trimethylsilyl)methyl Lithium with Trihologenides of Earth-Metals and Iron. *Z. Anorg. Allg. Chem.* **627**, 715 (2001).

(13) N. H. Bruttrus, C. Eaborn, P. B. Hitchcock, J. D. Smith, A. C. Sullivan. Preparation and Crystal Structure of a Two-Coordinate Manganese Compound, Bis[(tris(trimethyl)silylmethyl)]manganese. *J. Chem. Soc., Chem. Commun.* **0**, 1380 (1985).

(14) C.-Y. Lin, J. C. Fettinger, N. F. Chilton, A. Formanuik, F. Grandjean, G. J. Long, P. P. Power. Salts of the Two-Coordinate Homoleptic Manganese(I) Dialkyl Anion $[Mn(C(SiMe_3)_3)_2]^-$ with Quenched Orbital Angular Momentum. *Chem. Commun.* **51**, 13275 (2015).

(15) X.-N. Yao, J.-Z. Du, Y.-Q. Zhang, X.-B. Leng, M.-W. Yang, S.-D. Jiang, Z.-X. Wang, Z.-W. Ouyang, L. Deng, B.-W. Wang, S. Gao. Two-Coordinate Co(II) Imido Complexes as Outstanding Single-Molecule Magnets. *J. Am. Chem. Soc.* **139**, 373 (2017).
(16) P. E. Kazin, M. A. Zykin, L. A. Trusov, A. A. Eliseev, O. V. Magdsyuk, R. E. Dinnebier, R. K. Kremer, C. Felser, M. Jansen. A Co-based single-molecule magnet confined in a barium phosphate apatite matrix with a high energy barrier for magnetization relaxation. *Chem. Commun.* **53**, *5416* (2017).
(17) H. Li, A. J. A. Aquino, D. B. Cordes, F. Hung-Low, W. L. Hase, C. Krempner. A Zwitterionic Carbanion Frustrated by Boranes – Dihydrogen Cleavage with Weak Lewis Acids via an "Inverse" Frustrated Lewis Pair Approach. *J. Am. Chem. Soc.* **135**, 16066 (2013).
(18) S. S. Al-Juaid, C. Eaborn, A. Habtemariam, P. B. Hitchcock, J. D. Smith, K. Tavakkoli, A. D. Webb. The Preparation and Crystal Structures of the Compounds $(Ph_2MeSi)_3CMCl$ (M = Zn, Cd, or Hg). *J. Organomet. Chem.* **462**, 45 (1993).
(19) S. S. Al-Juaid, C. Eaborn, S. El-Hamruni, A. Farook, P. B. Hitchcock, M. Hopman, J. D. Smith, W. Clegg, K. Izon, P. O'Shaughnessy. Tris(triorganosilyl)methyl Derivatives of Potassium and Lithium Bearing Dimethylamino or Methoxy Substituents at Silicon. Crystal Structures of $KC(SiMe_3)_2(SiMe_2NMe_2)$, $KC(SiMe_2NMe_2)_3$ and $[LiC(SiMe_3)(SiMe_2OMe)_2]_2$. *J. Chem. Soc., Dalton Trans.* 3267 (1999).
(20) T. Viefhaus, W. Schwarz, K. Hübler, K. Locke, J. Weidlein. Das unterschiedliche Reaktionsverhalten von basefreiem Tris(trimethylsilyl)methyl-Lithium gegenüber den Trihalogeniden der Erdmetalle und des Eisens. *Z. Anorg. Alla. Chem.* **627**, *715* (2001).
(21) M. Westerhausen, B. Rademacher. Trimethylsilyl-substituierte Derivate des Dimethylzinks — Synthese, spektroskopische Charakterisierung und Struktur. *J. Organomet. Chem.* **421**, 175 (1991).
(22) M. Nishio. The CH/π hydrogen bond in chemistry. Conformation, supramolecules, optical resolution and interactions involving carbohydrates. *Phys. Chem. Chem. Phys.* **13**, 13873 (2011).
(23) C.-Y. Lin, J.-D. Guo, J. C. Fettinger, S. Nagase, F. Grandjean, G. J. Long, N. F. Chilton, P. P. Power. Dispersion Force Stabilized Two-Coordinate Transition Metal–Amido Complexes of the −N(SiMe$_3$)Dipp (Dipp = C_6H_3-2,6-Pr^i_2) Ligand: Structural, Spectroscopic, Magnetic, and Computational Studies. *Inorg. Chem.* **52**, 13593 (2013).
(24) A. J. Wallace, B. E. Williamson, D. L. Crittenden. CASSCF-based explicit ligand field models clarify the ground state electronic structures of transition metal phthalocyanines (MPc; M = Mn, Fe, Co, Ni, Cu, Zn). *Can. J. Chem.* **94**, 1163, (2016).
(25) R. F. W. Bader. *Atoms in Molecules: A Quantum Theory*. (Clarendon Press, 1990).
(26) R. Marx, F. Moro, L. Ungur, M. Waters, S. D. Jiang, M. Orlita, J. Taylor, W. Frey, L. F. Chibotaru, J. van Slageren. Spectrocsopic Determination of Crystal Field Splittings in Lanthanide Double Deckers. *Chem. Sci.* **5**, 3287 (2014).
(27) Y. Rechkemmer, F. D. Breitgoff, M. van der Meer, M. Atanasov, M. Hakl, M. Orlita, P. Neugebauer, F. Neese, B. Sarkar, J. van Slageren. A Four-Coordinate Cobalt(II) Single-Ion Magnet with Coercivity and a Very High Energy Barrier. *Nature Commun.* **7**, 10467 (2016).
(28) D. Gatteschi, R. Sessoli. Quantum Tunneling of Magnetization and Related Phenomena in Molecular Materials. *Angew. Chem. Int. Ed.* **42**, *268* (2003).
(29) K. N. Shrivastava. Theory of Spin-Lattice Relaxation. *Phys. Stat. Sol. B.* **117**, 437 (1983).

(30) R. Orbach. Spin-Lattice Relaxation in Rare-Earth Salts. *Proc. R. Chem. Soc. A.* **264**, 458 (1961).
(31) A. Lunghi, F. Totti, R. Sessoli, S. Sanvito. The role of anharmonic phonons in under-barrier spin relaxation of single-molecule magnets. *Nature Commun.* **8**, 14620 (2017).
(32) A. Lunghi, F. Totti, S. Sanvito, R. Sessoli. Intra-molecular Origin of the Spin-Phonon Coupling in Slow-Relaxing Molecular Magnets. *Chem. Sci.* **8**, 6051 (2017).
(33) S.-D. Jiang, B.-W. Wang, G. Su, Z.-M. Wang, S. Gao. A Mononuclear Dysprosium Complex Featuring Single-Molecule Magnet Behavior. *Angew. Chem. Int. Ed* .**49**, 7448 (2010).
(34) H. A. Kramers. A General Thoery of Paramagnetic Rotation in Crystals. *Proc. R. Acad. Sci. Amsterdam* **33**, 959 (1930).
(35) M. Gonidec, E. S. Davies, J. McMaster, D. B. Amabilino, J. Veciana. Probing the Magnetic Properties of Three Interconvertible Redox States of a Single-Molecule Magnet with Magnetic Circular Dichroism Spectroscopy. *J. Am. Chem. Soc.* **132**, 1756 (2010).
(36) L. Margheriti, D. Chiappe, M. Mannini, P.-E. Car, P. Sainctavit, M.-A. Arrio, F. B. de Mongeot, J. C. Cezar, F. M. Piras, A. Magnani, E. Otero, A. Caneschi, R. Sessoli. X-Ray Detected Magnetic Hysteresis of Thermally Evaporated Terbium Double-Decker Oriented Films. *Adv. Mater.* **22**, 5488 (2010).
(37) M. Gonidec, R. Biagi, V. Corradini, F. Moro, V. De Renzi, U. del Pennino, D. Summa, L. Muccioli, C. Zannoni, D. B. Amabilino, J. Veciana. *J. Am. Chem. Soc.* **133**, 6603 (2011).
(38) D. Klar, A. Candini, L. Joly, S. Klyatskaya, B. Krumme, P. Ohresser, J.-P. Kappler, M. Ruben, H. Wende. Hysteretic Behavior in a Vacuum Deposited Submonolayer of Single Ion Magnets. *Dalton Trans.* **43**, 10686 (2014).
(39) M. Mannini, F. Bertani, C. Tudisco, L. Malavolti, L. Poggini, K. Misztal, D. Menozzi, A. Motta, E. Otero, P. Ohresser, P. Sainctavit, G. G. Condorelli, E. Dalcanale, R. Sessoli. Magnetic Behavior of $TbPc_2$ Single-Molecule Magnets Chemically Grafted on Silicon Surface. *Nat. Commun.* **5**, 4582 (2014).
(40) J. Dreiser, C. Wäckerlin, M. E. Ali, C. Piamonteze, F. Donati, A. Singha, K. S. Pedersen, S. Rusponi, J. Bendix, P. M. Oppeneer, T. A. Jung, H. Brune. Exchange Interaction of Strongly Anisotropic Tripodal Erbium Single-Ion Magnets with Metallic Surfaces. *ACS Nano* **8**, 4662 (2014).
(41) C. Wäckerlin, F. Donati, A. Singha, R. Baltic, S. Rusponi, K. Diller, F. Patthey, M. Pivetta, Y. Lan, S. Klyatskaya, M. Ruben, H. Brune, J. Dreiser. Giant Hysteresis of Single-Molecule Magnets Adsorbed on a Nonmagnetic Insulator. *Adv. Mater.* **28**, 5195 (2016).
(42) M. Getzlaff. *Fundamentals of Magnetism.* (Springer-Verlag Berlin Heidelberg, 2008)
(43) A. Jesche, R. W. MacCallum, S. Thimmaiah, J. L. Jacobs, V. Taufour, A. Kreyssig, R. S. Houk, S. L. Bud'ko, P. C. Canfield. Giant magnetic anisotropy and tunneling of the magnetization in $Li_2(Li_{1-x}Fe_x)N$. *Nature Commun*. **5**, 3333 (2014).
(44) C. J. Schaverier, A. G. Orpen. Chemistry of (Octaethylporphyrinato)lutetium and -yttrium Complexes: Synthesis and Reactivity of (OEP)MX Derviatives and the Selective Activation of O_2 By (OEP)Y(.mu.-Me)$_2$AlMe$_2$. *Inorg. Chem.* **30**, 4968 (1991).
(45) K. D. Safa, S. Tofangdarzadeh, H. H. Ayendadeh. Reactions of tris(dimethylsilyl)methane and polymers containing Si-H groups with various hydroxy compounds under aerobic and mild conditions. *Heteroatom Chem.* **19**, 365 (2008).
(46) G. M. Sheldrick. SADABS, version 2.03, Bruker Analytical X-Ray Systems, Inc. Madison, WI, 2000.

(47) G. M. Sheldrick. SHELXT – Integrated Space-Group and Crystal-Structure Determination. *Acta Cryst. A* **71**, 3 (2015).
(48) G. M. Sheldrick. Crystal Structure Refinement with SHELXL. *Acta Cryst. C* **71**, 112 (2008).
(49) O. V. Dolomanov, L. J. Bourhis, R. J. Gildea, J. A. K. Howard, H. Puschmann. OLEX2: A Complete Structure Solution, Refinement and Analysis Program. *J. Appl. Crystallogr.* **42**, 339 (2009).
(50) G. A. Bain, J. F. Berry. Diamagnetic Corrections and Pascal's Constants. *J. Chem. Ed.* **85**, 532 (2008).
(51) K. S. Cole, R. H. Cole. Dispersion and Absorption in Dielectrics I. Alternating Current Characteristics. *J. Chem. Phys.* **9**, 341 (1941).
(52) C. Sangregorio, T. Ohm, C. Paulsen, R. Sessoli, D. Gatteschi. Quantum Tunneling of the Magnetization in an Iron Cluster Nanomagnet. *Phys. Rev. Lett.* **78**, 4645 (1997).
(53) P.-Å. Malmqvist, B.O. Roos. The CASSCF State Interaction Method, *Chem. Phys. Lett.* **155**, 189 (1989).
(54) K. Wolinski, P. Pulay. Generalized Möller–Plesset perturbation theory: Second order results for two-configuration, open-shell excited singlet, and doublet wave functions. *J. Chem. Phys.* **90** 3647 (1989).
(55) K. Andersson, P.A. Malmqvist, B.O. Roos, A.J. Sadlej, K. Wolinski, Second-order perturbation theory with a CASSCF reference function. *J. Phys. Chem.* **94**, 5483 (1990).
(56) K. Andersson, P.Å. Malmqvist, B.O. Roos, Second-order perturbation theory with a complete active space self-consistent field reference function. *J. Chem. Phys.* **96**, 1218 (1992).
(57) B.O. Roos, P.-A. Malmqvist. Relativistic quantum chemistry: the multiconfigurational approach. *Phys. Chem. Chem. Phys.* **6**, 2919 (2004).
(58) B. Roos, M. Fülscher, P.-Å. Malmqvist, M. Merchán, L. Serrano-Andrés. Theoretical Studies of the Electronic Spectra of Organic Molecules, in: S. Langhoff (Ed.) Quantum Mechanical Electronic Structure Calculations with Chemical Accuracy, Springer Netherlands, pp. 357-438 (1995).
(59) C. Angeli, R. Cimiraglia, S. Evangelisti, T. Leininger, J.-P. Malrieu. Introduction of n-electron valence states for multireference perturbation theory. *J. Chem. Phys.* **114**, 10252 (2001).
(60) C. Angeli, R. Cimiraglia, J.-P. Malrieu, N-electron valence state perturbation theory: A fast implementation of the strongly contracted variant. *Chem. Phys. Lett.* **350**, 297 (2001).
(61) C. Angeli, R. Cimiraglia, J.-P. Malrieu. N-electron valence state perturbation theory: A spinless formulation and an efficient implementation of the strongly contracted and of the partially contracted variants. *J. Chem. Phys*. **117**, 9138 (2002).
(62) C. Angeli, B. Bories, A. Cavallini, R. Cimiraglia. Third-order multireference perturbation theory: The n-electron valence state perturbation-theory approach. *J. Chem. Phys*. **124**, 054108 (2006).
(63) F. Neese. The ORCA program system. *Comput. Mol. Sci*. **2**, 73 (2012).
(64) ORCA - An ab initio, DFT and semiempirical SCF-MO package - Version 4.0, Design and Scientific Directorship: F. Neese, Technical Directorship: F. Wennmohs, Max-Planck-Institute for Chemical Energy Conversion Stiftstr. 34-36, 45470 Mülheim a. d. Ruhr, Germany, tccec@mpi-mail.mpg.de, With contributions from: D. Aravena, M. Atanasov, U. Becker, D. Bykov, D. Datta, A. Kumar Dutta, D. Ganyushin, Y. Guo, A. Hansen, L. Huntington, R. Izsak, C. Kollmar, S. Kossmann, M. Krupicka, D. Lenk, D. G. Liakos, D.

Manganas, D. A. Pantazis, T. Petrenko, P. Pinski, C. Reimann, M. Retegan, C. Riplinger, T. Risthaus, M. Roemelt, M. Saitow, B. Sandhöfer, I. Schapiro, K. Sivalingam, G. Stoychev, B. Wezisla; And contributions from our collaborators: M. Kallay, S. Grimme, E. Valeev, G. Chan, J. Pittner; Additional contributions to the manual from: G. Bistoni, W. Schneider.
(65) F. Neese. Efficient and accurate approximations to the molecular spin-orbit coupling operator and their use in molecular g-tensor calculations. *J. Chem. Phys.* **2005**, *122*, 34107.
(66) D. Ganyushin, F. Neese. First-Principle Calculations of Zero-Field Splitting Parameters. *J. Chem. Phys.* **2006**, *125*, 024103.
(67) M. Atanasov, D. Ganyushin, K. Sivalingam, F. Neese. A Modern First-Principles View on Ligand Field Theory Through the Eyes of Correlated Multireference Wavefunctions. *Structure and Bonding*. **143**, 149 (2012).
(68) S. K. Singh, J. Eng, M. Atanasov and F. Neese. Covalency and chemical bonding in transition metal complexes: An ab initio based ligand field perspective. *Coord. Chen. Rev.* **344**, 2 (2017).
(69) J. R. Burdett. *Molecular Shapes: Theoretical Models of Inorganic Stereochemistry* (John Wiley & Sons Inc, 1980).

Chapter 3 Supporting Information

S3.1 Magnetic Relaxation Fitting Methods

Relaxation data from the dc relaxation experiments for **1** and **3** at 1.8 K were fit according to

$$\tau^{-1} = \frac{A_1}{1 + A_2 H^2} + BH^4T$$

where the first and second terms represent tunneling and direct relaxation pathways, respectively. For **1**: $A_1 = 30.$ s^{-1} $A_2 = 2.9\times10^5$ T^{-2}, and $B = 0.64$ s^{-1} K^{-1} T^{-4}, and for **3**: $A_1 = 1.2\times10^{-2}$ s^{-1} $A_2 = 6.6\times10^2$ T^{-2}, and $B = 0.75$ s^{-1} K^{-1} T^{-4}.

To fit the relaxation data from ac susceptometry we derived an expression based on the work of Lunghi et al. (*1*,*2*). The expression describing relaxation in Ref. *3* make the assumption $U > \hbar\omega_\alpha >> k_BT$, where U is the spin-relaxation barrier (450 cm^{-1} in this case) and $\hbar\omega_\alpha$ is the energy of the α-th phonon. As **1** shows slow magnetic relaxation at high temperatures we do not make this assumption. Using the formalism described in Supplementary Note 2 in Ref. *1* we have derived the more general equation

$$\tau^{-1} = \sum_\alpha \left(\frac{V_\alpha^2}{\hbar} \frac{\Delta_\alpha (2n_\alpha + 1)}{[\Delta_\alpha^2 + (\hbar\omega_\alpha)^2]} \right) \quad \text{(S1)}$$

with

$$\Delta_\alpha^2 = \frac{(\hbar\omega_\alpha)^2 \exp(ß\hbar\omega_\alpha)}{(\exp(ß\hbar\omega_\alpha) - 1)^2} \quad \text{(S2)}$$

and

$$n_\alpha = \frac{1}{\exp(ß\hbar\omega_\alpha) - 1} \quad \text{(S3)}$$

where n_α is the phonon occupation number and $\beta = 1/k_BT$. Eq. S2 defines the phonon line-shape. The energy Δ_α describes the amplitude of the Gaussian probability distribution of the phonon α mode's energy fluctuations.

The relaxation process described by Eq. S1 is one in which the ground Kramers doublets are directly coupled through specific phonon modes. The energies of the available phonon modes are given in the FIR spectra in Figure 3. We combine Eq. S1 with the equation for Orbach relaxation and a tunneling relaxation time to obtain the expression

$$\tau^{-1} = \tau_{tunnel}^{-1} + \sum_\alpha \left(\frac{V_\alpha^2}{\hbar} \frac{\Delta_\alpha (2n_\alpha + 1)}{[\Delta_\alpha^2 + (\hbar\omega_\alpha)^2]} \right) + \tau_0^{-1} \exp(-U/k_BT) \quad \text{(S4)}$$

as described in the main text. Energies of phonons that may facilitate relaxation are taken from peaks in the FIR spectrum and $U = 450$ cm^{-1} based on the applied field FIR spectra. The possible fit parameters are the tunneling relaxation time, spin-phonon coupling terms, and τ_0. The applied field data are fit sufficiently well with two phonon mediated processes and the high temperature Orbach relaxation process, while the zero-field relaxation data required an additional phonon mediate process as well as a tunneling relaxation process. The parameters for the Orbach relaxation process as well as the two higher energy phonon mediated processes are the same for both applied

and zero-field data. Fits were obtained by minimizing the sum of squared errors in the plot of ln τ vs. 1/T, not τ vs. 1/T, so that the low-temperature, large τ, data is not given extra weight in the fitting. As such, the standard errors of the estimate (σ_{EST}) are directly applicable to the ln τ vs. 1/T plots.

Though we did not fit relaxation data for **3**, the parameters used for the applied field data of **1** provide a reasonable fit. The need to include a tunneling process for the zero-field data for **1** is expected, however the additional phonon mediated process is surprising, as there is no field dependence in Eq. S1. Values of parameters used in Eq. S4 are given in Table S3. The contribution from each relaxation process is illustrated in Figures S11 and S12.

S3.2 Computational Methods and Details

Ab initio calculations based on the reported X-Ray geometry were used to calculate the electronic energy levels of **1**. The results are given in Tables S4 and S5 and are discussed in the main text. Correlated calculations were carried out using Complete Active Space Self Consistent Field (CASSCF) (*4*-9) in combination with N-Electron Valence Perturbation Theory to second order (NEVPT2) (*10*-*13*) as implemented in the ORCA package (*14*,*15*). The d^7 configuration of Co(II) gives rise to ten $S = {}^3/_2$ and forty $S = {}^1/_2$ electronic multiplets. Non-relativistic CASSCF energy levels and wave functions have been computed averaging over the electron densities of all considered states and taking an active space with 7 electrons distributed over the 5 3d-MOs (CAS(7,5)). Spin-orbit coupling (SOC) was taken into account using a mean-field spin-orbit coupling operator (*16*,*17*). Mixing of non-relativistic CI eigenfunctions and splitting of the corresponding eigenvalues are accounted for by Quasi Degenerate Perturbation Theory (QDPT) (*17*).

Ab initio Ligand Field Theory analysis

To extract ligand field orbital energies and ligand field parameters from the correlated calculations we applied Ab Initio Ligand Field Theory (*18*) that is implemented and generally available for users starting with ORCA 4.0 program release and later program updates (see Ref. *19* for a recent review on the method). With Ab Initio Ligand Field Theory, we have extracted ligand field parameters (the 5x5 ligand field matrix V(NEVPT2)), the Racah parameters of interelectronic repulsion (*B* and *C*), and the spin-orbit coupling parameter (ζ) from a converged CASSCF wave function, making it possible to analyze the term energy diagrams in terms of underlying ligand field concepts. The CASSCF/NEVPT2 calculation for **1** at the reported X-ray geometry gives the matrix of Eq. S1 for V(NEVPT2) and $B = 1006$, $C = 4010$, and $\zeta = 518$ cm^{-1}. They have been extracted using all 10 $S = {}^3/_2$ and 40 $S = {}^1/_2$ states from the d^7 configuration of Co(II) in the complex. These parameters reflect in a condensed way what the *ab initio* multireference method is able to give. The energies of electronic states computed using the given set of parameters differ from the NEVPT2 results of the same states, with standard deviations of 168 cm^{-1} for the $S = {}^3/_2$ states and 864 cm^{-1} for the $S = {}^1/_2$ states. A rather small standard deviation between the *ab initio* and LF computed matrix elements (σ=115 cm^{-1}) demonstrates the consistency of this fit.

$$V(NEVPT2) = \begin{array}{c} \begin{matrix} |d_{xy}> & |d_{yz}> & |d_{z2}> & |d_{xz}> & |d_{x2-y2}> \end{matrix} \\ \begin{bmatrix} -3700 & 56 & -1 & 55 & 0 \\ 56 & -792 & 1 & 0 & 66 \\ -1 & 1 & 1937 & 2 & -7 \\ 55 & 0 & 2 & -791 & 59 \\ 0 & 66 & -7 & 59 & -3699 \end{bmatrix} \end{array} \qquad \text{(S5)}$$

Diagonalization of the matrix of eq. S5 leads to orbital energies at 0, 0, 2913, 2913, 3423 and 5639 cm^{-1} (Table S6) and thus reflect an axial ligand field with the doubly degenerate (d_{x2-y2}, d_{xy}); (d_{xz},d_{yz}) pairs of 3d-MOs with δ and π-antibonding and the non-degenerate 3d-MO d_{z2} with σ symmetry. It follows from the small off-diagonal elements of V(NEVPT2) that trigonal components of the ligand field are negligible. Therefore, in analysis hereafter we will approximate the real S_6 symmetry of the complex using the linear $C_{\infty v}$ pseudosymmetry. We will further denote both orbitals (d_{x2-y2}, d_{xy}); (d_{xz},d_{yz}) and d_{z2} and their energies by δ,π and σ, respectively. For such a ligand field the d^7 configuration of Co(II) spans $S = {}^3/_2$ spectroscopic terms described by the Eqs. S6-S9:

$$^4\Sigma^-: \begin{array}{c} \begin{matrix} \delta^4\pi^2\sigma^1 & \delta^2\pi^4\sigma^1 \end{matrix} \\ \begin{bmatrix} 12B-\pi & 6B \\ 6B & 3B+\pi \end{bmatrix} \end{array} \qquad \text{(S6)}$$

$$^4\Phi \;\; \delta^3\pi^3\sigma^1: \;\; 0 \qquad \text{(S7)}$$

$$^4\Delta \;\; \delta^3\pi^2\sigma^2: \;\; \sigma\text{-}\pi \qquad \text{(S8)}$$

$$^4\Pi: \begin{array}{c} \begin{matrix} \delta^2\pi^3\sigma^2 & \delta^3\pi^3\sigma^1 \end{matrix} \\ \begin{bmatrix} 9B+\sigma & 3\sqrt{6}B \\ 3\sqrt{6}B & 6B \end{bmatrix} \end{array} \qquad \text{(S9)}$$

The ^4F and ^4P manifold of the Co(II) free ion experiences one-electron (δ, π, σ) and two-electron perturbations (*B*). Note that *C* does not contribute to Eqs. S6-S9. Employing the values of these parameters resulting from the CASSCF/NEVPT2 calculations (*vide supra*) we derive a set of matrix elements with contributions from the ligand field only, as well as diagonal and off-diagonal contributions from *B* (Table S7). Inspection of these values shows, as expected, that ligand field alone stabilizes $^4\Sigma^-$ below the $^4\Phi$ by −2914 cm^{-1}. Diagonal terms of the interelectronic repulsion lift $^4\Sigma^-$ above $^4\Phi$ by as much as 12,072 cm^{-1}, leading to a net stabilization (including LF and diagonal interelectron repulsion terms) of $^4\Phi$ against $^4\Sigma^-$ by 12,072−2914 = 9158 cm^{-1}. Finally, the off-diagonal term (6B) reduces the energy of $^4\Sigma^-$ to 1297 cm^{-1} above $^4\Phi$. It also follows that in difference to lowest non-relativistic excited state $^4\Sigma^-$, the $^4\Phi$ ground state is of single reference character. The results from Table S7 have been used to construct Figure 2B of the manuscript. Finally, it is interesting to compare the lowest $M_J = {}^9/_2$ to $M_J = {}^7/_2$ excitation energy

resulting from the approximate formula $(L/2S)\zeta$ = 515 cm^{-1} with the corresponding CASSCF/NEVPT2 result (476 cm^{-1}). The comparison shows quantitatively the extent of correctness of expressions of the type $(L/2S)\zeta$ broadly used in literature, here yielding an error of 8%.

The perturbation of the ^4F ground state of Co(II) by the ligands in **1** induces changes in the total energy with contribution from: i) destabilization of the d^7 configuration due to metal-ligand repulsive interactions (crystal field destabilization energy, CFDE); ii) stabilization due to the uneven occupation of the 3d-MOs split by the lowering of the spherical symmetry in the complex (crystal field stabilization energy, CFSE) and iii) atom-pairwise (dispersion) non-bonding interaction. For a complex with n electrons, the CFDE and CFSE energy terms are given by:

$$CFDE = \frac{n}{5}\sum_{i=1}^{5}\varepsilon_i \qquad \text{(S10)}$$

$$CFSE = \sum_{i=1}^{5} n_i\varepsilon_i - \frac{n}{5}\sum_{i=1}^{5}\varepsilon_i \qquad \text{(S11)}$$

where n is the 3d-MO occupation number and ε_i is the 3d-MO energy. Yet another measure of the net electronic stabilization put forward by J.R. Burdett (*20*) is the molecular orbital stabilization energy (MOSE), which describes the energy change due to the occupied d orbitals on forming the complex plus the stabilization due to their doubly occupied ligand centered orbital counterparts. If one assumes that energy changes due to bonding and antibonding are of the same magnitude (but are different in sign), this contribution to the total energy equals just the sum of the hole occupation number h_i times the corresponding orbital energy ε_i (Eq. S12).

$$MOSE = \sum_{i=1}^{5} h_i\varepsilon_i \qquad \text{(S12)}$$

Values for LFDE, LFSE, and MOSE for the $^4\Phi$ ground state electronic configuration $(d_{x^2-y^2}, d_{xy})^3(d_{xz}, d_{yz})^3(d_{z^2})^1$ for complex **1** are listed in Table S10. For the sake of comparison, we also include the corresponding parameters for the analogous Fe(II) and Fe(I) complexes with $^5\Delta$ and $^4\Delta$ electronic ground states with dominating electronic configurations $(d_{x^2-y^2}, d_{xy})^3(d_{xz}, d_{yz})^2(d_{z^2})^1$ and $(d_{z^2})^2(d_{x^2-y^2}, d_{xy})^3(d_{xz}, d_{yz})^2$ respectively, based on previously published calculations (*21*,*22*)

Inclusion of carbon orbitals in active space

A benchmarking of the extension of the active space with these orbitals and the effect of the number of states (roots) is the first step of each computational study. This benchmarking was done on a truncated complex where the six naphthol substituents were replaced by six methyl groups. While important for the stabilization of **1** such a replacement does not affect the electronic states, neither the non-relativistic one nor the magnetic sublevels (see Table S11). As documented in Table 3, there are almost no effect on the magnetic sublevels when going from a CAS(7,5) active space to a CAS(9,6) when the two bonding electrons are explicitly correlated with the other seven 3d electrons on Co(II). As shown in Table S12, there are minor changes of the energies of the 3d-MOs when extending the active space. Given the weakness of the ligand field such insensitivity of the results on the active space is not surprising.

Absorption Spectra Simulation

The field dependence of the intensity of the $M_J = \pm^9/_2$ to $\pm^7/_2$ magnetic dipole transitions was simulated. Restricting to the $M_J = \pm^9/_2$ $\pm^7/_2$ sublevels originating from the $^4\Phi$ non-relativistic ground state of **1**, the Hamiltonian ***H*** with contributions from spin-orbit and Zeeman terms written down in the basis $|M_J, M_L, M_S\rangle$ function taken in a standard order $|-9/2,-3,-3/2\rangle$, $|9/2,3,3/2\rangle$, $|-7/2,-3,-1/2\rangle$ and $|7/2,3,1/2\rangle$ is given by:

$$H = \begin{bmatrix} -(3/2\varsigma) - 6\beta_B B_z & 0 & (\sqrt{3}/2)\beta_B(B_x + iB_y) & 0 \\ 0 & -(3/2\varsigma) + 6\beta_B B_z & 0 & (\sqrt{3}/2)\beta_B(B_x - iB_y) \\ (\sqrt{3}/2)\beta_B(B_x - iB_y) & 0 & -(1/2\varsigma) - 4\beta_B B_z & 0 \\ 0 & (\sqrt{3}/2)\beta_B(B_x + iB_y) & 0 & -(1/2\varsigma) + 4\beta_B B_z \end{bmatrix} \quad \text{(S13)}$$

The matrix of Eq. S13 has been diagonalised for field values *B* between 0 to 11 T in steps of 1 T and *B* vector **B** components B_x, B_y, B_z using a Gauss-Legandre grid over a sphere of unit radius. This yields energies $E_{i(f)}$ in increasing order i=1,4 and energy eigenfunctions

$$|\Psi_{i(f)}\rangle = c_{i(f),1}|-9/2,-3,-3/2\rangle + c_{i(f),2}|9/2,3,3/2\rangle + c_{i(f),3}|-7/2,-3,-1/2\rangle + c_{i(f),4}|7/2,3,1/2\rangle \quad \text{(S14)}$$

with indices i(f) referring to the initial, i = 1,2 (final, f = 3,4) states. The spectral function using a magnetic dipole mechanism of intensity and a numerical integration over the three directions B_x, B_y, and B_z (assuming a powder distribution) has been evaluated employing the expression:

$$I(\hbar\omega) \propto \sum_{i=1,2} p_i \sum_{f=3,4} \left[\langle\Psi_f|\hat{S}_x|\Psi_i\rangle\langle\Psi_i|\hat{S}_x|\Psi_f\rangle + \langle\Psi_f|\hat{S}_y|\Psi_i\rangle\langle\Psi_i|\hat{S}_y|\Psi_f\rangle + \langle\Psi_f|\hat{S}_z|\Psi_i\rangle\langle\Psi_i|\hat{S}_z|\Psi_f\rangle \right] \delta(E_f - E_i - \hbar\omega) \quad \text{(S15)}$$

where p_i is initial state probability:

$$p_i = \frac{\exp(-E_i / k_B T)}{Z} \quad \text{(S16)}$$

and

$$Z = \sum_j \exp(-E_j / k_B T) \quad \text{(S17)}$$

is the statistical sum. The spectral function $\delta(E_f - E_i - \hbar\omega)$ has been approximated in terms of a sum of Gauss envelopes with full width at half maximum FWHM = 1 cm^{-1}. Computed transmission spectra are depicted in Figure S3. With increasing field, the absorption maximum shifts to higher frequencies while the band broadens. The blue computed shift is in nice agreement with the experimentally deduced one in Figure S5. The calculated spectra shown in Figure S6 look different than the experimental spectra because there are no underlying vibrational absorptions in the calculated spectra. By dividing the calculated applied field spectra by the calculated zero field spectrum the same general shape is seen as in the experimental spectrum, although the simulations slightly overestimate the amount of broadening with increasing applied fields.

Ab initio calculations on $CoOMg_5O_4$

In order to compare the electronic structure of **1** with the one deduced from differential conductance (dI/dV), X-ray absorption and XMCD spectroscopies on the Co on Mg(100) surface, we carried out calculations on a charge neutral $CoOMg_5O_4$ model cluster depicted on Figure S4. A constrained DFT geometry optimization was done keeping the geometry of Mg_5O_5 unit frozen with coordinates taken from those of the bulk MgO, while adjusting the position of the Co^{II} ad-atom bond to an oxide ligand on top of a MgO(1,0,0) surface (the optimized Co-O bond distance is 1.808 Å) . Such a choice of geometry correctly accounts for the Co-O bond and for the nearest neighbors of the O-ligand –the four counter polarizing Mg^{2+} atoms. The geometry from the output is visualized in Figure S4.

The energies of the ten quartet S=3/2 states (roots) from CASSCF/NEVPT2 calculations of $CoOMg_5O_5$ are compared with those of **1** in the Table S12 where relativistic spin-orbit sublevels originating from the $^4\Phi$ non-relativistic ground state are also included. While relativistic splitting of the lowest magnetic levels for the two complexes is very similar, higher excited states stemming from $^4\Pi(^4P)$ are definitely higher in energy for the Co-O complex. While Co-ligand interactions affecting the d_{xz},d_{yz} orbitals are similar for the two complexes (see 3d-MOs in Table 2), the position of dz2-MO is computed twice higher for the Co^{II} oxo-complex. Presumably, both covalence and electrostatics contribute to the difference. Based on these calculations we can conclude with some precaution, that the magnetic properties, in particular magnetic anisotropies of **1** and $CoOMg_5O_4$ are similar. This stems from the result the relativistic splitting of $^4\Phi(^4F)$ is governed mainly by the spin-orbit coupling with a value of the spin-orbit coupling constant which is almost the same for **1** (ζ=518 cm^{-1}) and $CoOMg_5O_5$ (ζ=517 cm^{-1}).

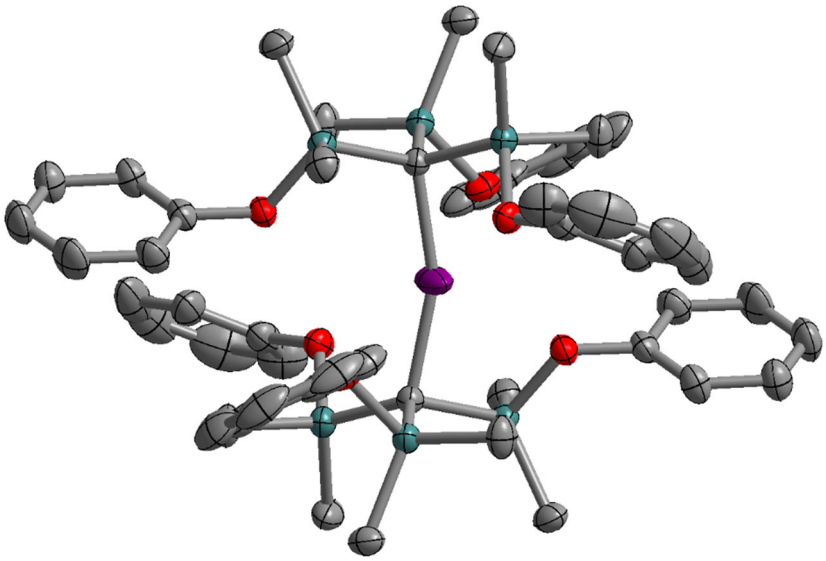

Fig. S3.1. Molecular structure of $Co(C(SiMe_2OPh)_3)_2$. Purple, gray, turquoise, and red spheres represent Co, C, Si, and O atoms, respectively. Hydrogen atoms are omitted for clarity.

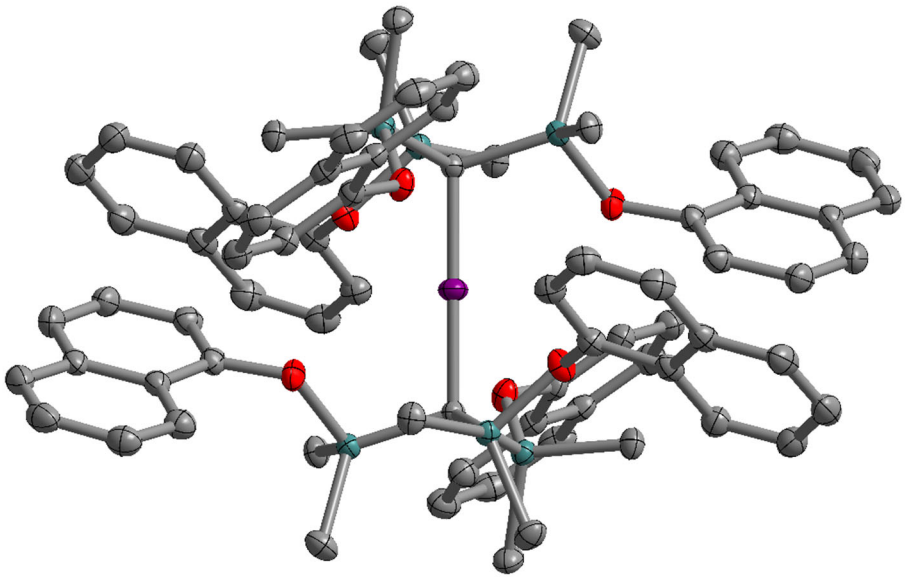

Fig. S3.2. ORTEP drawing of $Co(C(SiMe_2ONaph)_3)_2$. Purple, gray, turquoise, and red spheres represent Co, C, Si, and O atoms, respectively. Hydrogen atoms are omitted for clarity.

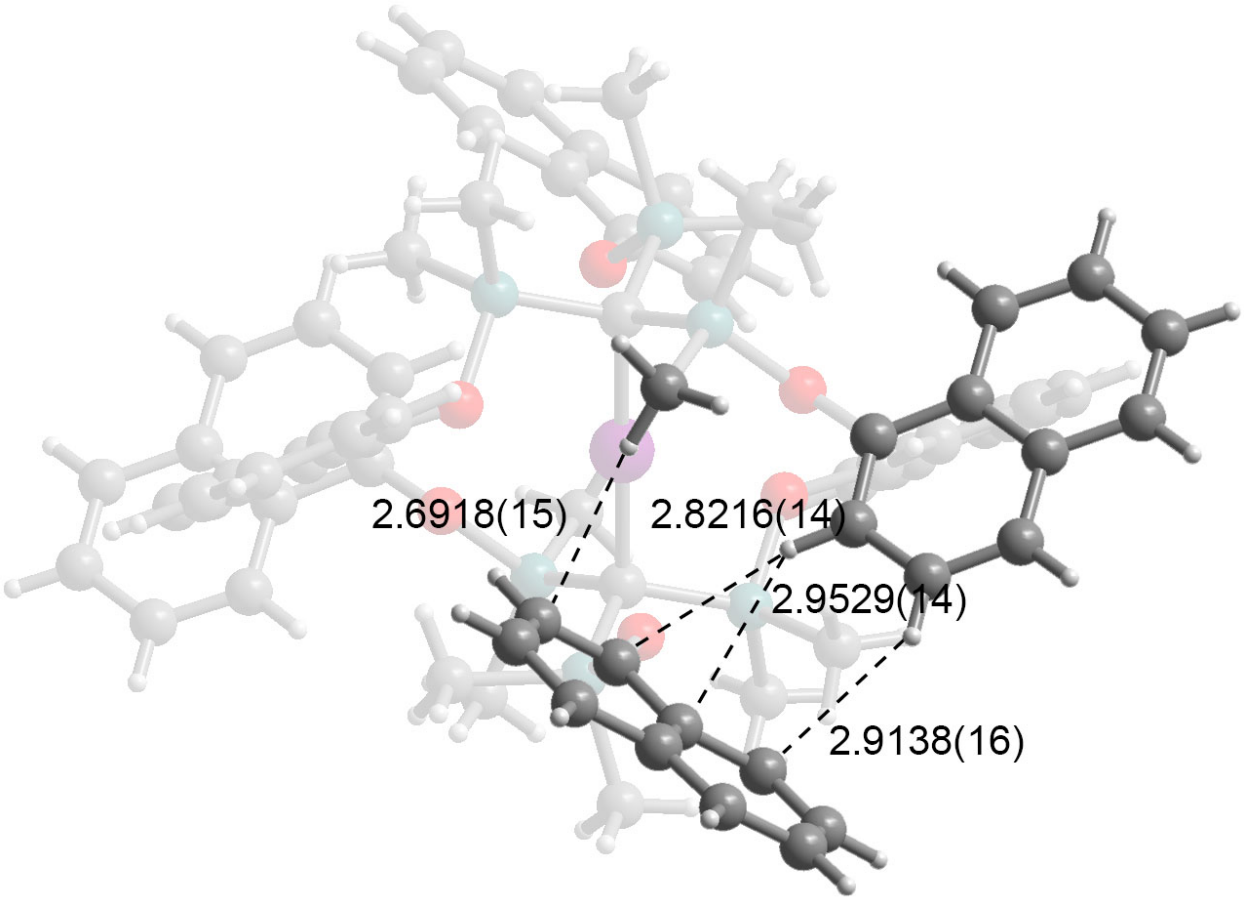

Fig. S3.3. Molecular structure of $Co(C(SiMe_2ONaph)_3)_2$, where the highlighted atoms are involved in sp^3-CH···π and sp^2-CH···π interactions. Purple, gray, turquoise, red, and light gray spheres represent Co, C, Si, O, and H atoms, respectively. Distances are given in Å.

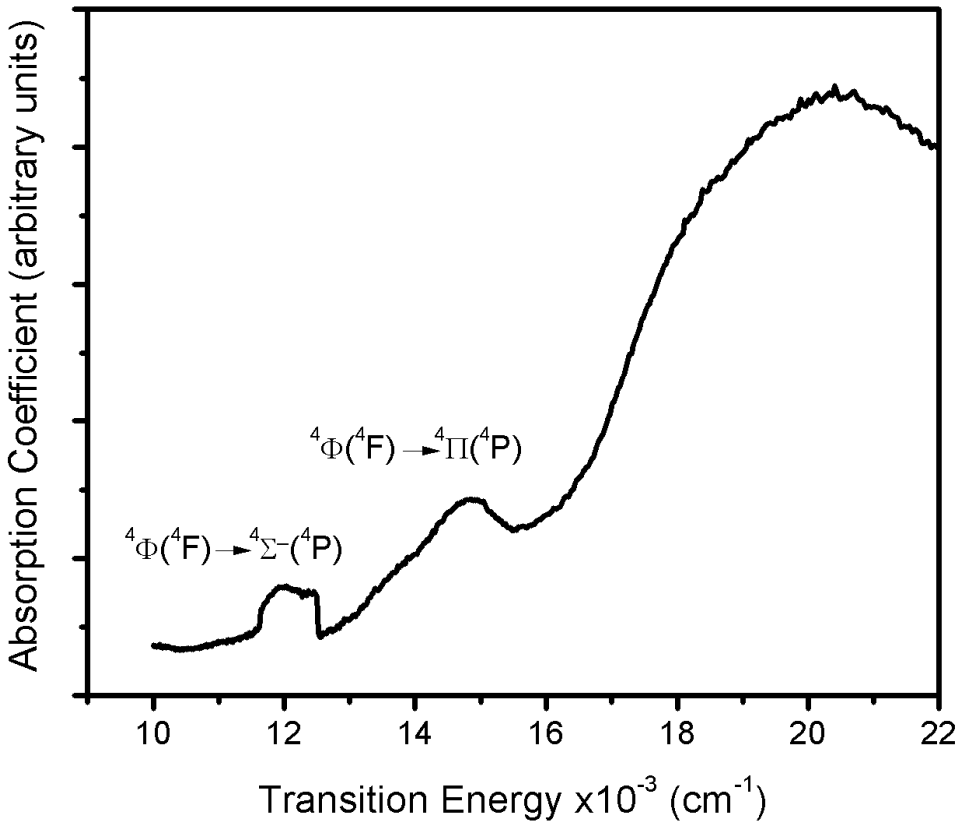

Fig. S3.4. UV-vis diffuse reflectance spectrum of **1**.

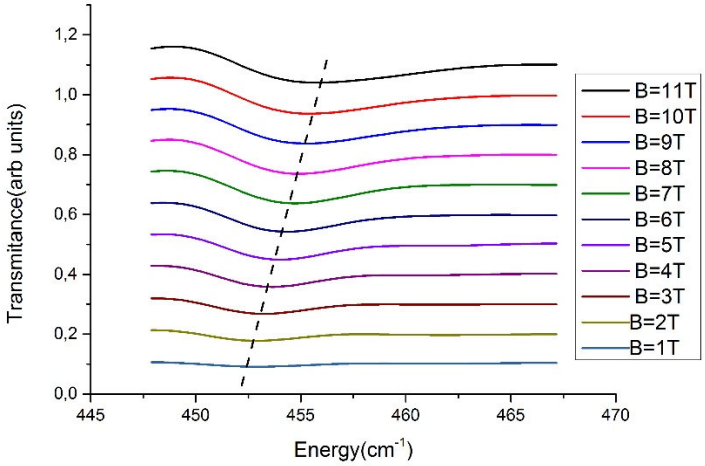

Fig. S3.5. Experimentally reported field dependencies due to the $M_J = \pm^9/_2$ to $\pm^7/_2$ magnetic dipole transition; the dominating vibrational background has been eliminated by dividing the spectrum recorded at the given field by the zero-field spectrum taken as reference.

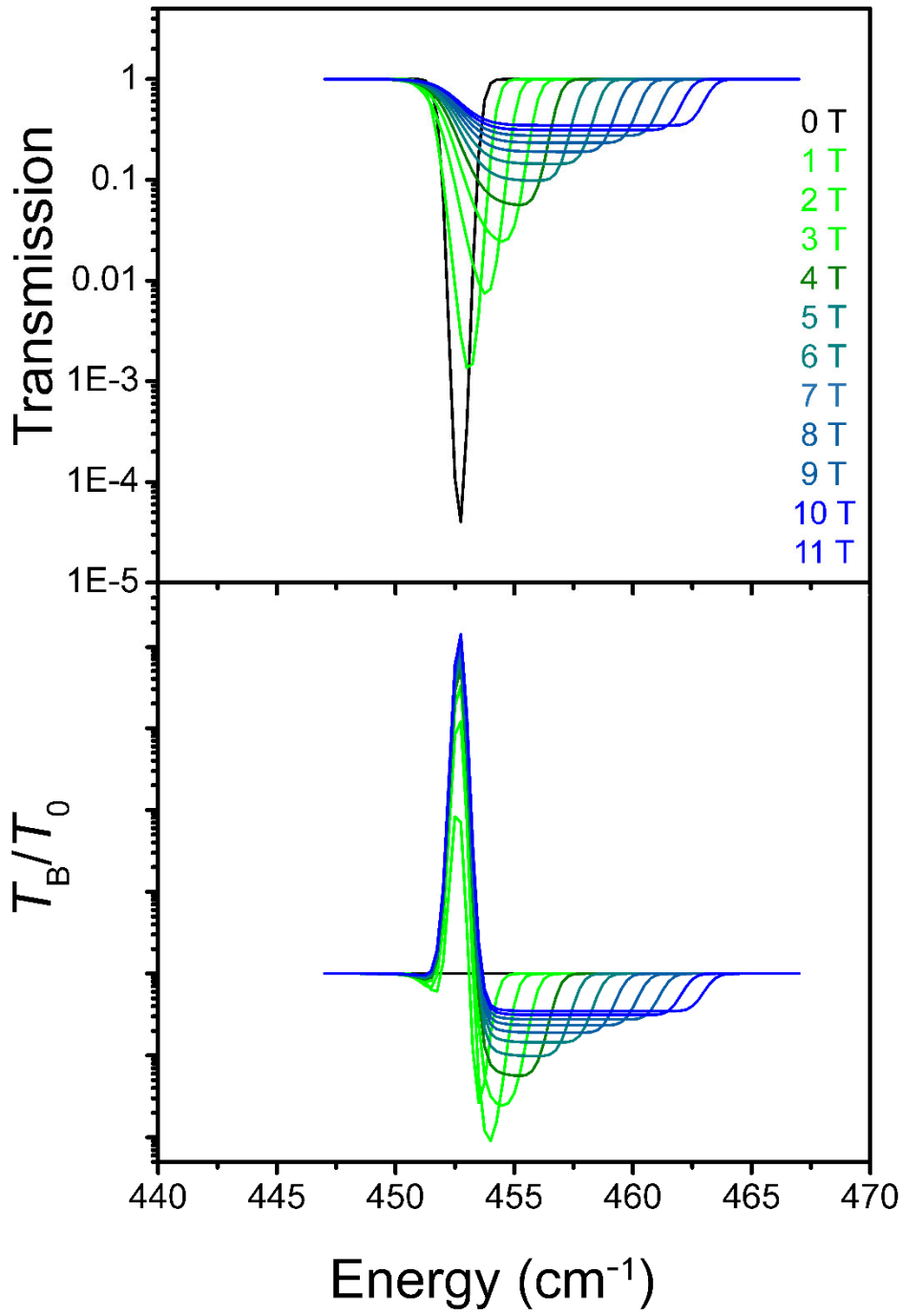

Fig. S3.6. (top) Simulated spectral shapes for $M_J = \pm^9/_2$ to $\pm^7/_2$ magnetic dipole transitions of **1**. (bottom) Normalized simulated spectral shapes for $M_J = \pm^9/_2$ to $\pm^7/_2$ magnetic dipole transitions of **1**, obtained by dividing the calculated applied field spectra by the calculated zero field spectra.

Fig. S3.7. The $CoOMg_5O_4$ complex modeling Co^{II} adatom on a Mg(1,0,0) surface. The Mg_5O_5 cage was fixed at a geometry of a bulk MgO while the position of Co(II) was adjusted using a BP86 DFT geometry optimization.

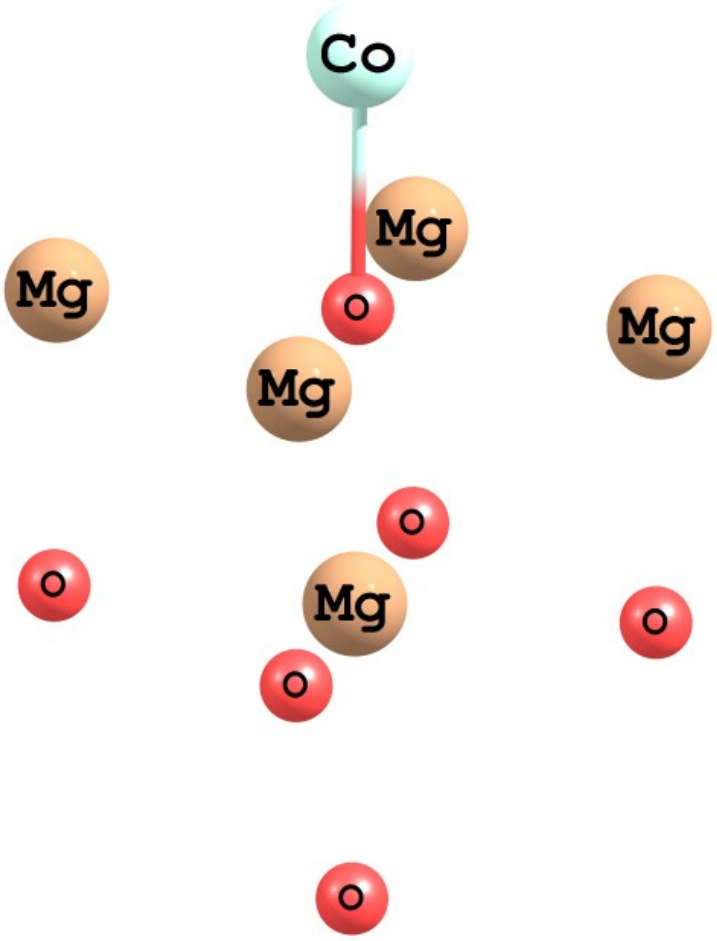

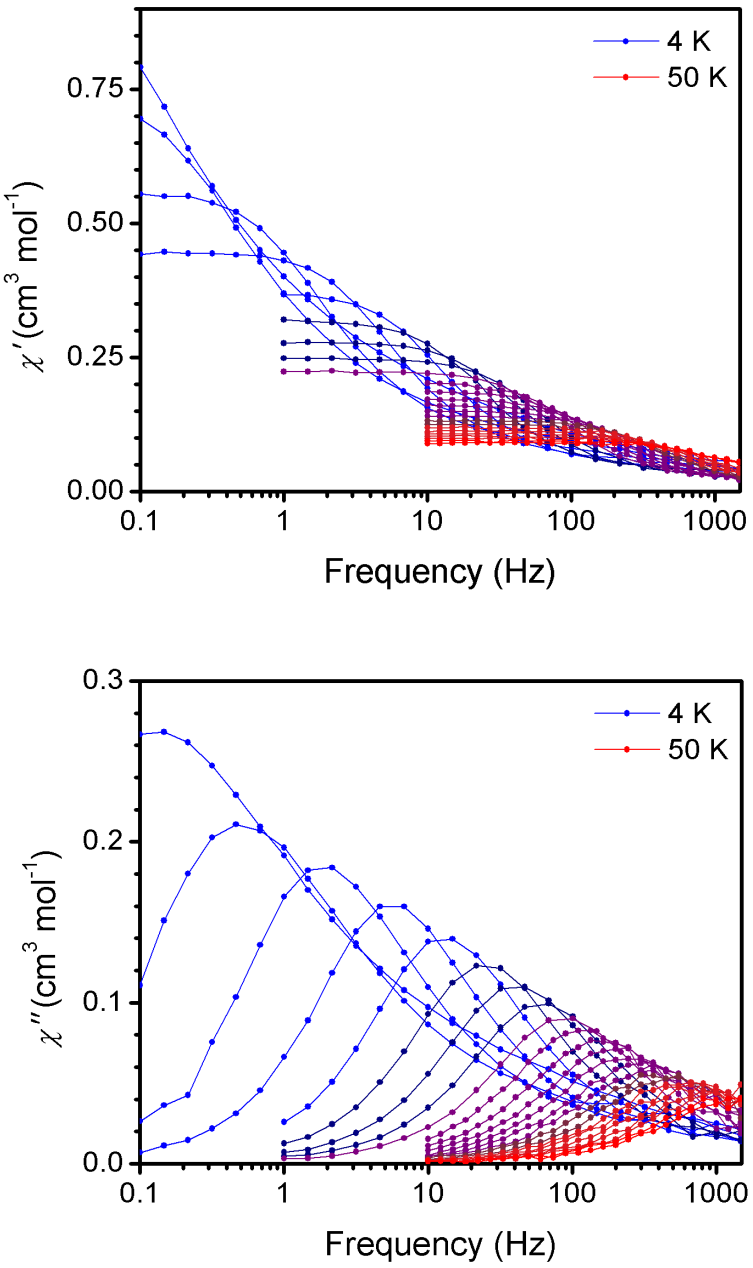

Fig. S3.8. In-phase (χ') and out-of-phase (χ'') magnetic susceptibility for **1** collected under zero applied dc field from 4 to 50 K. The lines are a guide for the eye.

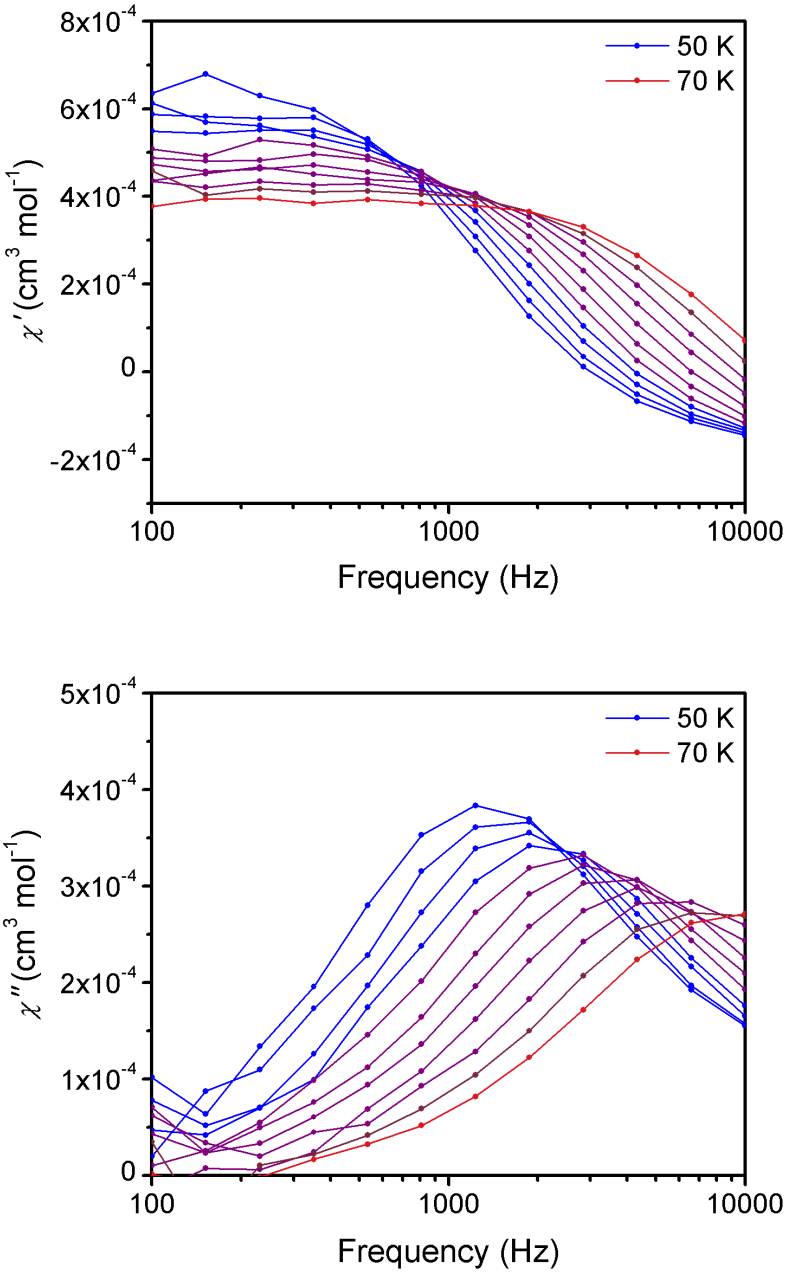

Fig. S3.9. In-phase (χ') and out-of-phase (χ'') magnetic susceptibility for **1** collected under zero applied dc field from 50 to 70 K. The lines are a guide for the eye.

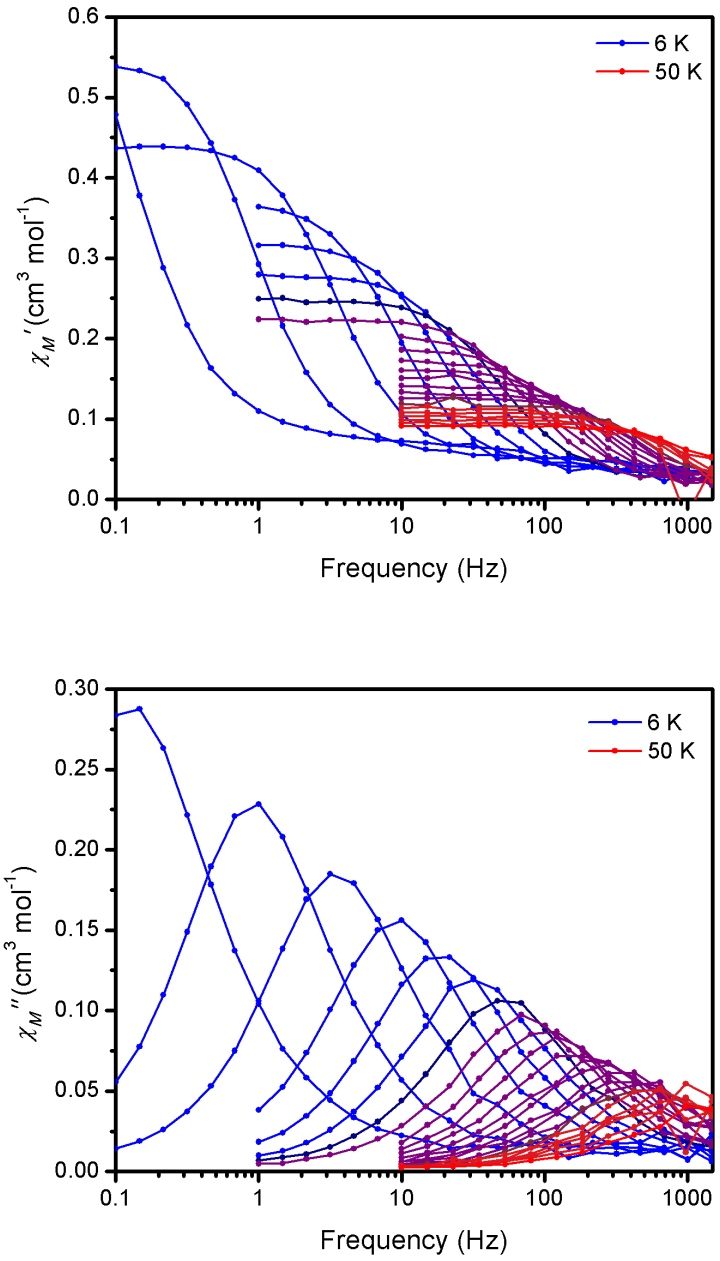

Fig. S3.10. In-phase (χ') and out-of-phase (χ'') magnetic susceptibility for **1** collected under a 3000 Oe dc field from 6 to 50 K. The lines are a guide for the eye.

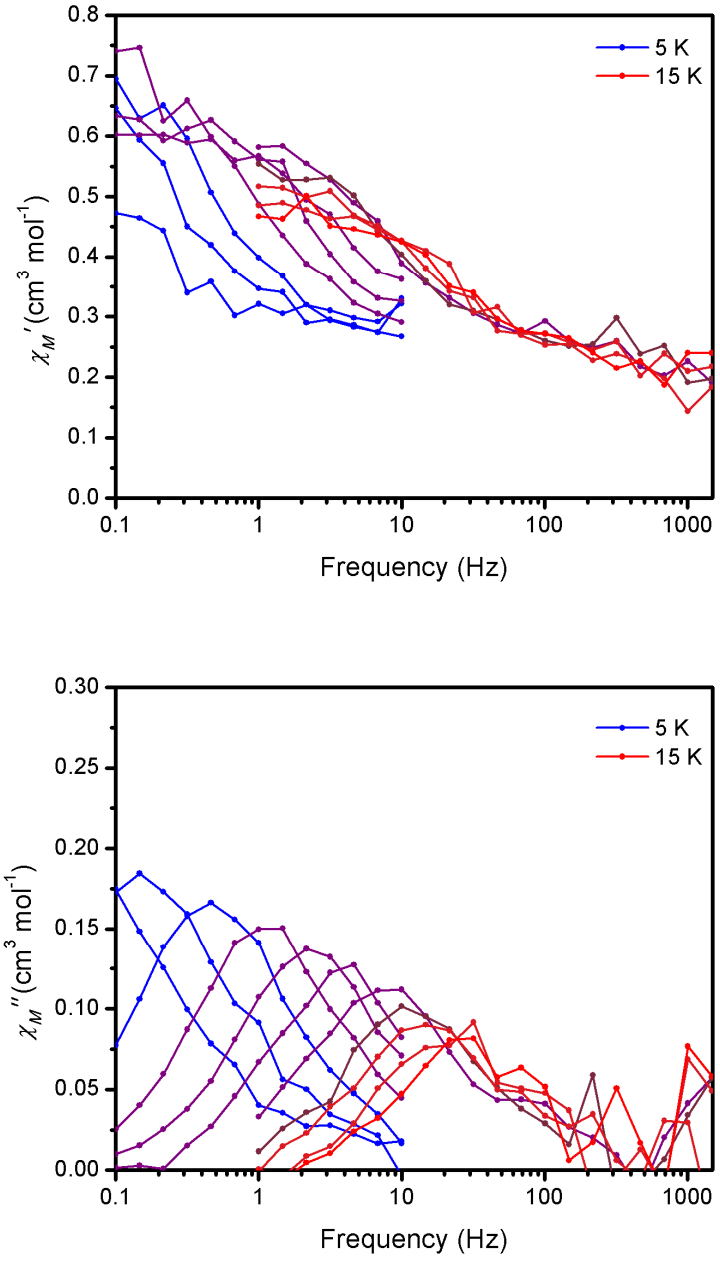

Fig. S3.11. In-phase (χ') and out-of-phase (χ'') magnetic susceptibility for **3** collected under zero applied dc field from 5 to 15 K. The lines are a guide for the eye.

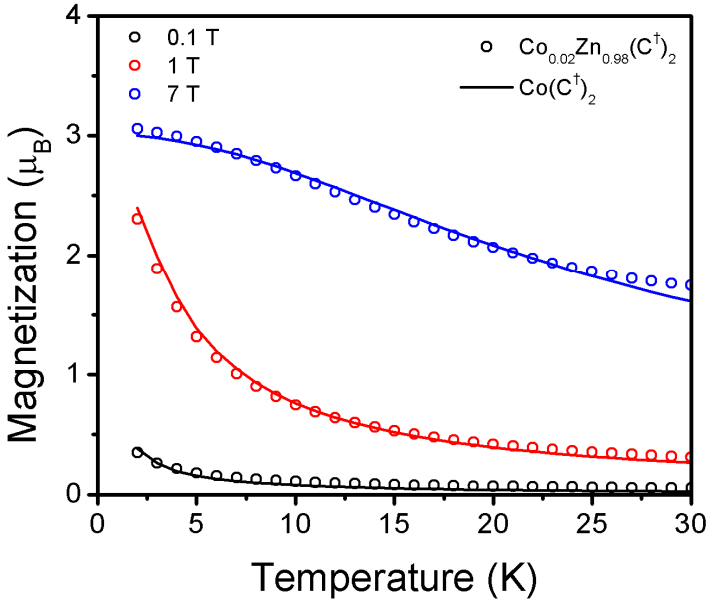

Fig. S3.12. Variable temperature for **3** under applied fields of 0.1 (black), 1 (red), and 7 (blue) T. The lines are data for **1** shown for comparison. Due to the low moment of the sample and the relatively high diamagnetic response the data becomes increasingly noisy with increasing temperature as the measured moment approaches the instrument's detection limit.

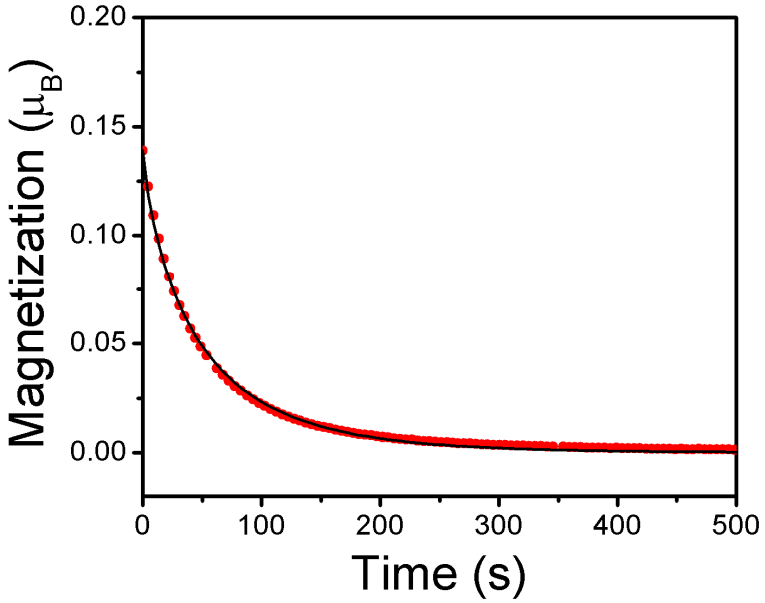

Fig. S3.13. Sample of the dc relaxation data for **3**. Data are shown in red and the black line is a fit. This dataset was collected at 1.8 K using a magnetizing field of 0.15 T.

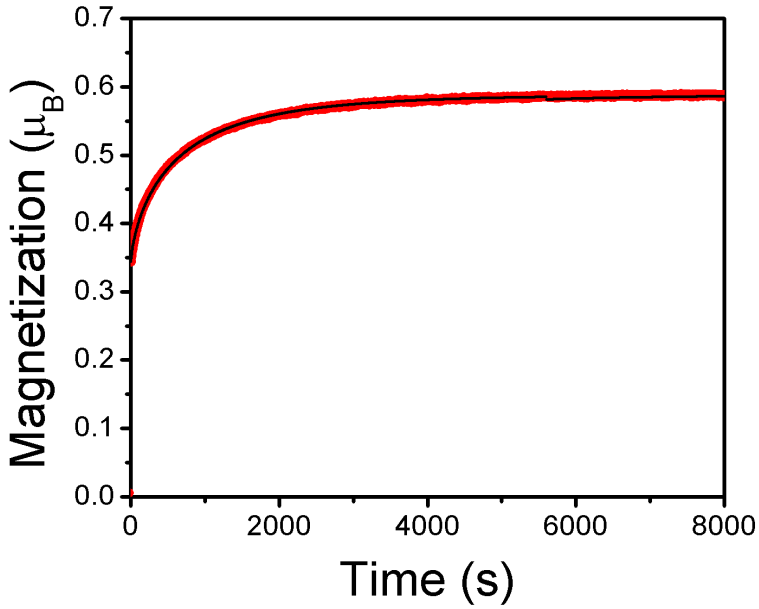

Fig. S3.14. Sample of the applied field dc relaxation data for **3**. Data are shown in red and the black line is a fit. This dataset was collected at 1.8 K by switching from 0.125 to 0.15 T.

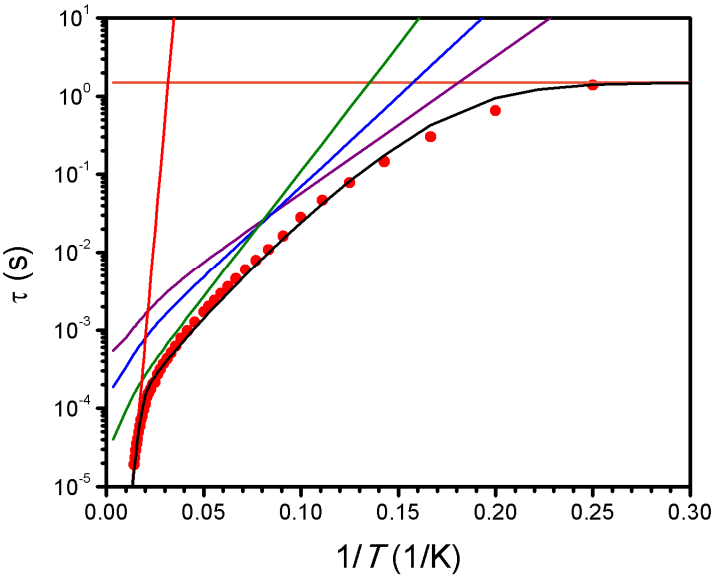

Fig. S3.15. Relaxation data (red) for **1** under 0 Oe dc field. The black line fit of the relaxation process as described by Eq. S4. The orange, purple, blue, green, and red lines represent contributions to relaxation from tunneling, the phonon at 56 cm^{-1}, the phonon at 74 cm^{-1}, the phonon at 103 cm^{-1}, and the Orbach process at 450 cm^{-1}, respectively.

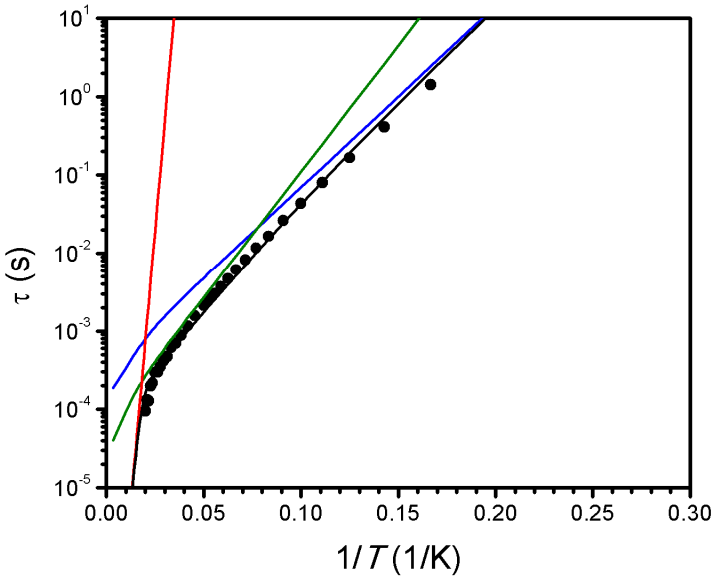

Fig. S3.16. Relaxation data (black) for **1** under 0 Oe dc field. The black line fit of the relaxation process as described by Eq. S4. The blue, green, and red lines represent contributions to relaxation from the phonon at 74 cm^{-1}, the phonon at 103 cm^{-1}, and the Orbach process at 450 cm^{-1}, respectively.

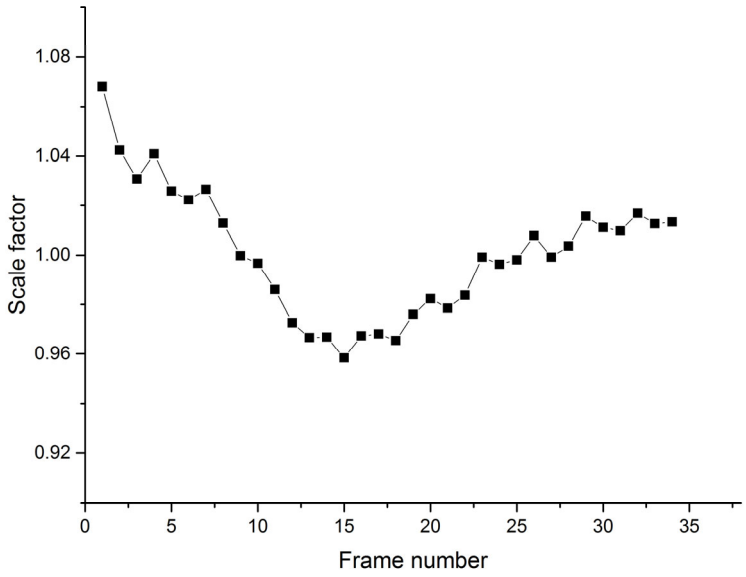

Fig. S3.17. Frame scale factor during the data collection.

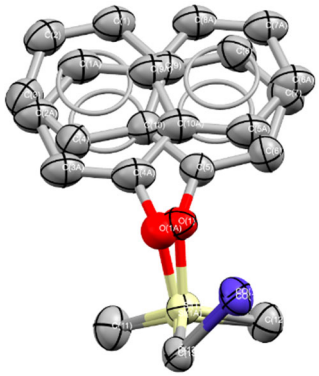

Fig. S3.18. ORTEP drawing showing the disorder in the crystallographic asymmetric unit of **1**. This model of disorder was used in the charge density modeling from the high-resolution data set.

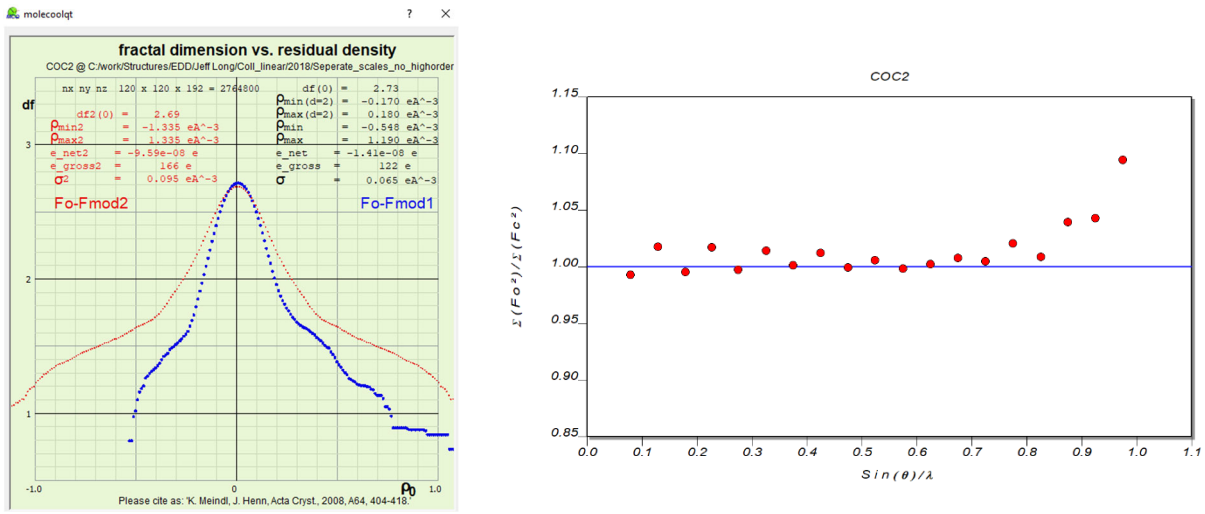

Fig. S3.19. (left) Fractal dimensionality plot and (right) binned ratio of F_o^2 over F_c^2.

Supplementary Table S3.1. Crystal data for structure refinement of **$Co(C(SiMe_2OPh)_3)_2$**.

Empirical formula	$C_{50}H_{66}CoO_6Si_6$
Formula weight	990.85
Temperature/K	100
Crystal system	monoclinic
Space group	C2/c
a/Å	21.9430(9)
b/Å	11.7066(5)
c/Å	20.8482(8)
α/°	90
β/°	95.249(2)
γ/°	90
Volume/Å^3	5333.0(4)
Z	4
ρ_{calc}g/cm^3	1.234
μ/mm^{-1}	0.501
F(000)	2100.0
Crystal size/mm^3	0.20 × 0.10 × 0.10
Radiation	MoKα (λ = 0.71073)
2Θ range for data collection/°	3.728 to 50.698
Index ranges	$-26 \leq h \leq 26$, $-14 \leq k \leq 14$, $-23 \leq l \leq 25$
Reflections collected	31144
Independent reflections	4879 [R_{int} = 0.0417, R_{sigma} = 0.0273]
Data/restraints/parameters	4879/0/296
Goodness-of-fit on F^2	1.068
Final R indexes [I>=2σ (I)]	R_1 = 0.0491, wR_2 = 0.1248
Final R indexes [all data]	R_1 = 0.0642, wR_2 = 0.1413
Largest diff. peak/hole / e Å^{-3}	0.716/-0.394

Supplementary Table S3.2. Crystal data for structure refinement of **1**.

Empirical formula	$C_{74}H_{78}CoO_6Si_6$
Formula weight	1290.80
Temperature/K	100.01
Crystal system	trigonal
Space group	R-3
a/Å	15.0655(7)
b/Å	15.0655(7)
c/Å	24.8535(13)
α/°	90
β/°	90
γ/°	120
Volume/Å^3	4885.2(5)
Z	3
ρ_{calc}g/cm^3	1.316
μ/mm^{-1}	0.428
F(000)	2043.0
Crystal size/mm^3	0.1 × 0.08 × 0.05
Radiation	MoKα (λ = 0.71073)
2Θ range for data collection/°	3.526 to 61.002
Index ranges	-21 ≤ h ≤ 21, -21 ≤ k ≤ 20, -35 ≤ l ≤ 35
Reflections collected	59062
Independent reflections	3315 [R_{int} = 0.0390, R_{sigma} = 0.0196]
Data/restraints/parameters	3315/0/134
Goodness-of-fit on F^2	1.075
Final R indexes [I>=2σ (I)]	R_1 = 0.0400, wR_2 = 0.1026
Final R indexes [all data]	R_1 = 0.0472, wR_2 = 0.1062
Largest diff. peak/hole / e Å^{-3}	0.96/-0.21

Supplementary Table S3.3. Crystal data for structure refinement of **2**.

Empirical formula	$C_{74}H_{78}O_6Si_6Zn$
Formula weight	1297.27
Temperature/K	100.03
Crystal system	trigonal
Space group	R-3
a/Å	15.0722(5)
b/Å	15.0722(5)
c/Å	24.7759(9)
α/°	90
β/°	90
γ/°	120
Volume/Å^3	4874.3(4)
Z	3
ρ_{calc}g/cm^3	1.326
μ/mm^{-1}	0.543
F(000)	2052.0
Crystal size/mm^3	0.06 × 0.05 × 0.05
Radiation	MoKα (λ = 0.71073)
2Θ range for data collection/°	3.526 to 54.906
Index ranges	$-19 \leq h \leq 19$, $-18 \leq k \leq 19$, $-23 \leq l \leq 32$
Reflections collected	18967
Independent reflections	2491 [R_{int} = 0.0291, R_{sigma} = 0.0191]
Data/restraints/parameters	2491/0/134
Goodness-of-fit on F^2	1.063
Final R indexes [I>=2σ (I)]	R_1 = 0.0419, wR_2 = 0.1148
Final R indexes [all data]	R_1 = 0.0495, wR_2 = 0.1201
Largest diff. peak/hole / e Å^{-3}	0.73/-0.35

Supplementary Table S3.4. Parameters used for the fits of relaxation data shown in Figure 4A.

H_{dc} (Oe)	τ_{tunnel} (s)	V_1 (cm^{-1})	$\hbar\omega_1$ (cm^{-1})	V_2 (cm^{-1})	$\hbar\omega_2$ (cm^{-1})	V_3 (cm^{-1})	$\hbar\omega_3$ (cm^{-1})	τ_0 (s)	U (cm^{-1})
0	1.5	1.7×10^{-2}	56	3.3×10^{-2}	74	9.0×10^{-2}	103	1.9×10^{-9}	450
3000				3.3×10^{-2}	74	9.0×10^{-2}	103	1.9×10^{-9}	450

Supplementary Table S3.5. Energies (in cm^{-1}) of the ten quartet ($S = {}^3/_2$) states (roots) from the state-average CASSCF and CASSCF/NEVPT2 calculations of **1** at the reported X-ray geometry. Term notations refer to the idealized point group $C_{\infty v}$.

Electronic State	CASSCF	NEVPT2
$^4\Phi(^4F)$	0, 28	0, 53
$^4\Sigma^-(^4F)$	1641	1500
$^4\Pi(^4F)$	2038	2104
$^4\Delta(^4F)$	2384	2768
$^4\Sigma^-(^4P)$	16822	13537
$^4\Pi(^4P)$	21412	18865

Supplementary Table S3.6. Energies (in cm^{-1}) of the magenetic sublevels split out by spin-orbit coupling from the lowest spin-free $^4\Phi(^4F)$ ground state from CASSCF and CASSCF/NEVPT2 correlated calculations of **1** at the reported X-ray geometry.

Electronic State	CASSCF	NEVPT2
$M_J = \pm {}^9/_2$	0	0
$M_J = \pm {}^7/_2$	468	476
$M_J = \pm {}^5/_2$	955	969
$M_J = \pm {}^3/_2$	1461	1469

Supplementary Table S3.7. Energies of the 3d-MOs (in cm^{-1}) for **1**.

Orbital	Energy
$\delta(d_{xy},d_{x2-y2})$	0
$\pi(d_{xz},d_{yz})$	2913
$\sigma(d_{z2})$	5639

Supplementary Table S3.8. Composition of the $^4\Phi(^4F)$ ground state of linear CoC_2.

Ground sublevel at 0	Excited sublevel 28(53) cm^{-1}
33% $d^2_{xy}d^1_{yz}d^1_{z2}d^2_{xz}d^1_{x2-y2}$	34% $d^2_{xy}d^1_{yz}d^1_{z2}d^2_{xz}d^1_{x2-y2}$
33% $d^1_{xy}d^2_{yz}d^1_{z2}d^1_{xz}d^2_{x2-y2}$	34% $d^1_{xy}d^2_{yz}d^1_{z2}d^1_{xz}d^2_{x2-y2}$
16% $d^2_{xy}d^2_{yz}d^1_{z2}d^1_{xz}d^1_{x2-y2}$	16% $d^2_{xy}d^2_{yz}d^1_{z2}d^1_{xz}d^1_{x2-y2}$
16% $d^1_{xy}d^1_{yz}d^1_{z2}d^2_{xz}d^2_{x2-y2}$	16% $d^1_{xy}d^1_{yz}d^1_{z2}d^2_{xz}d^2_{x2-y2}$
1% $d^1_{xy}d^2_{yz}d^1_{z2}d^2_{xz}d^1_{x2-y2}$	
1% $d^2_{xy}d^1_{yz}d^1_{z2}d^1_{xz}d^2_{x2-y2}$	

Supplementary Table S3.9. Energy contributions (in cm^{-1}) from the ligand-field (LF), the diagonal and off-diagonal interelectronic repulsion (IR) B terms and their entire effect on the non-relativistic $S = {}^3/_2$ term energies of **1** in comparison with the basis CASSCF/NEVPT2 results.

Term	Configuration	LF	IR Diagonal	LF+IR diagonal (off-diagonal B)	Full Diagonalization	CASSCF/ NEVPT2
$^4\Sigma^-(^4F)$	$\delta^4\pi^2\sigma^1$	-2914	12072	9158	13793	13537
	$\delta^2\pi^4\sigma^1$	2914	3018	5932	1297	1500
	$\delta^4\pi^2\sigma^1/\delta^2\pi^4\sigma^1$	0	0	(6036)	-	-
$^4\Phi(^4F)$	$\delta^3\pi^3\sigma^1$	0	0	0	0	0, 53
$^4\Delta(^4F)$	$\delta^3\pi^3\sigma^2$	2725	0	2725	2725	2768
$^4\Pi(^4F)$	$\delta^2\pi^3\sigma^2$	5639	9054	14693	18931	18865
	$\delta^3\pi^3\sigma^1$	0	6036	6036	1798	2104
	$\delta^2\pi^3\sigma^2/\delta^3\pi^3\sigma^1$	0	0	(7392)	-	-

Supplementary Table S3.10. Ligand-field stabilization energies (in kcal/mol) for **1**, $Fe(C(SiMe_3)_3)_2$ and $[Fe(C(SiMe_3)_3)_2]^-$.

	1	**$Fe(C(SiMe_3)_3)_2$**	**$[Fe(C(SiMe_3)_3)_2]^-$**
CFSE	-4.8	-28.6	-9.6
CFDE	45.9	59.0	4.4
CFSE+CFDE	41.1	30.4	-5.2
MOSE	-24.4	-42.1	-9.8

Supplementary Table S3.11. Energies (in cm^{-1}) of the ten quartet ($S = {}^3/_2$) states and magnetic sublevels split out by spin-orbit coupling from the lowest spin-free $^4\Phi(^4F)$ ground state from CASSCF and CASSCF/NEVPT2 correlated calculations of **1** in comparison with the **1′** truncated model complex.

Complex	**1**		**1′**	
Active Space	CAS(7,5) Five 3d-MOs	CAS(7,5) Five 3d-MOs	CAS(7,5) Five 3d-MOs	CAS(9,6) Five 3d-MOs plus C σ
Number of roots taken in state averaging	10 quartets 40 doublets	10 quartets 40 doublets	10 quartets	10 quartets
Non-relativistic				
$^4\Phi(^4F)$	0,28 (0,53)	0,18(0,30)	0,18(0,31)	0,18(0,33)
$^4\Sigma^-(^4F)$	1641(1500)	1732(1561)	1721(1512)	1684(1564)
$^4\Pi(^4F)$	2038(2014)	2227(2300)	2186(2206)	2152(2340)
$^4\Delta(^4F)$	2384(2768)	2602(3088)	2532(2846)	2531(2780)
$^4\Sigma^-(^4P)$	16822(13537)	16638(13319)	16729(13342)	16672(13056)
$^4\Pi(^4P)$	21412(18865)	21810(19366)	21916(19130)	21862(18722)
Relativistic				
$M_J = \pm{}^9/_2$	0(0)	0(0)	0(0)	0(0)
$M_J = \pm{}^7/_2$	468(476)	475(484)	466(472)	466(471)
$M_J = \pm{}^5/_2$	955(969)	966(979)	958(969)	958(967)
$M_J = \pm{}^3/_2$	1461(1469)	1479(1486)	1485(1493)	1483(1493)

Supplementary Table S3.12. Energies (in cm^{-1}) of the 3d-MOs for **1** and the truncated model complex **1′**.

Complex	**1**		**1′**	
Active Space	CAS(7,5) Five 3d-MOs	CAS(7,5) Five 3d-MOs	CAS(7,5) Five 3d-MOs	CAS(9,6) Five 3d-MOs plus C σ
Number of roots taken in state averaging	10 quartets 40 doublets	10 quartets 40 doublets	10 quartets	10 quartets
$\delta(d_{xy},d_{x2-y2})$	0(0)[a]	0(0)[a]	0(0)[a]	0(0)[b]
$\pi(d_{xz},d_{yz})$	3091(2913)[a]	3530(3319)[a]	3681(3120)[a]	3308(3670)[b]
$\sigma(d_{z2})$	6035(5639)[a]	6735(6331)[a]	5946(5628)[a]	5818(6442)[b]

[a] Orbital energies have extracted from the an initio ligand field theory output of the CASSCF/NEVPT2 results; [b] Orbital energies have extracted from a best fit of the parameters π and δ (see first column for their definition) to the energies of the ten quartet states from CASSCF and CASSCF/NEVPT2 (listed in parenthesis) calculations (values of B resulting from this fit are 1204(957) cm^{-1}).

Supplementary Table S3.13. Energies (in cm^{-1}) of the ten quartet ($S = {}^3/_2$) states and magnetic sublevels split out by spin-orbit coupling from the lowest spin-free $^4\Phi(^4F)$ ground state from CASSCF and CASSCF/NEVPT2 correlated calculations for **1** in comparison with a $CoOMg_5O_4$ cluster (Figure S3) modeling Co^{II} on a MgO(1,0,0) surface.

Electronic State	**1** CASSCF(NEVPT2)	$CoOMg_5O_4$ CASSCF(NEVPT2)
Non-relativistic		
$^4\Phi(^4F)$	0,28 (0,53)	0,62(0,92)
$^4\Sigma^-(^4F)$	1641(1500)	1565(1629)
$^4\Pi(^4F)$	2038(2014)	3016(3627)[a]
$^4\Delta(^4F)$	2384(2768)	6832(9629)[a]
$^4\Sigma^-(^4P)$	16822(13537)	16698(13152)
$^4\Pi(^4P)$	21412(18865)	24423(24650)[a]
Relativistic		
$M_J = \pm{}^9/_2$	0(0)	0(0)
$M_J = \pm{}^7/_2$	468(476)	498(503)
$M_J = \pm{}^5/_2$	955(969)	999(1009)
$M_J = \pm{}^3/_2$	1461(1469)	1494(1495)

[a] Average over the components of the nearly degenerate state split due to small structural distortions away from the C_{4v} symmetry.

Supplementary Table S3.14. Energies of the 3d-MOs (in cm^{-1}) for **1** and the $CoOMg_5O_4$ cluster modeling Co^{II} on a MgO(1,0,0) surface.

3d-orbital	**1** energy	$CoOMg_5O_4$ Energy
$\delta(d_{xy},d_{x2-y2})$	0[a]	0[a]
$\pi(d_{xz},d_{yz})$	2913[a]	2810[a]
$\sigma(d_{z2})$	5639[a]	10945[a]

[a] Orbital energies have extracted from the an initio ligand field theory output of the CASSCF/NEVPT2 results.

Supplementary Table S3.15. Fitted parameters for the Cole-Cole plots for **1** under zero applied dc field. Fits of 4-10 K data used two processes. The minor process is given at the end of the table.

T (K)	χ_T (cm^3 mol^{-1})	χ_S (cm^3 mol^{-1})	α	τ
4	1.377	0.018	0.518	2.16456
5	0.868	0.005	0.387	0.62867
6	0.592	0.012	0.238	0.29296
7	0.490	0.012	0.162	0.14848
8	0.423	0.016	0.100	0.08009
9	0.425	0.023	0.107	0.04419
10	0.392	0.024	0.091	0.02671
11	0.425	0.046	0.154	0.01615
12	0.384	0.042	0.133	0.01080
13	0.354	0.038	0.118	0.00783
14	0.328	0.037	0.103	0.00592
15	0.305	0.033	0.096	0.00454
16	0.285	0.030	0.088	0.00357
17	0.269	0.030	0.081	0.00293
18	0.254	0.027	0.081	0.00240
19	0.240	0.023	0.084	0.00199
20	0.229	0.023	0.080	0.00168
22	0.211	0.019	0.092	0.00125
24	0.192	0.018	0.078	0.00097
26	0.171	0.021	0.035	0.00078
28	0.160	0.018	0.058	0.00062
30	0.148	0.017	0.040	0.00051
32	0.139	0.016	0.037	0.00043
34	0.131	0.016	0.036	0.00037
36	0.123	0.015	0.017	0.00031
38	0.117	0.016	0.013	0.00027
40	0.112	0.009	0.061	0.00022
42	0.106	0.013	0.000	0.00020
44	0.100	0.014	0.000	0.00017
46	0.097	0.014	0.000	0.00016
48	0.093	0.017	0.000	0.00014
50	0.089	0.011	0.000	0.00011
		Minor Process		
4	0.153	0.001	0.594	0.00377
5	0.156	0.013	0.484	0.00157
6	0.194	0.000	0.567	0.00355
7	0.173	0.000	0.576	0.00302
8	0.149	0.000	0.538	0.00254
9	0.082	0.000	0.446	0.00073
10	0.062	0.001	0.353	0.00056

Supplementary Table S3.16. Fitted parameters for the Cole-Cole plots for **1** under zero applied dc field on the PPMS (100-10,000 Hz).

T (K)	χ_T ($\times 10^{-4}$ cm^3 mol^{-1})	χ_S ($\times 10^{-4}$ cm^3 mol^{-1})	α	τ
50	6.69	-1.90	0.0693	0.112
50	6.69	-1.90	0.0693	0.112
52	6.10	-1.83	0.0443	0.096
54	5.67	-1.82	0.0284	0.080
56	5.75	-1.85	0.0604	0.071
58	5.23	-1.84	0.0335	0.059
60	4.99	-1.89	0.0422	0.050
62	4.74	-1.92	0.0395	0.041
64	4.49	-1.56	0	0.035
66	4.28	-1.65	0	0.029
68	4.13	-1.62	0	0.023
70	3.89	-1.60	0	0.019

Supplementary Table S3.17. Fitted parameters for the Cole-Cole plots for **1** under a 3000 Oe applied dc field.

T (K)	χ_T (cm^3 mol^{-1})	χ_S (cm^3 mol^{-1})	α	τ
6	0.846	0.0546	0.194	1.48727
7	0.649	0.0528	0.110	0.40922
8	0.559	0.0492	0.078	0.16516
9	0.497	0.0447	0.070	0.07979
10	0.448	0.0409	0.068	0.04327
11	0.408	0.0369	0.067	0.02609
12	0.376	0.0332	0.071	0.01657
13	0.348	0.0391	0.057	0.01174
14	0.324	0.0288	0.064	0.00825
15	0.302	0.0275	0.056	0.00615
16	0.283	0.0266	0.057	0.00472
17	0.266	0.0226	0.061	0.00375
18	0.253	0.0218	0.060	0.00301
19	0.239	0.0207	0.059	0.00253
20	0.226	0.0210	0.054	0.00209
22	0.208	0.0203	0.054	0.00155
24	0.191	0.0181	0.047	0.00118
26	0.178	0.0118	0.079	0.00089
28	0.163	0.0133	0.066	0.00069
30	0.156	0.0130	0.068	0.00060
32	0.143	0.0123	0.054	0.00046
34	0.135	0.0134	0.048	0.00042
36	0.128	0.0208	0.008	0.00038
38	0.123	0.0111	0.059	0.00030
40	0.111	0.0108	0	0.00030
42	0.109	0.0113	0.012	0.00022
44	0.105	0.0111	0.034	0.00020
46	0.101	0	0.082	0.00014
48	0.097	0	0.136	0.00010
50	0.094	0	0.168	0.00008

Supplementary Table S3.18. Fitted parameters for the Cole-Cole plots for **3** under zero applied dc field.

T (K)	χ_T (cm^3 mol^{-1})	χ_S (cm^3 mol^{-1})	α	τ
6	0.0253	0.0100	0.163	1.0000
7	0.0223	0.0100	0.076	0.3331
8	0.0212	0.0105	0.048	0.1403
9	0.0197	0.0103	0.020	0.0685
10	0.0187	0.0107	0.000	0.0418
12	0.0162	0.0094	0.004	0.0131
13	0.0155	0.0093	0.020	0.0101
14	0.0146	0.0091	0.000	0.0065
15	0.0141	0.0091	0.000	0.0056

Supplementary Table S3.19. Fitted parameters for the dc relaxation data for **1**.

Magnetizing Field (T)	τ (s)	*n*
0.05	16.18	0.88
0.1	15.05	0.87
0.15	15.43	0.87
0.2	16.12	0.93
0.25	15.71	0.88
0.3	16.08	0.89
0.4	16.25	0.89
0.5	16.61	0.90
0.6	16.97	0.90
0.7	17.31	0.91
0.8	17.31	0.91
0.9	17.13	0.90
1	17.08	0.90
5	16.58	0.85

Supplementary Table S3.20. Fitted parameters for the dc relaxation data for **3**.

Magnetizing Field (T)	τ (s)	n
0.05	39.63	0.75
0.1	42.53	0.76
0.15	47.43	0.78
0.2	46.21	0.76
0.25	46.71	0.76
0.3	48.82	0.76
0.35	51.63	0.77
0.4	52.23	0.77
0.45	53.61	0.77
0.5	53.43	0.76

Supplementary Table S3.21. Fitted parameters for the applied field dc magnetization data for **1**.

H (T)	τ (s)	n
0.05	25.4	0.78
0.10	51.9	0.77
0.15	221.83	0.51
0.20	216.0	0.61
0.25	152.2	0.69
0.30	100.1	0.74
0.35	70.8	0.71
0.40	49.2	0.75
0.50	34.2	0.69
0.60	29.0	0.52

Supplementary Table S3.22. Fitted parameters for the applied field dc magnetization for **3**.

H (T)	tau	n
0	48.22	0.76
0.05	248.96	0.53
0.1	583.55	0.55
0.15	660.31	0.70
0.2	384.32	0.73
0.25	200.59	0.78
0.3	114.19	0.81
0.35	68.23	0.80
0.4	45.49	0.81
0.45	33.82	0.74

S3.3 References for Chapter 3 Supporting Information

(1) M. Gonidec, E. S. Davies, J. McMaster, D. B. Amabilino, J. Veciana, Probing the magnetic properties of three interconvertible redox states of a single-molecule magnet with magnetic circular dichroism spectroscopy. *J. Am. Chem. Soc.* **132**, 1756–1757 (2010).
(2) S.-D. Jiang, B.-W. Wang, G. Su, Z.-M. Wang, S. Gao, A mononuclear dysprosium complex featuring single-molecule-magnet behavior. *Angew. Chem. Int. Ed.* **49**, 7448–7451 (2010).
(3) A. Lunghi, F. Totti, R. Sessoli, S. Sanvito, The role of anharmonic phonons in under-barrier spin relaxation of single molecule magnets. *Nat. Commun.* **8**, 14620 (2017).
(4) P.-Å. Malmqvist, B. O. Roos, The CASSCF State Interaction Method. *Chem. Phys. Lett.* **155**, 189–194 (1989).
(5) K. Wolinski, P. Pulay, Generalized Möller–Plesset perturbation theory: Second order results for two-configuration, open-shell excited singlet, and doublet wave functions. *J. Chem. Phys.* **90**, 3647–3659 (1989).
(6) K. Andersson, P. A. Malmqvist, B. O. Roos, A. J. Sadlej, K. Wolinski, Second-order perturbation theory with a CASSCF reference function. *J. Phys. Chem.* **94**, 5483–5488 (1990).
(7) K. Andersson, P. Å. Malmqvist, B. O. Roos, Second-order perturbation theory with a complete active space self-consistent field reference function. *J. Chem. Phys.* **96**, 1218–1226 (1992).
(8) B. O. Roos, P.-A. Malmqvist, Relativistic quantum chemistry: The multiconfigurational approach. *Phys. Chem. Chem. Phys.* **6**, 2919 (2004).
(9) B. Roos, M. Fülscher, P.-Å. Malmqvist, M. Merchán, L. Serrano-Andrés, "Theoretical studies of the electronic spectra of organic molecules," in *Quantum Mechanical Electronic Structure Calculations with Chemical Accuracy*, S. Langhoff, Ed. (Springer Netherlands, 1995), pp. 357–438.
(10) C. Angeli, R. Cimiraglia, S. Evangelisti, T. Leininger, J.-P. Malrieu, Introduction of n-electron valence states for multireference perturbation theory. *J. Chem. Phys.* **114**, 10252–10264 (2001).
(11) C. Angeli, R. Cimiraglia, J.-P. Malrieu, N-electron valence state perturbation theory: A fast implementation of the strongly contracted variant. *Chem. Phys. Lett.* **350**, 297–305 (2001).
(12) C. Angeli, R. Cimiraglia, J.-P. Malrieu, N-electron valence state perturbation theory: A spinless formulation and an efficient implementation of the strongly contracted and of the partially contracted variants. *J. Chem. Phys.* **117**, 9138–9153 (2002).
(13) C. Angeli, B. Bories, A. Cavallini, R. Cimiraglia, Third-order multireference perturbation theory: The *n*-electron valence state perturbation-theory approach. *J. Chem. Phys.* **124**, 054108 (2006).
(14) F. Neese, The ORCA program system. *Wiley Interdiscip. Rev. Comput. Mol. Sci.* **2**, 73–78 (2012).
(15) Max Planck Institute for Chemical Energy Conversion, ORCA, an ab initio, DFT and semiempirical SCF-MO package, version 4.0;
(16) F. Neese, Efficient and accurate approximations to the molecular spin-orbit coupling operator and their use in molecular g-tensor calculations. *J. Chem. Phys.* **122**, 034107 (2005).
(17) D. Ganyushin, F. Neese, First-principles calculations of zero-field splitting parameters. *J. Chem. Phys.* **125**, 24103 (2006).

(18) M. Atanasov, D. Ganyushin, K. Sivalingam, F. Neese, A modern first-principles view on ligand field theory through the eyes of correlated multireference wavefunctions. *Struct. Bond.* **143**, 149–220 (2012).
(19) S. K. Singh, J. Eng, M. Atanasov, F. Neese, Covalency and chemical bonding in transition metal complexes: An ab initio based ligand field perspective. *Coord. Chem. Rev.* **344**, 2–25 (2017).
(20) J. R. Burdett, *Molecular Shapes: Theoretical Models of Inorganic Stereochemistry* (Wiley, 1980).
(21) J. M. Zadrozny, D. J. Xiao, J. R. Long, M. Atanasov, F. Neese, F. Grandjean, G. J. Long, Mössbauer spectroscopy as a probe of magnetization dynamics in the linear iron(I) and iron(II) complexes $[Fe(C(SiMe_3)_3)_2]^{1-/0}$. *Inorg. Chem.* **52**, 13123–13131 (2013).
(22) M. Atanasov, J. M. Zadrozny, J. R. Long, F. Neese, A Theoretical Analysis of Chemical Bonding, Vibronic Coupling, and Magnetic Anisotropy in Linear Iron(II) Complexes with Single-Molecule Magnet Behavior. *Chem. Sci.* **4**, 139–156 (2013).

Chapter 4: Pursuit of $M(SiR_3)_2$ Complexes for Enhanced Magnetic Anisotropy Through Heavy-Ligand Effect

4.1 Introduction

In transition metal complexes with unquenched orbital angular momentum, magnetic anisotropy has thus far been limited by the free-ion spin-orbit coupling constant of the magnetic ion and by the extent to which metal-ligand covalency decreases the effective spin-orbit coupling constant of the magnetic ion within the complex. Viewing ligand-field covalency solely as detrimental to magnetic anisotropy, the best approach to making highly magnetically anisotropic transition metal complexes would be to make a linear ML_2 complex where the M–L bond is as ionic as possible. However, there is one approach in which it may be possible to enhance magnetic anisotropy through metal-ligand covalency, and that is through the use of heavy ligands.[1]

There are no known paramagnetic two-coordinate transition metal complexes with heavy (4p, 5p, etc.) ligands, however there are many two coordinate complexes of d^{10} ions with heavy ligands. Focusing on 3d complexes with threefold symmetry (necessary for unquenched orbital angular momentum), there are several complexes known for Cu(I) with phosphine,[2] silyl,[3] and germanyl[4] ligands, and for Zn(II) with silyl[5] and germanyl[6] ligands. There has only been one apparent attempt at synthesizing a similar paramagnetic compound, which yielded the three-coordinate Fe(II) complex $[NEt_4][Fe(Si(SiMe_3)_3)_2Cl]$.[7] The chloride in this complex could be replaced to make the neutral complex, $Fe(Si(SiMe_3)_3)_2(Et_2O)$.

Herein we describe our efforts to synthesize a $[Fe(SiR_3)_2]^{0/-}$ complex. While we were unable to successfully synthesize the desired complex, we did synthesize a novel $Zn(SiR_3)_2$ complex and a heteroleptic complex which may be developed into the first $[Fe(CR_3)(SiR_3)]^{0/-}$ complex. Additionally, we have found a promising family of ligands based on $[Si(carbazolyl)_3]^-$; a derivative of which may ultimately yield the desired $[Fe(SiR_3)_2]^{0/-}$ complex.

Ligand design principles

In our initial attempts we repeated the work by Roddick *et al.*[7] by synthesizing the three-coordinate iron complexes $[NEt_4][Fe(Si(SiMe_3)_3)_2Cl]$ and $Fe(Si(SiMe_3)_3)_2(Et_2O)$. To isolate the two-coordinate $Fe(Si(SiMe_3)_3)_2$ complex we attempted vacuum sublimation of $Fe(Si(SiMe_3)_3)_2(Et_2O)$ but found that no product sublimed under 80 mtorr up to 160 °C, at which point $Fe(Si(SiMe_3)_3)_2(Et_2O)$ began to slowly decompose. Several two-coordinate M(I) complexes can be synthesized through reduction of three-coordinate M(II) complexes, suggesting an apparent stability of the linear coordination environment for the monovalent cation.[8] With this in mind, we also attempted chemical reduction of both $[NEt_4][Fe(Si(SiMe_3)_3)_2Cl]$ and $Fe(Si(SiMe_3)_3)_2(Et_2O)$, but all such reactions led only to intractable mixtures of black solids.

We believe the primary reason for the inability of $[Si(SiMe_3)_3]^-$ to support a two-coordinate iron disilyl complex is the long Fe–Si bond and lack of inter-ligand non-covalent interactions. Two-coordinate complexes, in general, are not greatly stabilized by metal-ligand bonding interactions and typically require some extent of inter-ligand non-covalent interactions to be isolable.[9] The Fe–Si bond lengths in $[NEt_4][Fe(Si(SiMe_3)_3)_2Cl]$ are 2.488(6) and 2.491(6) Å. In $Fe(C(SiMe_3)_3)_2$ the Fe–C bond length is 2.0505(14) and the nearest interligand H···H contact is 2.3 Å.[10] Adding nearly 1 Å between ligands for 3.3 Å separation between nearest H atoms makes it highly unlikely that $Fe(Si(SiMe_3)_3)_2$ would be stable.

A challenge when considering possible new silyl ligands is the high basicity of the silyl anion. For example, we briefly utilized $[Si(mes)_3]^-$ based on the favorable packing displayed in

[Au(P(mes)$_3$)$_2$][BF$_4$],[11] however we were unable to avoid self-deprotonation of a benzylic proton, as has been observed by others.[12]

Our design principles for new silyl ligands are as follows. Given the long Fe–Si bond length the silyl ligand must either be very large or have arms that direct out over the Fe ion. Given the success of Co(C(SiMe$_2$ONaph)$_3$)$_2$ in stabilizing the two-coordinate Co(II) ion, we focused primarily on ligands which would allow for interligand CH$\cdots\pi$ interactions, which are some of the strongest interligand non-covalent interactions possible.[13] Large aryl groups also increase the chances of interdigitation of the ligands across the metal ion, maximizing interligand interactions. Given the reactivity of the silyl anion we also tried to avoid the presence of any particularly acidic protons. We also considered the possibility that some silyl anions might be too reducing for Fe(II), as we observed with alkyl anions and Co(II),[14] and thus gave particular attention to ligands with electron withdrawing substituents.

4.2 Results and Discussion

Synthesis of the heteroleptic complex Fe(Si(SiMe$_3$)$_3$)(C(SiMe$_2$OPh)$_3$).

While attempting the synthesis of Fe(Si(SiMe$_3$)$_3$)$_2$ we considered the possibility that [Si(SiMe$_3$)$_3$]$^-$ was too reducing for Fe(II). At the same time we had just synthesized Co(C(SiMe$_2$OPh)$_3$)$_2$, in which the electron withdrawing phenoxides reduced the reducing strength of the carbanion[15] and allowed for isolation of the first dialkyl cobalt(II) complex. With [C(SiMe$_2$OPh)$_3$]$^-$ in hand, we attempted the synthesis of a heteroleptic Fe(II) complex with alkyl and silyl ligands. The synthesis of (THF)$_3$Li(Si(SiMe$_3$)$_3$)[16] and (DME)$_2$K(C(SiMe$_2$OPh)$_3$)[14] was carried out as previously reported. In an argon filled glovebox a THF solution (5 mL) of (DME)$_2$K(C(SiMe$_2$OPh)$_3$) was added to a THF suspension (5 mL) of FeCl$_2$. Once no more solid FeCl$_2$ remained, a THF solution (5 mL) of (THF)$_3$Li(Si(SiMe$_3$)$_3$) was added to the reaction mixture, which quickly turned bright orange. The reaction was allowed to stir for 4 h after which solvent was removed *in vacuo* and the remaining solid was dissolved in hexanes. The orange hexanes solution was concentrated to 2 mL and stored at −30 °C. No solid appeared over several days, however after 2 years the solution had slowly evaporated, leaving behind a purple crystalline solid, Fe(Si(SiMe$_3$)$_3$)(C(SiMe$_2$OPh)$_3$).

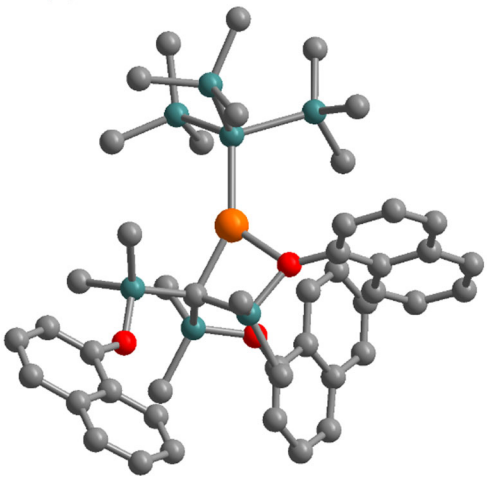

Figure 4.1. Molecular structure of Fe(Si(SiMe$_3$)$_3$)(C(SiMe$_2$OPh)$_3$). Orange, grey, turquoise, and red spheres represent iron, carbon, silicon, and oxygen, respectively. Hydrogen atoms have been omitted for clarity.

The structure of $Fe(Si(SiMe_3)_3)(C(SiMe_2OPh)_3)$ is shown in Figure 4.1. Notably, a phenoxide arm of $[C(SiMe_2OPh)_3]^-$ bends toward the Fe(II) ion to yield a three-coordinate Fe(II) with Fe–O, Fe–C, and Fe–Si bond lengths of 2.061(3), 2.099(4), and 2.4378(13) Å, respectively. Given the somewhat serendipitous nature of the isolation of this complex, the synthesis has not been repeated. However, given the minimal oxophilicity of Fe(I) (as discussed in the isolation of $[Fe(C(SiMe_2OPh)_3)_2]^-$ discussed in Chapter 2), it is possible that chemical reduction of $Fe(Si(SiMe_3)_3)(C(SiMe_2OPh)_3)$ would yield a two-coordinate Fe(I) without any Fe···O interactions. Such a complex would provide a testing ground for the use of heavy ligands to enhance magnetic anisotropy.

Reactions with tris(carbazolyl)silyl and tris(2,7-dimethylcarbazolyl)silyl

A particularly promising ligand scaffold is based on tris(carbazolyl)silyl, which, prior to this work, has not been used as a ligand in any form. Our attention was drawn to this system based on work with the phosphine analog, which suggests that it is a weak σ-donor and strong π-acceptor.[17] This is appealing in the silyl derivative in that it will not likely reduce Fe(II) and the π-accepting capability would provide a stabilizing affect with the d_{xz} and d_{yz} orbitals, an effect which is not seen for the alkyl analogs which are pure σ-donors. This additional stabilization may make the $Fe(SiR_3)_2$ complex more stable even without consideration of interligand interactions. Additionally, however, these ligands are well suited for interligand CH···π interactions and, with the exception of the weakly acidic protons in the 1 and 8 positions on the carbazole ring, there are few decomposition pathways for this ligand.

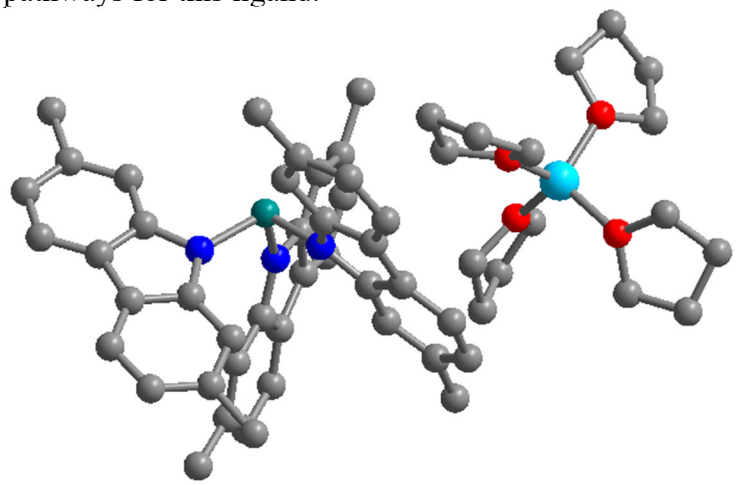

Figure 4.2. Molecular structure of $[Li(THF)_4][Si(^{Me2}carb)_3]$. Turquoise, blue, grey, red, and teal spheres represent silicon, nitrogen, carbon, oxygen, and lithium, respectively. Hydrogen atoms have been omitted for clarity.

$ClSi(carb)_3$ (carb = carbazolyl) was synthesized according to known procedures[18] and $ClSi(^{Me2}carb)_3$ (^{Me2}carb = 2,7-dimethylcarbazolyl) was synthesized following the same procedure but using 2,7-dimethylcarbazolyl, which was synthesized according to known procedures.[19] Clean metalation of both $ClSi(carb)_3$ and $ClSi(^{Me2}carb)_3$ proved challenging and no procedure yielded clean products by either elemental analysis or NMR, although crystals of $[Li(THF)_4][Si(^{Me2}carb)_3]$ were found in a mixture of products of one reaction (Figure 4.2). Attempted reactions with ^{t}BuLi at −78 °C followed by MX_2 salts yielded intractable oils. The most successful attempts at metalation used Li metal, however we found that these reactions were somewhat time sensitive and the most successful reactions with MX_2 were carried out without workup of the $LiSiR_3$

product. A typical reaction is as follows: in an Ar filled glovebox, 4 mL of dimethoxyethane (DME) were added to a vial containing 4.6 mg Li metal (0.66 mmol) and 10 mg of naphthalene (0.078 mmol) and stirred vigorously for 5 min. The resulting green solution was added to a vial containing a suspension of 215.0 mg ClSi(^{Me2}carb)$_3$ (0.33 mmol) in 6 mL DME. After the addition, the reaction mixture was transferred back to the first vial, which still contained solid Li, and stirred for 6 h. Filtration of this cloudy yellow solution through Celite removed a small amount of black solid and yielded a pale-yellow solution. 35.9 mg of $FeBr_2$ (0.17 mmol) was added as a solid to the stirring reaction mixture, which turned red-orange over the course of several hours. Solvent was removed *in vacuo*, leaving a sticky red-orange solid. 4 mL of toluene was added to the vial and the mixture was heated to 80 °C for 1 h, forming a cloudy, bright red solution. The reaction mixture was again filtered through Celite, removing a small amount of grey solid and leaving a bright red solution. We did not find any crystallization conditions which yielded single products; cooling a concentrated toluene or tetrahydrofuran solution or layering those solutions with hexanes always yielded mixtures of products. In the most successful crystallization attempts there were large amounts of both colored and colorless crystalline materials. Crystals were picked from these reactions and the structures will be discussed below in an effort to guide continued synthetic work and to aid in the design of this ligand scaffold.

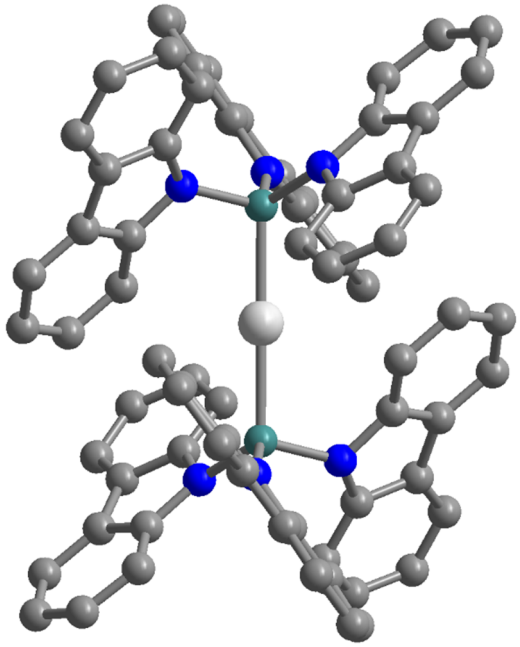

Figure 4.3. Molecular structure of Zn(Si(carb)$_3$)$_2$. White, turquoise, grey, and blue spheres represent zinc, silicon, nitrogen, and carbon, respectively. Hydrogen atoms have been omitted for clarity.

Reaction of the *in situ* generated LiSi(carb)$_3$ and $ZnBr_2$ yielded colorless crystals of Zn((Si(carb)$_3$)$_2$ (Figure 4.3). The compound crystallizes with two toluene molecules in the space group Pbcn. The Zn ion sits on an inversion center and the Zn–Si bond lengths are 2.3107(5) and 2.3108(5) Å; significantly shorter than the Zn–Si bond lengths in Zn(Si(SiMe$_3$)$_3$)$_2$ (2.342(4) Å).[5a] The arms of each ligand are interdigitated and have the necessary orientation for stabilizing sp^2-CH$\cdots\pi$ interactions, though the distances are somewhat long; the shortest of such distances is 2.9 Å. Accounting for the fact that Fe–Si bond lengths in an isostructural molecule would be longer, we quickly turned our attention to [Si(^{Me2}carb)$_3$]$^-$, which has methyl groups in the 2 and 7 positions

on the carbazole ring and should be oriented in such a way to allow for significantly shorter sp^3-CH···π distances.

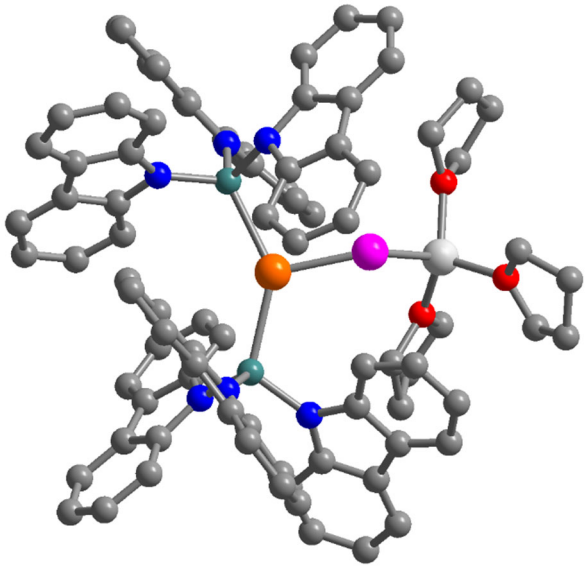

Figure 4.4. Molecular structure of $(Fe(Si(carb)_3)_2)(\mu\text{-}Br)(Li(THF)_3)$. Orange, turquoise, grey, blue, pink, white, and red spheres represent iron, silicon, carbon, nitrogen, bromine, lithium, and oxygen, respectively. Hydrogen atoms have been omitted for clarity.

Reaction of the *in situ* generated $LiSi(carb)_3$ and $FeBr_2$ yielded red crystals of $(Fe(Si(carb)_3)_2)(\mu\text{-}Br)(Li(THF)_3)$ (Figure 4.4). The iron center is in an approximately trigonal planar environment with Fe–Si1, Fe–Si2, and Fe–Br bond lengths of 2.4653(8), 4.866(8), and 2.4024(5) Å, respectively, and Si1–Fe–Si2, Si1–Fe–Br, and Si2–Fe–Br bond angles of 141.09(3)°, 104.57(2)°, and 114.34(2)°, respectively. In $[Fe(Si(SiMe_3)_3)_2Cl]$ the Fe–Si1, Fe–Si2, and Fe–Cl bond lengths are 2.488(6), 4.491(6), and 2.284(6) Å, respectively, and Si1–Fe–Si2, Si1–Fe–Cl, and Si2–Fe–Cl bond angles are 136.9(2)°, 111.7(2)°, and 111.2(2)°, respectively.

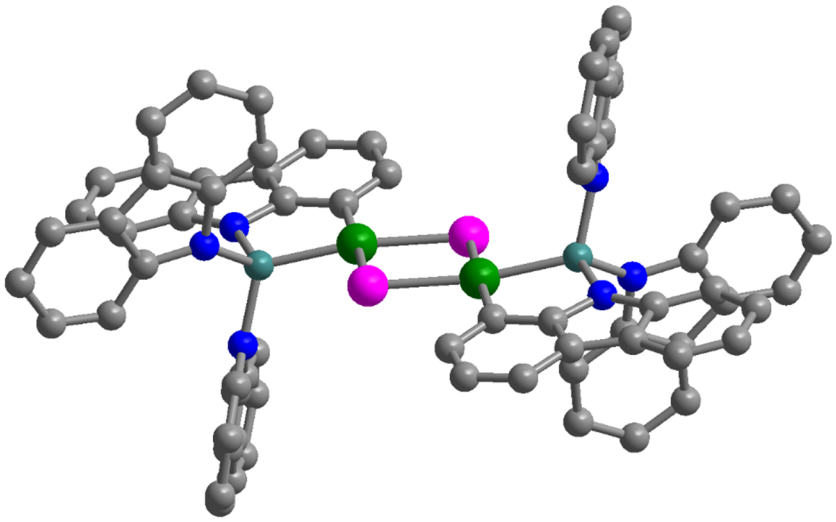

Figure 4.5. Molecular structure of $[\{Ni(Si(carb)_3)(\mu\text{-}Br)\}_2]^{2-}$. Green, pink, turquoise, blue, and grey spheres represent nickel, bromine, silicon, nitrogen, and carbon atoms, respectively. Hydrogen atoms have been omitted for clarity.

We tried several reactions of $LiSi(carb)_3$ with CoX_2 and NiX_2 salts. Reactions with CoX_2 salts yielded only intractable mixtures of black solids while reaction with $NiBr_2$ yielded red crystals of $[Li(THF)_4]_2[\{Ni(Si(carb)_3)(\mu\text{-}Br)\}_2]$ (Figure 4.5). Interestingly, this complex forms as the result of a deprotonation at the 1 position of one of the carbazole rings and suggests that without significant modifications this ligand is incompatible with Ni(II).

Based on the structure of $Zn((Si(carb)_3)_2$ we thought that methylation of the 2 and 7 positions on the carbazole rings would allow for better steric protection of the metal center and more favorable interligand non-covalent interactions. While several structures with this ligand are promising, several isolated products show Si–N bond cleavage not observed for reactions with $[Si(carb)_3]^-$.

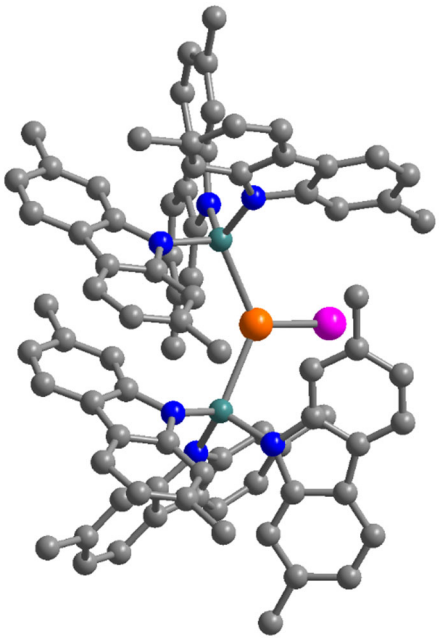

Figure 4.6. Molecular structure of the anion in $[Li(THF)_2(Et_2O)_2][Fe(Si(^{Me2}carb)_3)_2Br]$. Orange, pink, turquoise, blue, and grey spheres represent iron, bromine, silicon, nitrogen, and carbon, respectively. Hydrogen atoms have been omitted for clarity.

Reaction of the *in situ* generated $LiSi(^{Me2}carb)_3$ and $FeBr_2$ yielded red crystals of $[Li(THF)_2(Et_2O)_2][Fe(Si(^{Me2}carb)_3)_2Br]$ (Figure 4.6). The iron center is in an approximately trigonal planar environment with Fe–Si1, Fe–Si2, and Fe–Br bond lengths of 2.5243(9), 4.5205(10), and 2.3712(6) Å, respectively, and Si1–Fe–Si2, Si1–Fe–Br, and Si2–Fe–Br bond angles of 129.56(3)°, 114.21(3)°, and 115.87(3)°, respectively. In $[Fe(Si(SiMe_3)_3)_2Cl]$ the Fe–Si1, Fe–Si2, and Fe–Cl bond lengths are 2.488(6), 4.491(6), and 2.284(6) Å, respectively, and Si1–Fe–Si2, Si1–Fe–Cl, and Si2–Fe–Cl bond angles are 136.9(2)°, 111.7(2)°, and 111.2(2)°, respectively. Also isolated from this reaction were red crystals of $\{Fe(Si(^{Me2}carb)_3)(THF)\}_2(\mu\text{-}Br)_2$ (Figure 4.7). This structure type, not observed in the reactions with $[Si(carb)_3]^-$, may arise if the larger ligands prevent facile formation of the mononuclear complex. A similar structure, $\{Fe(Si(^{Me2}carb)_3)(THF)\}_2(\mu\text{-}Cl)_2$, was observed in the reaction with $FeCl_2$.

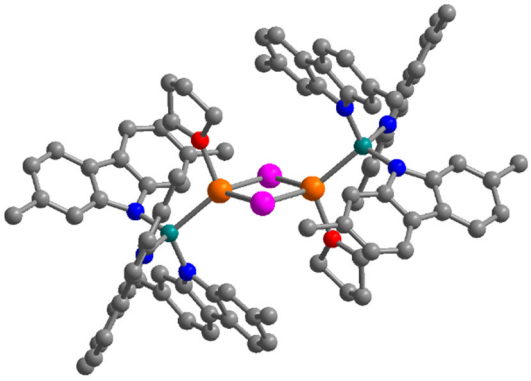

Figure 4.7. Molecular structure of the anion in $\{Fe(Si(carbazolyl)_3)(THF)\}_2(\mu\text{-}Br)_2$. Orange, pink, turquoise, blue, grey, and red spheres represent iron, bromine, silicon, nitrogen, carbon, and oxygen, respectively. Hydrogen atoms have been omitted for clarity.

Three structures displayed cleavage of the Si–N bond. A reaction of the *in situ* generated $LiSi(^{Me2}carb)_3$ and $ZnBr_2$ yielded colorless crystals of $[Li(THF)_4][Zn(Si(^{Me2}carb)_3)(^{Me2}carb)_2]$ (Figure 4.8), which features a three coordinate Zn(II) complex bound to a $[Si(^{Me2}carb)_3]^-$ and two ligand fragments $[^{Me2}carb]^-$. This is somewhat surprising as Zn(II) (and other d^{10} ions) easily forms two-coordinate complexes, suggesting that the ligand degradation occurs during lithiation.

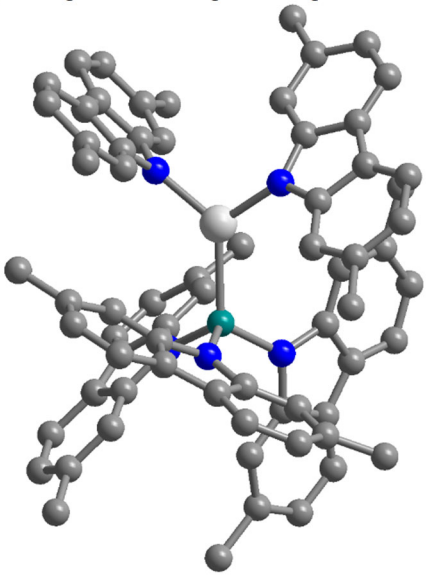

Figure 4.8. Molecular structure of the anion in $[Li(THF)_4][Zn(Si(^{Me2}carb)_3)(^{Me2}carb)_2]$. White, turquoise, blue, and grey spheres represent zinc, silicon, nitrogen, and carbon, respectively. Hydrogen atoms have been omitted for clarity.

Another reaction of the *in situ* generated $LiSi(^{Me2}carb)_3$ and $FeBr_2$ yielded red crystals of $\{\{Fe(Si(^{Me2}carb)_3)(^{Me2}carb)\}(\mu\text{-}Br)_2(Li(DME))\}_2$ (Figure 4.9) and yellow crystals of $[Li(DME)_2(Et_2O)][Fe(Si(^{Me2}carb)_3)_2)(\ ^{Me2}carb)]$ (Figure 4.10). This former complex features two four-coordinate Fe(II) centers bridged by a $Li_2(DME)_2$ core. Notably, one of the ligands on each Fe(II) center is 2,7-dimethylcarbazolyl. The anion in the latter complex, $[Fe(Si(^{Me2}carb)_3)_2)(\ ^{Me2}carb)]^-$ has several promising aspects for the isolation of $Fe(Si(^{Me2}carb)_3)_2$. Despite being three-coordinate, the Si1–Fe–Si2 bond angle is fairly large (139.04(4)°) and extending that to 180° may not alter the ligand orientation significantly. This is worth mentioning because the methylated carbazole arms have significant overlap across the Fe(II) ion. There are several sp^3-CH···π

contacts near 3 Å, and the contacts occur on the pyrrole ring on the center of the carbazole ring. Thus, while the Fe(Si(^{Me2}carb)$_3$)$_2$ complex would separate the opposing carbazole arms, there is significant room for similar sp^3-CH$\cdots\pi$ interactions lower on the benzene ring.

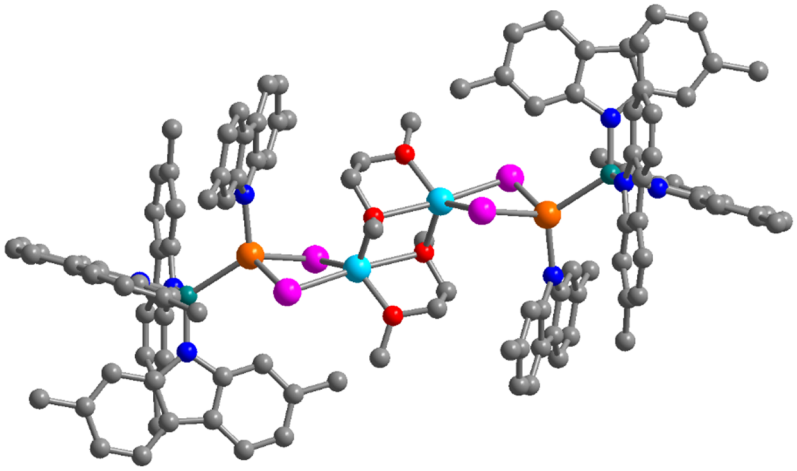

Figure 4.9. Molecular structure of {{Fe(Si(^{Me2}carb)$_3$)(^{Me2}carb)}(μ-Br)$_2$(Li(DME))}$_2$. Orange, pink, teal, turquoise, blue, red, and grey spheres represent iron, bromine, lithium, silicon, nitrogen, oxygen, and carbon, respectively. Hydrogen atoms have been omitted for clarity.

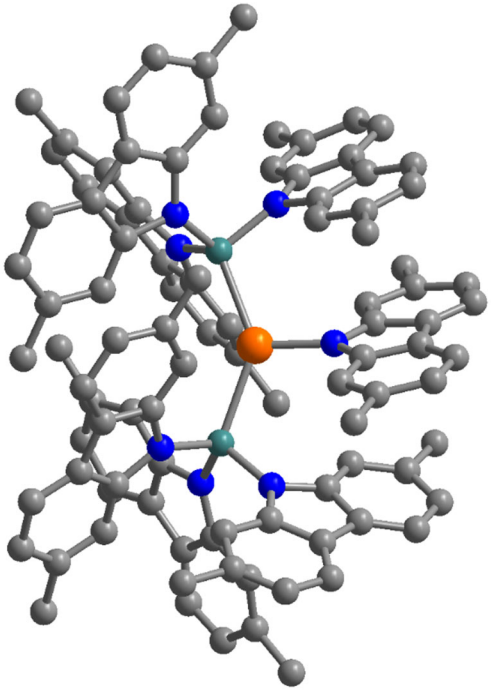

Figure 4.10. Molecular structure of the anion of [Li(DME)$_2$(Et$_2$O)][Fe(Si(^{Me2}carb)$_3$)$_2$)(^{Me2}carb)]. Orange, turquoise, blue, and grey spheres represent iron, silicon, nitrogen, and carbon, respectively. Hydrogen atoms have been omitted for clarity.

4.3 Outlook

The [Si(carbazolyl)$_3$]$^-$ ligand type is promising for the isolation of the first paramagnetic two-coordinate complex with heavy ligands. Taking the work described herein, there are several obvious directions to pursue. First, as none of these reactions provided clean products, it would be

wise to reinvest effort into finding suitable lithiation conditions which would allow for the isolation of Li[Si(carb)$_3$] and, subsequently, the avoidance of mixtures of products during crystallization. Of the complexes already described, (Fe(Si(carb)$_3$)$_2$)(μ-Br)(Li(THF)$_3$) and [Li(THF)$_2$(Et$_2$O)$_2$][Fe(Si(^{Me2}carb)$_3$)$_2$Br] are appealing in that, if isolated in reasonable yield, it would be possible to do further chemistry on these complexes to yield the desired linear Fe complex. There are two pathways here: first, a halide extraction reagent such as trimethylsilyl triflate may allow for isolation of the Fe(II) complex, and second, chemical reduction of the three-coordinate complex may yield a linear Fe(I) complex.

Regarding the stability of the [Si(^{Me2}carb)$_3$]$^-$ ligand, the cleavage of the Si–N bond is somewhat surprising given the strength of Si–N bonds, in general. However, it is possible that the electron withdrawing nature of the carbazole ring makes this bond particularly polar and susceptible to cleavage. This is somewhat by design, as we hoped to use electron withdrawing substituents to reduce the reducing strength of the central silyl anion. The Si–N could perhaps be strengthened by additional methylation at the 3 and 6 positions (para to the amine). This ligand, 2,3,6,7-tetramethylcarbazole, can be made analogously to 2,7-dimethylcarbazole, and based on the structure of Zn(Si(carb)$_3$)$_2$, methyl groups in these positions will not sterically hinder the isolation of the two-coordinate complex.

4.4 References

1. (a) Karunadasa, H. I.; Arquero, K. D.; Berben, L. A.; Long, J. R. *Inorg. Chem.* **2010**, *49*, 4738. (b) Ye, S.; Neese, F. *J. Chem. Theory Comput*. **2012**, *8*, 2344. (c) Zadrozny, J. M.; Telser, J.; Long, J. R. *Polyhedron* **2013**, *64*, 209. (d) Pearson, T. J.; Fataftah, M. S.; Freedman, D. E. *Chem. Commun.* **2016**, *52*, 11394. (e) Yao, X.-N.; Yang, M.-W.; Xiong, J.; Liu, J.-J.; Gao, C.; Meng, Y.-S.; Jiang, S.-D.; Wang, B.-W.; Gao, S. *Inorg. Chem. Front.* **2017**, *4*, 701. (f) Pearson, T. J.; Fataftah, M. S.; Freedman, D. E. *Chem. Commun.* **2016**, *52*, 11394.
2. (a) Akrivos, P. D.; Karagiannidis, P. P.; Raptopoulou, C. P.; Terzis, A.; Stoyanov, S. *Inorg. Chem.*, **1996**, *35*, 4082. (b) Ainscough, E. W.; Brodie, A. M.; Burrell, A. K.; Hanna, J. V.; Healy, P. C.; Waters, J. M. *Inorg. Chem.*, **1999**, *38*, 201. (c) Ainscough, E. W.; Brodie, A. M.; Burrell, A. K.; Freeman, G. H.; Jameson, G. B.; Bowmaker, G. B.; Hanna, J. V.; Healy, P. C. *J. Chem. Soc., Dalton Trans.*, **2001**, 144. (d) Mao, Z.; Chao, H.-Y.; Hui, Z.; Che, C.-M.; Fu, W.-F.; Cheung, K.-K.; Zhu, N. *Chem. Eur. J.*, **2003**, *9*, 2885.
3. (a) Lerner, H.-W.; Scholz, S.; Bolte, M. *Organometallics*, **2001**, *20*, 575. (b) Klinkhammer, K. W.; Klett, J.; Xiong, Y.; Yao, S. *Eur. J. Inorg. Chem.*, **2003**, 3417.
4. Orlov, N. A.; Bochkarev, L. N.; Nikitinsky, A. V.; Zhiltsov, S. F.; Zakharov, L. N.; Fukin, G. K.; Khorshev, S. Y. *J. Organomet. Chem.*, **1997**, *547*, 65.
5. (a) Arnold, J.; Tilley, T. D.; Rheingold, A. L.; Geib, S. J. *Inorg. Chem.*, **1987**, *26*, 2106. (b) Wiberg, N.; Amelunxen, K.; Noth, H.; Appel, A.; Knizek, J.; Polborn, K. *Z. Anorg. Allg. Chem.*, **1997**, *623*, 1861.
6. (a) Nanjo, M.; Oda, T.; Mochida, K. *Chem. Lett.*, **2002**, 108. (b) Nanjo, M.; Oda, T.; Mochida, K. *Bull. Chem. Soc. Jpn.*, **2003**, *76*, 1261.
7. Roddick, D. M.; Tilley, T. D.; Rheingold, A. L.; Geib, S. J. *J. Am. Chem. Soc.*, **1987**, *109*, 945.
8. (a) Werncke, C. G.; Bunting, P. C.; Duhayon, C.; Long, J. R.; Bontemps, S.; Sabo-Etienne, S. *Angew. Chem. Int. Ed.*, **2015**, *54*, 245. (b) Werncke, C. G.; Suturina, E.; Bunting, P. C.;

Vendier, L.; Long, J. R.; Atanasov, M.; Neese, F.; Sabo-Etienne, S.; Bontemps, S. *Chem. Eur. J.*, **2015**, *22*, 1668.
9. (a) Liptrot, D. J.; Power, P. P. *Nature Rev. Chem*. **2017**, 1, 0004. (b) Faust, M.; Bryan, A. M.; Mansikkamäki, A.; Vasko, P.; Olmstead, M. M.; Tuononen, H. M.; Grandjean, F.; Long, G. J.; Power, P. P. *Angew. Chem. Int. Ed.*, **2015**, *54*, 12914. (c) Lin, C.-Y.; Guo, J.-D.; Fettinger, J. C.; Nagase, S.; Grandjean, F.; Long, G. J.; Chilton, N. F.; Power, P. P. *Inorg. Chem.*, **2013**, *52*, 13593.
10. (a) Viefhaus, T.; Schwarz, W.; Hubler, K.; Locke, K.; Weidlein, J. *Z. Anorg. Allg. Chem.*, **2001**, *627*, 715. (b) LaPointe, A. M. *Inorg. Chim. Acta.*, **2003**, *345*, 359.
11. Bayler, A.; Schier, A.; Bowmaker, G. A.; Schmidibauer, H. *J. Am. Chem. Soc.*, **1996**, *118*, 7006.
12. (a) Turnblom, E. W.; Boettcher, R. J.; Mislow, K. *J. Am. Chem. Soc.* **1975**, *97*, 1766. (b) Zigler, S. S.; Johnson, L. M.; West, R. *J. Organomet. Chem.* **1988**, *341*, 187.
13. Nishio, M. *Phys. Chem. Chem. Phys.*, **2011**, *13*, 13873.
14. Bunting, P. C.; Atanasov, M.; Damgaard-Møller, E.; Perfetti, M.; Crassee, I.; Orlita, M.; Overgaard, J.; van Slageren, J.; Neese, F.; Long, J. R. *Science*, **2018**, *362*, eaat7319
15. Li, H.; Aquino, A. J. A.; Cordes, D. B.; Hung-Low, F.; Hase, W. L.; Krempner, C. *J. Am. Chem. Soc.*, **2013**, *135*, 16066.
16. Gutekunst. G.; Brook, A. G. *J. Organomet. Chem.*, **1982**, *225*, 1.
17. Burrows, A. D.; Kociok-Köhn, G.; Mahon, M. F.; Varrone, M. *C. R. Chim.*, **2006**, *9*, 111.
18. Appler, H. *J. Organomet. Chem.*, **1988**, *350*, 217.
19. Zhou, M.; Zhuang, J.; Li, W.; Liu, Y. *Faming Zhuanli Shenqing Patent No. CN 103087103*, **2013.**

Chapter 4 Supporting Information

Supplementary Table 4.1. Crystal data and structure refinement for $Fe(Si(SiMe_3)_3)(C(SiMe_2OPh)_3)$.

Identification code	pb6123
Empirical formula	CHOSiFe
Formula weight	112.96
Temperature/K	100(2)
Crystal system	monoclinic
Space group	$P2_1/n$
a/Å	12.6052(5)
b/Å	27.3239(10)
c/Å	16.0025(7)
α/°	90
β/°	97.291(4)
γ/°	90
Volume/Å^3	5467.1(4)
Z	76
ρ_{calc}g/cm^3	2.607
μ/mm^{-1}	5.345
F(000)	4180.0
Crystal size/mm^3	0.5 × 0.2 × 0.2
Radiation	MoKα (λ = 0.71073)
2Θ range for data collection/°	6.452 to 50.7
Index ranges	$-15 \leq h \leq 14$, $-32 \leq k \leq 32$, $-19 \leq l \leq 19$
Reflections collected	60908
Independent reflections	9992 [R_{int} = 0.0786, R_{sigma} = 0.0472]
Data/restraints/parameters	9992/0/529
Goodness-of-fit on F^2	1.056
Final R indexes [I>=2σ (I)]	R_1 = 0.0683, wR_2 = 0.2042
Final R indexes [all data]	R_1 = 0.0904, wR_2 = 0.2222
Largest diff. peak/hole / e Å^{-3}	2.54/-0.48

Supplementary Table 4.2. Crystal data and structure refinement for $[Li(THF)_4][Si(^{Me2}carb)_3]$.

Identification code	PB7060
Empirical formula	$C_{58}H_{68}LiN_3O_4Si$
Formula weight	906.18
Temperature/K	100
Crystal system	monoclinic
Space group	$P2_1/c$
a/Å	19.168(5)
b/Å	13.676(4)
c/Å	21.736(5)
α/°	90
β/°	107.777(3)
γ/°	90
Volume/Å^3	5426(2)
Z	4
ρ_{calc}g/cm^3	1.109
μ/mm^{-1}	0.093
F(000)	1944.0
Crystal size/mm^3	0.08 × 0.05 × 0.05
Radiation	? (λ = 0.7288)
2Θ range for data collection/°	3.816 to 56.614
Index ranges	$-24 \leq h \leq 24$, $-17 \leq k \leq 17$, $-28 \leq l \leq 27$
Reflections collected	94152
Independent reflections	12492 [R_{int} = 0.0809, R_{sigma} = 0.0428]
Data/restraints/parameters	12492/51/630
Goodness-of-fit on F^2	1.039
Final R indexes [I>=2σ (I)]	R_1 = 0.0480, wR_2 = 0.1226
Final R indexes [all data]	R_1 = 0.0655, wR_2 = 0.1348
Largest diff. peak/hole / e Å^{-3}	0.47/-0.30

Supplementary Table 4.3. Crystal data and structure refinement for $Zn(Si(carbl)_3)_2 \cdot 2C_7H_{10}$.

Identification code	pb7023
Empirical formula	$C_{72}H_{48}N_6Si_2Zn$
Formula weight	1118.71
Temperature/K	99.99
Crystal system	orthorhombic
Space group	Pbcn
a/Å	17.0366(4)
b/Å	17.5657(4)
c/Å	21.6840(5)
α/°	90
β/°	90
γ/°	90
Volume/Å^3	6489.1(3)
Z	4
ρ_{calc}g/cm^3	1.145
μ/mm^{-1}	0.460
F(000)	2320.0
Crystal size/mm^3	0.1 × 0.1 × 0.05
Radiation	MoKα (λ = 0.71073)
2Θ range for data collection/°	3.33 to 58.37
Index ranges	$-23 \leq h \leq 23$, $-22 \leq k \leq 22$, $-25 \leq l \leq 28$
Reflections collected	96143
Independent reflections	8081 [R_{int} = 0.0612, R_{sigma} = 0.0347]
Data/restraints/parameters	8081/0/431
Goodness-of-fit on F^2	1.044
Final R indexes [I>=2σ (I)]	R_1 = 0.0512, wR_2 = 0.1401
Final R indexes [all data]	R_1 = 0.0714, wR_2 = 0.1559
Largest diff. peak/hole / e Å^{-3}	0.54/-1.02

Supplementary Table 4.4. Crystal data and structure refinement for $(Fe(Si(carb)_3)_2)(\mu\text{-}Br)(Li(THF)_3)$.

Identification code	pb7026
Empirical formula	$C_{72}H_{72}N_6Si_2FeBr_{0.25}Li_{0.25}O_{0.25}$
Formula weight	1159.09
Temperature/K	100.01
Crystal system	triclinic
Space group	P-1
a/Å	13.4696(6)
b/Å	14.7520(7)
c/Å	20.5974(10)
α/°	86.990(2)
β/°	76.359(2)
γ/°	84.602(2)
Volume/Å^3	3957.7(3)
Z	4
ρ_{calc}g/cm^3	1.945
μ/mm^{-1}	0.769
F(000)	2446.0
Crystal size/mm^3	0.1 × 0.08 × 0.08
Radiation	MoKα (λ = 0.71073)
2Θ range for data collection/°	2.774 to 53.464
Index ranges	$-16 \le h \le 17$, $-18 \le k \le 18$, $-26 \le l \le 26$
Reflections collected	107872
Independent reflections	16818 [R_{int} = 0.0361, R_{sigma} = 0.0256]
Data/restraints/parameters	16818/0/1011
Goodness-of-fit on F^2	1.018
Final R indexes [I>=2σ (I)]	R_1 = 0.0508, wR_2 = 0.1367
Final R indexes [all data]	R_1 = 0.0607, wR_2 = 0.1438
Largest diff. peak/hole / e Å^{-3}	2.57/-1.42

Supplementary Table 4.5. Crystal data and structure refinement for $[Li(THF)_4][\{Ni(Si(carb)_3)(\mu\text{-}Br)\}_2]\cdot(C_4H_8O)_2$.

Identification code	pb7029
Empirical formula	$C_{111}H_{121}Br_2N_{13}Ni_2O_7Si_2Li_{0.5}$
Formula weight	2086.09
Temperature/K	100(2)
Crystal system	triclinic
Space group	P-1
a/Å	10.6167(2)
b/Å	21.0145(6)
c/Å	22.1434(6)
α/°	89.983(2)
β/°	80.151(2)
γ/°	89.804(2)
Volume/Å^3	4867.5(2)
Z	2
ρ_{calc}g/cm^3	1.423
μ/mm^{-1}	1.298
F(000)	2179.0
Crystal size/mm^3	0.13 × 0.05 × 0.03
Radiation	MoKα (λ = 0.71073)
2Θ range for data collection/°	6.252 to 50.698
Index ranges	$-12 \le h \le 12$, $-25 \le k \le 18$, $-26 \le l \le 26$
Reflections collected	48456
Independent reflections	16855 [R_{int} = 0.0714, R_{sigma} = 0.1150]
Data/restraints/parameters	16855/0/1225
Goodness-of-fit on F^2	1.042
Final R indexes [I>=2σ (I)]	R_1 = 0.0754, wR_2 = 0.1942
Final R indexes [all data]	R_1 = 0.1576, wR_2 = 0.2302
Largest diff. peak/hole / e Å^{-3}	1.36/-1.32

Supplementary Table 4.6. Crystal data and structure refinement for $[Li(THF)_2(Et_2O)_2][Fe(Si(^{Me2}carb)_3)_2Br]\cdot Et_2O$

Identification code	pb7036
Empirical formula	$C_{72}H_{72}LiN_6OSi_2FeBr$
Formula weight	1236.23
Temperature/K	100.01
Crystal system	monoclinic
Space group	$P2_1/c$
a/Å	13.0117(9)
b/Å	21.9563(15)
c/Å	32.342(2)
α/°	90
β/°	91.265(3)
γ/°	90
Volume/Å^3	9237.5(11)
Z	6
ρ_{calc}g/cm^3	1.333
μ/mm^{-1}	0.983
F(000)	3876.0
Crystal size/mm^3	0.2 × 0.18 × 0.15
Radiation	MoKα (λ = 0.71073)
2Θ range for data collection/°	2.52 to 54.206
Index ranges	$-16 \le h \le 16$, $-28 \le k \le 28$, $-41 \le l \le 40$
Reflections collected	246236
Independent reflections	20392 [R_{int} = 0.0563, R_{sigma} = 0.0349]
Data/restraints/parameters	20392/0/1099
Goodness-of-fit on F^2	1.061
Final R indexes [I>=2σ (I)]	R_1 = 0.0669, wR_2 = 0.1837
Final R indexes [all data]	R_1 = 0.0907, wR_2 = 0.1998
Largest diff. peak/hole / e Å^{-3}	2.42/-1.22

Supplementary Table 4.7. Crystal data and structure refinement for $\{Fe(Si(carbazolyl)_3)(THF)\}_2(\mu\text{-}Br)_2$.

Identification code	pb7045
Empirical formula	$C_{46}H_{44}BrFeN_3OSi$
Formula weight	1181.34
Temperature/K	273.15
Crystal system	triclinic
Space group	P-1
a/Å	13.451(9)
b/Å	13.464(10)
c/Å	13.977(9)
α/°	71.117(18)
β/°	74.842(17)
γ/°	77.98(3)
Volume/Å^3	2290(3)
Z	2
ρ_{calc}g/cm^3	1.713
μ/mm^{-1}	0.883
F(000)	1243.0
Crystal size/mm^3	0.12 × 0.08 × 0.06
Radiation	MoKα (λ = 0.71073)
2Θ range for data collection/°	3.15 to 54.206
Index ranges	$-16 \le h \le 17$, $-17 \le k \le 17$, $-17 \le l \le 17$
Reflections collected	35774
Independent reflections	10078 [R_{int} = 0.0434, R_{sigma} = 0.0503]
Data/restraints/parameters	10078/0/484
Goodness-of-fit on F^2	1.107
Final R indexes [I>=2σ (I)]	R_1 = 0.0649, wR_2 = 0.2190
Final R indexes [all data]	R_1 = 0.0828, wR_2 = 0.2326
Largest diff. peak/hole / e Å^{-3}	2.66/-0.41

Supplementary Table 4.8. Crystal data and structure refinement for $\{Fe(Si(carbazolyl)_3)(THF)\}_2(\mu\text{-}Cl)_2$.

Identification code	pb7047
Empirical formula	$C_{88}H_{100}LiN_6O_4Si_2ClFe$
Formula weight	1460.15
Temperature/K	273.15
Crystal system	monoclinic
Space group	$P2_1/n$
a/Å	15.577(8)
b/Å	13.543(7)
c/Å	22.317(12)
α/°	90
β/°	103.521(12)
γ/°	90
Volume/Å^3	4577(4)
Z	2
ρ_{calc}g/cm^3	1.059
μ/mm^{-1}	0.267
F(000)	1552.0
Crystal size/mm^3	0.14 × 0.08 × 0.04
Radiation	MoKα (λ = 0.71073)
2Θ range for data collection/°	2.898 to 50.054
Index ranges	$-18 \leq h \leq 18$, $-16 \leq k \leq 14$, $-26 \leq l \leq 26$
Reflections collected	31658
Independent reflections	8085 [R_{int} = 0.0504, R_{sigma} = 0.0586]
Data/restraints/parameters	8085/0/540
Goodness-of-fit on F^2	1.025
Final R indexes [I>=2σ (I)]	R_1 = 0.0609, wR_2 = 0.1595
Final R indexes [all data]	R_1 = 0.0892, wR_2 = 0.1812
Largest diff. peak/hole / e Å^{-3}	0.94/-0.68

Supplementary Table 4.9. Crystal data and structure refinement for {{Fe(Si(^{Me2}carb)$_3$)(^{Me2}carb)}(μ-Br)$_2$(Li(DME))}$_2$.

Identification code	pb7062A
Empirical formula	$C_{79}H_{95.5}Br_2FeLi_2N_4O_8Si$
Formula weight	1486.73
Temperature/K	100
Crystal system	triclinic
Space group	P-1
a/Å	13.0646(19)
b/Å	13.585(2)
c/Å	23.999(4)
α/°	86.132(2)
β/°	89.713(2)
γ/°	62.673(2)
Volume/Å^3	3773.8(10)
Z	2
ρ_{calc}g/cm^3	1.308
μ/mm^{-1}	1.412
F(000)	1555.0
Crystal size/mm^3	0.143 × 0.064 × 0.057
Radiation	? (λ = 0.7288)
2Θ range for data collection/°	3.768 to 62.906
Index ranges	$-18 \leq h \leq 18$, $-19 \leq k \leq 19$, $-34 \leq l \leq 34$
Reflections collected	83907
Independent reflections	23035 [R_{int} = 0.0512, R_{sigma} = 0.0509]
Data/restraints/parameters	23035/407/1081
Goodness-of-fit on F^2	1.051
Final R indexes [I>=2σ (I)]	R_1 = 0.0468, wR_2 = 0.1209
Final R indexes [all data]	R_1 = 0.0660, wR_2 = 0.1315
Largest diff. peak/hole / e Å^{-3}	0.71/-0.62

Supplementary Table 4.10. Crystal data and structure refinement for $[Li(THF)_4][Zn(Si(^{Me2}carb)_3)(^{Me2}carb)_2]$.

Identification code	pb7074
Empirical formula	$C_{86}H_{88}FeLiN_5O_4Si$
Formula weight	1346.49
Temperature/K	100
Crystal system	triclinic
Space group	P-1
a/Å	14.433(5)
b/Å	14.514(5)
c/Å	19.060(7)
α/°	78.187(4)
β/°	88.685(5)
γ/°	87.895(4)
Volume/Å^3	3905(2)
Z	2
ρ_{calc}g/cm^3	1.145
μ/mm^{-1}	0.275
F(000)	1428.0
Crystal size/mm^3	0.21 × 0.093 × 0.057
Radiation	? (λ = 0.7288)
2Θ range for data collection/°	2.238 to 40.214
Index ranges	$-13 \leq h \leq 13$, $-13 \leq k \leq 13$, $-17 \leq l \leq 17$
Reflections collected	32388
Independent reflections	6860 [R_{int} = 0.0861, R_{sigma} = 0.0639]
Data/restraints/parameters	6860/249/883
Goodness-of-fit on F^2	1.052
Final R indexes [I>=2σ (I)]	R_1 = 0.0919, wR_2 = 0.2495
Final R indexes [all data]	R_1 = 0.1148, wR_2 = 0.2754
Largest diff. peak/hole / e Å^{-3}	1.58/-0.45

Supplementary Table 4.11. Crystal data and structure refinement for $[Li(DME)_2(Et_2O)][Fe(Si(^{Me2}carb)_3)_2)(^{Me2}carb)]\cdot C_7H_{10}$.

Identification code	PB7062B
Empirical formula	$C_{103}H_{84}FeLiN_7Si_2O_{0.5}$
Formula weight	1546.74
Temperature/K	100(2)
Crystal system	triclinic
Space group	P-1
a/Å	13.09054(16)
b/Å	17.6786(3)
c/Å	22.9842(3)
α/°	101.3433(13)
β/°	100.4466(11)
γ/°	101.4246(12)
Volume/Å^3	4975.72(13)
Z	2
ρ_{calc}g/cm^3	1.032
μ/mm^{-1}	0.221
F(000)	1624.0
Crystal size/mm^3	0.62 × 0.37 × 0.26
Radiation	MoKα (λ = 0.71073)
2Θ range for data collection/°	5.592 to 52.744
Index ranges	$-16 \le h \le 16$, $-22 \le k \le 22$, $-28 \le l \le 28$
Reflections collected	167980
Independent reflections	20341 [R_{int} = 0.0455, R_{sigma} = 0.0257]
Data/restraints/parameters	20341/169/1213
Goodness-of-fit on F^2	1.050
Final R indexes [I>=2σ (I)]	R_1 = 0.0864, wR_2 = 0.2629
Final R indexes [all data]	R_1 = 0.1005, wR_2 = 0.2756
Largest diff. peak/hole / e Å^{-3}	1.94/-0.56